



FOUNDED 1894

SAIMM

JOURNAL OF THE SOUTHERN AFRICAN INSTITUTE OF MINING AND METALLURGY

VOLUME 116

NO. 1

JANUARY 2016

WEH

Minerals



Trusted partner of choice



Linatex[®] hoses

Cavex[®] hydrocyclones

Enduron[®] vibrating screens

Linatex[®] rubber lining

Warman[®] slurry pumps

We offer you the lowest cost of ownership

Weir Minerals is the world leader in the design and manufacture of mine dewatering solutions, slurry pumps, hydrocyclones, valves, screens, centrifuges, crushers, feeders, washers, conveyers, rubber lining, hoses and wear-resistant linings for the global mining and mineral processing, sand and aggregate, the power and general industrial sectors.

For more information contact us on +27 (0)11 9292600

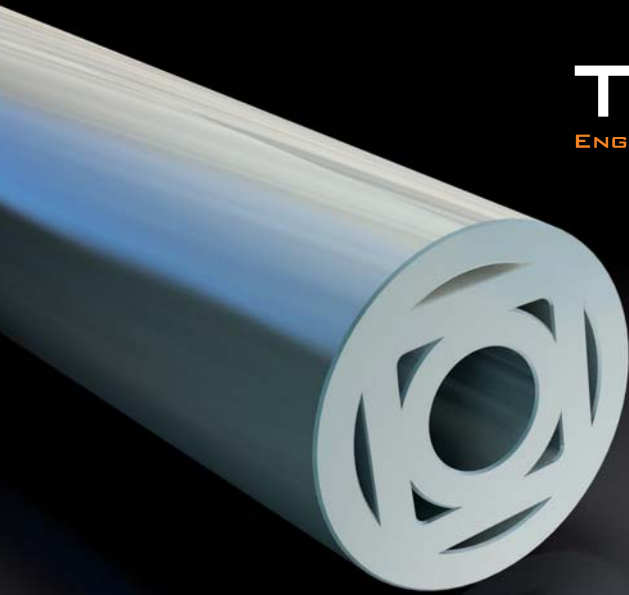
WEIR

Minerals
weirminerals.com



TREFIMET

ENGINEERING IN THERMAL LANCES



TAPPING LEADERS

TR - 25

Trefimet TR-25 lance is a tool capable of generating thermal energy efficiently and accurately. It is the right tool for tapping operations performed in small tap-holes. Thanks to its outstanding accuracy, the TR-25 can give an extended lifetime to all the elements of the tapping set.

ULTRAOXIBAR

Trefimet UltraOxibar lance is a tool that generates high melting thermal energy. It melts, cuts, drills and cleans with great speed and efficiency. It was designed to cut any material that requires high thermal energy to be melted.

THE INNOVATIVE TREFIMET LANCES DESIGN ALLOWS
A SAFER, FASTER AND CLEANER TAPPING OPERATION.



EFFICIENCY

A better use of the energy generated by the lance, means reduced tapping times, lower oxygen consumption and lower labor requirements.



SAFETY

Trefimet lances minimize operators' heat stress and reduces the molten metal spattering and off-gases emissions to the atmosphere.



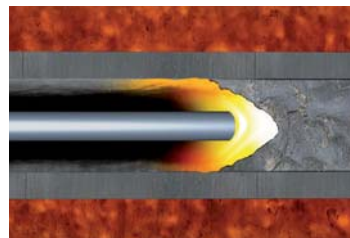
ACCURACY

By projecting the energy in an axial direction, Trefimet lances provide more accurate tapping, increasing the life cycle of the tap-hole passage and its elements.



INNOVATION

Trefimet's new "Easy Click"™ system leaves behind the old couple connection, replacing it with a mechanism that brings a quicker, simpler and safer joint.



WWW.TREFIMET.CL
CONTACT@TREFIMET.CL

ROBERTO PEÑA

E-MAIL: RPENA@TREFIMET.CL
PHONE: +562 2654 6000
MOBILE: +569 8299 8326

OFFICE BEARERS AND COUNCIL FOR THE 2015/2016 SESSION

Honorary President

Mike Teke
President, Chamber of Mines of South Africa

Honorary Vice-Presidents

Mosebenzi Zwane
Minister of Mineral Resources, South Africa

Rob Davies
Minister of Trade and Industry, South Africa

Naledi Pandor
Minister of Science and Technology, South Africa

President

R.T. Jones

President Elect

C. Musingwini

Vice-Presidents

S. Ndlovu
A.S. Macfarlane

Immediate Past President

J.L. Porter

Honorary Treasurer

C. Musingwini

Ordinary Members on Council

Z. Botha	G. Njowa
V.G. Duke	A.G. Smith
I.J. Geldenhuys	M.H. Solomon
M.F. Handley	J.D. Steenkamp
W.C. Joughin	M.R. Tlala
M. Motuku	D. Tudor
D.D. Munro	D.J. van Niekerk

Past Presidents Serving on Council

N.A. Barcza	G.V.R. Landman
R.D. Beck	J.C. Ngoma
J.R. Dixon	S.J. Ramokgopa
M. Dworzanowski	M.H. Rogers
F.M.G. Egerton	G.L. Smith
H.E. James	W.H. van Niekerk

Branch Chairmen

Botswana	L.E. Dimbungu
DRC	S. Maleba
Johannesburg	I. Ashmole
Namibia	N.M. Namate
Northern Cape	C.A. van Wyk
Pretoria	P. Bredell
Western Cape	A. Mainza
Zambia	D. Muma
Zimbabwe	S. Ndiyamba
Zululand	C.W. Mienie

Corresponding Members of Council

Australia:	I.J. Corrans, R.J. Dippenaar, A. Croll, C. Workman-Davies
Austria:	H. Wagner
Botswana:	S.D. Williams
United Kingdom:	J.J.L. Cilliers, N.A. Barcza
USA:	J-M.M. Rendu, P.C. Pistorius

PAST PRESIDENTS

*Deceased

* W. Bettel (1894–1895)	* H. Simon (1957–1958)
* A.F. Crosse (1895–1896)	* M. Barcza (1958–1959)
* W.R. Feldtmann (1896–1897)	* R.J. Adamson (1959–1960)
* C. Butters (1897–1898)	* W.S. Findlay (1960–1961)
* J. Loevy (1898–1899)	D.G. Maxwell (1961–1962)
* J.R. Williams (1899–1903)	* J. de V. Lambrechts (1962–1963)
* S.H. Pearce (1903–1904)	* J.F. Reid (1963–1964)
* W.A. Caldecott (1904–1905)	* D.M. Jamieson (1964–1965)
* W. Cullen (1905–1906)	* H.E. Cross (1965–1966)
* E.H. Johnson (1906–1907)	* D. Gordon Jones (1966–1967)
* J. Yates (1907–1908)	* P. Lambooy (1967–1968)
* R.G. Bevington (1908–1909)	* R.C.J. Goode (1968–1969)
* A. McA. Johnston (1909–1910)	* J.K.E. Douglas (1969–1970)
* J. Moir (1910–1911)	* V.C. Robinson (1970–1971)
* C.B. Saner (1911–1912)	* D.D. Howat (1971–1972)
* W.R. Dowling (1912–1913)	J.P. Hugo (1972–1973)
* A. Richardson (1913–1914)	* P.W.J. van Rensburg (1973–1974)
* G.H. Stanley (1914–1915)	* R.P. Plewman (1974–1975)
* J.E. Thomas (1915–1916)	* R.E. Robinson (1975–1976)
* J.A. Wilkinson (1916–1917)	* M.D.G. Salamon (1976–1977)
* G. Hildick-Smith (1917–1918)	* P.A. Von Wielligh (1977–1978)
* H.S. Meyer (1918–1919)	* M.G. Atmore (1978–1979)
* J. Gray (1919–1920)	* D.A. Viljoen (1979–1980)
* J. Chilton (1920–1921)	* P.R. Jochens (1980–1981)
* F. Wartenweiler (1921–1922)	G.Y. Nisbet (1981–1982)
* G.A. Watermeyer (1922–1923)	A.N. Brown (1982–1983)
* F.W. Watson (1923–1924)	* R.P. King (1983–1984)
* C.J. Gray (1924–1925)	J.D. Austin (1984–1985)
* H.A. White (1925–1926)	H.E. James (1985–1986)
* H.R. Adam (1926–1927)	H. Wagner (1986–1987)
* Sir Robert Kotze (1927–1928)	* B.C. Alberts (1987–1988)
* J.A. Woodburn (1928–1929)	C.E. Fivaz (1988–1989)
* H. Pirow (1929–1930)	O.K.H. Steffen (1989–1990)
* J. Henderson (1930–1931)	* H.G. Mosenthal (1990–1991)
* A. King (1931–1932)	R.D. Beck (1991–1992)
* V. Nimmo-Dewar (1932–1933)	J.P. Hoffman (1992–1993)
* P.N. Lategan (1933–1934)	* H. Scott-Russell (1993–1994)
* E.C. Ranson (1934–1935)	J.A. Cruise (1994–1995)
* R.A. Flugge-De-Smidt (1935–1936)	D.A.J. Ross-Watt (1995–1996)
* T.K. Prentice (1936–1937)	N.A. Barcza (1996–1997)
* R.S.G. Stokes (1937–1938)	R.P. Mohring (1997–1998)
* P.E. Hall (1938–1939)	J.R. Dixon (1998–1999)
* E.H.A. Joseph (1939–1940)	M.H. Rogers (1999–2000)
* J.H. Dobson (1940–1941)	L.A. Cramer (2000–2001)
* Theo Meyer (1941–1942)	* A.A.B. Douglas (2001–2002)
* John V. Muller (1942–1943)	S.J. Ramokgopa (2002–2003)
* C. Biccard Jeppe (1943–1944)	T.R. Stacey (2003–2004)
* P.J. Louis Bok (1944–1945)	F.M.G. Egerton (2004–2005)
* J.T. McIntyre (1945–1946)	W.H. van Niekerk (2005–2006)
* M. Falcon (1946–1947)	R.P.H. Willis (2006–2007)
* A. Clemens (1947–1948)	R.G.B. Pickering (2007–2008)
* F.G. Hill (1948–1949)	A.M. Garbers-Craig (2008–2009)
* O.A.E. Jackson (1949–1950)	J.C. Ngoma (2009–2010)
* W.E. Gooday (1950–1951)	G.V.R. Landman (2010–2011)
* C.J. Irving (1951–1952)	J.N. van der Merwe (2011–2012)
* D.D. Stitt (1952–1953)	G.L. Smith (2012–2013)
* M.C.G. Meyer (1953–1954)	M. Dworzanowski (2013–2014)
* L.A. Bushell (1954–1955)	J.L. Porter (2014–2015)
* H. Britten (1955–1956)	
* Wm. Bleloch (1956–1957)	

Honorary Legal Advisers

Van Hulsteyns Attorneys

Auditors

Messrs R.H. Kitching

Secretaries

The Southern African Institute of Mining and Metallurgy
Fifth Floor, Chamber of Mines Building
5 Hollard Street, Johannesburg 2001 • P.O. Box 61127, Marshalltown 2107
Telephone (011) 834-1273/7 • Fax (011) 838-5923 or (011) 833-8156
E-mail: journal@saimm.co.za



Editorial Board

R.D. Beck
 J. Beukes
 P. den Hoed
 M. Dworzanowski
 B. Genc
 M.F. Handley
 R.T. Jones
 W.C. Joughin
 J.A. Luckmann
 C. Musingwini
 J.H. Potgieter
 T.R. Stacey
 D.R. Vogt

Editorial Consultant

D. Tudor

Typeset and Published by

The Southern African Institute of Mining and Metallurgy
 P.O. Box 61127
 Marshalltown 2107
 Telephone (011) 834-1273/7
 Fax (011) 838-5923
 E-mail: journal@saimm.co.za

Printed by

Camera Press, Johannesburg

Advertising Representative

Barbara Spence
 Avenue Advertising
 Telephone (011) 463-7940
 E-mail: barbara@avenue.co.za
 The Secretariat
 The Southern African Institute of Mining and Metallurgy
 ISSN 2225-6253 (print)
 ISSN 2411-9717 (online)



THE INSTITUTE, AS A BODY, IS NOT RESPONSIBLE FOR THE STATEMENTS AND OPINIONS ADVANCED IN ANY OF ITS PUBLICATIONS.

Copyright© 1978 by The Southern African Institute of Mining and Metallurgy. All rights reserved. Multiple copying of the contents of this publication or parts thereof without permission is in breach of copyright, but permission is hereby given for the copying of titles and abstracts of papers and names of authors. Permission to copy illustrations and short extracts from the text of individual contributions is usually given upon written application to the Institute, provided that the source (and where appropriate, the copyright) is acknowledged. Apart from any fair dealing for the purposes of review or criticism under **The Copyright Act no. 98, 1978, Section 12**, of the Republic of South Africa, a single copy of an article may be supplied by a library for the purposes of research or private study. No part of this publication may be reproduced, stored in a retrieval system, or transmitted in any form or by any means without the prior permission of the publishers. **Multiple copying of the contents of the publication without permission is always illegal.**

U.S. Copyright Law applicable to users in the U.S.A.

The appearance of the statement of copyright at the bottom of the first page of an article appearing in this journal indicates that the copyright holder consents to the making of copies of the article for personal or internal use. This consent is given on condition that the copier pays the stated fee for each copy of a paper beyond that permitted by Section 107 or 108 of the U.S. Copyright Law. The fee is to be paid through the Copyright Clearance Center, Inc., Operations Center, P.O. Box 765, Schenectady, New York 12301, U.S.A. This consent does not extend to other kinds of copying, such as copying for general distribution, for advertising or promotional purposes, for creating new collective works, or for resale.

Contents

Journal Comment—Furnace Tapping 2014, by J.D. Steenkamp	iv-v
President's Corner—Mining Heritage, by R.T. Jones	vi-vii

Articles

Correspondence between J. Freer and R.E. Robinson	viii
A tribute to Prof. Robinson, by Jennifer Robinson	ix
Copperbelt Mining Trade Expo and Conference (CBM-TEC), by J. Delaurentis	22
Erratum: 'Coal quality and uranium distribution in Springbok Flats Coalfield samples' by M. Ndhlalose, N. Malumbazo, and N. Wagner published in the SAIMM Journal vol. 115, no. 12, pp. 1167-1174	53

PAPERS – FURNACE TAPPING CONFERENCE

Tap-hole monitoring technologies by W. Braun, P. GebSKI, R. MacRosty, R. Pula, A. Sadri, and W. Ying	1
Tapping of PGM-Ni mattes: an industry survey by I. Nolet	11
Monitoring, repair, and safety practices for electric furnace matte tapping by L. Thomson	17
SlagFlo™: modulating the flow in the tap-hole by S. Essack	23
An overview of the design, operation, and maintenance practices relating to tap-hole management on a PGM smelting furnace by B. van Beek, T.J. Goff, P.E. Nel, E. Rex.	27

PAPERS OF GENERAL INTEREST

Response surface optimization of process parameters for the removal of F and Cl from zinc oxide fume by microwave sulphating roasting by T. Hu, Z. Li, C. Liu, L. Zhang, J. Peng, and B. Wang	35
Application of finite element method and artificial neural networks to predict the rolling force in hot rolling of Mg alloy plates by Z.Y. Guo, J.N. Sun, and F.S. Du	43
Effects of rolling and cooling process on mechanical properties and microstructure of 600 MPa microalloyed dual-phase steel produced by compact strip production by G-L. Wu, X-B. Liu, and C-Y. Zhou	49
An algorithm for determining kinetic parameters for the dissociation of complex solid fuels by P. Mavhengere, T. Vittee, N.J. Wagner, and S. Kauchali	55
New gas nitriding technique using the interior of the nitrated pressure vessel as the process chamber by R.W. Nell, M. Kleingeld, and L. Liebenberg	65
Statistical analysis of coal mining safety in China with reference to the impact of technology by C. Chu, R. Jain, N. Muradian, and G. Zhang	73
Coal seam fracturing by a high-pressure waterjet technique to increase efficiency of coal mine gas drainage by T. Lu, Y. Guo, and X. Yang.	79
Virgin rock temperature study of Venetia diamond mine by M.Q.W. Jones	85

PAPERS – NUCLEAR MATERIALS DEVELOPMENT CONFERENCE

Solvent extraction and separation of hafnium from zirconium using Ionquest 801 by L. de Beer, D.J. van der Westhuizen, and H.M. Krieg	93
Insights into the potential for reduced refractory wear in silicomanganese smelters by J.D. Steenkamp, P.C. Pistorius, and J. Muller	101

International Advisory Board

R. Dimitrakopoulos, *McGill University, Canada*
 D. Dreisinger, *University of British Columbia, Canada*
 E. Esterhuizen, *NIOSH Research Organization, USA*
 H. Mitri, *McGill University, Canada*
 M.J. Nicol, *Murdoch University, Australia*
 E. Topal, *Curtin University, Australia*



Journal Comment

Furnace Tapping 2014

Furnace Tapping 2014 was the first event of its kind, focusing on the challenges associated with the tapping of furnaces and ways in which these challenges are currently addressed. The conference was inspired by an in-house event arranged by Dr Lloyd Nelson – then employed by Hatch Africa – in 2003, and the need for peer-reviewed papers published in the open literature. This was identified when I conducting a literature survey for my PhD studies, which focused on enhancing the tap-hole design for silicomanganese furnaces.

The event was hosted by the SAIMM, at Misty Hills, on 27–28 May 2014. It consisted of two days of presentations – produced as proceedings of peer reviewed papers—and a one day post-conference tour.

As first keynote speaker, Dr Lloyd Nelson (Anglo Platinum, South Africa), delivered a thoroughly researched review of the literature available on the design, operation, and maintenance of furnace tap-holes in ironmaking, ferroalloys, and base metals. Dr Nelson illustrated the extent of the work that has been done in blast furnace ironmaking to progress towards an understanding of the factors influencing tap-hole life, and highlighted the need for cross-commodity benchmarking of tapping practices and tap-hole management systems, to seek further incremental improvements in safety and performance.

Dr Nic Barcza (Mintek, South Africa) in his keynote address focused on process-related aspects influencing tap-hole life and furnace tapping in general. Using a number of examples, Dr Barcza explained why feed material characteristics and control, smelting conditions – in particular operating temperature, and slag and metal or matte compositions upon tapping created problems in tapping of furnaces. He emphasized the detrimental effect of excessive superheat when tapping either slag or metal/matte.



'Liquid magic' – metal and slag being tapped at Transalloys. The photograph was used on the cover of the printed proceedings for Furnace Tapping 2014 (photograph by Joalet Steenkamp)



Almost too close for comfort – conference delegates admiring the scale of blast furnace tapping at ArcelorMittal South Africa Vanderbijlpark Works (photograph by Maryke Pelsler)

The third keynote address was delivered by Ragnhild Jensen (Elkem, Norway), representing Dr Halvard Tveit, and focused on the improvements made in the tapping of silicon through research sponsored by the Norwegian Ferroalloy Producers Research Association (FFF).

Of the 17 peer-reviewed papers, five documented tapping practices at existing operations. P.G. Geyer and Z. Halifa described blast furnace tapping practice at ArcelorMittal South Africa Vanderbijlpark Works; W.S.B. van Beek, T.J. Goff, P.E. Nel, and E. Rex gave an overview of the design, operation, and maintenance practices relating to tap-hole management of a PGM smelting furnace (Lonmin); S.G. Mgenge and J.D. Steenkamp described furnace tapping practice at Tronox Namakwa Sands; L. Thomson described the monitoring, repair, and safety practices for electric furnace matte tapping (Sudbury Integrated Nickel Operations, Canada), and D.J. Rioux reviewed Teck's KIVCET lead tapping experience (Teck Metals, Canada). The papers by Thomson and Rioux were sourced by Dr Lloyd Nelson.

The 12 remaining papers included reviews of current operations and descriptions of technologies available for tap-hole design, monitoring, closure, and maintenance.

I. Nolet reported on an industry survey conducted on the tapping of PGM-Ni mattes; L. Els, P. Cowx, P. Smith, and R. Nordhagen analysed and optimized fume extraction from a ferromanganese furnace tapping operation (Eramet Sauda, Norway), and J.D. Steenkamp, J. Gous, P.C. Pistorius, M. Tangstad, and J.H. Zietsman conducted a wear analysis of a tap-hole from a SiMn production furnace (Transalloys, South Africa).

Journal Comment *(continued)*

Tap-hole design technologies were addressed by I. McDougall, who described the use of water-cooled tap-hole blocks at Tenova Pyromet.

Tap-hole monitoring technologies were discussed by M. Hopf, who described the monitoring of wear of water-cooled tap-hole blocks by the OPTISAVE fibre-optic method (Saveway), and W. Braun, P. Gebski, R. MacRosty, R. Pula, A. Sadri, and W. Ying addressed tap-hole monitoring technologies (Hatch Goba).

A. Diententhal related the history of the development of tapping equipment and tap-hole closure technologies (TMT Tapping Measuring Technology) and S.C. Essack explained how a slag tap-hole could be closed using a slag flow valve (Tenova Pyromet).

Tap-hole repair technologies were addressed by P. O'Shaughnessy, H. van der Merwe, and S. Botes, who explained how the UCAR®V repair solution could be used to repair tap-holes (Graftech), and L.H. Lindstad, who described the maintenance and larger repairs of tap-holes and tapping spouts (Elkem Carbon).

A. Rödfalk, J.P. Nilsson, N. Brogden, P. Bloemer, A. Lyons, and O.J. Østensen described an automatic ladle level measurement system for monitoring ladle fill rate during tapping (AGELLIS Group), and A. Filzwieser, S. Konetschnik, and E. Dreyer explained why ionic liquid cooling technology would be the safest way of furnace tapping (METTOP).



'That high' – Dr Lloyd Nelson explaining the intricacies of furnace tapping during one of the tea breaks (photograph by Joalet Steenkamp)

Of the 203 delegates, who filled the venue to capacity, the majority (161) were from South Africa. Other delegates were from Austria (5), Canada (4), Chile (2), Germany (5), Namibia (3), The Netherlands (2), New Caledonia (1), Norway (13), Sweden (4), UK (1), and Zimbabwe (2). Companies well represented at the event were Anglo American Platinum Ltd (16), DMS Powders (7), Elkem Carbon (7), Exxaro Resources (6), Hatch Goba (8), Mintek (11), Samancor Ferrometals (13), Samancor Middelburg Ferrochrome (6), Tronox (12), and the University of Pretoria (12).

The post-conference tours to Anglo Platinum Waterval Smelter, Transalloys and the blast furnaces at ArcelorMittal South Africa Vanderbijlpark Works were well attended.

The event was sponsored by RHI AG, Thos Begbie & Co, Agellis Group, Hatch, Dango and Diententhal South Africa, Trefimet, and Elkem.

The organizing committee consisted of Renier Meyer and Isabelle Nolet (Hatch Goba), Buhle Xakalash (Mintek), Hannes Goosen and Vicky Visser (Dango and Diententhal South Africa), Johan Gous (Transalloys), Kevin Hay (independent), Hennie Burger (Tronox South Africa), and Nanne Vegter (Exxaro Resources). The proceedings were edited by Antony Cowey (independent).

The SAIMM takes pride in announcing that it will be hosting a follow-up conference, Furnace Tapping 2018, in South Africa in May 2018. To maintain the high standard of technical papers in the proceedings of Furnace Tapping 2014, the SAIMM envisages for Furnace Tapping 2018 further documentation of tapping practices by existing operators, as well as reviews of current operations and descriptive case studies in which technologies available for tap-hole design, monitoring, closure, and maintenance were applied. Furthermore, the SAIMM would like to include papers with strong contributions from research institutions (focusing on the application of CFD modelling with associated assumptions, including properties of materials and validation of these models; studies on tap-hole clay; studies on refractory interaction with slag/metal/matte specifically under the tap-hole conditions); as well as papers addressing health and safety aspects related to the tapping of furnaces.

Looking forward to meeting you at Furnace Tapping 2018.

J.D. Steenkamp

*Chairperson of the Organizing Committee
Furnace Tapping 2014*



Mining Heritage

Visitors to the SAIMM offices in the Chamber of Mines Building in downtown Johannesburg cannot fail to notice the rather imposing stamp mill in the adjacent pedestrian walkway that was once Hollard Street. This 10-stamp mill went into operation at the Robinson Mine in Langlaagte in September 1886, making it one of the earliest stamp mills on the Witwatersrand. On the nearby noticeboard the fascinating story is told of how the mill was buried in a deep slimes dump and later recovered, exhibited at the Empire Exhibition in 1936, and then erected at George Harrison Park, before being relocated to the Main Street Mining Mall in 2004.

One block west along Main Street is an impressive display of a mine headgear, 23 m high, originally built in 1950 for Rustenburg Platinum Mines. Over the road from that is a mineworker's monument, sculpted by Andile Msongelwa, that was recently erected to recognize the role played by mineworkers in developing the economy of South Africa. Further along the attractive walkway of Main Street, from the mining-house headquarters in the west to Gandhi Square in the east, are other mining-related displays that include cocopans and a replica of the golden rhino from Mapungubwe. A walk around this area leaves one feeling that the mining history of Johannesburg, and indeed the wider region, has been well acknowledged.

There are numerous other places where some local mining history can be explored. Gold Reef City presents a display of mining history that is popular with tourists, including a descent of a 226 m shaft (to Level 5 of Shaft 14 of Crown Mines), and a gold pour. The Sci-Bono Discovery Centre has an interactive mining display aimed primarily at schoolchildren. Fred and Harry Struben's Confidence Reef Mine (a declared Provincial Heritage Site) in the Kloofendal Nature Reserve periodically has guided tours that can be arranged to see the site of an early discovery of the gold-bearing conglomerates of the Witwatersrand in September 1884. The Blaauwbank gold mine near Magaliesburg provides an opportunity to explore the narrow workings inside an early shallow gold mine.

The discovery of the world's most prolific gold mining area certainly transformed the place that became Johannesburg. The discovery of the main reef of gold in 1886 set off one of the largest gold rushes in history, and within ten years Johannesburg was the largest city in South Africa. The Witwatersrand Basin represents the richest goldfield ever discovered. It has been claimed that 40% of all of the gold ever mined has come out of the Basin. About 50 million kilograms of gold has been extracted from the Wits Basin to date. In 1970, South Africa's output accounted for nearly 80% of the world's gold production; forty years later, South Africa's share of world gold production had dropped to less than 8%.

Have we done enough to recognize the site of the discovery of the main gold reef? George Harrison, a bricklayer and prospector, is credited with the discovery, on the farm Langlaagte where he was employed to help build a small house. George Harrison Park, the site of his mining claim, is a very important part of our mining heritage, but is unfortunately in a sad state of disrepair. The site became a National Monument in 1944, and in terms of current heritage legislation is now considered a Provincial Heritage Site. Illegal miners and vagrants inhabit the original mine shaft, and are apparently working the remaining reef in the nearby Central Rand Gold open pit. The historic Langlaagte stamp mill had to be removed from the site when vagrants started using it for firewood. The site custodian, Johannesburg City Parks, seems to be unable to take action to rectify the filthy and unsafe condition of this historic site. In 2010, there were plans to restore and develop the park with designated pathways surrounded by lush grass and trees, a small play area for children, a mining headgear and viewing deck, and a museum showcasing the area's historical value. The viewing deck was erected, but since then, a commemorative plaque has been removed, there has been fire damage to the memorial panel, and metal railings within the old workings have been stolen, making the area somewhat dangerous. Surely we should be doing more to commemorate the official discovery of the gold-rich Main Reef pebble conglomerate.

Mining Heritage *(continued)*

Other areas reported to be under threat include the central avenue of Crown Mines Village (which has been invaded by squatters) with its fine corrugated iron buildings and beautiful plane trees. Last year saw the illegal demolition of the old ERPM Recreation Hall off Cason Road, near Main Reef Road in Boksburg. Until then, the Recreation Hall Annex was one of the few surviving industrial structures designed by Sir Herbert Baker. Further afield, Pilgrim's Rest is also struggling, as the provincial government has failed to maintain the buildings of the town appropriately (as required by various pieces of legislation), and the central reduction works are in urgent need of restoration.

A more controversial part of our mining heritage has been the array of mine dumps that formed a very visible outline of the mining areas along the reef. To nearby residents they were a nuisance, a source of much dust, and a health hazard. To others, they had a romantic appeal and charm – manmade golden mountains with a beauty of their own. One of the most prominent landmarks in Johannesburg was the Top Star drive-in cinema on the top of a mine dump, with a spectacular view of the city skyline. This disappeared a few years ago.

The extravagant homes of some of the early mining magnates (Randlords) on Parktown Ridge have been well preserved thanks to the stalwart efforts of bodies such as the Johannesburg Heritage Foundation. These are well worth visiting on days when special tours are arranged.

Many of the mining magnates (including Cecil John Rhodes) spent a great deal of time at the Rand Club, the most prestigious of the early gentlemen's clubs of Johannesburg. The Rand Club was founded in 1887, the year after the gold rush city came into being. In 1905, the third version of the Rand Club building was completed on the site bounded by Fox, Commissioner, and Loveday Streets. This building has been the site of many historical developments, including the 1895 Reform Committee and the plotting of the Jameson Raid, being a target in the 1913 Miners' Strike, and the tumultuous events of 1922. The building contains many historical artefacts, photographs, paintings, and sculptures (prominently featuring the rather diverse group of Rhodes, Paul Kruger, Queen Elizabeth II, and Nelson Mandela), as well as a well-equipped library. However, the Rand Club has a somewhat uncertain future, as it is not as well frequented today as it was a few decades ago, and it suspended its operations on 30 September 2015, after 128 years. Perhaps it will start up again with the support of a hotel group, or perhaps it could become a museum of mining-related history that provides a venue for special events.

Historical conservation preserves memories and reminds us of the accomplishments of the past – the successes and the failures. What can individuals do to preserve our heritage? One simple practical contribution could be to document what is known today. Wikipedia celebrated its 15th anniversary this month (15 January 2016) and provides a wonderful information resource. There is currently a project underway that intends to document heritage sites in Johannesburg and provide quick response (QR) codes outside buildings that can be scanned with smartphones to automatically link to websites with information (in a variety of languages) about the place being visited. If we all contributed information about people and places that we know about, I am sure the world would be at least a slightly better place.

R.T. Jones
President, SAIMM

Correspondence between J. Freer and R.E. Robinson

Comment on the Journal Comment

Letter from J. Freer to R.E. Robinson

The first thing I read on receipt of the *SAIMM Journal* is the Journal Comment.

In the August 2015 issue, I was captivated by the third paragraph of your Comment as it reflects my thinking as part of the wider issue of energy for eternity – for what I call The Hydrogen Age.

Nor was your thinking missed by Cynthia Carol, one-time CEO of AAC, when she chaired the UN's Conference of Parties in Durban some years ago (COP approx. 16). She noted that what platinum sales to the motor industry were lost through 'Hydrocarbons Must Fall' would be more than made up by platinum sales to the same industry for their hydrogen fuelled fuel cells for the electric propulsion of vehicles of all sizes.

Regarding the wider issue, I would refer to a book titled 'Smelling Land – The Hydrogen Defense Against Climate Catastrophe' by David Sanborn Scott, published in 2007 by the Canadian Hydrogen Association www.h2.ca. I left two copies with the Dept. of Chemical and Metallurgical Engineering's library at Wits for loan to anyone who may be interested.

In it Scott defines what he calls 'hydricity' as the reversible reaction of electricity through water, which produces hydrogen and oxygen while hydrogen through a fuel cell produces electricity and water. The recovery of the water makes hydricity a form of activity for renewable energy where water is the energy source and hydrogen the energy carrier.

Toshiba has designed and is now manufacturing a hydrogen generator mounted in a container. Photovoltaic cells collect rays from the sun to generate electricity on-site for the electrolysis of water. Such a container could be sold to any 'garage' to produce hydrogen on-site to fuel the increasing number of hydrogen fuelled vehicles, especially all those present in the northern hemisphere.

So that's how I spend a lot of my time, gleaning new information where I can and then studying and deducing some interactions.

Reply to J. Freer from R.E. Robinson

Your letter brings back many happy associations of our work together for 50 years in the uranium and mining-metallurgy industry. I apologize for the delay in replying, but this letter has been dictated to my daughter who is punching the keys!

I am a very keen proponent of the fuel cell, particularly after Anglo American's announcement of their sponsorship in South Africa of the fuel cell supply installation for the Chamber of Mines building in Central Johannesburg. This along, with other world projects, makes me a strong supporter of this fuel cell technology as an area where South Africa should play a vital role, given our unique resources of platinum.

The most efficient development of platinum resources is critical if this evolution is to occur, with South Africa at the forefront. The second consideration is a portable, safe, and economic supply of hydrogen gas and its production from other materials (natural gas, methane, methanol), that can be easily and cheaply converted.

It is in this later aspect that we in South Africa can make an additional contribution of great significance. Recovery of mine by-products maximizes the opportunity for not only production of hydrogen gas, but also promotion of sustainable, educated, and prosperous communities.

We have a large and increasing number of engineering graduates emerging from our universities, along with a number of platinum-related projects to be defined and evaluated.

A tribute to Prof. Robinson from his daughter

I write this to honour the life and work of my Dad, Dr R.E. Robinson, who passed away on 21 January 2016. I was privy to the last words that he submitted to the Journal, which was his letter to John Freer, agreeing with the exciting possibilities of a hydrogen age and its potential as a key factor in escalating the viability of the platinum industry in South Africa and prosperity for the nation. I believe the readers of his past Journal Comments may recognize in his response his enigmatic allusion to previously published ideas. The need for efficient processing methods (Platinum in the 21st Century, August 2015) and the possibility of prosperous and productive multidisciplinary communities (Black Swans *versus* White Swans, January 2013, Sustainability: Environmental, Economic, and Social, March 2015).



In his September 2015 unpublished writings he foresaw the declining demand for commodities, the closure and sale of mines, and predicted the predicament facing the industry today. But with optimism he highlighted a few key areas to temper the gloom. Foremost among these was his recognition of the rising role of the platinum fuel cell, which he envisaged coupled with a bipolar electrolysis cell to provide the hydrogen. Together with a small voltage input, these cells would cycle through, one to the other, creating hydrogen fuelled energy and producing a wide variety of valuable by-products, not least of which is water. He had written before on use of this water for agriculture through hydroponic fertigation for production of biomass with enormous potential for food, biofuel, and methane production. To provide an economical source of platinum for the fuel cells, Dad suggests the use of hydrometallurgical 'Kell' recovery processes and new mining techniques to reduce costs and increase yield; he also recognized that new innovations in this field warrant research through a suite of possibilities, sufficient to employ dozens of new graduates. Research, he anticipated, could be funded by improvements in materials processes and sales of valuable by-products, products derived efficiently from the integration of systems. His hopes were that within the communities of South Africa, led by the mining and agriculture industries, graduates would mentor, teach and motivate youngsters, fostering a cycle of enquiry, enthusiasm, and curiosity.

I believe it was his desire to foster curiosity that led him to write the final words of his letter: the ambiguous reference to a number of platinum-related projects to be defined and evaluated. When I challenged Dad to be more specific for the reader, he confirmed that the ambiguity was intentional. He hoped to provoke curiosity in the reader, to challenge you to question, to debate, to comment, and to critique. His hope was that the next generation of graduates will, through shared education, innovation, and research, create a nation where communities can flourish, and South Africans can prosper.

Jennifer Robinson



HATCH GOBA

Member of the
Hatch Group

Hatch Goba (a member of the Hatch Group of Companies) is an employee-owned, multi-disciplinary professional services firm that delivers a comprehensive array of technical and strategic services, including management consulting, information technology, engineering, process development, operational performance, environmental services and project and construction management to the metals and mining, energy and infrastructure sectors.

Our Group has served clients for over 80 years and has project experience in more than 150 countries around the world. With 10,000 employees globally, we have more than US\$35 billion in projects currently under management.



Metals

- Coal
- Industrial Minerals
- Iron Ore
- Iron and Steel
- Light Metals
- Mining and Mineral Processing
- Non-Ferrous

Energy

- Oil and Gas
- Renewable Power
- Thermal Energy
- Nuclear
- Power Delivery and Integration

Infrastructure

- Infrastructure Services
- Ports and Marine Terminals
- Rail
- Roads and Transportation
- Water and Tailings Management

www.hatch.co.za



Safety • Quality • Sustainability • Innovation

+27 (0) 11 239 5300

PAPERS IN THIS EDITION

These papers have been refereed and edited according to internationally accepted standards and are accredited for rating purposes by the South African Department of Higher Education and Training

Papers – Furnace Tapping Conference

Tap-hole monitoring technologies by W. Braun, P. GebSKI, R. MacRosty, R. Pula, A. Sadri, and W. Ying	1
<i>This paper provides an update on three different tap-block monitoring technologies for non-ferrous smelting furnaces that have been developed by Hatch Ltd and some of their clients.</i>	
Tapping of PGM-Ni mattes: an industry survey by I. Nolet	11
<i>Matte tapping and tap-hole repair are critical aspects of matte smelter operations, but very little information has been published on these topics. The paper provides information that was gathered from a survey conducted in the PGM and Ni matte industries on matte tapping practices and tap-hole maintenance strategies.</i>	
Monitoring, repair, and safety practices for electric furnace matte tapping by L. Thomson	17
<i>The smelter at Sudbury Integrated Nickel Operations has two shutdowns per year in order to carry out significant repairs to the matte tap-holes. Work is underway to improve wall and matte end performance in an attempt to extend the time between rebuilds. This paper reviews the approach taken, together with developments in monitoring systems that enable better prediction of tap-hole wear.</i>	
SlagFlo™: modulating the flow in the tap-hole by S. Essack	23
<i>This paper discusses the design, installation and operational performance of the SlagFlo™ control valve that has been developed by Tenova Pyromet. The valve, which throttles the flow of slag in order to control the tapping rate, has proved to be a reliable tool for closing the furnace during normal operation as well as emergency conditions.</i>	
An overview of the design, operation, and maintenance practices relating to tap-hole management on a PGM smelting furnace by B. van Beek, T.J. Goff, P.E. Nel, E. Rex	27
<i>An overview is presented of the tap-hole management approach that is followed at Lonmin's Western Platinum Smelter. The monitoring, alarming, and safety systems related to matte and slag tapping are also discussed.</i>	

Papers of General Interest

Response surface optimization of process parameters for the removal of F and Cl from zinc oxide fume by microwave sulphating roasting by T. Hu, Z. Li, C. Liu, L. Zhang, J. Peng, and B. Wang	35
<i>The effect of parameters such as roasting temperature, holding time, and vapour flow on the removal of fluorine and chlorine from zinc oxide fume were investigated and the process conditions optimized using response surface methodology. The results indicate that the removal of F and Cl from zinc oxide fume using a microwave direct roasting process is feasible and reliable.</i>	
Application of finite element method and artificial neural networks to predict the rolling force in hot rolling of Mg alloy plates by Z.Y. Guo, J.N. Sun, and F.S. Du	43
<i>A computational model combining a finite element method (FEM) with an artificial neural network (ANN) was developed to predict the rolling force in the hot rolling of Mg alloy plates. A comprehensive validation of the prediction model is presented. The resultant ANN model was found to be suitable for online control and rolling schedule optimization.</i>	

**These papers will be available on the SAIMM website
<http://www.saimm.co.za>**

Papers of General Interest

- Effects of rolling and cooling process on mechanical properties and microstructure of 600 MPa microalloyed dual-phase steel produced by compact strip production
by G-L. Wu, X-B. Liu, and C-Y. Zhou 49
The effects of finishing temperature, cooling method, and coiling temperature on the mechanical properties and microstructure of a dual-phase steel produced by compact strip production were investigated. The results show that the appropriate microstructure is acquired by decreasing the finishing temperature using an accelerated cooling and stage-cooling method, and controlling the cooling temperature below the start temperature of martensite transformation of 352°C.
- An algorithm for determining kinetic parameters for the dissociation of complex solid fuels
by P. Mavhengere, T. Vittee, N.J. Wagner, and S. Kauchali 55
A distributed activation energy model was successfully modified for the dissociation of complex fuels according to the random pore reaction model. The ability to accurately determine multiple reactions and changes in the kinetic parameters during the reaction distinguishes the algorithm as a unique and robust method for determining kinetic parameters for the pyrolysis of complex fuels.
- New gas nitriding technique using the interior of the nitrided pressure vessel as the process chamber
by R.W. Nell, M. Kleingeld, and L. Liebenberg. 65
The need to nitride the interior of large machine housings, which are also pressure vessels, for use in a high-temperature gas reactor resulted in the development of a suitable new nitriding technique whereby the vessel interior is successfully used as a process chamber while being heated in a conventional top-hat heat treatment furnace.
- Statistical analysis of coal mining safety in China with reference to the impact of technology
by C. Chu, R. Jain, N. Muradian, and G. Zhang 73
A statistical analysis is presented that shows a positive correlation between technological development, financial investment in safety, and coal mine safety in China. Some suggestions are proposed to further improve safety from the perspective of risk assessment, an interdisciplinary approach, and safety culture.
- Coal seam fracturing by a high-pressure waterjet technique to increase efficiency of coal mine gas drainage
by T. Lu, Y. Guo, and X. Yang. 79
A high-pressure waterjet fracturing technique has been developed in an effort to eliminate the hazard posed by coal seam gas in underground coal mines. A field trial showed that the gas production rate can be more than doubled by using the waterjet-assisted technique before and during longwall extraction.
- Virgin rock temperature study of Venetia diamond mine
by M.Q.W. Jones 85
A comprehensive database of rock temperatures and geothermal gradients at Venetia diamond mine was compiled from borehole temperature surveys. The data demonstrates the value of such detailed virgin rock temperature studies for mine refrigeration purposes.

Papers – Nuclear Materials Development Conference

- Solvent extraction and separation of hafnium from zirconium using Ionquest 801
by L. de Beer, D.J. van der Westhuizen, and H.M. Krieg 93
The solvent extraction characteristics of Ionquest 801 were investigated to determine its suitability for the selective extraction of hafnium (Hf) over zirconium (Zr).
- Insights into the potential for reduced refractory wear in silicomanganese smelters
by J.D. Steenkamp, P.C. Pistorius, and J. Muller. 101
Thermodynamic calculations were conducted on eight sets of data, obtained for seven furnaces on three South African silicomanganese plants, to obtain insight into the potential causes of refractory wear. Theoretical indications suggest that chemical reaction between carbon refractory and slag, as well as dissolution of carbon and silicon carbide refractory in metal, contribute to tap-hole refractory wear. The dissolution of carbon in metal contributes to hearth refractory wear.



Tap-hole monitoring technologies

by W. Braun*, P. Gebski*, R. MacRosty*, R. Pula*, A. Sadri*,
and W. Ying*

Synopsis

This paper provides a progress update on three tap-block monitoring technologies that Hatch has been developing with our clients for non-ferrous smelting furnaces.

The Tapblock Diagnostic System (TDS) is an advanced on-line monitoring system that uses temperature data along with embedded thermal model results to evaluate the condition of a tap-block over its campaign life. Hatch recently installed a second TDS and this paper provides some details on this second installation.

The Taphole Acoustic Monitoring (TAM) system is installed on water-cooled copper tap-blocks and uses the noise from the tapping channel to provide a qualitative indication of wear and deterioration of the tapping channel refractory. In addition, TAM can be used to monitor drilling and lancing performance and potentially could also be used in the future as a guide for automatic drilling and lancing systems.

The third technology is the use of fibre optic sensors to measure temperature on the hot face and in the tapping channel of a tap-block. Fibre optic technology allows installation of numerous sensors in key locations where they are very sensitive to tap-block condition, and also provide more extensive spatial coverage than is possible with traditional instruments. This paper provides an update on our efforts to address issues with premature failure of the sensor cables due to corrosion, and also to turn the vast amount of data from the sensor cable into information that can be used by furnace operators.

Keywords

Tap-block, furnace, fibre optic temperature measurement, tap-block diagnostics, condition monitoring, thermal modelling, refractory condition.

Introduction

Electric arc smelting furnaces contain highly intensive processes to smelt the charge and retrieve the metal content. The challenge with the furnace is to keep the molten material and the slag safely contained inside the crucible, and this requires plant staff to monitor and maintain the furnace and associated equipment very carefully. The tap-block is the fastest wearing component of the furnace and as a result requires a maintenance programme. The aim of the technologies described in this paper is to obtain reliable measurements from the harsh environment inside and around the furnace and to interpret the measurement data so that the plant staff can make informed decisions early enough to maintain safe and reliable operation of tap-blocks.

Hatch is a major supplier to the platinum and nickel industries, where a tap-block

consists of a 1 m³ block of copper lined with approximately 300 mm of ceramic refractory. The copper block is water-cooled internally with an intricate pattern of channels. During tapping, the flow of molten metal or slag through the tap-block gradually erodes the refractory and if the refractory is not maintained correctly, an uncontrolled tap can result. This is obviously very dangerous for operators. Equipment may also be damaged during an uncontrolled tap, resulting in extremely costly repairs and a lengthy maintenance downturn. Hence, the tap-block must be maintained regularly. The plant personnel usually rightly take a conservative approach and maintain the tap-block frequently to reduce the risks of an uncontrolled tap. Better monitoring enables a condition-based maintenance plan, thereby enabling the tap-block to be safely maintained and keeping production losses to a minimum.

The development of the tap-block monitoring systems described in this paper is driven by the desire for a real-time monitoring system.

Tap-hole acoustic monitoring

Background

An acoustic monitoring system for assessing the condition of the refractory lining in a tap-block was developed in close cooperation with Kennecott Utah Copper (KUC). The Taphole Acoustic Monitoring system, or TAM, makes use of acoustic emission events from the tap-block to evaluate the condition of the refractory lining and copper within the block. The prototype TAM system was installed on two KUC tap-blocks for continuous monitoring. A detailed description of TAM can be found in Gebski *et al.* (2013).

* Hatch, Limited.

© The Southern African Institute of Mining and Metallurgy, 2016. ISSN 2225-6253. This paper was first presented at the, Furnace Tapping Conference 2014, 27–28 May 2014, Misty Hills Country Hotel, Muldersdrift, South Africa.

Tap-hole monitoring technologies

Development and installation

The TAM software processes and displays data from a set of acoustic emission (AE) sensors installed around the tap-hole, typically on the cooling water pipes. Using these pipes as waveguides implies that the computed location of an AE event is always related to a specific position along the cooling coil. This is converted to a particular location in the nearest brick in the tapping channel. However, technically this is not a 3D source location algorithm. The 3D presentation of the results is added only to simplify the interpretation. A potential enhancement to this design would be the installation of specially designed waveguides to improve the sensitivity of the AE sensors. This would also allow use of the actual 3D source location algorithm for evaluating the damage in the tap-block. In either case, the AE signal is transferred from the sensors via preamplifiers to the processing unit.

There are numerous sources of AE around a tap hole. In general, AE is defined as high-frequency elastic waves generated with a material. These are detected and converted to electrical signals. The TAM system aims at detecting the signals related directly to the deterioration of the tap-hole brick inserts in the copper block. This degradation of the tap-hole bricks occurs as a result of the flow of molten material (when the bricks are exposed to a high temperature and corrosive environment) and during the lancing or drilling through the tap-hole. The AE activity (understood as the occurrence of the acoustic events) and AE intensity (defined as the strength of the AE signals) are analysed. The activity is linked to the location of the AE source within the tap-hole, while the intensity translates to the severity of the related damage. The intensity is measured by the signal amplitude and energy, as well as the number of acoustic events. The high-amplitude and high-energy events indicate severe damage to the brick inserts. During lancing or drilling, if similar AE activity is measured at the top, bottom, left, and right sections of the tap-hole then it means that the lancing or drilling was done at the intended location and at the desired angle. If the acoustic activity is shifted towards one area (more events are generated from a specific area) then it indicates damage to that specific zone.

It is important to emphasize the need for calibration of the TAM system for each tap-hole. The first part of the calibration is done during the installation of a new tap-hole brick inserts. Calibrated mechanical impactors are used to generate AE sources at known locations within the block. The system parameters, including the wave speed and the warning and alarm levels, are established through this process. The second stage of the calibration must be done during normal operation of the furnace. One outcome of the calibration process is the noise level. The system thresholds and filters must be programmed accordingly in order to remove the irrelevant data. The noise will typically be related to the flow of the cooling water and other normal operations around the tapping area.

An example installation of selected TAM components is shown in Figure 1. The required number and the optimal type of sensors are determined individually for each tap-hole based on its design and through a calibration process. At KUC, four AE sensors were installed on the cooling pipes. The drilling and lancing activities cause acoustic emissions

which travel through the refractory and cooling pipes to the sensors.

In the design of the TAM system, it was critical that both the furnace operators and the personnel on the tapping floor be able to respond accordingly to the TAM's feedback. The design included a human-machine interface (HMI) screen for furnace operators and a light pole near the tap-block for personnel on the tapping floor. Figure 2 shows the main operator screen with a frontal view of a tap-block divided into twelve zones, *i.e.* four zones on the left, four at the bottom, and four on the right.

Depending on the difference in time in arrival time at the four sensors, the source of the AE can be localized to one of the twelve zones. The operator screen gives a qualitative indication of the copper or brick erosion rate in the tapping channel, or indicates off-centre lancing or drilling based on the number and intensity of AE events detected in each zone.

The image presented in Figure 2 shows a higher rate of brick erosion in the bottom right section of the block towards the hot face. This parameter is measured and updated on the screen frequently to show which area of the block is currently most affected, allowing lancing and drilling performance to be displayed in real time.

Optimal drilling should result in a uniform distribution of the AE signals detected in the left, right, and bottom sections of the block. Skewed drilling or lancing is detected by an unequal distribution of AE signals as shown in Figure 3, where the drilling and lancing activity is skewed to the right. These results displayed on the screen in the control room and

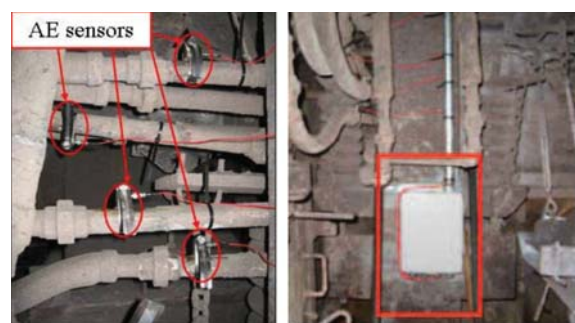


Figure 1—AE sensors and preamplifiers installed near a tap-hole

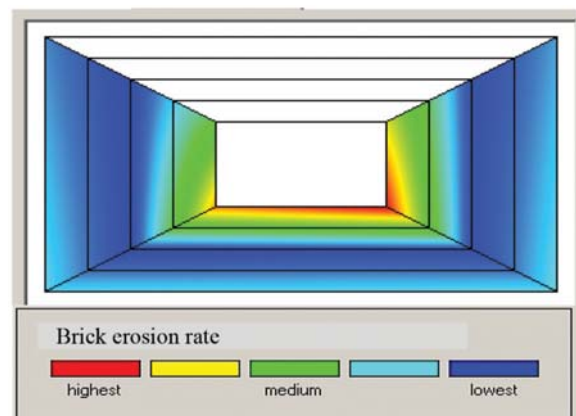


Figure 2—Brick erosion in the tapping channel (TAM screen capture)

Tap-hole monitoring technologies

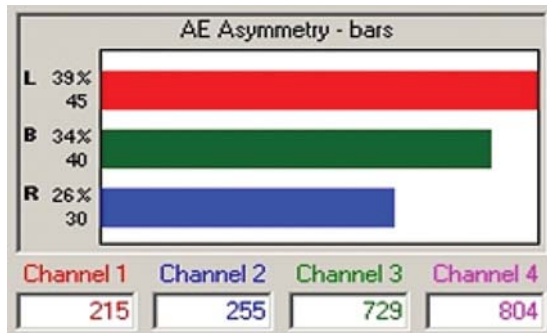


Figure 3—Orientation of drilling or lancing (skewed to the right (R) – the red bar) as indicated by the increase in AE activity

on the tapping floor light pole allow the tapper to take corrective actions and avoid damaging the tap-block. The recorded data is also archived and over the long term it provides trends regarding the tapping practices and the resulting deterioration of the tap-block. This in turn helps to improve the maintenance schedule and to develop optimized tapping routines.

Case study: off-centre lancing

Within the first several months of operation, the TAM system performance and reliability was validated by several incidents, one of which is discussed below.

Due to off-centre lancing of a tap-hole, the refractory inserts were severely damaged. Towards the hot face, the hole was drilled approximately 7.6 cm (3 inches) lower than normal and oriented to the right side of the tap-hole. The opening was as close as 2.5 cm (1 inch) from the copper block. The reduction in refractory thickness resulted in less attenuation of the AE signals compared to normal. The locations of the high acoustic intensity zones identified by TAM within the tapping channel are shown in the top part of Figure 4. For comparison, the lower part of Figure 4 shows the acoustic intensity map during normal operation. Clearly, the off-centre lancing results in a cluster of high-intensity AE signals towards the right side of the tapping channel near the hot face. When the refractory inserts were removed, the inspection revealed erosion of the bricks in the area identified by TAM. The most damaged areas were found on the right and bottom of the tapping channel as shown in Figure 5.

Summary of acoustic monitoring

During the initial two years of operation, the TAM system proved its capability of providing real-time monitoring of tap-holes. In summary:

1. TAM provides a means to reduce the risk of off-centre drilling and lancing to extend the lifespan of a tap-hole
2. The sensors can be retrofitted to a tap-block already in service
3. Although the TAM system can be used for long-term continuous monitoring of tap-hole deterioration, it also provides instant indication of faulty lancing and drilling practices
4. The acoustic emissions are recorded and analysed

throughout the furnace operations to monitor for any events related to a potential tap-block breakdown. This includes lancing, drilling, tapping, and the periods when a tap-block is plugged

5. TAM may provide feedback for future automatic drilling and lancing systems.

Fibre optic temperature monitoring for tap-blocks

Background

Several years ago, Hatch introduced fibre optic temperature sensing technology to enhance tap-block monitoring (Gerritsen *et al.*, 2009). This technology, which uses light to measure temperature, was invented decades ago but has more recently found application in industry. The basic principle of operation is that an etched pattern on the core of a fibre optic strand will reflect light at a specific wavelength. The etched pattern changes with temperature such that the wavelength of the reflected light is proportional to the temperature change. Like any temperature sensor, the response to changes in temperature is calibrated to provide absolute temperature measurements.

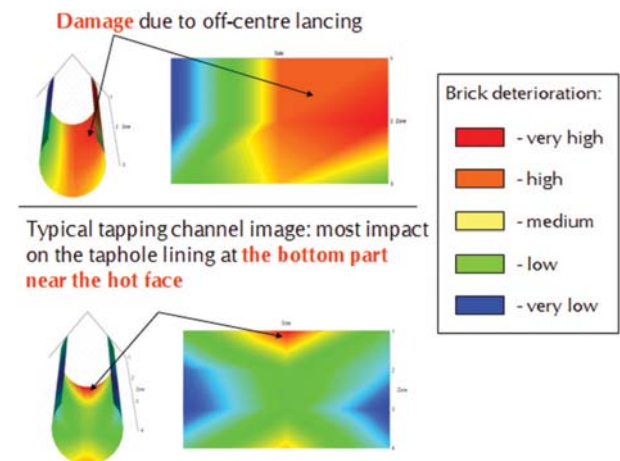


Figure 4—Brick deterioration measured by TAM. Left side shows the tapping channel and right side shows the developed view of the tapping channel

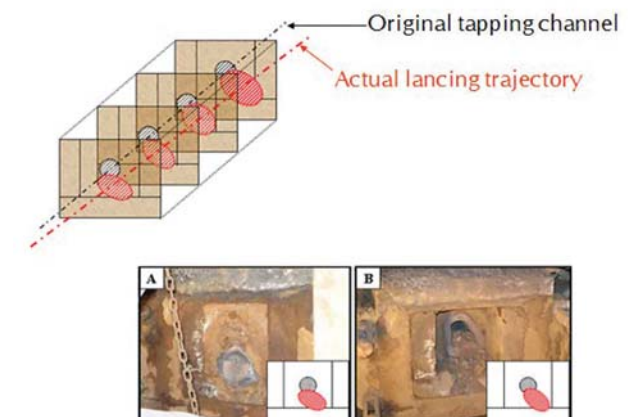


Figure 5—Actual brick damage in the tapping channel

Tap-hole monitoring technologies

Prior to the use of fibre optics, the best practice to evaluate tap-block condition was a combination of thermocouples to monitor spot locations in the copper and resistive temperature devices (RTDs) and flow meter measurements to monitor the overall heat flux from changes in water temperature. The key benefits of the fibre optic temperature sensors are the small size of the fibre and the ability to install many sensors along a single fibre optic strand. In the case of the tap-block, the fibres are installed across the hot face, on or just below the surface of the copper. Figure 6 shows an example of an installation with two fibre strands (in red) on the copper surface. Sensors are typically spaced at 50–100 mm intervals over the regions of interest. A typical installation will involve the addition of 50 fibre optic sensors per tap-block. In contrast, the yellow tubes show a typical thermowell arrangement where this tap-block can accommodate only eight thermocouples.

In addition to the benefits of increased spatial coverage, the small diameter of the fibre allows the sensors to be located such that sensitivity and longevity can be optimized. In general, the closer the sensors are positioned to the molten bath, the greater the response to changes in refractory thickness. However, in order to ensure survival the sensors need to be located on or inside the copper face to protect them from excessive heat and corrosion.

Installation challenges

In the original installation design in 2009, an alloy tube was used to protect the fibre optic sensor cable. The tube is mounted onto the copper surface and shielded from the bath by refractory. This design works well in furnaces that do not suffer from corrosion, as it provides excellent sensitivity to changes in refractory thickness.

In the installations in South Africa, this design did not work well due to the high rates of corrosion. Even though the alloy tube is corrosion resistant, the temperature readings became unreliable after a period of approximately six months due to the corrosion of the alloy tube. Surprisingly, the fibre cable remained intact even after the protective tube was corroded away.

During the subsequent installation in 2012, several changes were made to the design to increase corrosion resistance. The objective was to increase the life of the sensor and keep it on the surface of the copper to ensure the sensitivity to changes in refractory were maintained. To do

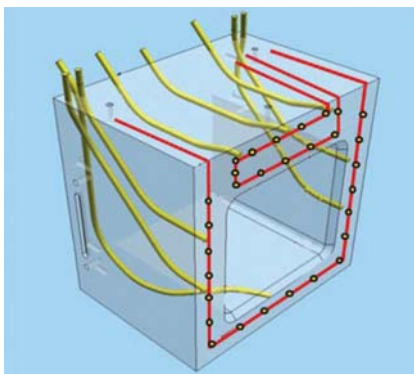


Figure 6—Tap-block showing location of thermowells and fibre optic cables

this, the corrosion allowance was substantially increased by installing the fibre optic cable in a bar of larger cross-section. While the alloy used in the bar design was similar to the tube alloy, the specific grade was further refined, based on the corrosion mechanisms at the copper-refractory interface.

The bar design lasted substantially longer than the tube design in these furnaces. In most locations it lasted the full year-long campaign. On one of the tap-blocks, in the chamfer area (just above the tap-hole on the hot face) the sensor was still compromised towards the end of the campaign. In terms of longevity, the installation was more successful. However, there were some issues with consistency of measurements between different tap-blocks, which made translating the temperature into refractory condition difficult.

In 2013, two new designs were implemented. The first design is a modified sensor bar where pockets are machined into the surface of the tap-block so as to slightly recess the sensor bar. The pocket and sensor bar surfaces are also machined to a high tolerance to ensure that there is excellent thermal contact between them. Better contact and cooling of the sensor bar will improve both measurement consistency and corrosion resistance. A corrosion-resistant coating was also applied to the sensor bar. The thermal conductivity of the coating is equivalent to the thermal conductivity of the castable refractory, and so it is thermally indistinguishable.

The second design implemented in 2013 involves casting the protective tubes into the copper block. This has clear advantages with respect to protecting the tube from corrosion. Consultation with the designers of the tap-block was crucial to ensure the heat removal capability of the tap-block was not compromised by the addition of the sensor tube. Another important consideration is positioning the tubes to maximize sensitivity to changes occurring on the hot face. This involves a trade-off to keep the protective tubes as far as possible from the water pipes, but still embedded deep enough to avoid the risk of exposing the tube through the hot face during the casting process or subsequent corrosion.

After the tap-block was fabricated, ultrasonic testing (Sadri *et al.*, 2009) was carried out to confirm the position of sensor tube relative to the water pipes and hot face of the tap-block. This was essential to confirm that the tubes had not shifted during the casting process, for the following reasons:

1. The tubes must be a minimum distance from the hot face
2. The relative location of the tubes with respect to the copper hot face surface and the water pipes greatly affects the ability to determine refractory condition from the temperature reading.

Both of these systems were installed in June 2013 and are currently being evaluated. This paper was written relatively early in terms of the planned two-year campaign, but both designs were performing well.

Relating measurements to tap-block condition

Once installed, the sensors greatly increase the monitoring capability on the tap-block. However, the full value of these measurements cannot be realized unless one can interpret the data. For example, it is difficult to understand the significance of a 10°C change unless it can be put into context and related to the refractory wear on the tap-block.

Tap-hole monitoring technologies

variations can be eliminated from the fibre optic temperature measurements by measuring the inlet water temperature and subtracting the variations.

Evaluation of temperature measurements

Figure 8 shows the measured temperature response of one of the fibre optic sensors to a sequence of tapping events. This sensor is physically located on the copper hot face above the tapping channel in the centre of the tap-block. The vertical black lines show the tapping events. The green, yellow, and red lines show the expected steady-state tapping temperatures for that sensor for a new, half worn, and fully worn refractory condition.

Several interesting observations can be made from the measured temperature data in Figure 8:

1. Installation of the sensor at the copper-refractory interface provides very good sensitivity to changes in refractory thickness. This expected temperature at this particular sensor covers a range of over 60°C as the refractory deteriorates from a new to fully worn condition. In contrast, thermocouples embedded in the copper may show only 2–3°C increase for the same change in refractory condition from new to fully worn. The increase in sensitivity provided by the surface-mounted sensor greatly enhances the ability to discern a change in the condition of the refractory and confidence in the results
2. The delayed response following the start of the tap is consistent with the refractory's low conductivity and the slow absorption of the energy from the molten material. It is also evident that the temperature continues to rise at the copper-refractory interface after tapping ceases as a result of the energy stored in the refractory (see times between 20:00 and 21:00 in Figure 8). The transient response of the temperature reading is directly related to the amount of refractory. Work is currently under way to develop a relationship between the transient temperature response and the refractory thickness. It is necessary to have an understanding of this relationship for smelting operations that tap occasionally and where the tap-block never reaches thermal equilibrium, as shown following the first two taps in Figure 8
3. Shortly after 23:00, it can be observed that with subsequent tapping there is no associated increase in the temperature above 80°C. This is defined as the steady-state condition for continuous tapping, where the heat load from exposure to the molten material is balanced by the cooling water. In this state, it is possible to evaluate the refractory condition on a consistent basis each time. Based on the wear reference lines (new, half worn, and fully worn) determined from the thermal model, it is expected that this tap-block is approaching a half-worn condition.

The pre-tapping temperature (about 53°C at 19:00 in Figure 8) of the tap-block depends on a number of parameters that cannot be measured and are related to variables such as the time since the last tap and clay plug position. The consequence is that condition assessment during the non-tapping period is very challenging. It has been found that the most reliable time to evaluate the

condition of the tap-block is during a period of continuous tapping (see 23:30 to 00:00 in Figure 8). In this state there are fewer unknown parameters that confound the assessment.

Through both simulations and evaluation of plant data from our fibre optic temperature sensors, it has been shown that the tap-block may reach a steady-state temperature corresponding to the refractory condition. In reality, a steady-state temperature is approached by tapping for a sufficient duration, or tapping repeatedly in quick succession as shown around time 23:00 in Figure 8. Through thermal modelling simulations it has been established that this 'steady-state' temperature achieved by tapping in quick succession is within 2–3°C of the temperature reached during continuous tapping. Considering the 60°C temperature ranges from new to worn conditions, this deviation from the temperature reached during continuous tapping is negligible.

Summary of fibre optic sensors

1. A large number of measurements on a small fibre cable allows good spatial resolution to be obtained and enables temperature readings in locations where it is not possible to install thermocouples
2. Thermal modelling is necessary to put the measured values into context and understand the condition of the refractory
3. Evaluation of the temperatures at a steady-state condition approaching continuous tapping provides a consistent basis to evaluate refractory condition
4. Work is ongoing to relate the transient temperature reading from a single tap to refractory thickness for plants where a steady-state tapping temperature is not achieved.

Tapblock Diagnostic System

Background

The Tapblock Diagnostic System (TDS) is an advanced real-time monitoring system that continuously monitors the tap-block throughout its life and accumulates probable wear events to assess the remaining life of the tap-block (Gunnawiek *et al.*, 2008; Gerritsen and Gunnawiek, 2006). The main purpose of the diagnostic system is to help the furnace operators safely manage the operation and maintenance of furnace tap-blocks. The TDS was first developed in 2003 for Teck Cominco and Lonmin Platinum, prior to the fibre optic temperature system, and uses the operating data such as tap-block thermocouple

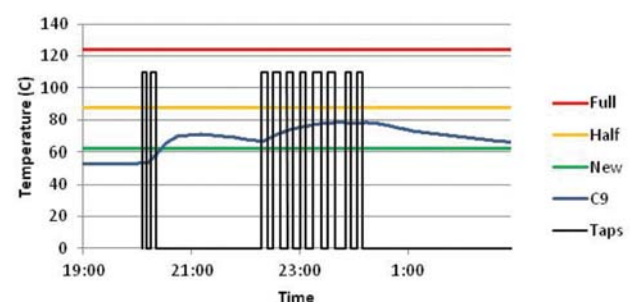


Figure 8—Thermal response of sensors to a tapping event

Tap-hole monitoring technologies

measurements, cooling water temperatures and flow rates to perform the diagnostic calculations and evaluate the residual integrity of the tap-block. Key benefits of this system include the ability to provide early warnings of refractory wear so as to improve safety and maintenance planning.

Since the diagnostic system uses temperature measurements from the thermocouples that are embedded in the tap-block, it is important to verify that the temperature measurements are sensitive to the changes in refractory conditions. Otherwise, the diagnostic system could be ineffective in assessing the tap-block condition and may require more instrumentation closer to the refractory to provide a reliable assessment. In such a case, fibre optic temperature sensors can provide a large number of temperature measurements on the tap-block, as discussed previously, and the diagnostic system can analyse those measurements to assess the condition of the tap-block.

Currently, the diagnostic system is operating at two sites, namely Teck Cominco, Canada, installed in 2003, and Portovesme s.r.l., Italy, installed in 2013. Both plants operate a Kivcet furnace with four tap-blocks, and the diagnostic system simultaneously monitors all the tap-blocks. Several changes have been made to the diagnostic system since the first installation. One of the main changes is the development of a new bump test procedure that can now be performed at any facility to estimate the tap-block thermal resistance. An update on the new bump test procedure and test results are discussed in the following sections. A more general description of the TDS can be found in Gunnewiek *et al.* (2008).

Bump test procedure

Tap-block thermal resistance is the overall thermal resistance between the thermocouple and the cooling water, which includes the copper block resistance, bonding resistance between the copper block and water pipe, and the cooling pipe resistance together with the resistance of any scale build-up that may be present in the water pipes. It is important to measure the tap-block thermal resistance to obtain an accurate estimate of the refractory thickness from temperature measurements.

A bump test is a field trial that can be performed on a tap-block to measure the thermal resistance. The cooling water is used to temporarily lower the tap-block temperature so that the response of the thermocouples can be analysed to estimate the block's thermal resistance. The response of thermocouples to an induced change in the tap-block temperature is typically characterized by a first-order decay function, and the dynamics of this response vary with block thermal resistance. For example, a higher tap-block thermal resistance results in slow thermocouple response, and a lower thermal resistance produces a faster response. Consequently, the thermocouple data collected during a bump test can be compared to thermal model simulations to estimate the tap-block thermal resistance.

At the Teck Cominco installation, bump tests were performed by abruptly lowering the inlet cooling water temperature. This procedure has produced good results for several years; however, it is difficult to decrease the inlet cooling water temperature for a bump test without access to a source of cold water, which was available at Teck Cominco. A

new bump test procedure was therefore designed that instead manipulates the cooling water flow rates to cause an abrupt decrease in tap-block temperature. A graphical representation of the procedure and the expected response is shown in Figure 9. The cooling water flow rate is first reduced to allow the temperature of the tap-block to increase. Once a sufficient temperature rise is obtained, the bump test is initiated by abruptly increasing the cooling water flow rate back to normal so that the tap-block temperature decreases. The actual thermocouple measurements are then analysed to estimate the tap-block thermal resistance.

This procedure can be easily performed at any location once the appropriate bump test flow rates are selected to induce the required change in the block temperature. Thermal model simulations are used to establish the flow rates and duration of the test that achieve a balance between providing sufficient change in tap-block temperature to identify the thermal resistance and maintaining the temperatures within acceptable limits. Furthermore, thermal modelling is also used to determine the transient response of the tap-block to a sudden increase in water flow rate for different tap-block thermal resistances. Such simulation results are used to calibrate the bump test models (essentially first-order transfer functions) that are used together with field bump test data to estimate the block thermal resistance at each thermocouple location.

Results and discussion

A bump test was recently performed on one of the tap-blocks at a client facility using the new procedure. During the test, as expected, the thermocouple temperatures increased upon lowering of the flow rates, reached a steady state, and finally decreased following a first-order response as shown in Figure 10.

Figure 11 shows the normalized thermocouple data collected during the cooling portion of the bump test overlaid on the simulation data. The simulation curves are obtained at different block thermal resistances represented by 0, 10, 20, 30 and 40 μm gaps in the bonding between the copper block and water pipe. This range of gaps is taken as a generic way to represent any factor affecting the heat transfer through the copper block to the water pipe. Generally, there is no physical

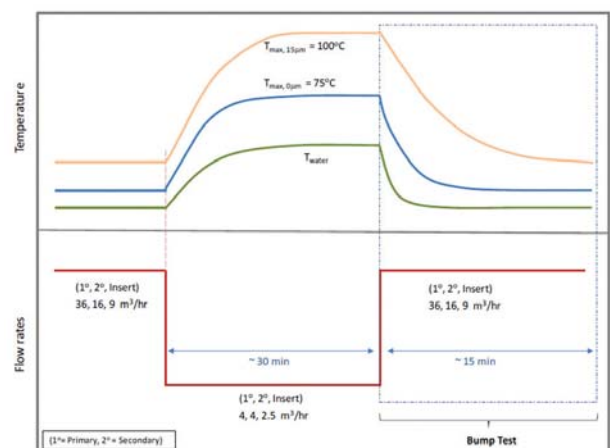


Figure 9—Graphical representation of the new bump test procedure

Tap-hole monitoring technologies



Figure 10—Field bump test trends

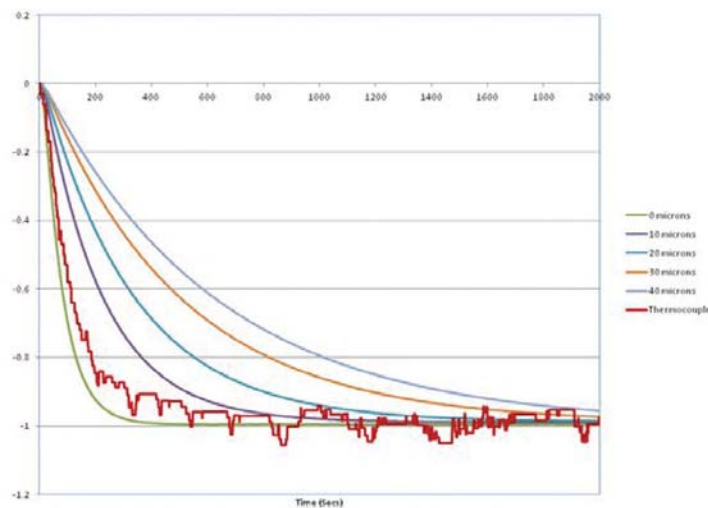


Figure 11—Block thermal resistance estimation

gap at the boundary between the copper block and cooling water pipe. A zero gap represents perfect thermal bonding and results in the fastest thermocouple response, whereas a 40 μm gap results in a slower thermocouple response as the gap impedes the heat flow from the copper casting into the cooling water. Although this range of block resistance does not represent a problem with the tap-block cooling, the range of values has a significant impact on the interpretation of the temperature readings.

The sample field data shown in Figure 11 clearly indicates that the block thermal resistance is between 0 and 10 μm and the diagnostic system has precisely calculated the values to be 4 μm . Similar analysis at different thermocouple locations indicated the tap-block thermal resistance is between 2 and 6 μm . These values are in the same range as those obtained for the Teck Cominco tap-blocks using the previous bump test procedure, and thus provide confidence in the new procedure.

Once calibrated with the tap-block thermal resistance, the diagnostic system estimates the tap-block health during subsequent taps. It was found that after about six months of operation and nearly 300 taps, the health of the tap-block was about 87%. This means that the tap-block is still in good

condition and can safely be used for an extended period of time.

Details of the recent installation

The TDS recently installed at Portovesme s.r.l. was developed in National Instruments control software 'LabVIEW' to simultaneously monitor four tap-blocks. The system was configured to retrieve the operating data from two Siemens S7 programmable logic controllers (PLCs) via OPC, and write important information obtained from diagnostic calculations (tap-block health) to another PLC so that the operators can access the data from anywhere in the plant through the PI historian. So far, the operation of the diagnostic system has been stable, without any reported issues.

In general, the diagnostic system must be designed to present the results in a meaningful way to highlight significant events, and the HMI must quickly point out key conditions that require operator attention and provide the process engineer with insight into particular events of interest with a first-pass analysis. Figure 12 shows a sample operator display for the TDS screen with easy-to-interpret colour indicators (red/yellow/grey) that are used to alert operators to warnings ranging from instrument failure to tap-block

Tap-hole monitoring technologies

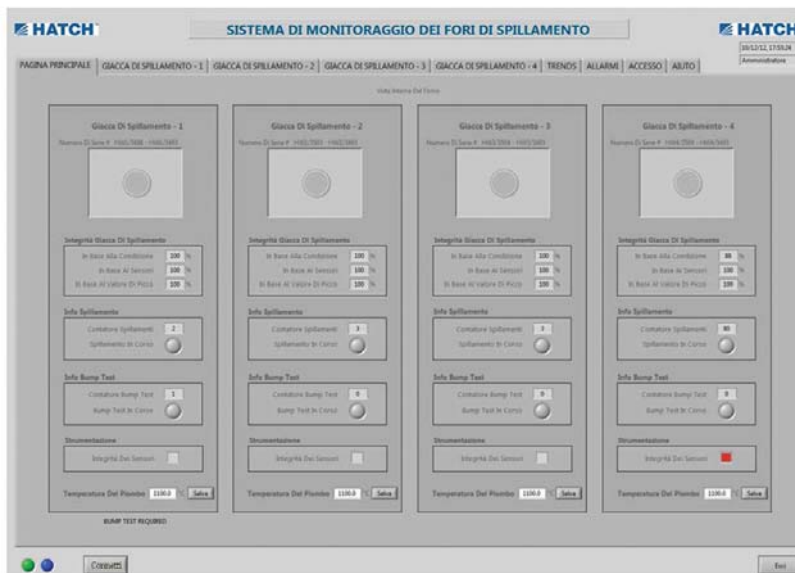


Figure 12—Overview screen of the Tapblock Diagnostic System at Portovesme s.r.l

degradation. The HMI also permits further investigation into warnings as required by using the sub-screens for each tap-block.

Summary of Tapblock Diagnostic System

1. It is important to know the tap-block thermal resistance to accurately evaluate the condition of the tap-block
2. The new bump test procedure was recently tested at a client facility to measure the tap-block thermal resistance, and the estimated thermal resistances appeared to be reasonable and in the expected range
3. The new bump test based on changing the cooling water flow rate can be used at many more operating plants than the previous test, which required a source of cold water.

Conclusions

Hatch remains committed to the continual improvement of furnace technologies. The Taphole Acoustic Monitoring system provides on-line and real-time information to tapping personnel at smelters on the tap-hole condition and can assist with tapping practices. As a result, TAM has strong potential for becoming an integral component of future automated tapping systems that are of interest to many furnace operators.

The new fibre optic temperature measurement technique provides the capability to monitor tap-blocks accurately and with an increased number of measurements. The vast amount of data provided by this system is difficult for plant operational staff to interpret manually, and therefore the computer-based Tapblock Diagnostic System has been developed to assist with the analysis of the data and prediction of the health of the tap-block.

The TDS has been successfully implemented in two plants. The system has made use of a new bump test technique to verify the thermal resistance of a tap-block. The field results have provided confidence in the new test procedure, and this approach can be used at any facility to measure the tap-block thermal resistance.

Acknowledgements

The authors would like to thank the input received from the corporations that have implemented the various Hatch technologies in their tap-blocks. The contributions from staff at Anglo American, Lonmin Platinum, Teck Cominco, Portovesme s.r.l., and Xstrata have been invaluable for the understanding of water-cooled tap-block condition monitoring in the industry and furthering knowledge of a very complex and vital piece of furnace equipment.

The authors also gratefully acknowledge the help of D. George-Kennedy, J. Mullen, R. Van Wagoner, and A. Mattys of Kennecott Utah Copper (KUC) for their help in the development of the Taphole Acoustic Monitoring (TAM) system.

References

- GEBSKI, P., SADRI, A., YING, W., GEORGE-KENNEDY, D., NEXHIP, C., KRIPPNER, D., and KAUR, R. 2015. Advances in continuous monitoring of water-cooled tapblocks for pyrometallurgical furnaces, *CIM Journal*, vol. 4, no. 1. pp. 1–12.
- GERRITSEN, T. and GUNNEWIEK, A.H. 2011. Diagnostic system and method for metallurgical reactor cooling elements. US patent 7 976 770. Hatch Ltd.
- GUNNEWIEK, L., SUER, J.L., MACROSTY R., GERRITSEN, T., and KARGES, A. 2008. Developing a tapblock diagnostic system. *Third International Platinum Conference, 'Platinum in Transformation'*, Sun City, South Africa, 5–9 October 2008. South African Institute of Mining and Metallurgy, Johannesburg. pp. 203–210.
- MACROSTY, R., NITSCHKE, S., GERRITSEN, T., and CROWE, C. 2007. Advances in furnace monitoring: instrumentation. *6th International Copper-Cobalt Conference (Cu2007)*, Toronto, Canada, 25–30 August 2007. The Metallurgical Society of CIM, Westmount, Quebec.
- SADRI, A., GEBSKI, P., and GEORGE-KENNEDY, D. 2008. Development of the Taphole Acoustic Monitoring (TAM) system for water-cooled copper tapblocks. *47th Annual Conference of Metallurgists*, Winnipeg, Manitoba, 24–27 August 2008. CIM, Montreal.
- SADRI, A., GEBSKI, P., GHORBANI, H., MCGARRIE, G., and DE VRIES, T. Monitoring deterioration of waffle cooler thickness at Polokwane Smelter, *JOM*, vol. 61, no. 10. pp. 69–73. ◆

Leader in Refractory Solutions



Adding value to the pyrometallurgical and chemical industries of Southern Africa and the world.

Verref Shaped is a leading manufacturer of refractories and provider of solutions to the pyrometallurgical, chemical and manufacturing industries.

Our team of experienced refractory engineers, metallurgists and technicians can assist with problem identification, areas for improvement and training

Verref Shaped is focused on building long term partnerships, adding value to our partner's businesses from product specification to product disposal.

www.verrefshaped.co.za Email: sales@verrefshaped.co.za

VERREF SHAPED (Pty) LTD.
Barrage Road, Vereeniging
P.O. Box 3560, Vereeniging, 1930
Republic of South Africa
Tel: +27 (0) 16 450 6111
Fax: +27 (0) 86 623 9296



Verref Shaped (Pty) Ltd.
Your Preferred Refractory Solutions Provider



A South African
Manufacturing
Company

The SAIMM Journal all you need to know!

- ★ Less 15% discount to agents only
- ★ PRE-PAYMENT is required
- ★ The Journal is printed monthly
- ★ Surface mail postage included
- ★ ISSN 2225-6253

The SAIMM Journal gives you the edge!

- * with cutting-edge research
- * new knowledge on old subjects
- * in-depth analysis

SUBSCRIBE TO 12 ISSUES
January to December 2016

of the SAIMM Journal

R1 910.00

LOCAL



US\$515.90

OVERSEAS

per annum per subscription



For more information please contact: Kelly Mathee The Journal Subscription Department
Tel: 27-11-834-1273/7 • e-mail: kelly@saimm.co.za or journal@saimm.co.za
Website: <http://www.saimm.co.za>

A serious, 'must read' that equips you for your industry—Subscribe today!



Tapping of PGM-Ni mattes: an industry survey

by I. Nolet*

Synopsis

Matte tapping is one of the most critical operations of a matte smelter. Every smelter has developed particular matte tapping practices and tap-hole repair strategies that are often based on the experience of the smelter personnel. As a result, very little information has been published on these critical topics. This paper aims at providing the information gathered from a survey conducted in the PGM and Ni matte industries on matte tapping practices and tap-hole maintenance strategies for different PGM-Ni matte smelting operations.

Keywords

matte tapping, platinum group metals, nickel, tap-hole maintenance, tap-hole design.

Introduction

During tapping operations, a matte tap-hole and its environment encounter some of the highest heat fluxes in an operating furnace, which make the operations around the tap-hole critically important for safe and reliable tapping. This is particularly the case for platinum group metal (PGM) mattes, which are tapped at higher temperatures and typically superheated by 300–650°C (Shaw *et al.*, 2012), making them aggressive to the tap-hole refractories. Nickel mattes are tapped at lower temperatures and are less aggressive than PGM mattes (Table I).

Matte tap-holes require frequent maintenance involving repairs either with furnace power off or at reduced power, which impacts the overall smelter availability and utilization. The objective of all producers is to tap matte out of the furnace safely and reliably while minimizing downtime associated with tap-hole maintenance. This is done at various levels of sophistication in the industry, depending on factors such as the smelter matte production (*i.e.* furnace size), the dependency on downstream converting (on-site or off-site), smelter personnel experience, *etc.*

Very little information is published within the industry on matte tapping practices and tap-hole maintenance. A questionnaire was distributed to PGM and nickel matte producers regarding three key aspects of matte tapping: tap-hole design, tap-hole operation/tapping practices, and tap-hole maintenance. The responses received from these producers are summarized and presented in this paper.

Methodology

A questionnaire was composed with key questions on each key aspect of matte tapping: tap-hole design, tap-hole operation/tapping practices, and tap-hole maintenance. The questionnaire was sent via e-mail to a large number of producers and responses were returned by e-mail. When required, clarifications were obtained to ensure the data was interpreted correctly. The responses received were compiled and summarized in tabular format, as presented in this paper.

Tap-hole design

All participating smelters (apart from Northam) use a water-cooled copper block surrounding the refractory tapping channel (Table II). The design consists of either several pieces or a single piece of copper and the style of the block depends on several aspects, such as tap-hole location (sidewall *vs.* endwall, above or below skew), wall thickness, cooling configuration in the area, *etc.*

Table I

Overview of PGM and nickel matte compositions and tapping temperatures

	PGM mattes	Ni mattes
Tapping temperature (°C)	1180–1480	1165–1200
Matte composition		
Fe (wt%)	34–44	22–36
Ni (wt%)	14–19	16–48
Cu (wt%)	9–12	1–14
S (wt%)	22–30	25–30
Cr (wt%)	0.1–2.5	-
Superheat (°C)	300–650	100–520

* Hatch, South Africa.

© The Southern African Institute of Mining and Metallurgy, 2016. ISSN 2225-6253. This paper was first presented at the, Furnace Tapping Conference 2014, 27–28 May 2014, Misty Hills Country Hotel, Muldersdrift, South Africa.

Tapping of PGM-Ni mattes: an industry survey

All smelters use water-cooled faceplates (Table II), which are installed external to the metal tap-blocks. They are used to retain the refractory tap-hole modules against the internal hydrostatic bath pressure. At the same time the faceplate provides a flat face for the mudgun to bear against, ensuring a good seal for closing.

All participating smelters (excluding Stillwater) use multiple bricks in their tap-holes, allowing sequential repairs and requiring deep tap-hole repairs only very infrequently. The number of tap-hole bricks varies between 4 and 10 (Figure 1), depending on the length of the tapping channel.

Table II

Matte tapping survey data for primary PGM and nickel matte smelting furnaces (Part A)

PARAMETER	UNITS	Waterval F1-F2	Polokwane	Mortimer	Northam	Lonmin F1	Zimplats	Stillwater EF2	BCL Flash	Anonymous
INFORMATION ON PLANT, TYPE OF FURNACE AND MATTE/METAL PRODUCED										
Plant name	-	Waterval Smelter	Polokwane Metallurgical Complex	Mortimer Smelter	Northam Platinum Smelter	Lonmin	Zimplats	Stillwater Mining Smelter	BCL	-
Plant location	-	South Africa	South Africa	South Africa	South Africa	South Africa	Zimbabwe	USA	Botswana	-
Type of furnace	-	electric furnace	electric furnace	electric furnace	electric furnace	electric furnace	electric furnace	electric furnace	flash furnace	other
Furnace name	-	Furnace 1-2	Furnace 1	Furnace 2	-	Furnace 1	Furnace 1	Furnace 2	FU 508	-
Nature of matte/metal (primary commodity produced)	-	PGM	PGM	PGM	PGM	PGM	PGM	PGM	Ni	Ni
Metal/matte tapping temperature	°C	1350	1480	1450	1350	1480	1250-1400	1180-1280	1200	1165
Estimated matte/metal liquidus temperature	°C	900	900	900	-	850	-	-	1100	645-720
Matte/metal Composition										
Fe	wt%	40	40	38	44	38	42-43	34	36	22
Ni	wt%	16	15	17	14.6	16	14-15	19	16	48
Cu	wt%	9	9	10	9	10	9-10	12	14	1
S	wt%	30	30	29	24	30	22	29	-	25
MATTE/METAL PRODUCTION										
Number of matte/metal tap-holes	#	2	3	3	2	3	2	2	4	6
Number of metal/matte taps per day (from all tap-holes)	#/d	12	6-12	9	1	8	10	6	40	50
Number of ladles per tap	#	1	1	1	2	1	1	1	1	1
Duration of each tap	min	15	20-35	15	60	18	>12	3	15	8-15
Total mass matte/metal per tap	tonnes	15	28-32	17	30	12	9-11	5	21	15
TAPPING PRACTICES										
Tap-hole opening practice (drilling, lancing or combination)	-	combination	combination	combination	lancing	combination	lancing	combination	lancing	combination
Tap-hole closing practice (manual plugging or mud gun)	-	mud gun	mud gun	mud gun	manual plugging	mud gun	mud gun	mud gun	manual plugging	mud gun
Total depth of tapping channel	mm	1374	1465	1773	250	1200	750	540	305	770
Average drilling depth (if drilling)	mm	800	850	1000	-	900	N/A	640	N/A	350
Number of mudgun/drilling units on matte/metal side	#	2	2	2	0	2	2	1	N/A	2
If lancing, is a lance guide being used for alignment purposes?	Y/N	Y	Y	Y	Y	Y	Y	N	N	N
Tap-hole Clay - Binder type	-	pitch	pitch	pitch	water	pitch	water	water	water	resin
Tap-hole clay - Type of aggregate used (material composition)	-	alumina-based	alumina-based	alumina-based	other	alumina-based	alumina-based	other	alumina-based	alumina-based
TAPHOLE DESIGN										
Number of bricks in tap-hole	#	7	10	10	7	6	4	1- 540mm block	5	6
Primary refractory type used	-	alumina-based	alumina-based	magnesia-based	magnesia-based	magnesia-based	magnesia-based	alumina-based	magnesia-based	magnesia-based
Water-cooling used	-	Water-cooled Block and Faceplate	Water-cooled Block and Faceplate	Water-cooled Block and Faceplate	Water-cooled Faceplate Only	Water-cooled Block and Faceplate	Water-cooled Block and Faceplate	Water-cooled Block and Faceplate	Water-cooled Block and Faceplate	Water-cooled Block and Faceplate
Single block or multiple brick tapping channel design	-	multiple brick modules	multiple brick modules	multiple brick modules	multiple brick modules	multiple brick modules	multiple brick modules	single block	single block	multiple brick modules
Use of a maintainable faceplate	Y/N	yes	yes	yes	no	yes	yes	yes	yes	yes
TAP-HOLE REPAIRS										
Typical taphole life before replacement	months	24	24	24	N/A	4	30	1	2-4	12
Preventative maintenance - frequency of repair of a given tap-hole	days	14	25-30	30	Weekly	14 (Alternate between tap-holes. 2 out of 3 tap-holes are used for a week)	3 days (for insert)	30	30 days (5-brick repair)	90 taps-graphite components 630 taps MgCr brick
Preventative maintenance basis	-	Number of taps and tapping time	number of taps	number of taps	time-based	tapping time	tapping time	number of taps	number of taps	number of taps

Table II (continued)

Matte tapping survey data for PGM and nickel matte slag cleaning furnaces (Part A)

PARAMETER	UNITS	Waterval SCF	Stillwater EF1	BCL SCF1	BCL SCF2
INFORMATION ON PLANT, TYPE OF FURNACE AND MATTE/METAL PRODUCED					
Plant name	-	Waterval Smelter	Stillwater Mining Smelter	BCL	BCL
Plant location	-	South Africa	USA	Botswana	Botswana
Type of furnace	-	slag cleaning (electric)	slag cleaning (electric)	slag cleaning (electric)	slag cleaning (electric)
Furnace name	-	SCF	Furnace 1	FU 501	FU 502
Nature of matte/metal (primary commodity produced)	-	PGM	PGM	Ni	Ni
Metal/matte tapping temperature	°C	1250	1230	1200	1200
Estimated matte/metal liquidus temperature	°C	1200	-	1100	1100
Matte/metal Composition					
Fe	wt%	35	39	-	-
Ni	wt%	35	14	24	23
Cu	wt%	15	12	19	17
S	wt%	15	28	-	-
MATTE/METAL PRODUCTION					
Number of matte/metal tap-holes	#	2	2	2	2
Number of metal/matte taps per day (from all tap-holes)	#/d	6	0.03	6	2
Number of ladles per tap	#	1	1	1	1
Duration of each tap	min	15	3	15	15
Total mass matte/metal per tap	tonnes	15	5	21	21
TAPPING PRACTICES					
Tap-hole opening practice (drilling, lancing or combination)	-	combination	combination	lancing	lancing
Tap-hole closing practice (manual plugging or mud gun)	-	mud gun	mud gun	manual plugging	manual plugging
Total depth of tapping channel	mm	1050	540	305	305
Average drilling depth (if drilling)	mm	800	640	N/A	N/A
Number of mudgun/drilling units on matte/metal side	#	2	1	N/A	N/A
If lancing, is a lance guide being used for alignment purposes?	Y/N	Y	N	N	N
Tap-hole Clay - Binder type	-	pitch	water	water	water
Tap-hole clay - Type of aggregate used (material composition)	-	alumina-based	other	alumina-based	alumina-based
TAPHOLE DESIGN					
Number of bricks in tap-hole	#	7	1- 540mm block	5	5
Primary refractory type used	-	alumina-based	alumina-based	magnesia-based	magnesia-based
Water-cooling used	-	Water-cooled Block and Faceplate			
Single block or multiple brick tapping channel design	-	multiple brick modules	single block	single block	single block
Use of a maintainable faceplate	Y/N	yes	yes	yes	yes
TAP-HOLE REPAIRS					
Typical taphole life before replacement	months	24	125 taps	1	1
Preventative maintenance - frequency of repair of a given tap-hole	days	14	not known yet	30	30
Preventative maintenance basis	-	Number of taps and tapping time	number of taps	number of taps	number of taps

Tapping of PGM-Ni mattes: an industry survey

Material selection in tap-hole bricks is often driven by risk management, and these trials have to be carried out judiciously due to the potential loss in production associated with selection of an unsuccessful material. Alumina may be at risk if the tap-hole is frequently washed with slag; in such cases, MgO or MgCr are generally better suited. Figure 1 indicates that 44% of all respondents use alumina-based matte tap-hole refractories, whereas 56% use magnesia-based refractories. As seen in Figure 2, matte tapping temperature is not a criterion in refractory selection.

Tap-hole operation and tapping practices

For the purposes of this paper, tap-hole productivity is defined as the tons of matte tapped per day per tap-hole. When comparing the PGM, nickel matte, and copper matte smelting industries, three distinct regimes are observed (Figure 3).

The tap-hole productivity is lowest for PGM smelting furnaces (1590 t/d per tap-hole). The productivity per tap-hole is higher for the nickel matte furnaces (25–210 t/d per tap-hole), despite operating with more tap-holes (from two to six). Literature data for copper flash smelters (operating with four to six matte tap-holes) shows a step change in tap-hole productivity to 220–470 t/d per tap-hole. The productivity

benchmark for PGM smelting (>1350°C) is currently set by Polokwane and Waterval at 90 t/d per tap-hole (on average).

For a given matte tapping temperature, there is a large variability in tap-hole productivity. This is due to the fact that regardless of the size of the furnace, there is a minimum number of two matte tap-holes for redundancy and maintenance purposes. Hence, while the Stillwater furnace and the Waterval furnace both have two matte tap-holes, the Waterval furnace has a much higher matte production rate, resulting in higher tap-hole productivity.

With regard to tapping frequency, it is important to consider if tapping a particular furnace needs to be synchronized with a downstream converter operation. The tapping frequency at operations that are decoupled from converter operation should be driven by furnace levels, whereas furnaces feeding downstream converters (as molten feed) are typically tapped 'on demand' to suit the converter cycles (Figure 4).

At Northam in particular, matte is tapped only once per day to feed the daily converter cycle. This is the only operation tapping two ladles at a time in order to have sufficient material to feed the converter; all other furnaces tap one ladle at a time. This results in a very long time of 1380 minutes between taps for Northam.

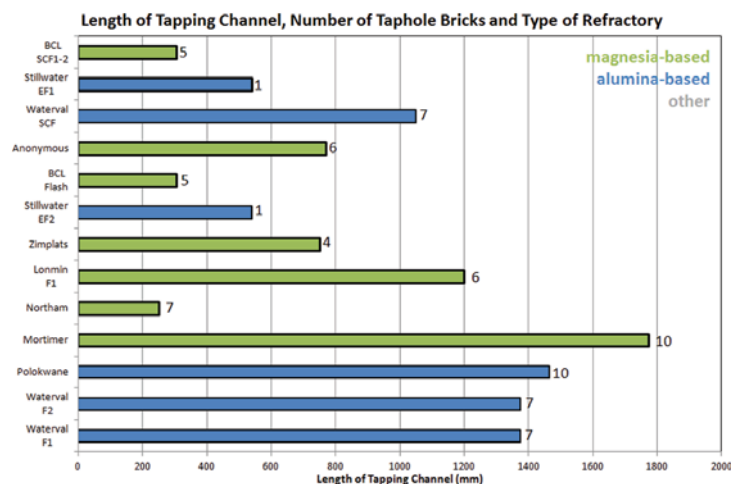


Figure 1—Length of tapping channel, number of tap-hole bricks, and type of refractory

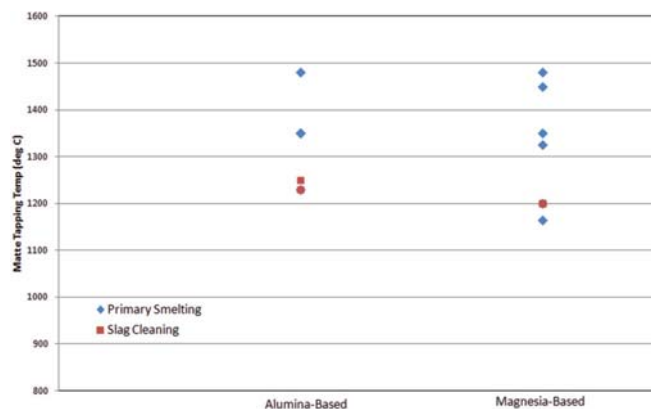


Figure 2—Matte tapping temperature vs. tap-hole brick type

Tapping of PGM-Ni mattes: an industry survey

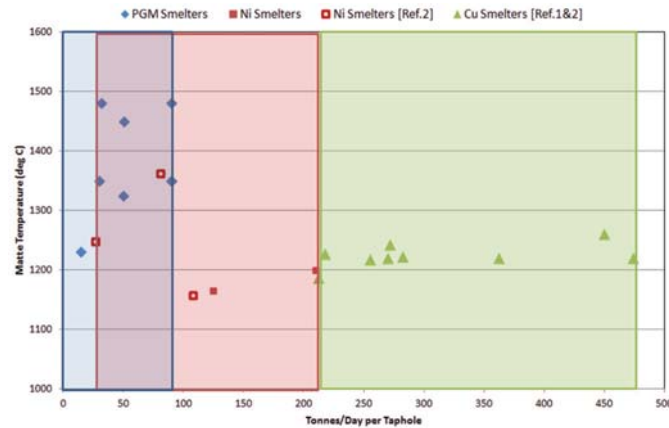


Figure 3—Matte tapping temperature vs. productivity per tap-hole. PGM and Ni smelters based on survey, selected Ni and Cu smelters based on literature data (Schlesinger *et al.*, 2011; Davenport *et al.*, 2003)

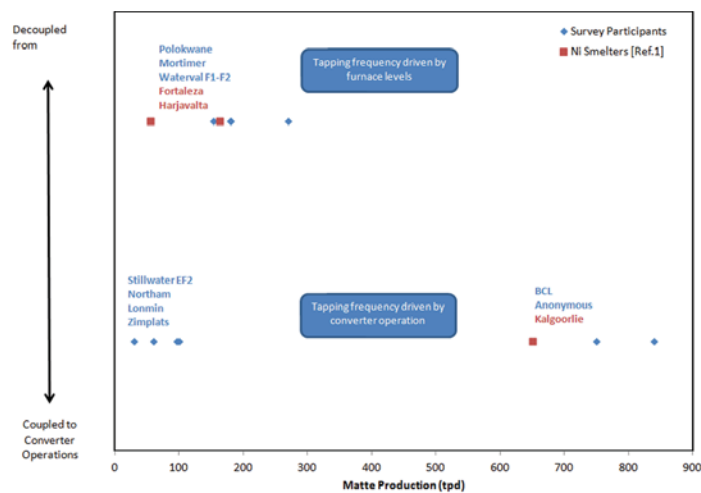


Figure 4—Level of coupling to converter operations vs. smelter matte production for survey participants and literature data (Schlesinger *et al.*, 2011)

BCL and the anonymous smelter produce a large amount of matte (750–840 t/d) and need to regularly feed downstream converters, resulting in a time of 17–21 minutes between taps (*i.e.* many short taps). PGM operations produce less matte (30–270 t/d), resulting in longer times of 100 to 237 minutes between taps (excluding Northam).

The slag cleaning furnaces are different in nature and typically tap between two to six times per day (225 to 700 minutes between taps), except for Stillwater EF1, which taps only once a month. The time between taps can be plotted against tap-hole productivity, clearly showing three different zones for the slag cleaning furnaces (excluding Stillwater EF1), PGM smelting furnaces (excluding Northam), and Ni smelting furnaces (Figure 5).

Most furnaces have a tap duration of 10–15 minutes (Figure 6), except for Northam (60 minutes to fill two ladles) and the 68 MW Polokwane furnace (20–35 minutes due to their larger tap size of 28–32 t). Stillwater has very short tapping times of three minutes, because of the very small tap size of 5 t.

Excluding Stillwater because of the very short tap duration, average matte tapping rates vary between 0.5 and

1.4 t/min (Figure 6). None of the PGM smelting furnaces tap faster than 1.2 t/min. The nickel smelters tap faster (between 1.2 and 1.4 t/min), but at a lower matte temperature. Matte tapping time (obviously related to tapping rate) is an official tap-hole repair trigger criterion for five of the participating furnaces: all five participants show an average matte tapping rate of ≤ 1 t/min. Stillwater, Polokwane, and Mortimer are the only PGM smelters tapping matte at rates faster than 1 t/min (on average).

The majority (66%) of the participating primary furnaces use alternate tap-holes for consecutive taps, allowing a given tap-hole some ‘resting’ time before its next thermal event. The objective of this practice is to enable the tap-hole temperature to return to its baseline level before the next tap. Other smelters use the same tap-hole for consecutive taps and the tap-hole remains ‘hot’ between taps.

For tap-hole opening, 36% of participating furnaces use oxygen lancing whereas the majority use a combination of drilling and lancing. Best-practice operations make use of a lance guide to minimize the potential for damaging the tap-hole when lancing it open. All participating smelters use mudguns for tap-hole closing, with the exception of Northam

Tapping of PGM-Ni mattes: an industry survey

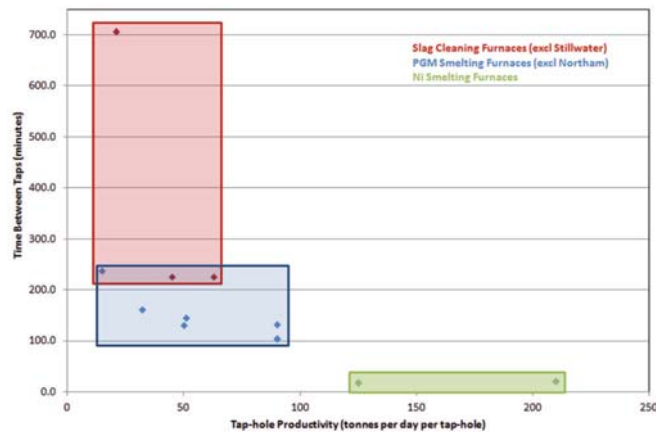


Figure 5—Time between taps vs. taphole productivity for slag cleaning furnaces, PGM smelting furnaces, and Ni smelting furnaces

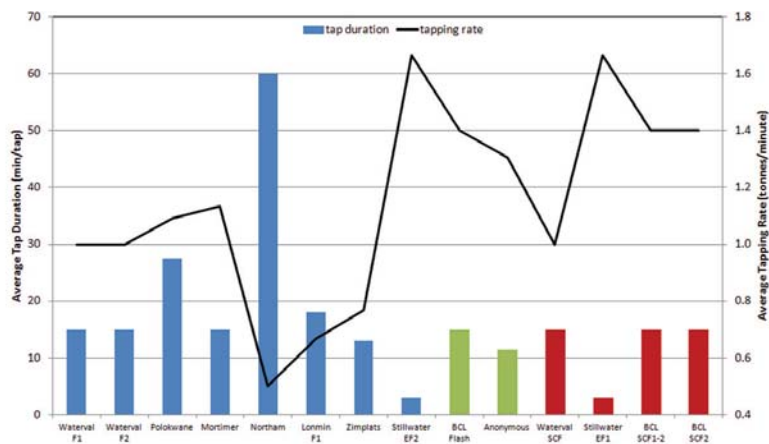


Figure 6—Average tap duration and tapping rate

and BCL (Table II). Tap-hole clay also plays a role in tap-hole life. The quantity of clay injected must be monitored to avoid excessive clay causing gas bubble-driven turbulence in front of the tap-hole hot face. Best-practice operations measure and monitor the amount of clay injected for each tap-hole closure event.

Tap-hole clay technology constantly evolves with new aggregates, binders, and additives. For example, in the blast furnace industry, additives such as SiC, SiN, and zirconium are used to modify the flowing/hardening behaviour of the tap-hole clay. Water-based clays are no longer used in the blast furnace industry as they contribute to the oxidation of the carbon-based tap-hole refractories. Tar-bonded clays are still widely used but raise health concerns due to the carcinogenicity of their volatile component. Phenolic resins and pitch/resin mixtures can also be used as binders. In PGM and nickel matte smelting, water-based clays and pitch-bonded clays are widely used (Figure 7). Resin-bonded clay is used at only one smelter (anonymous), which also reports using graphite components in their taphole. Most furnaces (79%) use alumina-based aggregates. One smelter (Northam Platinum) uses locally sourced soil, and one other smelter (two furnaces) uses an unspecified tap-hole clay aggregate (Figure 7).

Tap-hole maintenance

The tap-hole repair cycle affects furnace availability and utilization (productivity). The downtime associated with tap-hole repairs depends on many factors: the number of tap-holes that are simultaneously repaired, the number of bricks replaced, the ramp-down and ramp-up schedules, operating load during a repair (reduced load, no load), etc.

Most smelters repair only one tap-hole at a time. This could lead to an increased overall downtime for the furnace if the repairs are not scheduled optimally, depending on the duration and ramp-up/down schedule surrounding the repair. In some cases, the loss in production associated with the ramp-up/down can be as, if not more, important than the duration of the repair itself. Some smelters make use of nitrogen or plant air to cool the tap-hole during a rebuild.

It is standard practice to carry out both partial tap-hole repairs, in which only a certain number of bricks from the tapping channel are changed, and deep repairs. In some cases, deep repairs are done with furnace power on (idling power).

Each smelter has developed its own set of criteria to trigger tap-hole repairs. Some smelters use the number of taps, others the tapping time, and some a combination of

Tapping of PGM-Ni mattes: an industry survey

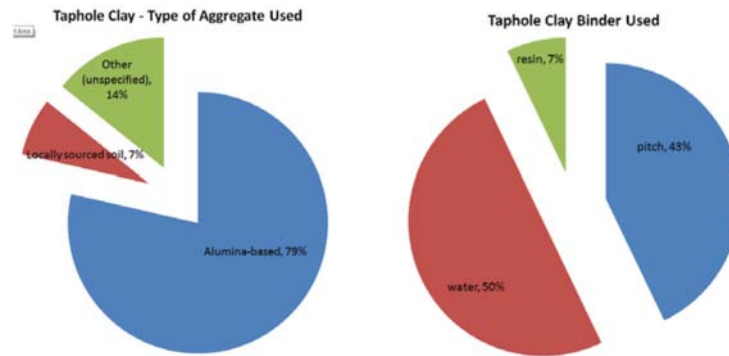


Figure 7—Tap-hole clay – type of aggregate and binder used

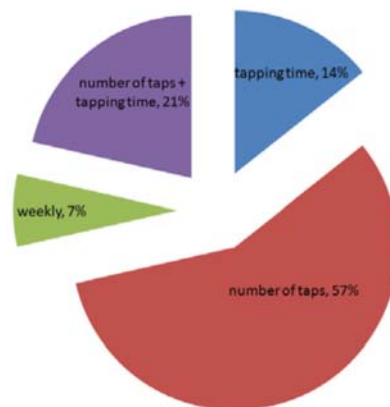


Figure 8—Primary tap-hole repair trigger criteria

these parameters. One smelter simply repairs the tap-holes on a weekly basis, regardless of production indexes (Figure 8). In addition, some smelters also evaluate other factors such as copper temperatures and observations of inner brick condition during partial repairs as secondary repair trigger criteria.

It is difficult to compare tap-hole campaign life reported in the survey because the basis varies from one smelter to another. For example, some smelters reported life of the entire tap-hole, whereas others reported life before a partial repair.

Conclusions

A survey of this nature provides the means to compare matte tapping practices across operations and across industries. It can provide stimulus for operators to challenge their own criteria for maximizing the life of the tap-hole refractories before a repair is triggered. Beyond having an understanding of current practice in the industry, it is critical to have a good knowledge of one's own tapping practices. Records should be maintained of the following:

- Brick types and specifications, and when they were installed and removed from the tap-hole
- Tap-hole clay type
- Tap-hole opening/closing events for each tap-hole, including time open, time closed, duration, tons tapped (and derived tapping rate), *etc.*
- Matte tapping temperatures and matte compositions for each tap

- Photographic records of each tap-hole repair, including a photograph of each brick before it is broken out and as it is re-installed.

The intent is to keep updating this matte tapping database and to obtain more participants across a wider range of matte smelting industries. Anyone wishing to participate in this effort is invited to contact the author at inolet@hatch.co.za.

Acknowledgements

All participants to this survey are gratefully acknowledged. Special thanks to Johan Nell (Hatch), Lloyd Nelson (Anglo American), and Terrence Koehler (Hatch) for their input into the questionnaire.

References

- DAVENPORT, W.G., JONES, D.M., KING, M.J., and PARTELPOEG, E.H. 2003. Flash Smelting: Analysis, Control and Optimization. 2nd edn. TMS Publications, Warrendale, PA.
- SCHLESINGER, M.E., KING, M.J., SOLE, K.C., and DAVENPORT, W.G. 2011. Extractive Metallurgy of Copper. 5th edn. Elsevier, Amsterdam.
- SHAW, A., DE VILLIERS, L.P. vs., HUNDERMARK, R.J., NDLOVU, J., NELSON, L.R., PIETERSE, B., SULLIVAN, R., VOERMANN, N., WALKER, C., STOBER, F., and MCKENZIE, A.D. 2012. Challenges and solutions in PGM furnace operation: high matte temperature and copper cooler corrosion. *5th International Platinum Conference: 'A Catalyst for Change'*, Sun City, South Africa, 18–20 September 2012. Southern African Institute of Mining and Metallurgy, Johannesburg. pp. 193–216. ◆



Monitoring, repair, and safety practices for electric furnace matte tapping

by L. Thomson*

Synopsis

The smelter at Sudbury Integrated Nickel Operations, located in Sudbury, Ontario, operates a single AC electric furnace. This furnace treats nickel sulphide concentrates produced by Glencore and third-party feeds, and as such its performance is critical to the company's nickel supply chain. Currently the plant has two shutdowns per year in order to carry out significant repairs on the matte tap-holes.

Improved monitoring systems that enable better prediction of tap-hole wear have been a continued focus. The electric furnace is an essential part of the smelter flow sheet, requiring planned tap-hole maintenance together with robust systems to manage to this plan.

The ability to meet our goal of zero harm depends on ensuring that safe practices are in place. Detailed procedures and cool-down practices have been implemented to ensure that the required matte chemistry and temperature criteria are met prior to a shutdown for tap-block maintenance.

A major repair of the furnace will take place in 2015. During this rebuild, the sidewalls and matte endwall will be replaced. There is work underway to improve wall and matte end performance in an attempt to extend the time between rebuilds. This paper reviews the approach taken.

Keywords

Tap-block, electric furnace, monitoring systems, safe practices, matte tap-hole repairs, copper coolers, lintel cooler, nickel smelter.

Introduction

The smelter at Sudbury Integrated Nickel Operations, located in Sudbury, Ontario processes approximately 550 000 t of nickel-, copper-, and cobalt-bearing feeds annually. This results in an annual production of more than 70 000 t of nickel and 2300 t of cobalt. The smelter receives concentrate from internal and custom sources. Two company-owned mines, Nickel Rim South Mine and Fraser Mine, located in Sudbury, supply the Strathcona Mill with feed for processing into nickel concentrate. The Raglan Mine in northern Quebec feeds the Raglan Mill. Raglan concentrate is shipped and railed to the smelter. Other custom feeds, comprising both concentrates and secondary materials, are also treated to maximize the smelter capacity.

A single electric furnace treats all nickel sulphide concentrates produced by Glencore as well as third-party feeds, and as such its performance is critical to the company's nickel supply chain.

Tap-hole monitoring and maintenance systems are critical for keeping high online

time on this furnace. This paper will outline these systems as well as our plan for a major furnace rebuild in 2015.

The three main topics that will be discussed in the paper are ensuring tap-hole reliability through monitoring, safety in operation and repairs, and the continued development of matte endwall performance.

Smelter flow sheet description

The flow sheet (Figure 1) consists of a feed preparation area, two slurry-fed fluid bed roasters (with acid plant), a single electric furnace, a four-vessel converter aisle, and matte granulation.

The concentrates are blended in the feed preparation area. The blended slurry at 70% solids density is fed into the two fluid bed roasters. Flux is also added to the roasters to provide a bed and to be pre-heated prior to feeding to the furnace. The roasters operate at 765°C and remove over 70% of the sulphur from the feed. The roaster off-gas stream is directed through the gas handling system, with the calcine dust collected and fed to the furnace and the cleaned gas sent to a single contact acid plant.

Roaster calcine from both roasters is fed into the electric furnace via drags and fettling pipes. The operating temperatures of the furnace slag range from 1350–1400°C, while that of the furnace matte ranges from 1250–1300°C. The slag from the furnace is granulated and pumped to an on-site disposal area. The matte is tapped from one of three matte tap-holes into steel ladles and is transported by molten metal crane to the countercurrent converter aisle for further processing.

* Sudbury Integrated Nickel Operations, Glencore, Canada.

© The Southern African Institute of Mining and Metallurgy, 2016. ISSN 2225-6253. This paper was first presented at the, Furnace Tapping Conference 2014, 27–28 May 2014, Misty Hills Country Hotel, Muldersdrift, South Africa.



Monitoring, repair, and safety practices for electric furnace matte tapping

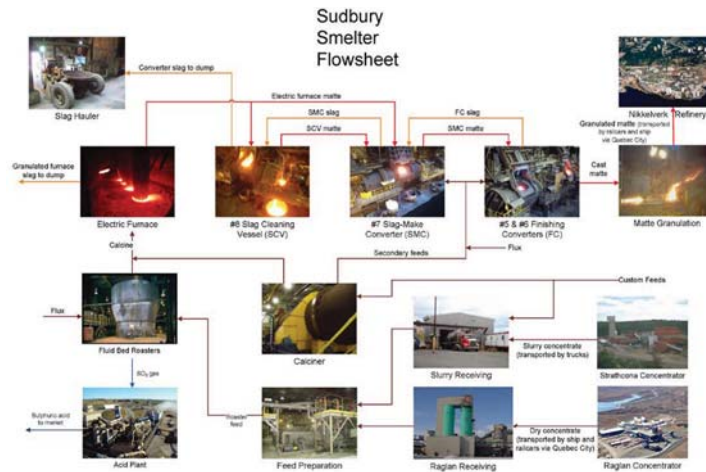


Figure 1—Smelting flow sheet at Sudbury Integrated Nickel Operations smelter

The converter aisle includes a slag cleaning vessel, slag make converter, and two identical finishing vessels.

Matte from the finishing vessels has an iron content of 2% and a pay-metal content of about 76%. This finished matte is granulated, dried, and loaded into railcars for shipment to Glencore’s Nikkelverk refinery in Norway.

Electric furnace operation

The furnace is a six-in-line electric furnace measuring 30 m × 10 m. The furnace operates at power levels up to 45 MW and calcine is directed along the length of the furnace through fettling pipes toward the electrodes. A calcine layer is maintained and regular dips are taken to confirm bath levels.

As well as the calcine fed to the furnace, reverts, secondary materials, and coke are added by mixing in with the calcine in the drag conveyors. The coke is added to maintain reductive conditions and create a metallized furnace matte for improved pay-metal recoveries.

The matte fall in the furnace accounted for approximately 40% of the total calcine fed to the furnace in 2012. On average, 18 matte taps are conducted each twelve-hour shift. The nature of this process requires that furnace matte be tapped ladle by ladle, and transported via cranes to the converter aisle. Ventilation hoods over the tap-holes and launder (Figure 2) pull fume and gas to a dedicated baghouse. More information regarding the hygiene improvements in this area has been previously presented by Salt and Cerilli (2009).

The tap-hole wear at the matte end of this furnace is caused primarily by the frequent tapping and closing of the tap-holes. Water-based clay is used when plugging the holes, and boiling of this clay is a significant contributor to wear. The matte temperature is also controlled to manage tap-hole wear.

There are three matte tapping channels on the furnace, and tapping (Figure 3) is rotated on a shift-by-shift schedule to allow time for cooling and lengthen the time between repairs.

Regular maintenance is performed on the tap-holes, with significant repairs to the blocks in the tapping channel during shutdowns twice per year. The furnace endwalls and sidewalls are repaired only every ten years. The original furnace hearth has been in service since 1978.

Monitoring systems

At the smelter, robust monitoring systems are used as a key means of providing information on tap-hole wear.

Multiple rows of shallow-cooled copper coolers are present on the furnace sidewalls and slag endwall. At the matte end, both shallow-cooled and deeper-cooled copper elements are used. Several thermocouples located in the copper coolers measure the cooler temperatures and this information is fed into the operating control system and data historian. Temperature and flow rate are also monitored on the cooling water streams.



Figure 2—Matte tapping area at Sudbury Integrated Nickel Operations smelter



Figure 3—Matte tapping at Sudbury Integrated Nickel Operations smelter

Monitoring, repair, and safety practices for electric furnace matte tapping

Alarms are configured into the control system to alert the control room supervisor to high temperatures and low water flow rates. Temperature alarming related to the copper blocks has been developed from heat flux modelling to ensure the protection and integrity of each copper element within its design criteria.

Specifically on the matte end tapping channel thermocouples, a predictive temperature monitoring system was installed to identify any shifts in temperature trends or unusual temperature behaviour. This system is able to identify and advise of changes even while the temperatures are still within normal values.

Fibre optic temperature measurement is also being tested on the cooling elements called 'doghouses' in two of the three matte tapping channels. The intent at this stage is to provide more resolution on the tap-hole temperatures to validate the measured trends on the existing copper cooler thermocouples. With further development, the fibre optic system may allow for better characterization of the rate of tap-hole wear.

Procedures are in place to respond to all alarms on the furnace cooling systems. Managing high temperatures on coolers at the matte end can include options such as reducing furnace power and limiting tapping from a specific tap-hole where high temperatures are detected. Tap-hole repairs may also be scheduled in response to higher temperature readings.

In general, the facility has a conservative culture when managing risk in regard to furnace integrity. Intensive reviews are completed prior to any changes to operating practices and cooler design at the matte end. The site uses a Management of Change system for tracking when changes are made to the process, practices, or equipment in the area. This system includes a formal and stepwise approval process and criteria to determine if a specific risk review assessment is required. The risk review must include representation from operators, maintenance personnel, technical resources, supervision, and joint health and safety committee members. Following the risk review, final approval is required to ensure all identified risks can be mitigated or managed prior to making the change.

For significant changes on the furnace a peer or third-party review may be conducted. This step is determined at the smelter management level.

There is a comprehensive risk register in place for the electric furnace integrity system to monitor key activities and track continued improvements. The key performance metrics are summarized for management on a monthly basis. All recurring activities are tracked in a risk-based document system called CURA.

The deep copper coolers at the matte end (Figure 4) have either Monel or Cu/Ni alloy tubing and all connections for water piping are located outside the furnace wall. This set-up is the same for both the shallow- and the deep-cooled elements. Sand seals are in place above each matte end tap-hole covering the coolers and instrumentation cables. A moisture detection system that alarms back to the operating control system DCS is used to detect any leaks in these areas.

Several of the systems and practices in place at the Sudbury smelter have been developed through correlation of key tapping parameters with on-site monitoring of the tap-block condition during both the frequent and semi-annual

block replacements, as well as during test campaigns with new deep-cooling blocks.

To date, there has been good success in managing refractory wear rates with no major events related to unexpected temperatures. The systems in place have been able to ensure appropriate response to temperature trends and for completing appropriate tap-hole repairs. During removals, the copper coolers have been found to be in good condition.

In August 2012, elevated temperatures were detected in the zone above the middle tap-hole on the deep lintel copper cooler that was being tested at that time. The monitoring systems were able to detect these temperatures and alarm appropriately. In response to these temperature trends, tapping times on this hole were reduced, allowing for time to plan for repair in this tapping channel and removal of the deep lintel for inspection. Further information on the deep lintel development is given below.

Tap-hole repairs – ensuring safety

To maintain tap-hole integrity given the high matte tapping rates on the furnace, regular first- and second-level repairs are required. To meet the goal of zero harm we want to ensure that safe practices are in place while carrying out these repairs. Prior to repair, specific criteria must be met to ensure frozen matte conditions behind the repair zone.

Over the years, detailed procedures and cool-down practices have been implemented to ensure that the required matte chemistry and temperature criteria are met prior to repair. The philosophy behind the cool-down practice is to ensure there is solid material ten inches past the working face.

Prior to a scheduled tap-block repair, the tap-hole is taken out of service to allow for cooling. An air sparge may also be used to increase the rate of cooling.

In the first two levels of repair, molten conditions still exist behind the frozen matte. In the highest level of repair, conducted during twice-annual shutdowns, the furnace level is reduced, cold charge material is added behind the tap-hole, and power is reduced to ensure frozen conditions behind all tap-holes on the matte endwall.

With the exception of the first-level repair, a stainless steel sheath is inserted in the matte tap-hole at least 24 hours ahead of the planned repair. The hollow sheath is inserted ten inches past the planned working face. The depth for sheath installation will change based on the specific number of blocks to be repaired. Two thermocouples are

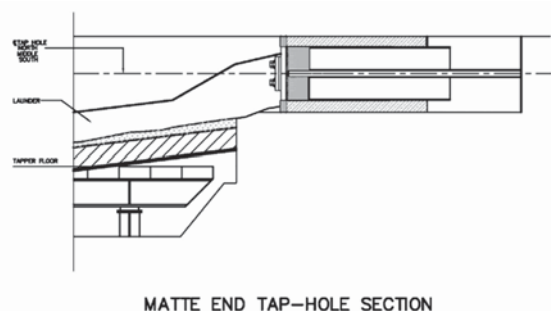


Figure 4—Matte end tap-hole section – side view

Monitoring, repair, and safety practices for electric furnace matte tapping

inserted inside the sheath to measure both the working face temperature and the temperature ten inches past it. These thermocouples are connected to the operating DCS for trending the cooling rate and remain in place until the start of the repair.

Once the sheaths are in place, the roaster rate and power input are controlled to ensure that matte temperature, matte superheat, and bath level criteria are met for the start of the repair. Temperature and chemistry data is reviewed by the leader of the repair crew on the morning of the repair. If the outlined criteria are not met, further discussion must be held to assess risks and determine if the repair is to proceed.

The furnace operates with a metallized matte. This degree of metallization is controlled during the time leading into repairs. For the third-level repairs, the metallization is lowered to aid in chipping of the matte plug.

Table I summarizes the criteria for three typical levels of tap-block repairs.

Development of deeper cooling on the matte endwall

The most recent furnace wall rebuild was in 2004. For the five years following this wall rebuild, very few elevated temperatures were detected in the tapping channels. In June 2009, elevated temperatures began occurring in the tapping channels toward the end of the campaigns. In the last few years, elevated temperatures have required close management of tap-hole rotation leading up to each of the major repairs.

Since 2009, work has been underway to improve the wall and matte end performance in an attempt to extend the time between rebuilds. The goal is to improve the design such that elevated temperatures are eliminated, allowing regular tapping rotation to be maintained up to the end of the campaigns. This improvement would provide greater flexibility on the timing for the twice-annual maintenance outages.

With higher nickel production targets continuing to be achieved at similar smelter feed grades, a higher throughput is required in the two roasters and furnace. Given the single furnace operation and close tie-in to the converting aisle, the required matte tapping rates per shift have increased. To increase smelting rates, the matte temperatures and superheats have also been increased. Figure 5 summarizes the matte taps per day on an average annual basis since

2008. Average daily tapping rates for 2013 are 28% higher than in 2008.

Until three years ago, repairs were made to the matte tapping blocks twice per year, with the cooling elements, specifically called the doghouses, being pulled out only once per year to allow for bricking repair in front. Based on the increased temperatures being recorded on the cooling elements, this strategy has been changed, with the doghouse now being pulled during both of the two outages to allow for more extensive repairs.

In 2009, in response to elevated temperatures on the doghouse cooling blocks, the focus was to develop deeper cooling above the tapping channel (Figure 6). The objective is to extend the matte endwall life by extending the tapping channel away from the doghouse edge.

The initial design for the deep lintel was for a larger copper cooler with refractory lining at the hot face to be inserted past the doghouse in order to push out the isotherm. This lintel (Figure 7) was installed on the middle tap-hole in the summer of 2011 and remained in service for two six-month campaigns. The deeper cooling above the tapping channel was found to be successful in protecting the doghouse from elevated temperatures. However, elevated temperatures that required closer management occurred near the end of the campaigns on the deep lintel cooler itself.

The second design (Figure 8) incorporated a graphite block at the hot face that was installed on the middle tap-hole in the summer of 2012. After two months' service, elevated temperatures were measured on this block. The tapping on

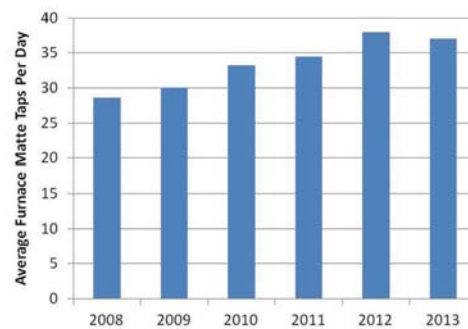


Figure 5—Furnace matte taps averaged on an annual basis for the last 5 years

Table I

Summary of criteria for matte tap-hole repairs

Level of tap-block repair	Cool down time (h)	Temperature criteria (Must be met prior to repair)	Bath level criteria	Superheat criteria (deg C)	Other steps
First Level	Min 24 h	T/C inserted to working face depth - ensure frozen conditions	Total bath and matte level at normal operating levels	matte < 150	Temp check on each block during removal
Second Level	Min 24 h	Sheath inserted 10" past working face. Two T/Cs to measure temp 10" past and temp at working face	Total bath and matte level 92% of normal operating levels	matte <100	Roaster rate limited once sheaths in place, phase 1 (matte end) power idle
Third Level	Typical 48-72 h	Sheath inserted 10" past working face. Two T/Cs to measure temp 10" past and temp at working face	Total bath 50% of normal operating levels, slag present at matte taphole level	matte <100, slag < 100	Roasters off, phase 1 power off, cold charge and roof T/Cs inserted and trended

T// - Thermocouple

Monitoring, repair, and safety practices for electric furnace matte tapping

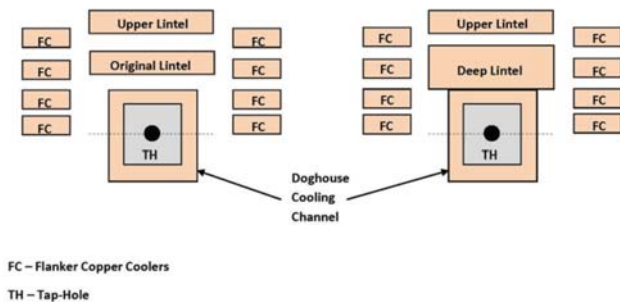


Figure 6—Schematic of matte end tap-hole design front view. Left: original design, right: current design



Figure 7—Refractory-lined copper deep lintel



Figure 8—Graphite-lined copper deep lintel prior to installation

this tap-hole was reduced to manage the temperatures, and after one month the tap-hole was taken offline to complete a tap-hole repair and removal of the graphite-lined copper lintel. At this time, the refractory-lined copper lintel was put back in service.

Upon removal and inspection, the graphite was found to be worn back in the bottom section (Figure 9), consistent with the location of the thermocouples where the highest temperatures were recorded. Further analysis showed that, given the elevation of the lintel cooler near the slag-matte interface, maintaining an adequate build-up layer was difficult. At the furnace re-start in June 2012 with the new cooler in place, the solid slag build-up in front of the cooler was present, but with time and tapping frequency, this build-up could not be maintained to provide an adequate protective layer in front of the cooler (Cerilli, 2012).

Furnace wall rebuild in 2015

The last major repair to the furnace was conducted in June 2004 when the sidewalls, endwalls, and arched roof were rebuilt. Copper cooling on the furnace was also improved at this time, with the previous finger cooler arrangement being replaced by a plate cooler design.

A significant repair of the furnace is planned for 2015. During this rebuild, the sidewalls and both endwalls will be repaired.

The walls have been in place for nine years and have worn back over time. Currently, the wall thickness limits the extent of repair in the tapping channel and ultimately the ability to shift the matte isotherm.

The new bricking of the matte endwall will improve the wall condition. This, together with the improved cooler design, will allow for more refractory to be installed and maintained in front of the coolers during the twice-annual shutdowns.

While the deep lintel has improved protection of the doghouse, trials have proven the need for further improvement to the upper wall zone above the deeper lintel. Thermal modelling has also been carried out to confirm the impacts on the matte tidal zone and isotherms in the area.

With the upcoming furnace wall rebuild, plans are in place to incorporate deeper cooling elements higher up the endwall. This arrangement is expected to allow for a more robust matte end design as well as enable deeper refractory repair with proper tie-in support from above to keep the refractory securely in place during operation.

The current repair procedure for removing the doghouse while supporting the upper wall relies on the installation of temporary jacks. When the jacks are in place, access to the area for repair is very tight, making the installation awkward. As a result of the new supporting system and the new bridge cooler design, these jacks will no longer be required. Improvements to the repair procedure are expected owing to better access, ultimately allowing for a deeper refractory replacement.

On the future design, while the cooling blocks will be pushed deeper, it is planned for the bridge lintel cooling coil to extend past the doghouse but still within the deep lintel and plate cooler to minimize the risk of matte attack.

Additional cooling water piping will be added to the matte end of the furnace. Currently, several coolers are tied into each cooling water line. Inlet and outlet temperatures and water flow rates are monitored on each line and no major



Figure 9—Graphite-lined copper deep lintel removed in September 2012

Monitoring, repair, and safety practices for electric furnace matte tapping

deficiencies have been seen. However, having many coolers on one line complicates the ability to detect a rise in temperature on an individual cooler. With the new piping, key coolers will be placed on dedicated cooling lines to improve resolution on this aspect.

Summary

The single electric furnace at the smelter at Sudbury Integrated Nickel Operations is a key element in the company's nickel supply chain, requiring robust systems to ensure optimal furnace integrity and long campaign life.

Development work continues on improving the monitoring systems to provide a better prediction of tap-hole refractory wear.

With the high matte tapping rates due to the nature of the process, frequent tap-hole repairs are required on the tapping blocks. Repair procedures and cooldown practices have been implemented and are followed closely to ensure that required

matte chemistry and temperature criteria can be met during the period leading into a shutdown for tap-block maintenance.

Development work to improve matte end performance has been underway since 2009, and has focused on deeper cooling elements above the tapping channel and deeper installation of refractory to extend the tapping channel away from the doghouse edge.

A significant repair of the electric furnace will take place in 2015 and will incorporate improvements to the matte endwall.

References

CERILLI, E. 2012. Findings on removal of graphite deep lintel. Internal Communication, Sudbury Integrated Nickel Operations, Sep. 29, 2012

SALT, B and CERILLI, E. 2009. Evolution of the converter aisle at Xstrata Nickel's Sudbury Smelter. The Minerals, Metals & Materials Society Conference, San Francisco, CA. ◆

Copperbelt Mining Trade Expo and Conference (CBM-TEC) Dates and Venue confirmed for 2016

Industry heavyweights will once again be making their way to the heart of the Zambian mining region to participate in the Copperbelt Mining Trade Expo and Conference (CBM-TEC). The 2016 show will be the third in the annual CBM-TEC series, and follows on from a positive response received from stakeholders involved in the previous two events.

The show dates have been confirmed from 12 to 13 May 2016, 'says Nicole Smith, CBM-TEC event director.' The event will take place at the Kitwe Showgrounds, which is able to accommodate the growth of CBM-TEC. The additional space will be used by exhibitors to showcase large equipment and run product demonstrations. It also enables us to provide more technical workshops and other initiatives we have planned.'

CBM-TEC is a mining technical supplies and equipment trade expo for the Copperbelt region, hosted exclusively within the Copperbelt. The product focus of CBM-TEC is leading-edge mining and related products; industrial, engineering, and manufacturing; energy; electrical engineering; materials handling; safety, health, and environment; and construction.

In association with the Electra Mining Africa exhibition in Johannesburg, South Africa, CBM-TEC is organized jointly by Specialised Exhibitions Montgomery and Spintelligent, the leading Cape Town-based trade exhibition and conference organizer, and the African office of Clarion Events Ltd, based in the UK.

Issued by: Joanne Delaurentis, The PR Partnership
On behalf of: Specialised Exhibitions Montgomery
email: joanne@prpartner.co.za

J. Delaurentis
The PR Partnership



SlagFlo™: modulating the flow in the tap-hole

by S. Essack*

Synopsis

Tenova Pyromet's SlagFlo™ control valve is designed to throttle the flow of molten slag in order to control the tapping rate. In addition, the SlagFlo™ valve has proved to be a reliable tool for remotely closing the slag tap-hole during normal operation, as well as emergency conditions.

This piece of equipment makes use of a water-cooled copper element that is hydraulically operated and attached directly to the slag tap-hole. The equipment is compact, simple to maintain, and cost-effective to purchase and install. It can be retrofitted to most existing slag tap-holes with minimal modifications.

During the development phase, finite element method (FEM) and computational fluid dynamics (CFD) software was extensively used to model predicted operating conditions and to optimize the design. By using CFD, it was possible to understand the flow patterns inside the copper element and to optimize these to improve overall performance.

The SlagFlo™ valve was installed and commissioned in 2011/2012 on a 12 MW furnace as part of a new mineral wool plant built in the USA. It has performed well since its installation, despite operating under conditions in excess of the original design criteria. During the first 6 months of operation it quickly became the preferred method of closing the furnace, although the design intent was for occasional use during emergency shut down conditions only. Since replacing the mudgun as the main method of closing the tap-hole, a few minor changes were made to the installation in order to cope with the increased heat load and much higher frequency of use.

The SlagFlo™ valve has also been installed in South Korea, on two mineral wool furnaces designed and supplied by Tenova Pyromet in 2015. Both furnaces are scheduled to be in full production by the second quarter of 2016.

Tenova Pyromet is investigating modifications needed to suit other commodity furnaces with more aggressive slag chemistries.

Keywords

slag valve, flow control, mineral wool, water-cooled copper, slag tapping.

Introduction

During 2010, Tenova was awarded the contract to design and supply a 12 MW mineral wool furnace in the USA. This furnace required a slag flow control device for each of the two tap-holes. This provided the opportunity to develop a slag flow control valve based on previous experience. A robust design was required, as this is a continuous tapping process and the demands placed on the equipment are extreme. In addition, space constraints in the tap-hole area of a relatively small furnace meant a compact design that is easy to maintain was a requirement upfront.

Mineral wool manufacture

Mineral wool is manufactured by spinning molten aluminosilica slag into fibres. Fibres can be manufactured by blowing or spinning. Fibre lines can be fed by coke-fired cupola or by electric arc furnace. The mineral wool fibres are deposited in layers and may be combined with a resin binder, pressed, and baked depending on the final product. The mineral wool product has very good thermal and sound insulation properties.

Mineral wool is also referred to as slag wool or stone wool, depending on the raw material that is used. Slag wool is made from blast furnace slag, which is a by-product of steel production, while stone wool is made using aluminosilicate (basalt) rock as the raw material. (Crane and McLaren, 2008).

Depending on the raw material used and the final processing, a wide variety of products can be made servicing the following roles (Saint-Gobain ISOVER, 2008; Eurima, 2011):

- Fire protection
- Ceiling boards/dry walling
- Filtering and gasket elements
- Growth medium for hydroponics
- Fibre addition to reinforce various plastics, friction materials, and coatings.

The typical slag composition and operating temperature range of a so-called 'stone wool' is shown in Table I.

The slag viscosity is plotted as a function of temperature for these two slag compositions in Figure 1.

The challenge

Functional requirements

The slag valves are designed to modulate the flow of slag. This is a requirement imposed by the downstream spinning equipment. In order to maintain consistent fibre quality, the slag stream must be consistent and controlled.

* Tenova Mining and Minerals (Pty) Ltd.

© The Southern African Institute of Mining and Metallurgy, 2016. ISSN 2225-6253. This paper was first presented at the, Furnace Tapping Conference 2014, 27-28 May 2014, Misty Hills Country Hotel, Muldersdrift, South Africa.

SlagFlo™: modulating the flow in the tap-hole

Table I

Typical slag composition and liquidus temperatures

Description	Units	Formula 1	Formula 2
Slag liquidus temperature	°C	1340	1290
Tapping temperature range	°C	1450–1550	
SiO ₂	[% , w/w]	41.04	40.77
Al ₂ O ₃	[% , w/w]	19.17	18.87
MgO	[% , w/w]	6.27	5.64
CaO	[% , w/w]	18.83	18.98
Fe ₂ O ₃	[% , w/w]	0.43	0.40
MnO	[% , w/w]	9.61	10.12
TiO ₂	[% , w/w]	0.21	0.14
Na ₂ O	[% , w/w]	0.48	0.70
K ₂ O	[% , w/w]	1.38	1.38
P ₂ O ₅	[% , w/w]	0.06	0.018

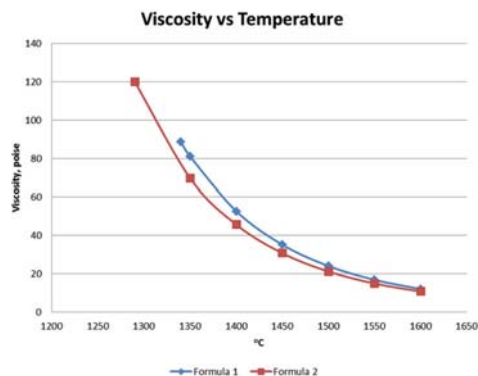


Figure 1—Slag viscosity as a function of temperature (Muchena, 2012)

The client specified that the slag valve should also be able to shut the slag tap-holes under emergency conditions, freezing slag inside the tap-hole and closing the furnace.

The mineral wool furnace is tapped on a continuous basis, with a scheduled stop approximately twice a month during which maintenance can be performed on downstream equipment. Before the stop in the production line, the slag tap-hole is closed and the furnace power reduced to idle the furnace. This quasi-continuous operation subjects all equipment in the tap-hole area, including the slag valve, to very high heat loads and does not allow for frequent maintenance.

As with many furnaces, space is at a premium in the tap-hole area. Since this is a relatively small furnace with two closely spaced tap-holes, the problem of space was compounded.

Figure 2 shows the slag tap-hole equipment, which comprises the following items:

- Slag tap-hole inner block
- SlagFlo™ valve assembly
- Tap-hole faceplate
- Integrated valve guide
- Steel flange.

Equipment dimensions and operating data are shown in Table II.

The slag tap-hole inner block and tap-hole faceplates are both water-cooled copper elements. These pieces of equipment use a freeze lining design to protect the tap-hole equipment. The water cooling channels are designed to minimize the risk of explosion in the unlikely event of a burn-through of the tap-hole cooling elements. The water cooling circuits have fixed piping sections extending outward from the copper equipment. This is done in order to move the flexible hoses away from the high radiation and potential slag splash zone. The flexible pipes, which are less temperature-resistant than the fixed piping, are thus protected from the very high heat loads, extending their life.

The guide for the valve is integrated into the faceplate design. This guide acts as a mechanical limit to excessive horizontal movement of the slag valve.

Consistent flow of slag to the spinners is paramount, so position changes to the copper piston are made incrementally. The SlagFlo™ valve is actuated remotely by a set of push-button controls or remotely from the SCADA. The control of the valve is a simple operator-controlled task. A combination of visual feedback of the slag stream and feedback from the spinner is used by the furnace operators to decide on what changes must be made to the position of the valve. If an emergency shut is required, the furnace operator lowers the SlagFlo™ valve completely. This action slows the flow of slag, and the water-cooled elements freeze the slag inside the tap-hole, effectively closing the furnace. The SlagFlo™ valve can be set up to close automatically under certain circumstance, like a furnace trip or loss of water, should the specific operation warrant this action. Using feedback from the spinning equipment to introduce an element of automation would be an area for future work.

The steel flange shown in Figure 2 is installed in order to facilitate tap-hole repair and replacement from the outside of the furnace. This flange is designed to act as a lifting support frame when the inner block is removed for maintenance or replacement and during first installation.

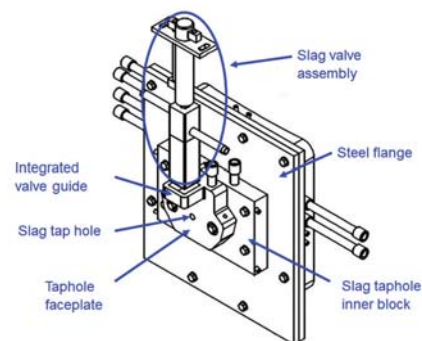


Figure 2—Slag tap-hole assembly showing the SlagFlo™ valve (heat shield is not shown for clarity)

Table II

Equipment dimensions/operating data

Description	Units	Value
Tap hole diameter	mm	38
SlagFlo™ valve dimensions (incl cylinder) – length x width x height	mm x mm x mm	275 x 100 x 780
Slag flow rate	tons/hour	6

SlagFlo™: modulating the flow in the tap-hole

Modelling the design

A model of the SlagFlo™ valve was created using ANSYS software. A combination of FEA and CFD modelling was used to predict the equipment temperatures. This paper includes only the results of the CFD modelling. The boundary conditions for the CFD analysis are presented in Table III.

The heat transfer in the SlagFlo™ copper piston is largely due to two mechanisms; (1) slag in contact with the copper and (2) cooling water on the copper. The heat transfer from the slag was represented by a convection heat transfer coefficient, on two faces of the copper. The heat transfer between the copper and the water, on the internal water passages, was modelled using the 'conservative interface flux' condition in ANSYS. The heat transfer on the remaining external faces of the copper is negligible compared with the other heat loads. No freeze lining was modelled on the copper. This represents the moment that the molten slag comes into first contact with the new copper valve.

A thin freeze lining in the region of 2 mm has been reported to form almost instantly (Nourse, 2014) but the purpose of the model was to confirm that the SlagFlo™ valve would withstand the highest heat load incidents.

As shown in Figure 3, the initial simulations predicted temperatures in excess of 627°C (900K). As copper begins to lose its mechanical strength at approximately 360°C (Matweb, 1999), this temperature profile is unacceptable.

By optimizing the design of the flow channels inside the SlagFlo™ valve, the simulated temperatures were brought down to within the acceptable range. Figure 4 shows that there are small areas, closest to the contact area with the slag, where the expected copper temperatures are at the limit of the acceptable range.

The SlagFlo™ valve is subjected to the force of the slag flow and the force of closing the copper piston against frozen slag build-up that may occur during the tapping cycle. Since these forces are relatively low, the acceptable design temperature for this specific case is higher than for other copper equipment typically specified by TENOVA.

The SlagFlo™ copper piston is a consumable item and is expected to be replaced periodically as it wears. The wear pattern on the copper piston is expected to be asymmetrical, with the hot face side of the valve wearing faster than the cold face. The slag valve has been designed with enough material between the water channel and the slag to allow for approximately 30 mm of wear on the slag valve. Once the valve has worn back by 30 mm it must be replaced. If it is

replaced at this stage, there will still be a safe amount of copper between the water and the slag.

Installation and operation

The equipment was installed at a plant in the USA at the end of 2011, and the furnace was switched-in during the first quarter of 2012. Reports of initial operation were positive and in line with client expectations. The SlagFlo™ device operates consistently with the tap-hole partially closed. With the taphole 30–40% closed, production is consistent and stable at the required tapping rate of approximately 6 t/h. Once the tap-hole approaches 60% closed, the slag flow becomes inconsistent due to freezing in the tap-hole (Mogotlhong, 2015).

Shortly after switch-in, the SlagFlo™ valve became the preferred method of closing the furnace, rather than the clay gun. The tap-hole is reopened directly by drilling, with lancing often not required at all. The SlagFlo™ valve in the USA has been used to close the tap-hole at least 50 times between switch-in and the middle of 2015, excluding unplanned and emergency shuts (Mervos, 2015).

In Figure 5 the slag valve can be seen in operation. Note the uniform slag stream with the SlagFlo™ valve partially closed. Figure 5 also shows how the flexible piping is largely shielded by surrounding equipment, which reduces the heat load (most of the flexible piping is not visible in this photograph).

Figure 6 is a photograph taken of the SlagFlo™ copper piston to show the wear pattern that was seen after some months in operation. The lower edge of the valve shows signs of erosion where the slag stream impinges on the valve. This occurs when heat flux in the area is high, before the slag has frozen against the valve. The horizontal striations are a result of the furnace operator removing the frozen slag from the copper piston. Overall, the wear on the

Description	Units	Value
Copper		
Heat transfer mechanism		Convection
Heat load applied – (convection heat transfer coefficient)	W/m ² K	2034
Slag temperature	°C	1427
Water		
Reference pressure	Atm	1
Inlet normal speed	m/s	2
Inlet temperature	°C	45
Outlet pressure	Pa	0

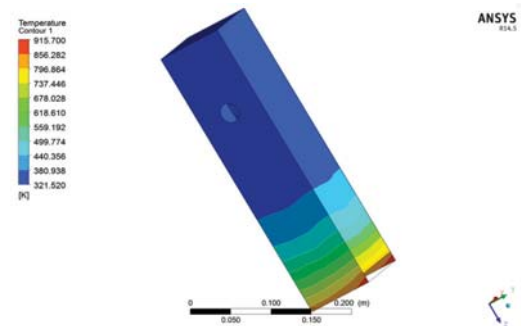


Figure 3—Initial temperature profile [in Kelvin] for the SlagFlo™ valve

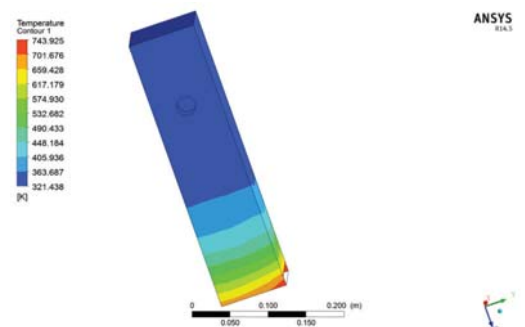


Figure 4—Optimized temperature profile [in Kelvin] for the SlagFlo™ valve

SlagFlo™: modulating the flow in the tap-hole

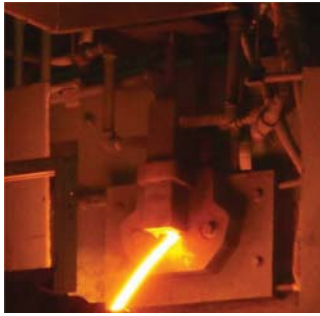


Figure 5—Installed slag valve in operation



Figure 6—Wear pattern on the SlagFlo™ copper piston – circled area shows erosion

slag valve is minimal, which supports the view taken on the acceptable temperature limits when modelling this piece of equipment.

There are no significant signs of chemical attack, which is as expected for the mineral wool slags. Modifications are being investigated for processes where chemical attack would present a significant source of wear.

It has not been possible to collect data on the temperature profile inside the copper piston to date. However, the measured slag temperatures reported from the plant (Mitchell, 2014) have, on average, been 137°C higher than the maximum temperature expected and used in the modelling. These higher operating temperatures have not materially affected the life of the copper piston. The consumable portion is being replaced at 12-week intervals, which is consistent with initial expectations.

Modifications made after installation

Approximately 6 months after switch-in, the performance of the SlagFlo™ valves was reviewed. Minor deformation had occurred in the support structure of the valve assemblies. This increased the clearance between the tap-hole faceplate and the slag valve and increased the time required to close the slag tap-holes. These support structures were replaced with an alternative design, and no further problems have been reported.

In addition, the client was experiencing accelerated wear on the seals of the hydraulic cylinder on one of the tap-holes. The cause was traced to localized degradation of the hydraulic fluid (water glycol) since the hydraulic supply pipes are routed past tap-hole one to reach tap-hole two (Mitchell, 2014). Additional modelling was done taking into account the higher temperatures recorded during operation. Based on the modelling work, a much longer water-cooled shield was designed to protect the SlagFlo™ cylinder. Shielding was also added to protect the hydraulic fluid supply piping.

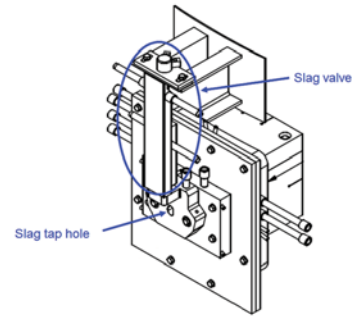


Figure 7—Slag tap-hole assembly showing the modified heat shield (yellow) and support frame

Figure 7 shows the slag tap-hole assembly with the longer water-cooled shield, which is approximately twice the length of the previous heat shield. Note how the shield extends to the top of the SlagFlo™ valve guide on the tap-hole faceplate. This extended shield protects the hydraulic cylinder rod and seals from the high radiant heat loads.

What value does the SlagFlo™ valve add?

As a means of closing a slag tap-hole, the SlagFlo™ valve offers a substantial saving in terms of equipment costs. The typical cost of the assembly is around 15% that of a mudgun machine. In addition to the cost saving, the space required for a SlagFlo™ valve is substantially less than for a mudgun. The equipment does not require operating space since it is permanently attached to the shell.

For a very low capital investment, the SlagFlo™ valve allows the furnace to be remotely closed under normal conditions and emergency conditions.

Conclusion

The use of computational modelling allowed for a relatively simple design optimization process and resulted in a design that performed well on the first installation. This design is well suited to slag tapping operations where there is a need to modulate slag flow, and has proved to be a reliable and robust method of shutting the slag tap-hole. The SlagFlo™ valve can easily be installed as an emergency back-up to most slag tap-holes. It can also be installed in order to add a level of control upstream of slag granulation processes and improve their consistency and safety.

Tenova Pyromet is interested in further developing the SlagFlo™ valve to accommodate more aggressive slags and incorporate a level of automated feedback.

References

- CRANE, A.E and McLAREN, L 2008. Insulation materials: Rock and slag wool insulation: A sustainable choice. *Insulation Outlook*, July 2008. <http://www.insulation.org/articles/article.cfm?id=IO080707> [Accessed 22 January 2014].
- EUROPEAN INSULATION MANUFACTURERS ASSOCIATION (EURIMA). 2011. Mineral wool applications. <http://www.eurima.org/about-mineral-wool/mineral-wool-applications> [Accessed 13 January 2014].
- MATWEB. MATERIAL PROPERTY DATA. 1999 Electrolytic tough pitch Copper, UNS C11000. <http://www.matweb.com/search/datasheet.aspx?matguid=3c78d450e90f48c48d68e2d17a8e51f7> [Accessed 13 January 2014].
- MERVOS, B. 2015. Armstrong World Industries Inc. Personal communication.
- MITCHELL, D. 2014. Armstrong World Industries Inc. Personal communication.
- MOGOTLHONG, L. 2015. Tenova Minerals (Pty) Ltd, Personal communication.
- MUCHENA, D. 2012. Tenova Minerals (Pty) Ltd. Personal communication.
- NOURSE, R.B.N. 2014. Tenova Minerals (Pty) Ltd. Personal communication.
- Saint-Gobain ISOVER. 2008. Insulation materials, mineral wool. <http://www.isover.com/Our-solutions/Insulation-materials/Mineral-wool/Glass-or-stone> [Accessed 13 January 2014].



An overview of the design, operation, and maintenance practices relating to tap-hole management on a PGM smelting furnace

by B. van Beek*, T.J. Goff*, P.E. Nel*, E. Rex*

Synopsis

PGM smelting furnaces are known for operating at significant high superheats. Safe and efficient tapping of both the slag and matte phases can be achieved only through sound tap-hole management practices. This paper gives an overview of the tap-hole management approach followed at Lonmin's Western Platinum smelter.

Five circular AC furnaces are operated, with each furnace comprising essentially a crucible and auxiliary equipment. Within the crucible, the slag and matte tap-holes are situated at different elevations. The slag phase is tapped at a higher elevation than the matte phase. At the three older furnaces, tapping is done by the conventional method of lancing open the tap-hole and closing it with a dolly. However, at the two newer furnaces, tap-holes are opened with the aid of a drill and closed with a mudgun.

Tap-hole management can be divided in a number of aspects. In order to achieve a safe opening and closure every time, Lonmin distinguishes between three important aspects; namely, the design of the tap-hole system, the operating practices followed, and care and maintenance. The paper briefly explains the design of the tapping channel and cooling requirements in order to handle superheated matte, and the difference in design of the matte and slag tap-holes. Mention is also made of the importance of auxiliary equipment, which includes the launders, fume extraction, granulation water, and mudgun and drill units. Improvements made to the matte tap-block design are discussed.

The monitoring, alarming, and safety systems related to matte and slag tapping are reviewed, and tap-hole life and different wear mechanisms are described. Tapping can be done in a safe manner only if the tap-holes and equipment are maintained properly. This topic includes tap-hole refractory repair practices, as well as improvements made in order to reduce repair time and to extend the time between deep repairs. The importance of the correct tap-hole clay selection in order to nurse the tapping channel after each tap is also discussed.

Finally, the paper touches on some research and development work that was done in order to improve the monitoring of the condition of the tap-block by means of fibre optic temperature sensors.

Keywords

PGM smelting, tap-hole management, matte tapping, superheat

Introduction

Lonmin's Western Platinum smelter commenced operations in December 1971 with the commissioning of a 7.5 MVA six-in-line furnace smelting Merensky Reef concentrate. Since then a number of process changes and improvements have been made to the smelting complex. The latest addition was the 12 MVA furnace no. 2, commissioned in July 2012.

As can be seen from the smelter process flow sheet in Figure 1, concentrated slurry or filter cake produced from the concentrators is dispatched to the smelter complex. After offloading, the slurry is blended to a base metal range of 3.2–5.5%. Plate filters are used to dewater the slurry to produce a filter cake, which is then dried through a flash dryer with hot air and stored in silos before being fed to the furnaces.

The smelting furnaces make use of electrical energy to melt the dried concentrate. As the concentrate melts, two liquid phases form – a lighter magnesium-iron silicate-based slag, and a denser molten matte. The platinum group metals, together with the base metal sulphides, report to the furnace matte phase, which settles to the bottom of the furnace via gravity separation. The matte is tapped from the furnace at a temperature of 1400–1500°C. Five furnaces are used in different combinations to achieve the required production output. The focus of this paper will be on the tap-hole management on the 60 MVA furnace no. 1, which was commissioned in 2002.

The liquid furnace matte is poured into Peirce-Smith converters, where it is further processed to produce a converter matte that is transported to the base metal refinery.

The furnace matte and slag are tapped on a regular basis. Such tapping needs to be performed as safely and efficiently as possible. In order to achieve safe opening and closure every time, Lonmin smelting operations distinguish between three important aspects; namely the design of the tap-hole system, the operating practices followed, as well as care and maintenance.

* Lonmin, South Africa.

© The Southern African Institute of Mining and Metallurgy, 2016. ISSN 2225-6253. This paper was first presented at the, Furnace Tapping Conference 2014, 27–28 May 2014, Misty Hills Country Hotel, Muldersdrift, South Africa.



An overview of the design, operation, and maintenance practices

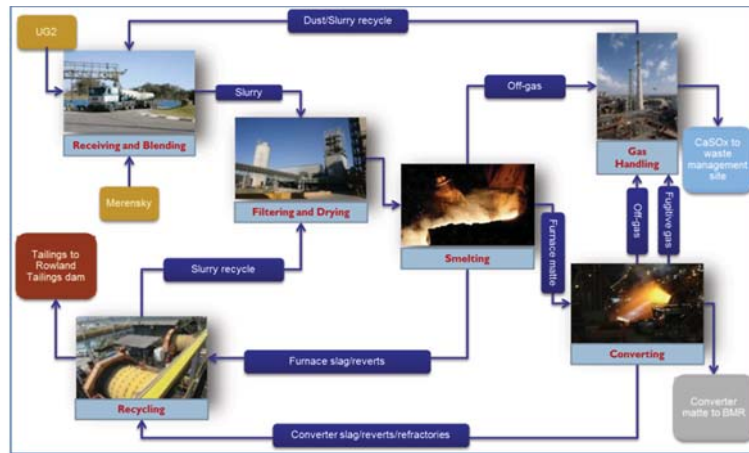


Figure 1 – Smelter process flow sheet

Tap-hole system layout and design

Owing to the different physical properties of liquid matte and slag, the tap-hole layouts and designs for these two phases are completely different.

Slag tap-hole system layout and design

A total of three deep-cooled copper slag tap-blocks are installed at furnace no. 1 (Figure 2). The slag is in direct contact with the water-cooled copper and a freeze lining is formed between the liquid slag and copper during tapping. The centre of the slag tap-hole is situated 860 mm higher than the centre of the matte tap-hole.

The slag tapping system (Figure 3) consists of a slag tap-block, slag insert (also known as a ‘monkey’), and a slag launder. A total of six thermocouples are used to monitor the copper of the slag tap-block in order to detect any temperature excursions for alarming purposes. The slag insert tap-hole diameter is initially 65 mm and the tap-hole needs to be decommissioned when it is eroded to 80 mm. At an estimated slag thermal conductivity of 1.8 W/mK, the heat flux removal capacity is sufficient to maintain a slag freeze lining, but not to freeze matte. Thus it is important to maintain the matte and slag levels within the control limits.

A constant supply of cooling water at a velocity of 3 m/s is of utmost importance in order to ensure safe tapping of the slag. For this reason, apart from the normal cooling water supply pumps, an emergency header tank as well as a diesel-generated pump, is installed for emergency conditions.

The slag launder is constructed of steel and is also water-cooled. The impact area of the slag stream is protected sacrificial refractories installed in the first part of the launder. The slag that is being tapped from the furnace is granulated in a jet of water at flow rate of 800–900 m³/h, as can be seen in Figure 4. Tapping temperatures range from 1550–1650°C, depending on the feed composition.

A mudgun and drill were used for a brief period in 2004 on the slag side to assist with tap-hole opening and closing, but after an incident, the review recommended reversion to the conventional opening and closing of the slag tap-hole. A fume extraction hood is installed above each slag tap-hole to limit the tapping operators’ exposure to fumes.



Figure 2 – Slag tap-block layout

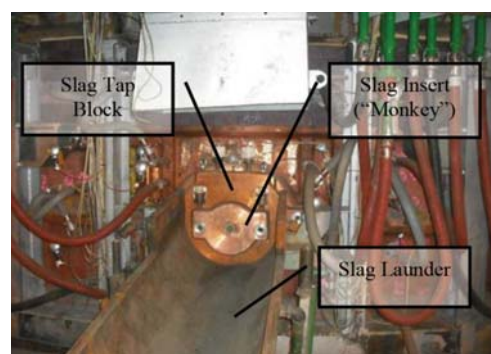


Figure 3 – Slag tapping system



Figure 4 – Slag granulation

An overview of the design, operation, and maintenance practices

Matte tap-hole system layout and design

The matte tap-hole system comprises three deep-cooled matte tap-blocks. As a result of the high superheat ($>600^{\circ}\text{C}$ above liquidus) of the furnace matte, it is necessary to deep-cool the tapping channel in order to avoid frequent refractory repairs and consequent production delays. However, not only the tapping channel but also the area around the tapping channel needs to be cooled. Each matte tap-block is surrounded by flanker coolers on the sides as well as a lintel cooler above, as can be seen in Figure 5. A total of 24 thermocouples are used per tap block to monitor hot face copper temperatures.

Key learning outcomes from tapping incidents have led to several improvements being made to the tap-block design over the years. One of the first improvements, made in 2004, was the extension of the mag-chrome tapping channel length and the introduction of a larger tapping module called the 'Mickey block'. As can be seen from Figure 6, the original tapping channel was much shorter than the current design. It was difficult to do online tap-hole repairs on the short tapping channel design as the original design consisted of only four tapping modules.

The Mickey block with its surrounding blocks was positioned deeper into the furnace in order to protect the copper-cooled area above the tap-hole. Currently, the tapping channel consists of five tapping modules plus the Mickey block. The longer tapping channel of just over 1 m assists in throttling the flow rate as well as enabling more intermediate online repairs to extend the life of the Mickey block.

Originally the furnace was commissioned with only two matte tap-blocks (Figure 7), but a third tap-block was added to the furnace in 2008 as a second improvement to the tap-hole system. The third tap-hole assisted in increasing the duration between deep tap-hole repairs. An additional benefit is that in the event that a problem is experienced with one of the tap-holes, production can still continue while preparation is made for a deep tap-hole repair.

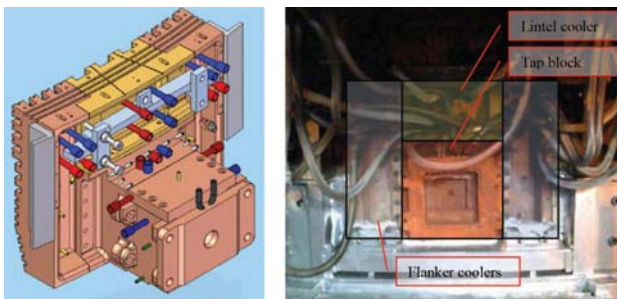


Figure 5—Matte tap block and surrounding coolers

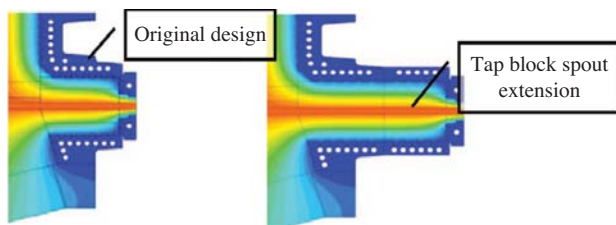


Figure 6—Extended tapping channel

Experienced gained during repairs indicated that the area above the matte tap-hole experiences the highest heat flux during and after tapping. This results in a higher wear rate, thus the need for additional cooling and protection in this wash zone area. The risk to the wash zone, which can be seen in Figure 8, was that any high matte level excursion could result in copper damage as heat fluxes up to 130 kW/m^2 were measured. This initiated the third improvement, which focused on reinforcing the area above the matte tap-hole.

A number of design changes were made in this regard. The first was the introduction of a copper-cooled lip in order to cool the refractories above the tapping channel. This worked well, but wear was still experienced on the copper-cooled lip, due to both corrosion and erosion. As a result of the success of the graphite cooler design in the slag zone it was decided to protect the copper above the tap-hole with graphite as well. The alternative design was implemented in 2010 with the introduction of a graphite-protected copper lintel cooler situated in the wash zone above the matte tap-hole. Results from the furnace rebuild in 2013 indicated that the graphite design lintel cooler performed well. Copper corrosion in the area above the tap-hole still occurred, but to a lesser extent. The corrosion was as a result of the loss of graphite contact in some of the areas.

During the 2013 rebuild a different design of graphite lintel cooler was installed. The graphite is now slotted in horizontally and it is foreseen that the graphite will maintain in contact with the copper for longer during the next campaign.

Auxiliary equipment

Apart from all the changes mentioned above on the matte tap-holes, tapping matte from furnaces also requires some auxiliary equipment. At furnace no.1, two mudgun and drill



Figure 7—Two and three tap-hole layouts

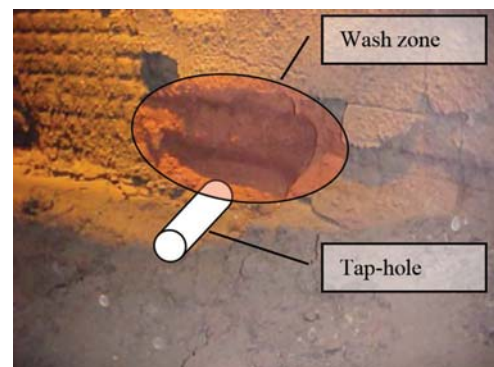


Figure 8—Wash zone above matte tap-hole

An overview of the design, operation, and maintenance practices

units are used to assist in the opening and closing of the matte tap-holes. The design of these units allows for manual as well as semi-automatic operation. In semi-automatic, the mudgun moves and stops at the selected tap-hole to be drilled or plugged. The lowering, drilling, and plugging action is still left to the tapping operator.

A number of improvements have been made to the mudgun and drill units over the years. These include modifications to the positioning limits, moving the clay loading panel further away from the clay loading chamber, introducing a castle key system during clay loading, as well as controlling the units from a dedicated PLC with its own UPS systems.

The alumina-chrome refractory-cast matte launder, mudgun unit, and fume extraction hood can be seen in Figure 9. The matte launder consists of two pieces, the spout and the launder itself from where matte is transferred to a 12 t refractory-lined ladle.

Tap-hole monitoring and alarming

As mention above, the hot face copper temperatures of both the matte and slag tap-blocks are monitored. Based on results of finite element analysis a *high* and *high-high* alarm have been set for each copper temperature. The philosophy followed is that a *high* temperature alarm will send an action alarm to the SCADA operator and a *high-high* alarm will trip the furnace power. Similarly, the differences between the inlet and outlet water temperature are also monitored. Alarms are raised on these water temperature differences based on predefined alarm limits.

It is also important to detect any water leaks on the cooling circuits. For this reason the outlet flow rates of each water-cooled circuit are monitored. The low flow alarms are used to alarm and trip the furnace. The water temperatures and flow rates are used to calculate a heat flux for that specific area in the furnace. Alarming is also done based on the specific heat flux in that area. An online pressure testing system is also used on a daily basis to test the pressure drop over each cooling circuit while no tapping is taking place.

From the analysis of previous tapping incidents the high-high alarm limit is sometimes not sufficient to warn the tapping floor personnel to evacuate the area. The time from the start of the rise in temperature until the actual incident was in some cases between 1 to 2 minutes. For this reason a rate of change (ROC) alarm was introduced, which measures the rise rate of both the water and copper temperatures. The ROC alarms are based on the difference between two sample

means. Figure 10 shows the SCADA pop-up of the lintel cooler on furnace no. 1.

These initiatives to improve the tap-hole design and monitoring are, however, only one aspect of tap-hole management. The physical tapping operation, as well as the maintenance and repair of the tap-holes, are equally important.

Matte and slag tapping operations

Matte tapping is carried out to control the desired matte level in the furnace. The matte is tapped four to five times per shift, depending on the percentage matte fall. The tapping operation consists of drilling, lancing, tapping, and plugging steps as discussed below.

Drilling with mud-gun and drill

When opening a matte tap-hole during normal operations, a hydraulic mudgun and drill is used to partially drill open the clay-filled tap-hole until the solidified matte layer is reached. The average drilling depth to achieve this is normally between 700 and 900 mm. Before commencing with lancing, an operator measures the depth drilled and reports the measurement to the control room. In general, good drilling depths were achieved from 2011 to 2013, as indicated in Figure 11. An alignment check on the drilled hole is also done with a T-bar to prevent the operator from lancing skew in the event that the drill was misaligned.

After the measurement has been done, the mud-gun and drill unit is moved to the park position before lancing commences.

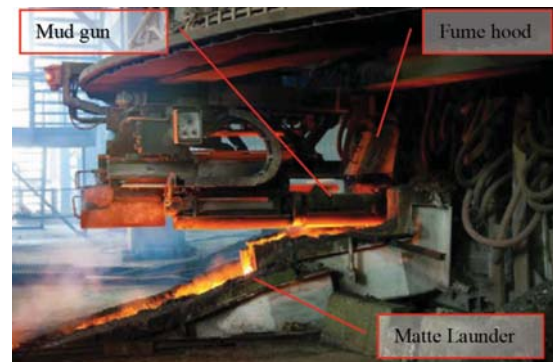


Figure 9—Mudgun and launder configuration

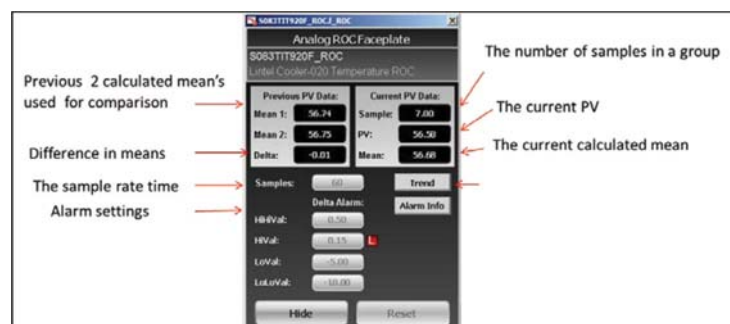


Figure 10—ROC pop-up configuration on SCADA

An overview of the design, operation, and maintenance practices

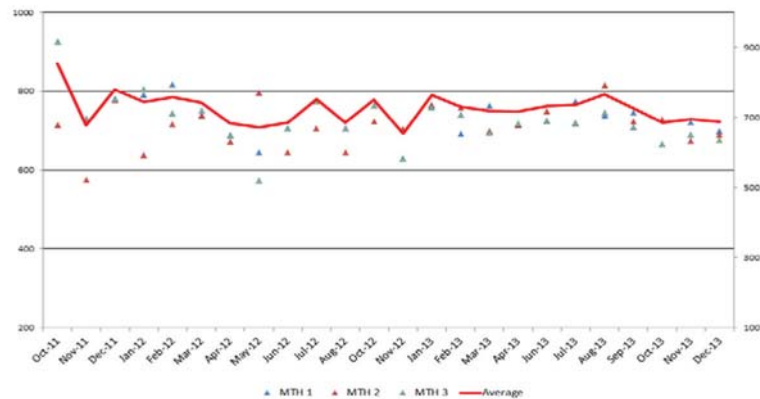


Figure 11—Average drilling depth per month

Oxygen lancing of matte tap-hole

Oxygen lancing is performed by two operators to penetrate into the solidified matte. One operator is responsible for regulating oxygen flow through the lance pipe, while the second operator burns through the tap-hole with a 3 m long lance pipe until the liquid matte starts to flow. A V-shaped lance guide used by the operator (Figure 12) ensures straight lancing. The experience of the furnace tappers is of utmost importance to ensure prolonged tap-hole life. Every effort is made to limit the use of oxygen and the number of lance pipes used per tap is recorded for this purpose.

Matte tapping

The furnace matte is tapped into a 12 t refractory-lined ladle which is then transported to the converter by an overhead crane. The matte tapping temperature is measured using an optical pyrometer and must not exceed 1570°C. A furnace matte temperature exceeding 1570°C will cause the furnace to automatically power down. The tapping duration is monitored in order to determine the wear on the tap-hole refractories. Matte spoon samples are taken from the tapping stream and the analyses are used for metallurgical accounting and process control purposes.

Particular care is also taken to ensure that all three matte tap-holes are used evenly and that one tap-hole is not used more than the others. All tapping data from tapping events is manually recorded into the SCADA and stored on the INSQL server. This data is monitored on a weekly and monthly basis as matte tap-hole usage forms part of the furnace key performance indicators (KPIs).

Another important aspect during matte tapping is to ensure that limited amounts of slag are tapped through the matte tap-hole (slagging). The slag is chemically much more aggressive towards the refractory. Consequently, it is a practice to slag the matte tap-holes on a weekly basis to ensure that all matte and chromite layers are tapped out of the furnace.

Plugging of the matte tap-hole

When the matte ladle is almost full or when a mixture of matte and slag is detected, the mudgun and drill unit is brought from the parked position into the plugging position in semi-automatic mode. This operation is conducted from a

refractory-protected mudgun cabin. The operator then lowers the mudgun and rams the clay into the tap-hole. In the event of a mudgun failure, manual clay stoppers are used to close the tap-hole.

Clay consumption is measured after every matte tap. On average 4 litres of clay per tap is used, and any anomalies are reported so that the counter can be fixed by the instrumentation department. Any excess clay can cause more gas to be released from the clay, which could damage the copper above the tap-hole. Less than 4 litres of clay could result in the tapping channel containing matte rather than being full of clay. Consequently, the next tap will take considerably longer and could result in damage to the tap-block due to excessive lancing. The clay consumption forms part of the weekly and monthly KPIs.

Slag tapping operation

Slag tapping is semi-continuous with a slag tap-hole open approximately 15–18 hours per day. The higher elevation of the slag tap-hole ensures that no matte is pulled into the slag stream when tapping. This is especially important when granulating slag with water as the presence of matte in the slag can lead to violent explosions.

The slag tap-holes are opened manually by oxygen lancing. No mudgun and drill unit is used. The liquid slag is granulated and the granulation water enters the slag pond with the granulated slag. The slag is scooped out of the pond using an automated grab crane and transported for further processing. The three slag tap-holes are used sequentially to ensure an even load on the wall and prevent cold spots developing, which will require vigorous lancing and will damage the tap block.



Figure 12—V-shaped lance guide ensuring straight lancing

An overview of the design, operation, and maintenance practices

When the slag tap-hole must be closed, a manual clay stopper ('dolly') is used. This device is simply a cone-shaped clay plug on the end of a long steel bar. Using the bar, an operator inserts the clay plug into the running slag stream. When the plug is in position, a second operator taps the end of the steel bar with a hammer, driving the plug deeper into the slag tap-hole and stopping the flow of slag. A 10 mm steel bar is then hammered through the clay stopper to act as a 'leader bar' when opening the tap-hole the next time.

The slag temperature is measured during tapping and recorded similar to the matte temperatures. The slag temperature is normally between 1550 and 1650°C and slag viscosity is not a problem at these temperatures. As mentioned previously, the slag insert can wear back to a maximum of 80 mm before requiring replacement. Generally, damage to the water-cooled 'monkey' occurs during lancing operations. By following proper lancing procedures, the working life of the insert can be extended. The current life of a 'monkey' insert is approximately two years.

Spoon samples of the molten slag stream are taken and the analysis is used to calculate the PGM recovery.

Matte tap-hole repair and maintenance

The tap-hole refractories are deep-cooled with copper cooling elements. There are three copper cooling elements cooling the matte tapping channel – the deep matte waffle cooler, matte tapping spout, and the faceplate. All of these copper components rely upon the protection given by the tapping channel refractory bricks, and the refractory bricks are reliant on the cooling received from the copper components. It is imperative that these refractories are maintained on a regular basis.

Tapping channel refractory configuration

As indicated in Figure 7, the tapping channel consists of five tapping modules and one larger tapping module (the Mickey block). These tapping modules are surrounded by so-called 'doghouse refractories'.

The copper faceplate is also fitted with a refractory insert. The design allows for proper contact between the refractory insert and the first tapping module in order to prevent any matte leaking through between the copper-cooled faceplate and the first tapping module. The initial tap-hole diameter is 38 mm.

A summary of refractory modules with dimensions is given in Table 1.

The tapping channel will wear over time and require periodic maintenance. Therefore, at furnace no.1 the matte tapping channel repair is split into two stages:

- One-to-five block repair (tapping modules)
- Deep matte tap-block repair (Mickey repair).

Each repair is discussed in more detail below.

One-to-five block repair philosophy

The decision to conduct a tapping module repair is based on the time it takes to fill a 12 t refractory-lined ladle. From operational experience, a tapping time of less than 11 minutes indicates possible wear of the tap-hole and requires a tap-block repair. The tapping modules on every tap-hole are replaced on a bi-weekly basis. From one to five tapping modules can be replaced, depending on the physical condition

of the tapping modules during the repair. During this intermediate repair no doghouse refractories are replaced. The condition of the Mickey block is also monitored during these repairs.

Deep matte tap-block repair philosophy

A deep matte tap-block hot repair is done every 3 to 4 months, depending on the condition of the Mickey block. As mentioned above, the cold face measurements of the Mickey block will indicate when to plan for a deep block repair. From historical data and operational experience, a deep repair is planned when matte penetration into the Mickey block is so severe that only 20–30 mm of refractory brick remains. From a safety perspective, 20–30 mm brick is very close to the doghouse refractories and could lead to premature failure of the copper cooled block. The possibility also exists that the operators could lance skew, damaging the copper and cause a major breakdown.

Procedures for five and deep matte tap-block repair

The five and Mickey block repairs follow similar procedures. The only difference is the duration of the repair and the extent to which preparations must be made. For a one-to-five block repair, the tap-block is decommissioned at least eight hours before the repair and only the faceplate and tapping modules are removed during the repair.

For a Mickey block, however, the entire furnace is drained (Figure 13) and all the matte launders and spout have to be removed. Two schools of thought exist around whether to drain the furnace or to conduct the deep tap-block repair with a full liquid charge. It is Lonmin's opinion that the risk of doing a deep repair without draining the furnace is too high, and that the additional throughput achieved with this practice is not worth pursuing.

Table 1

Summary of refractories of the matte tapping channel

Tapping channel name	Type	Dimensions (mm)
Five tapping modules	Fused-grain Mg-Cr	230 × 230 × 114
Faceplate insert	Fused-grain Mg-Cr	∅164/118 × 111
Mickey block	Fused-grain Mg-Cr	230 × 230 × 500



Figure 13—Draining of furnace for deep tap-block repair

An overview of the design, operation, and maintenance practices

A five-block repair can take two to four hours to complete. Power is reduced to between 2–3 MW only when the fifth block is reached. Power is increased again after the fourth block is replaced. Mickey block repair time ranges between eight to twelve hours, excluding the draining and heat-up period. During this repair, contact is maintained on two phases to keep the bath liquid.

For additional precautionary measures during a five-block repair, a hole is drilled deeper than the fifth module with the mudgun. The surface temperature at the end of the drilled-in hole is measured before the repair. A surface temperature in excess of 300°C or rise rate of 1°C/min indicates that additional cooling is needed before the repair can be done. Forced cooling by means of fans and air blowing through a hose is used to cool the matte tap-holes.

The surface temperature is monitored continuously throughout the repair by a hand-held pyrometer, with each tapping module's surface temperature being recorded. Photographs and dimensions are taken of the tapping modules as they are removed for quality control purposes. Any signs of cracking of the modules or surrounding refractories are highlighted to management and the relevant action is taken.

During a deep tap-block repair, the surface temperature is also monitored. Extra care is taken in order to ensure that no liquid matte runout occurs while breaking out the Mickey block. A typical repair and wear pattern of the tapping modules and Mickey block can be seen in Figure 14. As can be seen, the tap-hole diameter and penetration increases the deeper one breaks into the tapping channel.

After all the refractory has been replaced, the copper faceplate is reinstalled. Finally, a small fire is made in front of the tap-block to cure the castable refractories between the faceplates and launder.

Improvements made during deep tap-block repairs

Over the last six years, efforts were made to reduce the time taken to conduct a Mickey block repair. The aim was to prevent the hearth refractories from cooling rapidly, which can lead to gap formation. This could pose a major problem during the initial heating-up phase, as the bricks might not be completely sealed and matte penetration could occur, causing ratcheting of the hearth.

Since the re-commissioning of furnace no.1 in 2004, the average power-off time for a Mickey block repair has decreased from 60 hours to 12 hours in 2013. This power-off time excludes the draining and bath-building stages of the repair. Currently, the matte tap-to-tap duration is 3.5 days for a deep repair.

Figure 15 indicates how Mickey repair times have been reduced. It can be seen that the frequency of Mickey repairs has been reduced between 2004 and 2008. The Mickey repairs between 2010 and 2013 during annual shutdowns or after furnace incidents are considered as special causes and could not be documented and compared with the rest of the data, as the Mickey repair time could not be distinguished from other activities during these events.

The main contributors to the improvement were:

- Improved draining of the furnace to ensure a safe matte level
- Change in cooling method from liquid nitrogen to air

- Improvement in refractory preparation for faster Mickey block installation
- Repairs conducted at low power, typically between 1–2 MW (on/off) instead of switching off power to the furnace completely.

Apart from the reduction in repair time, a number of other improvements were made, as discussed below.

Improvements in matte tapping safety

As with any high-temperature operation, the risks of injury to tapping personnel are high. However, with the support of the dedicated tapping personnel, several changes were made to increase the safety of personnel and equipment.

Length of the tapping lance

The length of the oxygen lances was changed from 6 m to 3 m. This reduced the risk of skew lancing due to the flexibility of the lance, and also increased ease of operation.

Oxygen hose design

In the past, frequent incidents occurred where operators burnt their hands while lancing due to oxygen leaks. These leaks occurred between the connection of the bullnose and the flexible hose. The bullnose was subsequently re-designed to make the connection to the flexible hose more robust and less prone to leaks. Figure 16 indicates the new design.

Installation of a mild steel sacrificial plate

A sacrificial plate of mild steel is placed in front of the matte faceplate to protect the copper against hot matte splashes during the tapping process. The sacrificial plate is used as a consumable and is changed during every tap-block repair or when the plate is damaged during the tapping process. Figure 17 shows how the sacrificial plate is installed onto the copper faceplate.



Figure 14—Cold face of tapping modules

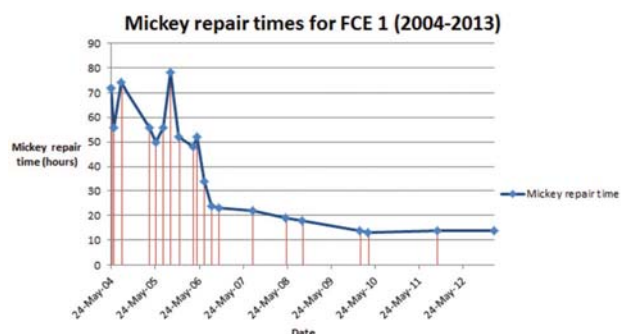


Figure 15—Reduction in Mickey repair times

An overview of the design, operation, and maintenance practices



Figure 16—New bullnose design for oxygen pipe



Figure 17—Sacrificial plate on copper faceplate

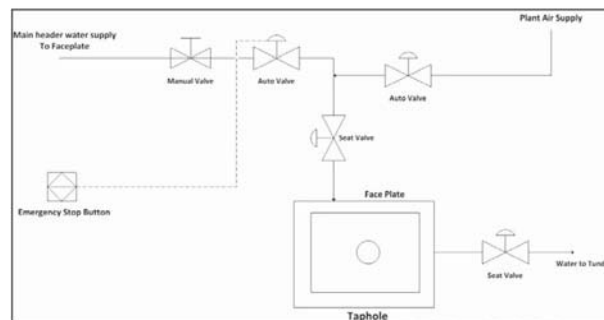


Figure 18—Emergency system for the cooling water supply

Tap-hole clay

Tap-hole clay is used during the operation of the mudgun. Operating the mudgun during tap-hole closures is safer for tappers than conventional manual plugging of the tap-hole. The tap-hole clay also assists with repairing the tap-hole as the clay penetrates deep into the tapping channel, forming a protective layer during the next tap. The original clay used for plugging of tap-holes had a high volatile content (LOI of 8%), which meant that a lot of boiling occurred inside the furnace after tap-hole closures. This led to an increase in the wear rate in the wash zone. Since 2011, an alternative tap-hole clay with lower volatiles (less than 3%) and a higher alumina content (75%) has been used. Less boiling is observed, and protective layer is visible in the tapping channel during repairs.

Installation of emergency push-buttons for faceplate

In the event that the copper face plate comes in contact with matte during the tapping process, water could leak from the faceplate into the liquid matte stream and cause violent explosions. In order to mitigate this risk, three emergency push-buttons were installed in each mudgun station for each matte tap-hole. When a leak at one of the tap-holes is detected, the emergency push-button is activated, closing the supply line valve of the cooling water to that circuit. The air supply valve automatically opens to flush the system, making it safe for the operators. The supply valve can also be closed from the SCADA or from a manual isolation valve in the tapping cabin. Figure 18 is a schematic diagram of the emergency system currently installed at furnace no. 1.

Fibre optic temperature measurement system

As part of continuous improvement on the condition monitoring of the tap-blocks, a fibre optic temperature

measurement system was installed and tested on the matte tap-blocks. These fibre optic sensors provided temperatures at the surface of the copper. The sensor cables were installed in a grooved channel on the hot face of the matte tap-blocks. A protective tube was mounted on the copper blocks to accommodate the fibre-optic sensor. During the initial work, the following problems were experienced:

- Gases from the process corroding the tube and damaging the sensors
- Cable connections to the junction box burning off during tapping
- Damage to the cable connections during tap-block repairs.

The latter two points were addressed, but to date corrosion is still a problem.

Useful data was obtained from the sensors and could have been correlated with process conditions. Currently, ways to embed the fibre optic tube below the copper cooler surface need to be developed.

Conclusion

The Lonmin smelter team has come a long way in ensuring that tapping is conducted as safely as possible every time. As this paper has shown, the design, operation, as well as the maintenance of the tap-holes is crucial for successful operation of a furnace when tapping superheated matte.

Acknowledgements

The authors would like to acknowledge the operational staff at furnace no. 1 for their contribution in assisting with inputs and ideas during the design and operational changes. The contributions of the furnace designers at Hatch are also acknowledged with thanks. ♦



Response surface optimization of process parameters for the removal of F and Cl from zinc oxide fume by microwave sulphating roasting

by T. Hu^{*†‡}, Z. Li^{*†‡}, C. Liu^{*†}, L. Zhang^{*†‡}, J. Peng^{*†‡}, and B. Wang^{*†‡}

Synopsis

Microwave sulphating roasting was applied to zinc oxide fume from a fuming furnace for the removal of F and Cl. The effect of important parameters such as roasting temperature, holding time, and vapour flow were investigated and the process conditions were optimized using response surface methodology. The results showed that the effects of roasting temperature and holding time on the removal efficiency of F and Cl were most significant, and the effect of vapour flow is of much lower importance. The defluorination and dechlorination efficiency increased rapidly as the roasting temperature and holding time increased, while the vapour flow had little effect. The defluorination efficiency could reach 91.3% while the dechlorination efficiency could reach 89.5%, under the process conditions of roasting temperature 655°C, holding time 65.2 minutes, and vapour flow of 6.8 ml/min. The results showed that the removal of F and Cl from zinc oxide fume using a microwave direct roasting process is feasible and reliable.

Keywords

zinc oxide fume, microwave sulphating roast, removal of F and Cl, response surface methodology.

Introduction

Zinc is one of the most important metals, which is required for various applications in the metallurgical, chemical, and textile industries. The depletion of high-grade ores of zinc and the accumulation of large quantities of metallic scrap, as well as metallurgical wastes, have led to a significant interest in processing these zinc secondary sources (Vahidi *et al.*, 2009; Dakhili *et al.*, 2011; Li *et al.*, 2012). Zinc secondary materials such as zinc ash, dross, flue dusts, sludge, and residues are generated in various chemical and metallurgical industries (Agrawal *et al.*, 2004; Sahu *et al.*, 2004; Jha *et al.*, 2001). Although the recovery of zinc from various secondary sources brings huge economic and environmental benefits, impurities result in decreasing recycling rates for these materials. In particular, the electrowinning of zinc is strongly influenced by chlorine and fluorine, which cause anode corrosion and sticking of zinc metal on the cathode (Lashgari and Hosseini, 2013; Güresin and Topkaya, 1998).

F and Cl ions in electrolytes have to be removed first to meet the requirements for zinc electrowinning (F < 80 mg/L, Cl < 100 mg/L) (Cinar Sahin *et al.*, 2000; Lan *et al.*, 2006).

The conventional pyrometallurgical processes to remove F and Cl are based on the volatilization of these low boiling-point and volatile halides. Lead and zinc chloride show high vapour pressures and low boiling points at relatively low temperature (Cinar Sahin *et al.*, 2000; Wang *et al.*, 2007). At elevated temperatures the halides convert to a vapour phase, enabling their removal from the solid matrix. In the conventional roasting process, zinc oxide fume is roasted in excess of 700°C for an extended time to volatilize the halides, but the removal efficiency is low (Barakat, 2003). Recently, the raw materials for zinc smelting have become more complex and the F and Cl contents in the residues are also increasing, creating many challenges for the multiple hearth furnace and fuming furnace, resulting in a low removal efficiency of F and Cl (Zeng *et al.*, 2007). This necessitates the development of better processes for the removal of F and Cl.

Based on the thermodynamic analysis of volatilization reactions, thermal hydrolysis and sulphate reactions of halides are viable. In the

* National Local Joint Laboratory of Engineering Application of Microwave Energy and Equipment Technology, Kunming, China.

† CKey Laboratory of Unconventional Metallurgy, Ministry of Education, China.

‡ Faculty of Metallurgy and Energy Engineering, Kunming University of Science and Technology, China

†† Faculty of Chemistry and Environment, Yunnan Minzu University.

© The Southern African Institute of Mining and Metallurgy, 2016. ISSN 2225-6253. Paper received Jul. 2014; revised paper received Sep. 2015.

Removal of F and Cl from zinc oxide fume

present work, the microwave sulphating roasting process was applied to remove F and Cl from zinc oxide fume, with the advantages of rapid and selective microwave heating. The roasting temperature, holding time, and air and steam flow were selected as the independent variables to test their effect on defluorination and dechlorination efficiency of zinc oxide fume. Response surface methodology (RSM) based on the central composite design (CCD) was employed to determine the optimal conditions, and a quadratic model correlating the removal efficiency of F and Cl to the three variables was then developed.

Materials and methods

Experimental materials

The zinc oxide fume used in the experiments was received from a fuming furnace smelting process in Yunnan Province in China. The chemical composition of the zinc oxide dust is listed in Table I. The zinc oxide fume contains high Zn and Pb contents, which are of significant economic value. F and Cl in the zinc oxide fume may be incorporated into the leaching solution during the zinc leaching process, resulting in excessive F and Cl concentrations, which is a serious issue in the zinc electrolysis process. Additionally, the S content is 3.84%, which provides the necessary reactant for sulphating roasting.

Experimental set-up and method

The main experimental equipment was a 3 kW box-type microwave reactor designed by the Key Laboratory of Unconventional Metallurgy, Kunming University of Science and Technology. A schematic of the experimental set-up is shown in Figure 1.

The experimental facilities comprised a microwave reactor, air inlet into the system, a stirring device, and an off-gas absorption system. Firstly, 300 g of sample was dried, ground, and placed in the mullite crucible, which was surrounded with heat insulation materials. The crucible was then transferred into the microwave reactor and heated at a microwave frequency of 2450 MHz and power of 0 kW to 3 kW, which could provide continuous adjustable and automatic temperature control. The mullite crucible had a diameter of 90 mm and a height of 120 mm, with a strong transparent wave performance and good thermal shock resistance. The temperature measuring device was a shielded sleeve thermocouple that could measure up to 1300°C. Before starting an experiment, the microwave, stirring, and off-gas absorption systems were switched on. The off-gas absorption system was developed to collect and absorb the flue dust. This off-gas system consisted of a buffer bottle, two water absorption bottles, an alkali absorption bottle, and a micro suction pump. The test equipment also had a stirring device, and the stirring speed ranged from 0 to 160 r/min to meet the required zinc oxide dust-stirring intensity. The stirring system enhanced the reactions by enabling the release of fluoride and chloride compounds. In this sulphating roasting, the stirring speed was set at 120 r/min. In each test the material was microwave-roasted while water vapour carried by the air flow passed into the reactor after the material was heated to the set roasting temperature. Reaction gases could be introduced via a rotameter and a mini air compressor pump, controlling the flow rate of air or water vapour. After a predetermined roasting time, the samples were taken out and cooled at ambient temperature in air. The fluorine ion-selective electrode and the silver chloride turbidimetric

Table
Chemical composition of zinc oxide dust sample (mass percentage)

Zn	Pb	Ge	Cd	Fe	Sb	S	As	F	Cl	SiO ₂	CaO
53.17	22.38	0.048	0.21	0.38	0.23	3.84	1.04	0.0874	0.0783	0.65	0.096

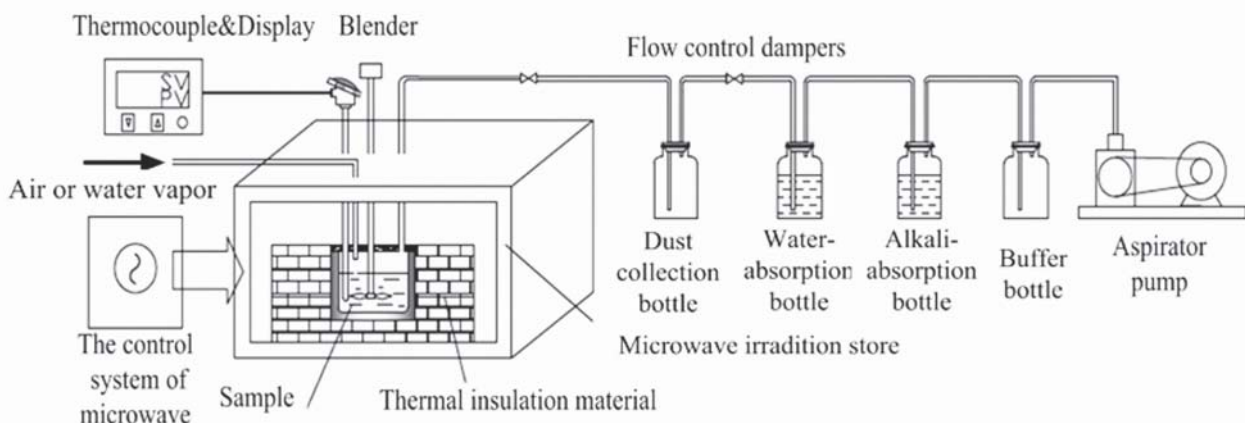


Figure 1—Connection diagram of microwave roasting experiment equipment

Removal of F and Cl from zinc oxide fume

method (d'Heilly *et al.*, 2007; Zenki and Iwadou, 2002) were used for the determination of the fluorine and chlorine content. The initial raw materials contained levels of 166.3 mg/L fluorine and 145.4 mg/L chlorine.

The fluorine and chlorine removal efficiencies were mathematically expressed as

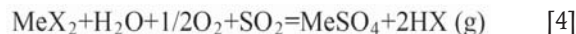
$$\eta = \frac{M - M'}{M} \times 100\% \quad [1]$$

where M represents the initial fluorine and chlorine content in zinc oxide dust, M' denotes the F and Cl content after roasting, and η represents the F and Cl removal efficiency.

Mechanism

In the conventional roasting process, the increase in temperature converts volatile halides into a gas phase, enabling their removal from the solid matrix. The removal of halides from zinc oxide dust by this high-temperature volatilization reaction is calculated using Equation [2].

The XRD analysis in Figure 2 shows that Zn existed mainly in the ZnO phase, while Pb existed mainly in the PbO and PbS phases. At high temperature, PbS reacts with O_2 in air and produces PbO and SO_2 , which provides the necessary reactant for the sulphating reaction. In the sulphating roasting, water vapour carried by air was added to the microwave roasting process to strengthen the halide thermal hydrolysis reaction (Equation [3]) and sulphate reaction (Equation [4]), in order to further reduce the reaction temperature, shorten the reaction time, and improve the removal efficiency of F and Cl. The reactions are:



where Me represents Pb^{2+} and Zn^{2+} and X denotes F^- and Cl^- .

Table II shows the Gibbs free energies ($kJ \cdot mol^{-1}$) of the Pb and Zn halide thermal hydrolysis reactions and the sulphate reactions in the temperature range 600–900°C. Table III shows the equilibrium constants of the Pb and Zn chloride chemical reactions in the range 600–800°C. Tables II and III show that the Gibbs free energy of the sulphate reaction is at its minimum and equilibrium constant is at its maximum, which means that sulphate reaction is thermodynamically most feasible. The Gibbs free energy increases gradually with the increase in temperature, and the reaction becomes difficult. Thus, the temperature of sulphate roasting does not need to be very high.

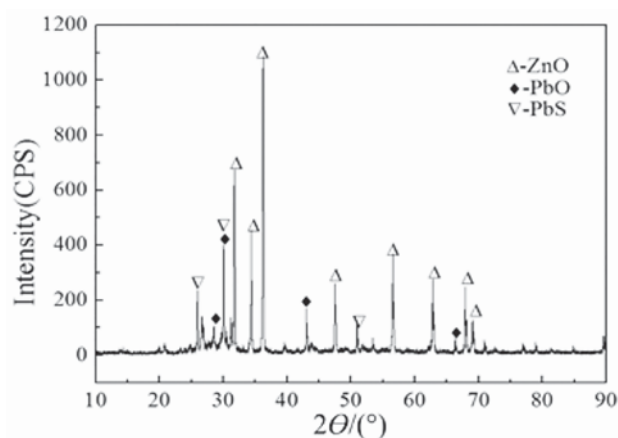


Figure 2—XRD patterns of zinc oxide dust sample

Table
Gibbs free energies ($kJ \cdot mol^{-1}$) of Pb and Zn halides reaction

Matter	Volatile reaction				Thermal hydrolysis reaction				Sulphate reaction			
	873K	973K	1073K	1173K	873K	973K	1073K	1173K	873K	973K	1073K	1173K
ZnCl ₂	3.76	0.91	-1.86	-4.54	27.44	18.65	18.27	21.38	-62.71	-43.79	-19.23	-9.31
PbCl ₂	9.33	6.53	3.86	1.32	104.66	97.69	90.95	83.16	-67.90	-48.22	-27.36	-14.72
ZnF ₂	26.47	22.61	18.8	15.12	0.33	-12.81	-25.77	-47.33	-89.82	-75.25	-63.27	-49.40
PbF ₂	19.52	16.11	12.79	9.79	63.38	54.91	47.10	38.87	-109.28	-91.00	-71.20	-59.01

Table
Equilibrium constant of Pb and Zn halides reaction

Matter	Volatile reaction			Thermal hydrolysis reaction			Sulphate reaction		
	873K	973K	1073K	873K	973K	1073K	873K	973K	1073K
ZnCl ₂	0.121	0.699	2.719	0.023	0.10	0.13	5651.63	224.45	8.63
PbCl ₂	5.06×10^{-3}	3.67×10^{-2}	0.172	5.46×10^{-7}	5.52×10^{-6}	3.74×10^{-5}	1.16×10^4	387.78	21.46
ZnF ₂	2.36×10^{-7}	8.35×10^{-6}	1.48×10^{-4}	0.960	4.870	17.980	2.37×10^5	1.10×10^4	1203.2
PbF ₂	1.30×10^{-5}	2.41×10^{-4}	2.48×10^{-3}	1.61×10^{-4}	1.13×10^{-3}	5.09×10^{-3}	3.46×10^6	7.68×10^4	2.93×10^3

Removal of F and Cl from zinc oxide fume

In a microwave field, the zinc oxide fume can be heated rapidly as a result of good microwave absorbance. The heating curves of 300 g of zinc oxide fume subjected to microwave power levels of 1200 W and 1800 W are plotted in Figure 3. The zinc oxide fume in a microwave field reaches 800°C within 8 minutes, which provides favourable thermodynamic and kinetic conditions for the removal of F and Cl by microwave sulphating roasting.

Method of analysis

The response surface methodology helps to optimize the effective parameters with a minimum number of experiments, and also analyses the interaction between the parameters and results (Azargohar and Dalai, 2005). Based on previous work, three influencing factors, namely the roasting temperature (X_1 , °C), holding time (X_2 , minutes), and vapour flow (X_3 , ml/min), were considered independent variables.

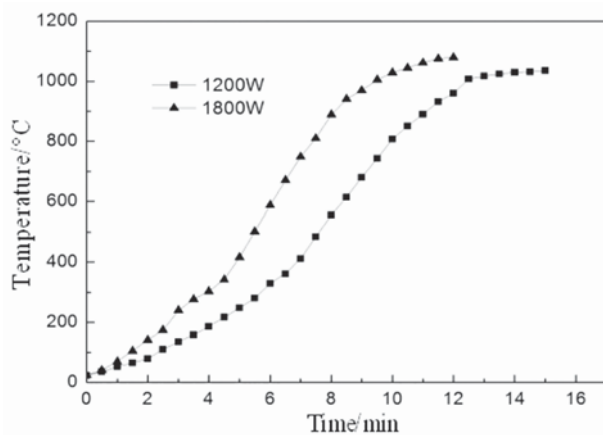


Figure 3—Heating behaviour of zinc oxide fume at different microwave powers

The dependent variables are the F and Cl removal efficiency from zinc oxide dust (Y_1 , Y_2 , %). Table IV shows the independent variables, experimental range, and levels of the design model. In order to describe the nature of the response surface in the optimum region, a central composite design with three coded levels was performed. In general, central composite designs need a total of $(2^k + 2k + N_0)$ runs where k is the number of factors studied, 2^k is the points from the factorial design, 2^k is the face-centered points, and N_0 is the number of experiments carried out at the centre.

Results and discussion

Response analysis and interpretation

The results of 20 runs of the CCD experiment are shown in Table V. The roasting temperatures of runs 9 and 10 were set as 566°C and 734°C, the holding times of runs 11 and 12 were set as 26 minutes and 94 minutes, and the vapour flows of runs 13 and 14 were set as 2.6 ml/min and 9.4 ml/min, respectively. The defluorination efficiency varied from 57.5% to 94.2% while the dechlorination efficiency varied from 53.5% to 93.4%.

The ANOVA results of the quadratic model for the defluorination efficiency and dechlorination efficiency are listed in Table VI and Table VII respectively. The model F-

Variables	Level code		
	-1	0	1
Roasting temperature X_1 (°C)	600	650	700
Holding time X_2 (min)	40	60	80
Vapour flow X_3 (ml/min)	4	6	8

Run	Roasting temperature X_1 (°C)	Holding time X_2 (min)	Vapour flow X_3 (ml/min)	Defluorination efficiency Y_1 (%)	Dechlorination efficiency Y_2 (%)
1	600	40	4	57.7	53.5
2	700	40	4	74.3	65.9
3	600	80	4	79.0	71.0
4	700	80	4	92.8	90.6
5	600	40	8	66.8	61.7
6	700	40	8	85.0	77.6
7	600	80	8	81.7	76.0
8	700	80	8	94.2	93.4
9	565.9	60	6	71.6	63.5
10	734.1	60	6	90.6	88.7
11	650	26.4	6	60.1	53.0
12	650	93.6	6	92.4	90.7
13	650	60	2.6	80.5	74.6
14	650	60	9.4	93.0	91.2
15	650	60	6	88.6	85.8
16	650	60	6	88.0	86.5
17	650	60	6	87.5	86.1
18	650	60	6	88.2	85.6
19	650	60	6	89.6	85.0
20	650	60	6	88.7	85.5

Removal of F and Cl from zinc oxide fume

Table
Defluorination efficiency analysis of variance for response surface quadratic model

Source	Sum of square	df	Mean square	F-value	P-value
Model	2263.21	9	251.47	62.99	< 0.0001
X_1	634.04	1	634.04	158.83	< 0.0001
X_2	1023.40	1	1023.40	256.37	< 0.0001
X_3	147.77	1	147.77	37.02	0.0001
X_1X_2	9.03	1	9.03	2.26	0.1635
X_1X_3	0.01	1	0.01	0.00	0.9587
X_2X_3	30.81	1	30.81	7.72	0.0195
X_1^2	130.99	1	130.99	32.81	0.0002
X_2^2	322.37	1	322.37	80.76	< 0.0001
X_3^2	14.91	1	14.91	3.74	0.0820
Residual	39.92	10	3.99	—	—

$$R_1^2=0.9827, R_{1\text{adj}}^2=0.9671$$

Table 1
Dechlorination efficiency analysis of variance for response surface quadratic model

Source	Sum of square	df	Mean square	F-value	P-value
Model	3065.20	9	340.58	64.22	< 0.0001
X_1	849.04	1	849.04	160.09	< 0.0001
X_2	1348.44	1	1348.44	254.26	< 0.0001
X_3	226.50	1	226.50	42.71	< 0.0001
X_1X_2	9.46	1	9.46	1.78	0.2113
X_1X_3	0.21	1	0.21	0.04	0.8458
X_2X_3	18.30	1	18.30	3.45	0.0929
X_1^2	228.55	1	228.55	43.09	< 0.0001
X_2^2	433.56	1	433.56	81.75	< 0.0001
X_3^2	35.89	1	35.89	6.77	0.0264
Residual	53.03	10	5.30	—	—

$$R_2^2=0.9827, R_{2\text{adj}}^2=0.9677$$

value of 62.99 and 64.22 implies that the model is significant. There is only a 0.01% chance that this large model F-value could occur by chance. Values of 'Prob.> F' of less than 0.050 indicate that the model terms are significant (Myers and Anderson-Cook, 2009). In this case, X_1 , X_2 , X_3 ,

X_1^2 , and X_2^2 are the significant model terms. That is, among the three independent variables tested, the roasting temperature ($p < 0.0001$), holding time ($p < 0.0001$), and vapour flow ($p < 0.050$) have significant linear effects as well as quadratic effects on the defluorination and dechlorination efficiency. According to (Myers and Anderson-Cook (2009), for a good fit of a model, the correlation coefficient should be at least 0.80. The 'Pred R-squared' of 0.9827 is in reasonable agreement with the 'Adj R-squared' of 0.9671 plotted in the Table VI and Table VIII. Hence, the model can be used to navigate the design space.

The constants and coefficients were obtained by fitting the data listed in Table VI and Table VII in to Equation [5] and Equation [6] respectively. The equation in terms of coded factors is obtained.

$$Y_1 = -654.79 + 1.77X_1 + 2.84X_2 + 7.40X_3 - 1.06E^{-3}X_1X_2 + 3.75E^{-4}X_1X_3 - 0.049X_2X_3 - 1.21E^{-5}X_1^2 - 0.0118X_2^2 - 0.254X_3^2 \quad [5]$$

$$Y_2 = -760.14 + 2.15X_1 + 1.66X_2 + 7.98X_3 + 1.09E^{-3}X_1X_2 + 1.63E^{-3}X_1X_3 - 0.0378X_2X_3 - 1.59E^{-4}X_1^2 - 0.0137X_2^2 - 0.395X_3^2 \quad [6]$$

It is important to confirm that the selected model provides an adequate approximation to the real system. By using the diagnostic plots, including normal probability vs. Studentized residuals and the predicted vs. actual value, the model adequacy can be judged (Myers and Anderson-Cook, 2009; Joglekar and May, 1987).

Figure 4 shows the normal probability plots of the Studentized residuals for the initial discharge capacity. The normal probability plot indicates that the residuals follow a normal distribution and the points follow a straight line, verifying that the model is valid and gives a plausible fit to the experimental data.

As seen in Figure 5, the actual response values are the experimental data for a particular run, and the predicted response values are evaluated by the approximating functions. The predicted values are in good agreement with the experimental values, indicating that the model is valid and successfully fits the experimental data.

Response surface

To achieve a better understanding of the interactions of the variables and to determine the optimum level of each variable for the maximum dechlorination efficiency of zinc oxide dust, three-dimensional response surfaces plots of the relationship between X_1 and X_2 , X_1 and X_3 , and X_2 and X_3 were calculated

Table
Optimization process parameters of regression model

Roasting temperature X_1 (°C)	Holding time X_2 (min)	Vapour flow X_3 (ml/min)	Defluorination efficiency Y_1 (%)		Dechlorination efficiency Y_2 (%)	
			Predicted	Experimental	Predicted	Experimental
655	65.2	6.8	92.0	91.3	90.0	89.5

Removal of F and Cl from zinc oxide fume

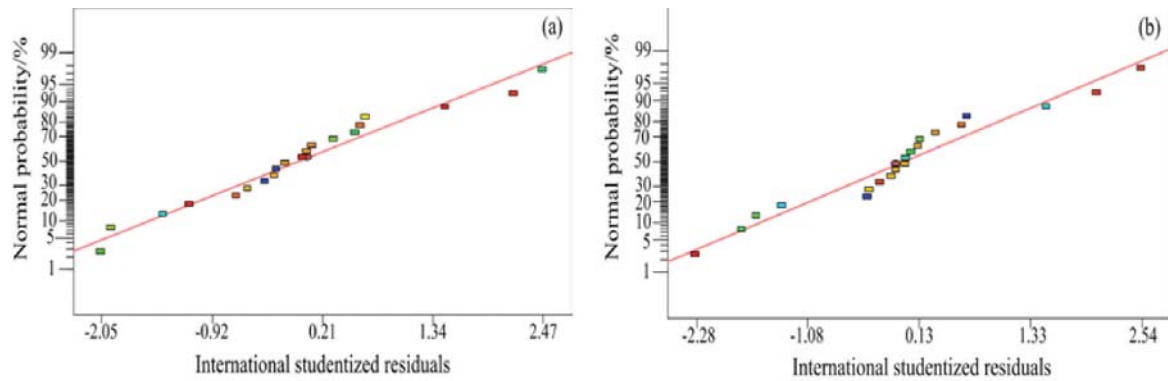


Figure 4—(a) Defluorination efficiency and (b) dechlorination efficiency: normal probability plots of Studentized residuals

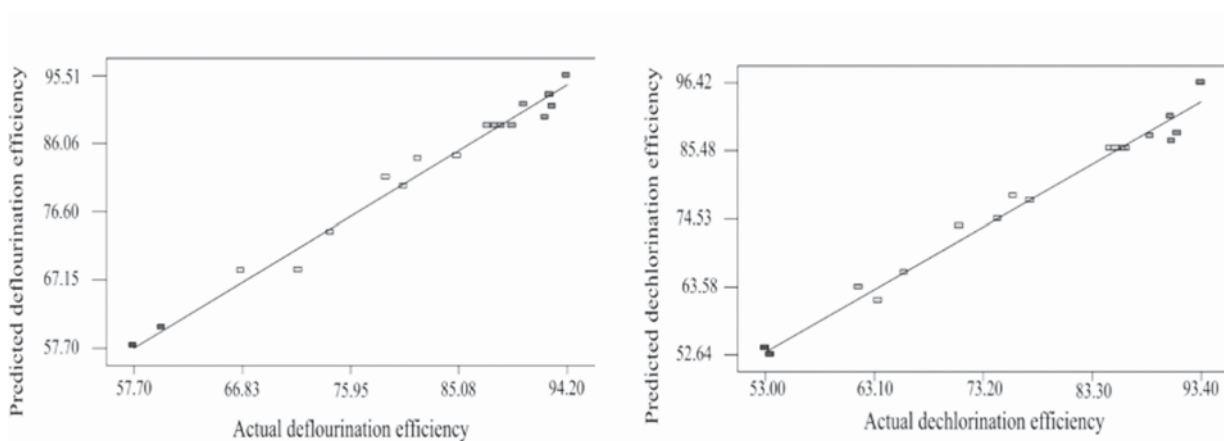


Figure 5—Linear correlation between (a) actual and (b) predicted defluorination efficiency and dechlorination efficiency

and are illustrated in Figure 7. X_1 , X_2 , and X_3 were held constant at their average values. The figures are constructed to assess the interactive relationships between the independent variables and the response.

Figure 7(a) and (d) show the defluorination and dechlorination efficiency of zinc oxide dust as a function of the roasting temperature and holding time, with the water vapour flow kept constant (6 ml/min). The roasting temperature has a significant positive effect on defluorination and dechlorination efficiency. The efficiency increased quickly as the roasting temperature increased. According to different Gibbs free energies of the selected three reactions (Table II), the sulphate reaction is easiest to carry out in this microwave sulphating roasting process. The higher equilibrium constant of the sulphate at elevated temperatures (Table III) indicates that the sulphate reaction is exothermic. Figure 6 shows that the PbS phase disappears in the roasting process. The oxidation of PbS is also exothermic. An appropriate roasting temperature is important to the sulphate reaction. The defluorination and dechlorination efficiency is therefore substantial at 600°C, with a further significant increase when the reaction temperature is increased to 700°C.

As shown in Figure 7(b) and (e), the defluorination and dechlorination efficiency increased with the vapour flow, but compared with roasting temperature, the vapour flow has a

smaller effect on the defluorination and dechlorination efficiency. The defluorination and dechlorination efficiency was controlled by the diffusion at a certain temperature. The reaction interface increased with an increase in the vapour flow rate, and a larger solid-gas interface improves the defluorination and dechlorination efficiency significantly.

Figure 7(c) and (f) show the effect of the holding time and the vapour flow on the defluorination and dechlorination efficiency for a constant roasting temperature. The defluorination and dechlorination efficiency increased with an increase in the holding time. Compared to the vapour flow rate, the holding time has a more significant effect on the efficiency. With substantial holding time, the residual F and Cl levels in zinc oxide fume are further reduced, with the optimum removal efficiency stabilizing at a certain temperature and vapour flow.

Optimal conditions and verification of model

The aim of this study was to investigate the values of the three operational parameters (roasting temperature, holding time, and vapour flow) that maximize the defluorination and dechlorination efficiencies, using response surface methodology. The experimental values were compared with those predicted in order to determine the validity of the model.

Removal of F and Cl from zinc oxide fume

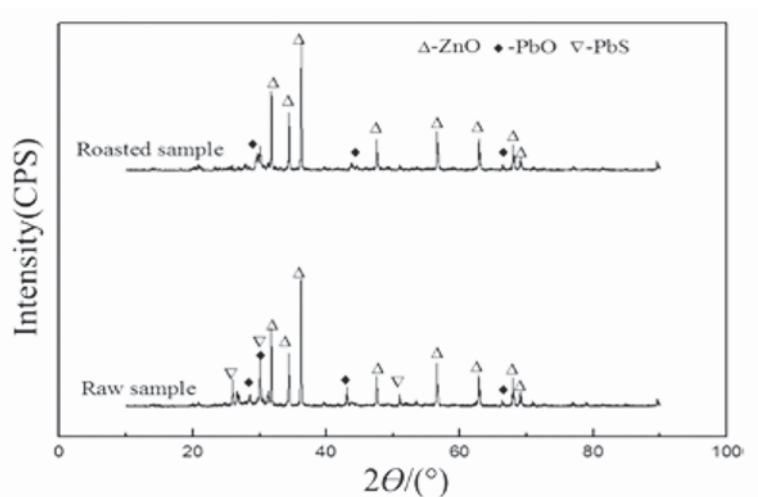


Figure 6—XRD patterns of raw sample and roasted sample of zinc oxide fume

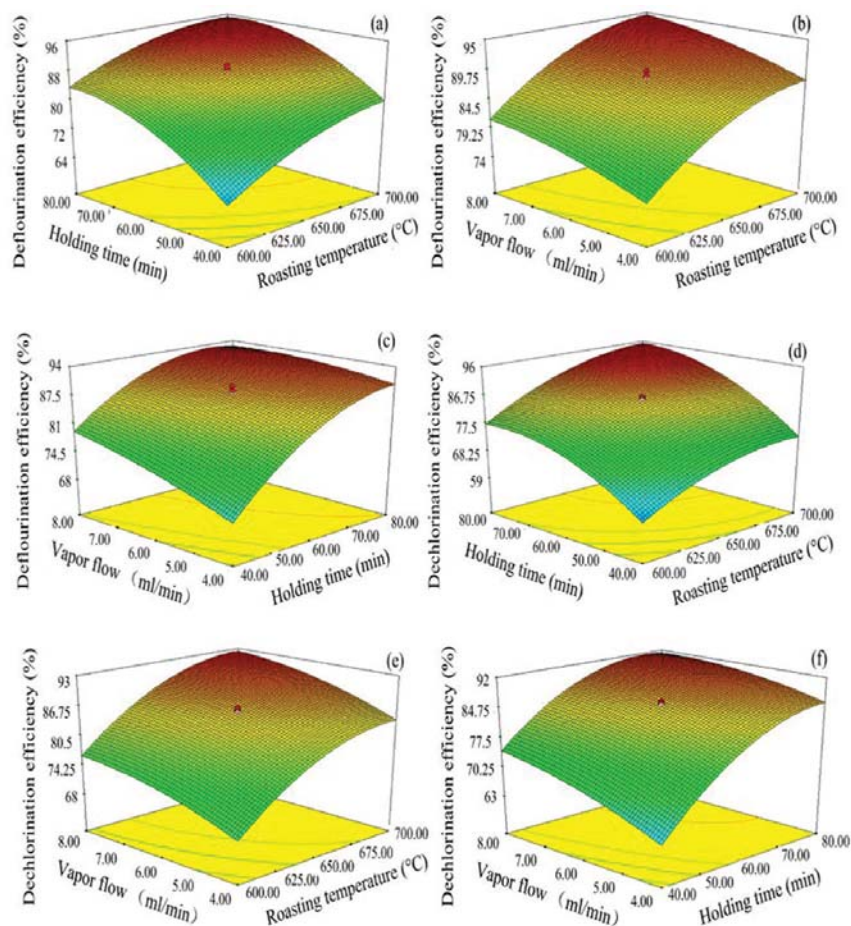


Figure 7—Response surface plots of defluorination efficiency for (a) roasting temperature vs holding time, (b) roasting temperature vs vapour flow (c) holding time vs vapour flow, and dechlorination efficiency for (d) roasting temperature vs holding time, (e) roasting temperature vs vapour flow, (f) holding time vs vapour flow

From the model, optimized conditions were obtained and are given in Table VIII. The optimum levels of the three variables were found to be a roasting temperature of 655°C, holding time of 65.2 minutes, and vapour flow at 6.8 ml/min

with a prediction of 92.0% for the defluorination efficiency and 90.0% for the dechlorination efficiency. In order to test the validity of the optimum conditions obtained by the empirical model, a confirmatory experiment was carried out

Removal of F and Cl from zinc oxide fume

using these optimal levels. The actual experimental value of defluorination efficiency is 91.3% with a relative error of 0.76% with respect to the predicted value, while the actual experimental value of dechlorination efficiency is 89.5% with a relative error of 0.56%. This indicates that the experimental values are in agreement with the predicted ones. The F and Cl contents of the roasted sample were measured as 14.5 mg/L and 15.3 mg/L respectively, satisfying the requirements ($F < 80$ mg/L, $Cl < 100$ mg/L) in the zinc electrolysis process.

Conclusions

1. The response surface methodology showed that it is feasible to removal the fluorides and chlorides from zinc oxide dust from a zinc fuming furnace by microwave sulphating roasting
2. The dechlorination efficiency is significantly affected by roasting temperature and holding time, and to a lesser degree by vapour flow rate
3. The optimized calcination conditions are as follows: roasting temperature 655°C, holding time 65.2 minutes, and vapour flow rate 6.8 ml/min. The defluorination and dechlorination efficiencies are 92.6% and 90.2% respectively, which agree well with the experimental values of 91.3% and 89.5% under the optimized conditions, suggesting that regressive equation fits the defluorination and dechlorination efficiencies perfectly
4. The F and Cl contents of the roasted sample under the conditions predicted by RSM were reduced to 14.5 mg/L and 15.3 mg/L respectively, satisfying the requirements in the zinc electrolysis process.

Acknowledgements

The authors are grateful for the financial support from the National Natural Science Foundation (No. 51104073), the National Technology Research and Development Program of China (No. 2013AA064003), the Yunnan Province Young Academic Technology Leader Reserve Talents (2012HB008), and Yunnan Provincial Science and Technology Innovation Talents scheme – Technological Leading Talent (No. 2013HA002).

References

- AGRAWAL, A., SAHU, K.K., and PANDEY, B.D. 2004. Recent trends and current practices for secondary processing of zinc and lead. Part I: lead recovery from secondary sources. *Waste Management and Research*, vol. 22. pp. 240–247.
- AZARGOHR, R. and DALAI, A. 2005. Production of activated carbon from Luscar char: experimental and modeling studies. *Microporous and Mesoporous Materials*, vol. 85. pp. 219–225.
- BARAKAT, M. 2003. The pyrometallurgical processing of galvanizing zinc ash and flue dust. *JOM*, vol. 55. pp. 26–29.
- CINAR SAHIN, F., DERIN, B., and Y CEL, O. 2000. Chloride removal from zinc ash. *Scandinavian Journal of Metallurgy*, vol. 29. pp. 224–230.
- D'HEILLY, J., SUN, Z., WEN, X., and WEST, S. 2007. Fluoride ion selective electrode. US patent 20070199816 A1.
- DAKHILI, N., RAZAVIZADEH, H., SALEHI, M., and SEYEDEIN, S.H. 2011. Recovery of zinc from the final slag of steel's galvanizing process. *Advanced Materials Research*, vol. 264. pp. 592–596.
- GRESIN, N. and TOPKAYA, Y. 1998. Dechlorination of a zinc dross. *Hydrometallurgy*, vol. 49. pp. 179–187.
- JHA, M.K., KUMAR, V., and SINGH, R.J. 2001. Review of hydrometallurgical recovery of zinc from industrial wastes. *Resources, Conservation and Recycling*, vol. 33. pp. 1–22.
- JOGLEKAR, A. and MAY, A. 1987. Product excellence through design of experiments. *Cereal Foods World*, vol. 32. pp. 857–868.
- LAN, Y., ZHAO, Q., and SMITH, R. 2006. Recovery of zinc from high fluorine bearing zinc oxide ore. *Mineral Processing and Extractive Metallurgy*, vol. 115. pp. 117–119.
- LASHGARI, M. and HOSSEINI, F. 2013. Lead-silver anode degradation during zinc electrorecovery process: chloride effect and localized damage. *Journal of Chemistry*, vol. 2013. Article ID 538462. DOI 10.1155/2013/538462
- LI, M., PENG, B., CHAI, L., PENG, N., YAN, H., and HOU, D. 2012. Recovery of iron from zinc leaching residue by selective reduction roasting with carbon. *Journal of Hazardous Materials*, vol. 237. pp. 323–330.
- MYERS, R.H. and ANDERSON-COOK, C.M. 2009. Response Surface Methodology: Process and Product Optimization using Designed Experiments. Wiley, New York.
- SAHU, K.K., AGRAWAL, A., and PANDEY, B.D. 2004. Recent trends and current practices for secondary processing of zinc and lead. Part II: zinc recovery from secondary sources. *Waste Management and Research*, vol. 22. pp. 248–254.
- VAHIDI, E., RASHCHI, F., and MORADKHANI, D. 2009. Recovery of zinc from an industrial zinc leach residue by solvent extraction using D2EHPA. *Minerals Engineering*, vol. 22. pp. 204–206.
- WANG, C., HU, X., MATSUURA, H., and TSUKIHASHI, F. 2007. Evaporation kinetics of the molten $PbCl_2$ - $ZnCl_2$ system from 973 to 1073 K. *ISIJ international*, vol. 47. pp. 370–376.
- ZENG, Z-G., DOU, C-L., LIU, W-P., XI, X-M., and XIAO, S-W. 2007. Measures to reinforce the de-halogen roasting of zinc oxide dust in multi-hearth furnace. *Mining and Metallurgical Engineering*, 2007–01.
- ZENKI, M. and IWADOU, Y. 2002. Repetitive determination of chloride using the circulation of the reagent solution in closed flow-through system. *Talanta*, vol. 58. pp. 1055–1061. ◆



Application of finite element method and artificial neural networks to predict the rolling force in hot rolling of Mg alloy plates

by Z.Y. Guo^{*†}, J.N. Sun^{*†}, and F.S. Du^{*†}

Synopsis

A computational model combining a finite element method (FEM) with an artificial neural network (ANN) was developed to predict the rolling force in the hot rolling of Mg alloy plates. FEM results were compared with experimental data to verify the accuracy of the finite element model. Numerous thermomechanical finite element simulations were carried out to obtain a database for training and validation of the network. The input variables were initial thickness, thickness reduction, initial temperature of the plate, friction coefficient in the contact area, and rolling speed. The optimal ANN model was obtained after repeated training and studying of the samples. The trained network gave satisfactory results when comparing the ANN predictions and FEM simulation results. A comprehensive validation of the prediction model is presented. The resulting ANN model was found to be suitable for online control and rolling schedule optimization in the hot rolling process of Mg alloy plate.

Keywords

Mg alloy, finite element method, artificial neural network, hot rolling, rolling force.

Introduction

Magnesium alloys have low density and high specific strength, high specific stiffness, and many other advantages (Mordike *et al.*, 2001). With the increased consciousness of energy saving and environmental protection, Mg alloys are becoming widely recognized as the candidates to replace steel and aluminium alloys in many fields, such as in vehicles and the electronics industry. Mg alloys are thus becoming known as new 'green' engineering materials in the 21st century (Hosokawa *et al.*, 2003). However, Mg and its alloys have very poor ductility at room temperature due to their hexagonal close-packed (HCP) crystal structure, and rolled Mg alloy sheets show a strong basal texture, therefore limiting their application (Thirumurugan *et al.*, 2011). Much research has been done to study the deformation mechanism of Mg alloys, with the aim of improving the ductility and strength (Li *et al.*, 2013; Choi *et al.*, 2007; Choi *et al.*, 2009). It has been shown that the microstructures, texture evolution, and mechanical properties of Mg alloys are highly reliant on their primary deformation process, such as differential-speed rolling (Lee *et al.*, 2010), cross-rolling (Kang *et al.*, 2008),

accumulative roll-bonding (Saito *et al.*, 1999), and asymmetrical rolling (Gao *et al.*, 2002). The microstructures have been studied extensively and most of the technology still remains at the research stage. In order to expand the application of Mg alloy products, production of rolled Mg alloy sheets must be commercialized.

The prediction model for rolling force is the crucial part of the computer-controlled system in the hot rolling of Mg alloys. Rolling force prediction methods include mathematical models, finite element models, intelligent methods (*e.g.* artificial neural networks, or ANNs), and a combination of ANNs and mathematical models. Using the mathematical model method to calculate rolling force is simple but has low precision. Using the finite element method (FEM) to simulate the rolling process decreases assumptions, but is time-consuming and EMS (expanded memory system) memory-intensive (Sun *et al.*, 2009). The intelligent method includes ANNs, genetic algorithms, and fish-net algorithms.

Recently, a computational model combining a FEM with an ANN was used for various metallurgical problems (Esmailzadeh *et al.*, 2012; Shabani *et al.*, 2012) and prediction of mechanical properties (Shabani *et al.*, 2011). ANN-FEM was used to predict residual stresses and the optimal cutting conditions during hard turning of bearing steel (Umbrello *et al.*, 2007), springback prediction for incremental sheet forming (Han *et al.*, 2013), and other aspects of metal forming processes (Kim *et al.*, 2000). However, to the best of the authors' knowledge, the computational method has rarely been used to

* National Engineering Research Center for Equipment and Technology of Cold Strip Rolling, Qinhuangdao, China.

† School of Mechanical Engineering, Yanshan University, China.

© The Southern African Institute of Mining and Metallurgy, 2016. ISSN 2225-6253. Paper received Jun. 2014; revised paper received Jul. 2015.



Application of finite element method and artificial neural networks

predict the rolling force in the hot rolling of Mg alloy plates. In the process of real production, the predictions of conventional models have relatively large errors in the rolling force. For the purpose of satisfying both computation speed and calculation precision in practical production, a computational model that combines FEM with ANN was developed to predict the rolling force. The commercial finite element software MSC.Marc was used to simulate the Mg alloy rolling process; then Matlab Toolbox was used to train a back-propagation neural network by applying the input variables and FEM simulation results. This new computational method makes full use of the advantages of the FEM and ANN. The resulting model can predict the rolling force of Mg alloy plate quickly and accurately, and can be used for the optimization of the Mg alloy rolling schedule and online control of the rolling process.

Finite element modelling

In this Mg alloy hot rolling process, the plate is more than 600 mm wide, so the modelling can be regarded as a plane-strain problem, which can save calculation time without losing too much accuracy. Thus, a three-dimensional problem can be reasonably described by a two-dimensional problem. Only half of the plate was modelled due to the symmetric nature of its rolling situation, as shown in Figure 1. The plate was taken to be 100 mm long for the purpose of reducing analysis time. The rolling was performed with a work roll temperature of 160°C (Zhang *et al.*, 2010) and a work roll diameter of 425 mm for all finite element models.

The steel work roll stiffness is very high relative to Mg alloys. For simplification, it can be assumed that the work roll is a rigid-thermal contact body and the rolling piece is a thermoplastic contact body. Thermomechanically coupled FE models of the Mg alloy plate hot rolling process were developed under various rolling conditions. An arbitrary Lagrangian-Eulerian (ALE) method was employed as a formulation technique through the use of the commercial general-purpose FE program MSC.Marc. The flow stress was coupled to the rolling temperature, strain rate, and strain. The boundary condition type was 'plastic - heat generation'.

The temperature of the plate will increase because of the heat of deformation. The governing partial differential equation for heat conduction is given by (Kobayashi *et al.*, 2009):

$$\rho c_p \frac{\partial T}{\partial t} = \frac{\partial}{\partial x} \left(k \frac{\partial T}{\partial x} \right) + \frac{\partial}{\partial y} \left(k \frac{\partial T}{\partial y} \right) + \frac{\partial}{\partial z} \left(k \frac{\partial T}{\partial z} \right) + q_v \quad [1]$$

where ρ is the density of the plate ($\text{kg}\cdot\text{m}^{-3}$), c_p is the specific heat of the plate ($\text{J}\cdot\text{kg}^{-1}\cdot\text{K}^{-1}$), k is the thermal conductivity of the rolled plate ($\text{W}\cdot\text{m}^{-1}\cdot\text{K}^{-1}$), q_v represents the volumetric rate of heat generation originated from the deformation ($\text{J}\cdot\text{m}^{-3}\cdot\text{s}^{-1}$), t represents time (s), T is the temperature of the plate (K), and the plate's location is described by using x, y, z coordinates. q_v is calculated using the equation (Freshwater *et al.*, 1996):

$$q_v = \psi \sigma \dot{\epsilon} t \quad [2]$$

where ψ is the efficiency of conversion of plastic plate into heat (assumed to be 0.9, which is considered reasonable for Mg alloys), σ is the true stress of the plate (Pa), and $\dot{\epsilon}$ is the true strain of the plate (Figure 2).

The friction stress on the contact surface between the plate and the work roll must be considered, as given by (Shahani *et al.*, 2009):

$$\tau = \mu p \quad [3]$$

where τ is the critical shear stress (Pa), μ is the coefficient of friction, and p is the contact pressure (Pa). Interfacial friction for the contact area is proportional to the normal force. The coefficient of friction has a wide range due to modelling assumptions and the range of tested rolling conditions.

The plate material was a commercial Mg alloy, AZ31B, which has wide industrial applications. Parameters such as deformation resistance, elastic modulus, thermal

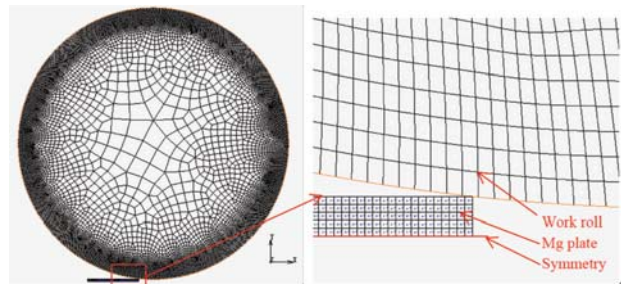


Figure 1 – Finite element analysis model

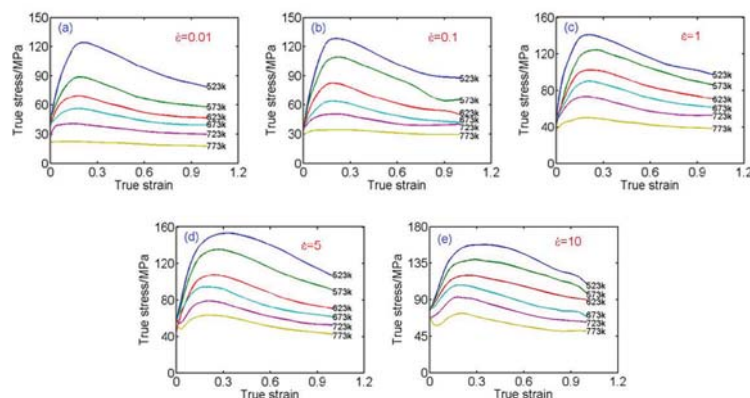


Figure 2—True stress-strain curves of AZ31B as a function of temperature and strain rate

Application of finite element method and artificial neural networks

conductivity, and heat capacity vary greatly at different temperatures for this alloy. The true stress-strain curves of AZ31B (Sun *et al.*, 2013) as a function of rolling temperature and strain rate are shown in Figure 2. The thermo-physical properties used for AZ31B are shown in Figure 3, and Table I summarizes those of the 40Cr work roll.

Calculation and experimental verification

The experimental rolling conditions used are summarized in Table II. A comparison between the FEM calculated roll force results and experimental data from a hot strip rolled 1725 mm wide Mg alloy plate is presented in Table III. As observed, the maximum relative error is 8.6%. The FEM results are shown to be in good agreement with the experimental data. The FEM predicted values can therefore be used as a substitution to generate the training data for neural network modelling.

Prediction of rolling force based on ANN

The predicted values of rolling force by the FE model for an industrial rolling process are encouraging. However, the FE method needs repeated setting up because of the different Mg alloy plate parameters and rolling conditions, and the calculation time is long. It is therefore not suitable for online prediction. ANNs are bionic techniques that imitate the basic principles of brain functions, and have undergone rapid development in the past decade. Utilizing the nonlinear reflecting and association learning abilities of the back-propagation neural network technique (BPNN), the hot plate rolling force of Mg alloys can be predicted relatively accurately and rapidly.

Artificial neural network model

The hot rolling of Mg alloys is a complicated nonlinear problem and many factors influence the rolling force. Omitting the less-important parameters such as work roll diameter, which changes little during the rolling process, benefits the development of the model. The selected independent input variables are initial thickness of the plate,

percentage thickness reduction, initial plate temperature, friction coefficient in the contact area, and rolling speed. The output parameter is rolling force.

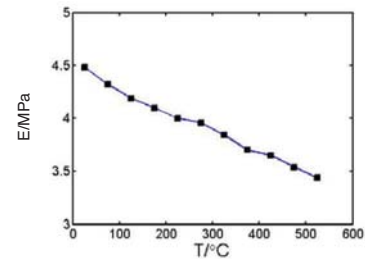


Figure 3a—Elastic modulus of AZ31B at different temperatures

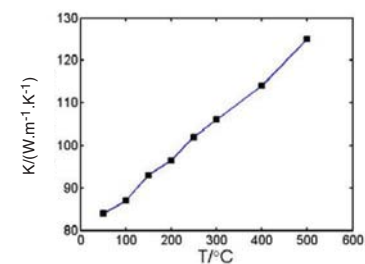


Figure 3b—Thermal conductivity of AZ31B at different temperatures

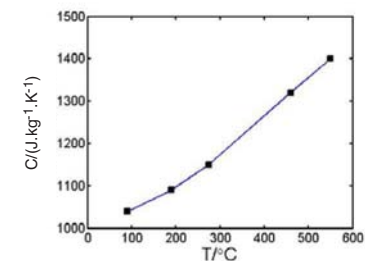


Figure 3c—Heat capacity of AZ31B at different temperatures

Table I
Thermo-physical properties used for the 40Cr steel work roll

Thermal conductivity, W.m ⁻¹ .K ⁻¹	Density, kg.m ⁻³	Poisson's ratio
15	1780	0.35

Table III
Results and comparisons of rolling force

Sample no.	Roll force (MN) experimental data	Roll force (MN) FEM results	Relative error (%)
1	5.05	5.01	0.8
2	5.02	5.45	-8.6
3	5.53	5.60	-1.3
4	5.58	5.78	-3.5
5	5.77	5.62	0.3

Table II
Conditions of hot rolling experiments employed for the simulation

Sample no.	Width (mm)	Incoming thickness (mm)	Outgoing thickness (mm)	Roll speed (m/s)	Temperature (°C)	Friction coefficient μ
1	700	11.50	5.15	0.6	325	0.2
2	680	10.50	4.60			
3	700	10.00	3.68			
4	700	9.00	3.40			
5	750	8.00	3.20			

Application of finite element method and artificial neural networks

The back-propagation algorithm is most commonly used to minimize the minimum mean square error by adjusting the weights and biases of the network. During training, Q sets of input and output data are given to the neural network. An iterative algorithm adjusts the weights so that the outputs (o_k) according to the input patterns will be as close as possible to their respective desired output patterns (d_k). Considering a neural network with K number of outputs, the mean square error (MSE) function to be minimized is (Kazan *et al.*, 1994):

$$MSE = \frac{1}{Q \times K} \times \sum_{q=1}^Q \sum_{k=1}^K M [d_k(q) - o_k(q)]^2 \quad [4]$$

In this study, the input variables and the simulation results were used for training samples through varying the FE model parameters. In a factorial design, variable space is divided into levels between the lowest and the highest values. A three-level full factorial design creates 3^n training data samples, where n is the number of variables. The constructed levels and factors of training samples are presented in Table IV. Hence, $3^5 = 243$ data samples were generated from the validated finite element model that was developed. Commercial 700 mm wide AZ31B Mg alloy plates were rolled. The training samples were divided into two subsets. The first subset of 195 randomly selected data was the training set used to adjust the network weights and biases. The second subset of 48 randomly selected data was the validation subset to monitor the training process in case the network overfitted the data.

In order to increase the training speed and to improve convergent behaviour, the data was normalized before developing the net. The following normalization equation processes input and target data from the original range to the range [0 1].

$$x = (x_k - x_{\min}) / (x_{\max} - x_{\min}) \quad [5]$$

where x_k is the original data, and x_{\min} is the minimum and x_{\max} is the maximum value of x .

One of the most important tasks in ANN studies is to determine the transfer function and the training function. In this model, the tangential sigmoidal function was used in the hidden and output layers, which can improve the accuracy and efficiency of the ANN model. The L-M algorithm was selected as the training function as it is the best choice for moderate-sized neural networks and it has the fastest convergence rate (Hagan *et al.*, 1994).

Input variables	Levels:		
	1	2	3
Initial thickness (mm)	8	10	12
Thickness reduction (%)	30	50	70
Temperature (°C)	250	300	350
Friction coefficient	0.15	0.2	0.25
Rolling speed (m/s)	0.4	1.2	2.0

Another important task in ANN studies is to determine the optimal network architecture, which is related to the number of hidden layers and neurons in them. In this study, the best architecture of the network was obtained by trying different numbers of hidden layers and neurons. The trial started using one hidden layer with three neurons, and the performance of each network was checked by the correlation coefficient (R). The neuron numbers in hidden layers have a direct effect on the ANN's nonlinear prediction ability. The goal is to maximize R to obtain a network with the best generalization. After training repeatedly, the optimal architecture of the ANN was constructed as 5-4-1, representing the number of inputs, neurons in the hidden layer, and outputs, respectively (Figure 4). The corresponding learning rate was 0.001, the value of the training goal was 10^{-5} , and the maximum training step was 2000. The functions and architecture used in the resulting model are summarized in Table V.

Model analysis and prediction results

By using the correlation coefficient R, the performance of each network can be examined in terms of the relationship between the outputs of the network and the targets. Although the structure of the net is simple, the network outputs and the targets show a high level of correlation in Figure 5, with correlation coefficients of 0.9964 and 0.99278 for training data-sets and validation data-sets, respectively.

An early stopping method was used during the training to reduce the effect of overfitting. The error on the validation set would typically begin to rise when the network starts to overfit the data, and the training will stop when the

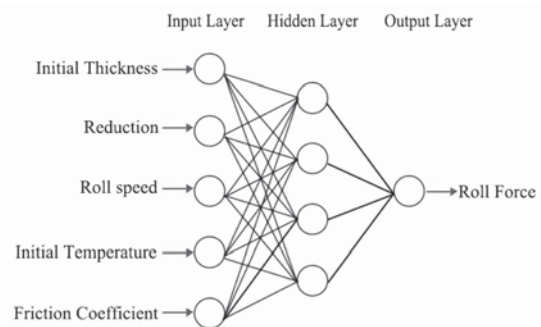


Figure 4—BP artificial neural network model

Network	Feed-forward back-propagation network
Transfer function	Tangential sigmoid
Training function	Levenberg–Marquardt
Learning function	Gradient descent with momentum weight and bias learning function
Performance function	Mean squared error (MSE)
Number of input layer unit	5
Number of hidden layers	1
Number of hidden layer units	4
Number of output layer units	1

Application of finite element method and artificial neural networks

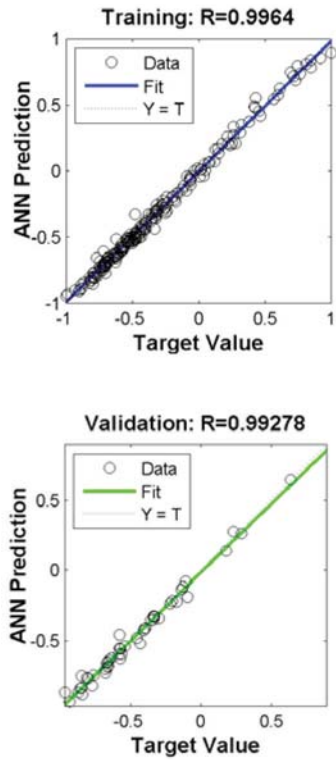


Figure 5a—Training performance of the proposed ANN model in prediction of roll force (5b) Validation performance of proposed ANN model in prediction of roll force

validation error increases for a specified number of iterations. Thus, the weights and biases at the minimum of the validation error would return (Bagheripoor *et al.*, 2013). As can be seen from Figure 6, the minimum MSE of the validation set was as low as 0.0017 after 222 iterations, and no significant overfitting had occurred.

In order to test the prediction precision of the ANN model, 2⁵=32 testing samples were developed from the validated finite element model. The constructed levels and factors of the testing samples are presented in Table VI.

A comparison between ANN predictions and FEM simulation results is presented in Figure 7. The maximum relative error of the roll force prediction was 6.9%, which

implies that this method may be used in practical prediction. The resulting model is quite suitable for online control of a Mg alloy plate hot rolling process and can be utilized to design the rolling schedule for Mg alloy plates.

Conclusions

1. Thermomechanically coupled finite element models of the Mg alloy plate hot rolling process were established. The correlation between the FEM-calculated roll force and experimental data verified the reliability of the FE model
2. FE simulation results were taken as training and validation samples for the BP neural network. The optimum network was obtained by training repeatedly. The ANN predictions agree well with the testing samples,

Table VI
Parameters of testing samples

Factors	Levels	
	1	2
Initial thickness (mm)	9	11
Reduction (%)	60	50
Temperature (°C)	275	325
Friction coefficient	0.175	0.225
Roll speed (m/s)	0.8	1.6

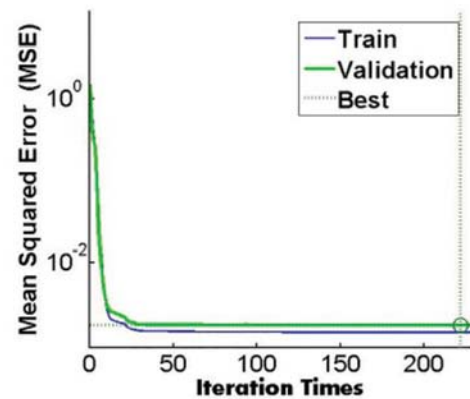


Figure 6—MSE of proposed ANN model in prediction of roll force

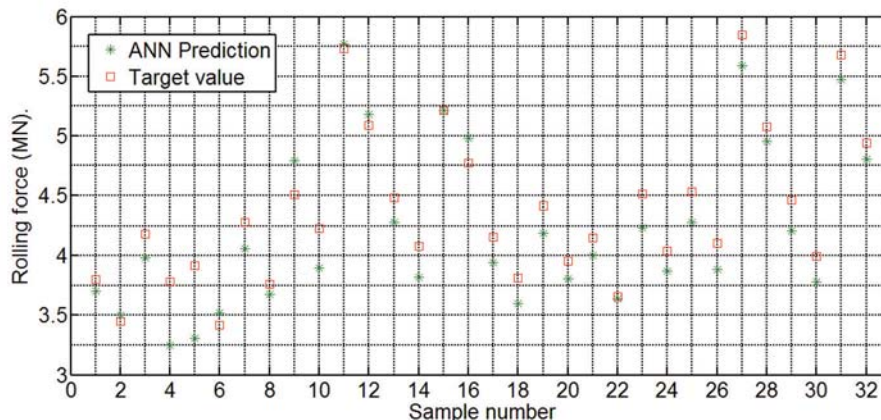


Figure 7—Comparison of ANN and FEM simulation results

Application of finite element method and artificial neural networks

which indicates the ability of the model to predict Mg alloy rolling forces accurately and quickly in different hot rolling conditions. The resulting ANN model is suitable for the optimization of Mg alloy rolling schedules and control of the rolling process, and can also be easily extended to other types of Mg alloy hot rolling mill. Accurate force prediction is an important factor in optimizing the rolling conditions and is critical for a good product shape.

References

- BAGHERIPOOR, M. and BISADI, H. 2013. Application of artificial neural networks for the prediction of roll force and roll torque in hot strip rolling process. *Applied Mathematical Modelling*, vol. 37, no. 7. pp. 4593–4607.
- CHOI, S.H., KIM, D.H., LEE, H.W., SEONG, B.S., PIAO, K., and WAGONER, R. 2009. Evolution of the deformation texture and yield locus shape in an AZ31 Mg alloy sheet under uniaxial loading. *Materials Science and Engineering A*, vol. 526. pp. 38–39.
- CHOI, S.H., SHIN, E.J., and SEONG, B.S. 2007. Simulation of deformation twins and deformation texture in an AZ31 Mg alloy under uniaxial compression. *Acta Materialia*, vol. 55. pp. 4181–4192.
- ESMAILZADEH, M. and AGHAIE-KHAFRI, M. 2012. Finite element and artificial neural network analysis of ECAP. *Computational Materials Science*, vol. 63. pp. 127–133.
- FRESHWATER, I.J. 1996. Simplified theories of flat rolling - I: the calculation of roll pressure, roll force and roll torque. *International Journal of Mechanical Sciences*, vol. 38. pp. 633–648.
- GAO, H., RAMALINGAM, S.C., BARBER, G.C., and CHEN, G. 2002. Analysis of asymmetrical cold rolling with varying coefficients of friction. *Journal of Materials Processing Technology*, vol. 124. pp. 178–182.
- HAGAN, M.T. and MENHAJ, M. 1994. Training feedforward networks with the Marquardt algorithm. *IEEE Transactions on Neural Networks*, vol. 5, no. 6. pp. 989–993.
- HAN, F., MO, J.H., QI, H.W., LONG, R.F., CUI, X.H., and LI, Z.W. 2013. Springback prediction for incremental sheet forming based on FEM-PSO. *Transactions of Nonferrous Metals Society of China*, vol. 23, no. 4. pp. 1061–1071.
- HOSOKAWA, H., CHINO, Y., and SHIMOJIMA, K. 2005. Mechanical properties and blow forming of rolled AZ31 Mg alloy sheet. *Materials Transactions*, vol. 44, no. 4. pp. 484–489.
- KANG, S.H., LEE, Y.S., and LEE, J.H. 2008. Effect of grain refinement of magnesium alloy AZ31 by severe plastic deformation on material characteristics. *Journal of Materials Processing Technology*, vol. 201. pp. 436–440.
- KAZAN, R., FIRAT, M., and TIRYAKI, A.E. 1994. Prediction of springback in wipe-bending process of sheet metal using neural network. *Materials and Design*, vol. 30. pp. 418–423.
- KIM, D.J. and KIM, B.M. 2000. Application of neural network and FEM for metal forming processes. *International Journal of Machine Tools and Manufacture*, vol. 40. pp. 911–925.
- KOBAYASHI, S., OH, S.I., and ALTAN, T. 1989. *Metal Forming and the Finite-Element Method*, Oxford University Press, New York.
- LEE, J.B., KONNO, T.H., and JENOG, H.G. 2010. Effect of differential speed rolling on anisotropy of mechanical properties and texture evolution of AZ31 Mg alloys. *Journal of Alloys and Compounds*, vol. 499, no. 2. pp. 273–277.
- LI, N.L., HUANG, G.J., XIN, R.L., and LIU, Q. 2013. Effect of initial texture on dynamic recrystallization and deformation mechanisms in AZ31 Mg alloy extruded at 573K. *Materials Science and Engineering A*, vol. 569, no. 1. pp. 18–26.
- MORDIKE, B.L. and EBERT, T. 2001. Magnesium, properties - applications - potential. *Materials Science and Engineering A*, vol. 302. pp. 37–45.
- SAITO, Y., UTSUNOMIYA, H., TSUJI, N., and SAKAI, T. 1999. Novel ultra-high straining process for bulk materials development of the accumulative roll-bonding (ARB) process. *Acta Materialia*, vol. 47, no. 2. pp. 579–583.
- SHABANI, M.O. and MAZAHERY, A. 2011. The ANN application in FEM modeling of mechanical properties of Al-Si alloy. *Applied Mathematical Modelling*, vol. 35, no. 12. pp. 5707–5713.
- SHABANI, M.O., MAZAHERY, A., RAHIMPOUR, M.R., and RAZAVI, M. 2012. FEM and ANN investigation of A356 composites reinforced with B4C particulates. *Journal of King Saud University - Engineering Sciences*, vol. 24, no. 2. pp. 107–113.
- SHAHANI, A.R., SETAYESHI, S., NODAMAIE, S.A., ASADI, M.A., and REZAEI, S. 2009. Prediction of influence parameters on the hot rolling process using finite element method and neural network. *Journal of Materials Processing Technology*, vol. 209, no. 5. pp. 1920–1935.
- SUN, J.N., HUANG, H.G., DU, F.S., and LI, X.T. 2009. Nonlinear finite element analysis of thin strip temper rolling process. *Journal of Iron and Steel Research*, vol. 16, no. 4. pp. 27–32.
- SUN, J.N., XUE, T., and GUO, Z.Y. 2013. Online calculation model of rolling force for Mg alloy rolling process. *Advanced Materials Research*, vol. 753–755. pp. 245–248.
- THIRUMURUGAN, M., KUMARAN, S., SUWAS, S., and SRINIVASA RAO, T. 2011. Effect of rolling temperature and reduction in thickness on microstructure and mechanical properties of ZM21 magnesium alloy and its subsequent annealing treatment. *Materials Science and Engineering A*, vol. 528, no. 29. pp. 8460–8468.
- UMBRELLA, D., AMBROGIO, G., FILICE, L., and SHIVPURI, R. 2008. A hybrid finite element method-artificial neural network approach for predicting residual stresses and the optimal cutting conditions during hard turning of AISI 52100 bearing steel. *Materials and Design*, vol. 29, no. 4. pp. 873–883.
- ZHANG, D.F., FANG, L., LIU, G.P., and DAI, Q.W. 2010. Research progress in rolling technology and process for magnesium alloy sheets. *Ordinance Material Science and Engineering*, vol. 33, no. 5. pp. 96–101. ◆



Effects of rolling and cooling process on mechanical properties and microstructure of 600 MPa microalloyed dual-phase steel produced by compact strip production

by G-L. Wu*, X-B. Liu*, and C-Y. Zhou*

Synopsis

The effects of finishing temperature, cooling method, and coiling temperature on the mechanical properties and microstructure of DP600 dual-phase steel produced by compact strip production (CSP) were investigated. Optical microscopy, scanning electron microscopy, transmission electron microscopy, and tensile testing were used to study the microstructure and mechanical properties. The results show that the appropriate microstructure is acquired by decreasing the finishing temperature, accelerated cooling and stage-cooling method, and controlling the coiling temperature below the start temperature of martensite transformation of 352°C. The DP steel produced by CSP contains 81% ferrite and 19% martensite, and the yield strength, tensile strength, and elongation are 350 MPa, 680 MPa, and 29.5%, respectively. The fine polygonal ferrite grain, high density of dislocations, and martensitic laths among the ferrite grains contribute to the excellent microstructure and mechanical properties.

Keywords

dual-phase steel, compact strip production, accelerated cooling, stage cooling.

Introduction

The application of advanced high-strength steels (AHSS) has been growing rapidly in the automotive industry because of their high strength, good formability, weight reduction potential, and energy savings (Jun, 2013; Maciej, 2014). In particular, dual-phase (DP) steels, which exhibit excellent mechanical properties such as high strength, low yield ratio, high work hardening rate, continuous yielding, and good formability, have received more attention (Yousef, 2014; Mukherjee, 2009). DP steel is composed of a soft ferrite matrix, which imparts good elongation, mixed with hard martensite islands, which impart high strength (Dulal, 2014; Ramazani, 2013). This microstructure leads to high strength and excellent ductility compared to conventional low-carbon and high-strength low-alloy steels. In conventional processing of hot-rolled DP steel, elements such as silicon, chromium, and molybdenum are added in order to produce ferrite and martensite phases after hot working, cooling, and coiling. However, there are some problems such as the high costs of alloying elements and the poor fatigue properties of steels produced by conventional

processing. To address these problems, an appropriate thermomechanical processing schedule, in conjunction with optimizing of microalloying, is needed to achieve suitable mechanical properties (Vervynckt, 2012). Compact strip production (CSP) technology, which is the most typical process in thin slab casting and rolling (TSCR), is more cost-efficient than the conventional process (Guangliang, 2012). Furthermore, as-rolled high-strength steels enable the replacement of heat-treated plates or strips with steels that attain equivalent strength (Hailong, 2008). Niobium, vanadium, and titanium are widely used as efficient microalloying elements. During rolling, the microalloying elements and their precipitate particles play a significant role in grain refining, dislocation hardening, and precipitation hardening, and consequently influence the microstructure and mechanical properties of DP steel (Opieła, 2014; Jaegil, 2013). It is therefore of interest to study the CSP route for producing microalloyed DP steel.

Microalloying of low-C Mn steel is widely used to produce high-strength structural steel with good toughness. During hot rolling, the mechanical properties of the final product are determined by a complex sequence of microstructural changes, which are influenced mainly by microalloying additions. In the majority of previous studies, a high volume fraction of martensite and the harmful bainite and/or pearlite phases were formed in hot-rolled DP steel produced by CSP, which led to high yield ratios and unsatisfactory microstructures. It is known that controlled rolling and cooling is a powerful method to improve the microstructures and mechanical properties of low-carbon steels (Zhuang, 2010; Mousavi, 2012). During the cooling process,

* School of Minerals Processing and Bioengineering, Central South University, China.

© The Southern African Institute of Mining and Metallurgy, 2016. ISSN 2225-6253. Paper received May 2015; revised paper received June, 2015.



Effects of rolling and cooling process on mechanical properties

the microstructure and properties are affected not only by the average cooling rate, but also by the different cooling modes (Zhengtao, 2012; Zhangwei, 2014). The object of this study is to investigate the influence of finishing temperature, cooling method, and coiling temperature on the microstructure and mechanical properties of microalloyed DP steel produced by CSP.

Experimental

Materials

The chemical composition of the investigated steel is shown in Table I. The concepts used to design the alloy chemistry are as follows. C and Mn are effective for strengthening steels. Silicon is useful in preventing pearlite and carbide formation, and also results in solid solution hardening of the ferrite phase. Manganese content also plays a key role in the processing of DP steels as it substantially enhances the grain size stability during intercritical annealing and the ability of austenite to undergo martensitic phase transformation. Nb and Ti are used in this steel in order to improve the strength by precipitation hardening and grain refinement hardening.

Experimental method

The 70 mm thick slabs were heated to 1200°C for 1 hour to ensure that the microstructure was austenitized. Rolling commenced at 1080–1150°C. The slab was reduced to a thickness of 4 mm by a seven-stand hot rolling mill. After rolling, the specimens were cooled to different coiling temperature by different methods and then coiled. The controlled rolling and cooling parameters are shown in Table II. The specimens were subjected to three different cooling practices:

- ▶ *Method A* – the specimen was cooled by an ultrafast cooling (UFC) device to 705°C at a cooling rate of 200–300°Cs⁻¹, then by air cooling (AC) for 3 seconds and laminar cooling (LC) to the coiling temperature (UFC+AC+LC)
- ▶ *Method B* – the specimen was fast-cooled to 705°C, then underwent laminar cooling to the coiling temperature (UFC +LC)
- ▶ *Method C* – the specimen was cooled to the coiling temperature by laminar cooling (LC).

The high-density UFC nozzle is adopted in the UFC device, which improves the heat transfer efficiency by reducing film boiling and the heat transfer area and increasing forced convection heat transfer and the nuclear boiling area.

The tensile tests were conducted at room temperature using a computerized tensile testing system to determine the mechanical properties, including the yield strength, tensile strength, and elongation. Microstructures were observed with a Leica DMI5000M optical microscope (OM) and H-800 transmission electron microscope (TEM)

Results and discussion

Effect of finishing temperature on microstructure and mechanical properties

Table III shows the mechanical properties of the specimens cooled by method A to different finishing temperatures. The

yield strength, tensile strength, and yield ratio increase, and elongation decreases, as finishing temperature increases with the same cooling method and coiling temperature.

Figure 1 shows the microstructures of the samples cooled by method A after finishing at 810°C, 840°C, and 870°C. All the microstructures are composed of ferrite and martensite. When the finishing temperature increases from 810 to 870°C, the grain size of ferrite and martensite becomes coarser, and the content of ferrite decreases. In Figure 1(a), the ferrite and martensite grains are much finer, and the ferrite grain size is 3–4 μm.

If the final rolling pass takes place below the no-recrystallization temperature, the deformed austenite grains should contain a greater density of dislocations, which would constitute potential sites for ferrite nucleation. The ferrite grains developed after the transformation would therefore be much finer, thus improving mechanical properties (Soheil, 2010). Reducing the finishing temperature increases the rate of ferrite transformation, improves plasticity and elongation, and decreases strength. The austenite-to-ferrite transformation start temperature (A_{r3}) is 800°C according to Equation [1] (Shen, 2014).

$$A_{r3} = 902 - 527\omega_C + 62\omega_{Mn} + \omega_{Si} \quad [1]$$

where ω_C , ω_{Mn} , and ω_{Si} are the mass percentages of C, Mn, and Si in the steel.

Table I
Composition of the test steel (mass %)

C	Mn	Si	Nb	Ti	N	S	P
0.06	1.42	0.28	0.025	0.016	0.0043	0.003	0.008

Table II
Controlled rolling and cooling procedures for experimental steels

Cooling method	Specimen no.	Finishing temperature, °C	Coiling temperature, °C
A	1	810	250
A	2	840	255
A	3	870	250
B	4	815	250
C	5	815	260
A	6	820	350
A	7	810	450

Table III
Effect of finishing temperature on the mechanical properties

No.	Finishing temperature, °C	$Rp_{0.2}$, MPa	Rm , MPa	A_{80} , %	Yield/tensile ratio
1	810	350	680	29.5	0.52
2	840	390	690	26.0	0.56
3	870	420	700	24.5	0.6

Effects of rolling and cooling process on mechanical properties

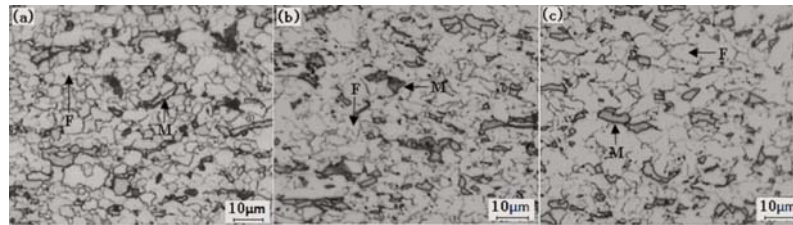


Figure 1—Microstructure of DP steel after finishing at (a) 810°C, (b) 840°C, and (c) 870°C

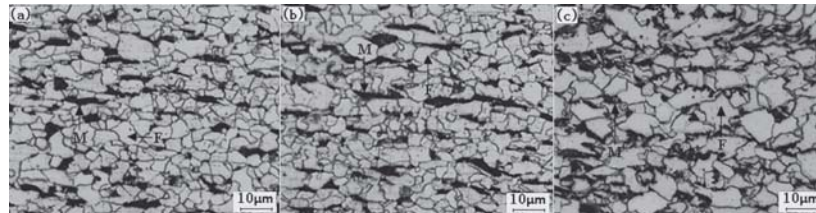


Figure 2—Microstructures of DP steel with different cooling methods. (a) UFC+AC+LC, (b) UFC+LC, (c) LC

Previous studies (Dong, 2011) also showed that finishing temperature should be controlled at 10–20°C above A_{r3} in order to obtain the appropriate microstructure.

Effect of cooling method on microstructure and mechanical properties

In the production of DP steels, the cooling method employed after hot rolling has an important bearing on the optimum phase transformation, grain size, and precipitation, thus determining the properties of the steel. Table IV summarizes the mechanical properties of selected specimens. The tensile strength is higher for methods A and B than for method C. Conversely, the yield strength is lower for methods A and B than for method C, which leads to a lower yield ratio. The high yield ratio after method A is mainly due to slow air cooling.

The microstructures of the specimens obtained after different cooling practices are shown in Figure 2. The microstructures of the specimens cooled using methods A and B are all composed of ferrite and martensite. The polygonal ferrite and the dispersive distribution of martensite islands obtained by method A make for a better performance compared with method B. The specimen cooled using method C consists of ferrite, martensite, and small fraction of bainite. The ferrite is much coarser than that obtained by methods A and B. The martensite contents obtained by methods A, B, and C are 19%, 15%, and 11% respectively.

After finish rolling and ultrafast cooling of DP steels, polygonal ferrite is mainly formed during slow cooling. It is known that increasing the cooling rate lowers the A_{r3} temperature, leading to increased undercooling, which increases the nucleation rate and promotes intragranular nucleation (Mousavi, 2012). The cooling rate after rolling plays an important role in microstructure development. The cooling rate of LC is typically 50–150°Cs⁻¹, and that of UFC 200–300°Cs⁻¹. Slow cooling promotes grain coarsening and suppresses martensite formation. Finer microstructures and improved mechanical properties can be obtained using high cooling rates. The stage-cooling method, such as

UFC+AC+LC, is a more effective way to obtain ferrite and martensite than continuous cooling methods such as UFC+LC and LC. It is an efficient way to improve the ferrite nucleation ratio and phase transformation by the air cooling process, in which ferrite can fully precipitate from austenite and the polygonal ferrite can be obtained. In the air cooling process, the quantity of ferrite is determined by the cooling time.

Effect of coiling temperature after method A on microstructure and mechanical properties

The mechanical properties of the specimens cooled by method A using different coiling temperature are summarized in Table V. The yield strength increases from 350 MPa to 440 MPa, the yield ratio increase from 0.52 to 0.68, and tensile strength decreases from 680 MPa to 645 MPa as coiling temperature increases from 250 to 450°C.

Table IV

Mechanical properties of specimens treated by different cooling methods

Cooling method	Specimen no.	$Rp_{0.2}$, MPa	Rm , MPa	A_{80} , %	Yield/tensile ratio
A	1	350	680	29.5	0.52
B	4	380	695	26.5	0.55
C	5	455	650	28.0	0.70

Table

Mechanical properties of specimens cooled by method A using different coiling temperatures

Specimen no.	Coiling temperature, °C	$Rp_{0.2}$, MPa	Rm , MPa	A_{80} , %	Yield/tensile ratio
1	250	350	680	29.5	0.52
6	350	385	665	28.0	0.58
7	450	440	645	29.5	0.68

Effects of rolling and cooling process on mechanical properties

Figure 3 shows the effect of different coiling temperatures on the microstructures of specimens cooled using method A. As the coiling temperature increases from 250 to 350 to 450°C, the microstructure changes from ferrite/martensite to ferrite/martensite/bainite to ferrite/bainitic.

After finish rolling, most phase transitions from austenite to ferrite are accomplished. The plate is cooled to temperatures below the M_s in order to obtain ferrite and martensite. The start temperature of martensite transformation (M_s) was calculated to be 352°C using empirical Equation [2] (Krajewski, 2014). Specimen no. 7 was coiled at 450°C, which is above M_s . Specimen no. 6 was coiled at 350°C, close to the M_s . Thus, bainite is formed during the coiling process.

$$M_s = 539 - 423\omega_C - 30.4\omega_{Mn} - 7.3\omega_{Si} + 30\omega_{Al} \quad [2]$$

The strength of second phase and the movable dislocation density increase as the coiling temperature decreases, resulting in tensile strength increasing and yield strength decreasing, respectively.

Strengthening mechanisms

The results, including the effect of finishing temperature, cooling method, and coiling temperature on microstructure and mechanical properties, show that specimen no. 1 has better performance, so it was chosen to investigate the strengthening mechanism. It can be seen that plenty of dislocations appear in the grain in Figure 4(a), due to rolling in the non-recrystallization zone. The fine polygonal ferrite grains with size of 1–10 μm contribute to the high strength. The high density of dislocations also improves the matrix

strength. Figure 4(b) shows the lath martensite among the ferrite grains, which improves the matrix strength.

Plastic deformation can be regarded as dislocation movement. During plastic deformation, the quantity and distribution of dislocation are affected by the interactions between dislocations, solute atoms, interstitial atoms, and voids (Ramazani, 2012). In the CSP process, dislocation density increases significantly with increasing deformation. During phase change, rapid cooling can retain quite a number of deformation dislocations in the matrix, thus greatly enhancing the intensity of the matrix (Mukherjee, 2009). The dislocation density decreases with lower cooling rate and higher coiling temperature (Anijdan, 2012).

Conclusions

1. The yield strength, tensile strength, and yield ratio increase as finishing temperature increases. The finishing temperature should be controlled at 10–20°C above A_{r3} . Accelerated cooling and stage cooling is an effective way to obtain a dual-phase microstructure with ferrite and martensite contents of 81% and 19%, respectively
2. The optimum cooling method and coiling temperature to produce DP steel have been established to achieve yield strength, tensile strength, and elongation of 350 MPa, 680 MPa, and 29.5% respectively. The fine polygonal ferrite grains, high density of dislocations, and martensitic laths among the ferrite grains contribute to the excellent microstructure and mechanical properties.

References

- DONG, Y., SHI, X., and HAN, X. 2011. Effect of finishing rolling temperature on microstructure and properties of fine grained hot-rolled dual-phase steel. *Heat Treatment of Metals*, vol. 36, no. 1. pp. 64–67.



Figure 3—Microstructure of DP steel with different coiling temperature. (a) 250°C, (b) 350°C, (c) 450°C

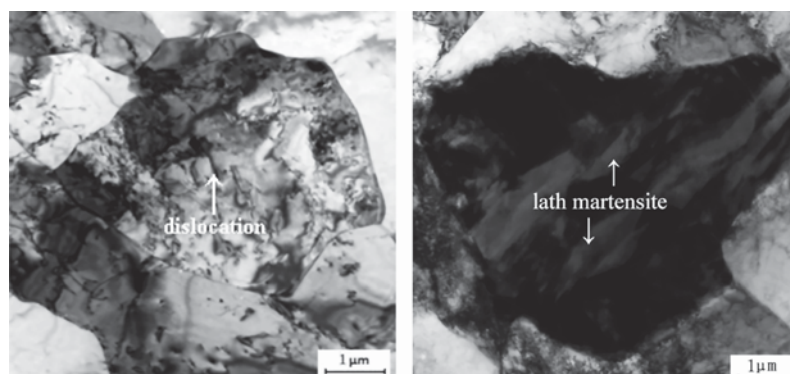


Figure 4—Microstructure of strength phase in specimen 1. (a) Dislocation, (b) lath martensite

Effects of rolling and cooling process on mechanical properties

- DUAN, Z., LI, Y., ZHANG, M., SHI, M., ZHU, F., and ZHANG, S. 2012. Effects of quenching process on mechanical properties and microstructure of high strength steel. *Journal of Wuhan University of Technology - Materials Science and Education*, vol. 27, no. 6. pp. 1024–1028.
- HU, J., DU, L-X., WANG, J-J., GAO, C-R., YANG, T-Z., WANG, A-Y., and MISRA, R.D.K. 2013. Microstructures and mechanical properties of a new as-hot-rolled high-strength DP steel subjected to different cooling schedules. *Metallurgical and Materials Transactions A*, vol. 44, no. 11. pp. 4937–4947.
- HU, Z., XU, G., YANG, H., ZHANG, C., and YU, R. 2014. The effects of cooling mode on precipitation and mechanical properties of a Ti-Nb microalloyed steel. *Journal of Materials Engineering and Performance*, vol. 23, no. 12. pp. 4216–4222.
- Jung, J-G., Bae, J-H., and Lee, Y-K. 2013. Quantitative evaluation of dynamic precipitation kinetics in a complex Nb-Ti-V microalloyed steel using electrical resistivity measurements. *Metals and Materials International*, vol. 19, no. 5. pp. 1159–1162.
- KRAJEWSKI, S. and NOWACKI, J. 2014. Dual-phase steels microstructure and properties consideration based on artificial intelligence techniques. *Archives of Civil and Mechanical Engineering*, vol. 14, no. 2. pp. 278–286.
- LI, Z. 2010. Controlled rolling and cooling process for low carbon cold forging steel. *Journal of Wuhan University of Technology - Materials Science and Education*, vol. 25, no. 1. pp. 89–93.
- MAZAHERI, Y., KERMANPUR, A., and NAJAFIZADEH, A. 2014. A novel route for development of ultrahigh strength dual phase steels. *Materials Science and Engineering A*, vol. 619. pp. 1–11.
- MOUSAVI ANJIDAN, S.H. and YUE, S. 2012. The effect of cooling rate, and cool deformation through strain-induced transformation, on microstructural evolution and mechanical properties of microalloyed steels. *Metallurgical and Materials Transactions A*, vol. 43, no. 4. pp. 1140–1162.
- MUKHERJEE, K., HAZRA, S.S., and MILITZER, M. 2009. Grain refinement in dual-phase steels. *Metallurgical and Materials Transactions A*, vol. 40, no. 9. pp. 2145–2159.
- OPIELA, M. 2014. Effect of thermomechanical processing on the microstructure and mechanical properties of Nb-Ti-V microalloyed steel. *Journal of Materials Engineering and Performance*, vol. 23, no. 9. pp. 3379–3388.
- PIETRZYK, M., KUSIAK, J., KUZIĄK, R., MADEJ, L., SZELIGA, D., and GOŁĄB, R. 2014. Conventional and multiscale modeling of microstructure evolution during laminar cooling of DP steel strips. *Metallurgical and Materials Transactions A*, vol. 45, no. 13. pp. 5835–5851.
- RAMAZANI, A., SCHWEDT, A., ARETZ, A., PRAHL, U., and BLECK, W. 2013. Characterization and modelling of failure initiation in DP steel. *Computational Materials Science*, vol. 75. pp. 35–44.
- RAMAZANI, A., MUKHERJEE, K., PRAHL, U., and BLECK, W. 2012. Transformation-induced, geometrically necessary, dislocation-based flow curve modeling of dual-phase steels: effect of grain size. *Metallurgical and Materials Transactions A*, vol. 43, no. 10. pp. 3850–3869.
- SAHA, D.C., NAYAK, S.S., BIRO, E., GERLICH, A.P., and ZHOU, Y. 2014. Mechanism of secondary hardening in rapid tempering of dual-phase steel. *Metallurgical and Materials Transactions A*, vol. 45, no. 13. pp. 6153–6162.
- SHEN, X., PEI, X., TANG, S., and WANG, G. 2014. Effects of coiling temperature on microstructure and mechanical properties of hot-rolled ferrite/bainite dual phase steel. *Journal of Northeastern University (Natural Science)*, vol. 35, no. 8. pp. 1120–1123.
- SOLHJOO, S. and EBRAHIMI, R. 2010. Prediction of no-recrystallization temperature by simulation of multi-pass flow stress curves from single-pass curves. *Journal of Materials Science*, vol. 45, no. 21. pp. 5960–5966.
- VERVYNCKT, S., THIBAUT, P., and VERBEKEN, K. 2012. Effect of niobium on the microstructure and mechanical properties of hot rolled microalloyed steels after recrystallization-controlled rolling. *Metals and Materials International*, vol. 18, no. 1. pp. 37–46.
- WU, G-L., MENG, Z-B., ZHOU, C-Y., LIU, X-B., and HUANG, T. 2013. HMPT-BOF-RH-CSP process for SPHE substrate of cold rolled deep drawing steel. *Journal of Central South University*, vol. 20, no. 4. pp. 871–876.
- YI, H-L., DU, L-X., WANG, G-D., and LIU, X-H. 2008. Strengthening mechanism of a new 700 MPa hot rolled high strength steel. *Journal of Iron and Steel Research International*, vol. 15, no. 2. pp. 76–80. ◆

Erratum

'Coal quality and uranium distribution in Springbok Flats Coalfield samples' by M. Ndhlalose, N. Malumbazo, and N. Wagner published in the SAIMM Journal vol. 115, no. 12, pp. 1167–1174. Acknowledgement of Figure 3 was omitted in the original paper.

Acknowledgement for Figure 3 should read courtesy of Ms V. Nxumalo.

Diamonds still Sparkling 2016 Conference

14–17 March 2016, Gaborone International Convention Centre

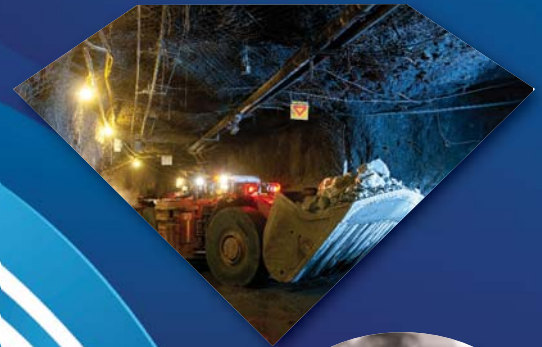
Workshop: 14 March 2016

Conference: 15–16 March 2016

Technical Visit: 17 March 2016

BACKGROUND

Being the sixth conference in the series, the Diamonds—still Sparkling Conference targets the full spectrum of the diamond pipeline from exploration through to sales and marketing. The last conference was held in 2013 at Misty Hills, Muldersdrift: the 2016 conference is returning to Botswana which previously hosted in 2010.



Photographs of diamonds courtesy of Petra Diamonds

OBJECTIVE

The objective of the conference will be to provide a forum for the dissemination of information relating to the latest mining methods and technologies applicable to the diamond mining industry. This will consider all stages of the value chain, from exploration through mine design, drilling and blasting production, and processing, to cutting, marketing and sales.

WHO SHOULD ATTEND

- > Processing engineers
- > Mining engineers
- > Geotechnical engineers
- > Geologists
- > Consultants
- > Suppliers
- > Cutting and polishing
- > Marketing and sales
- > Diamontiers
- > Mine managers
- > Mining companies
- > Students mining industry

TOPICS

- > Geology and exploration
- > Mine expansion projects
- > Mining, metallurgical and beneficiation technology
- > Rough diamond sales and marketing
- > Cutting and polishing
- > Financial services and industry analysis
- > Industry governance and legislation update
- > Mine specific case studies



For further information contact:

Raymond van der Berg • Head of Conferencing • SAIMM
P O Box 61127, Marshalltown 2107

Tel: (011) 834-1273/7 • Fax: (011) 833-8156 or (011) 838-5923
E-mail: raymond@saimm.co.za • Website: <http://www.saimm.co.za>

Sponsors:



Conference Supporter



Media Partner



Conference Announcement



An algorithm for determining kinetic parameters for the dissociation of complex solid fuels

by P. Mavhengere*, T. Vittee*, N.J. Wagner*, and S. Kauchali*

Synopsis

An established distributed activation energy model (DAEM)-based algorithm for the dissociation of complex fuels obeying linear kinetics was modified to determine the kinetic parameters of materials reacting in a CO₂ gas stream by incorporating the random pore reaction model (RPM). The algorithm was adapted to the RPM and was able to derive the activation energy, E , the grouped pre-exponential factor, A , and the number of reactions occurring in the thermal conversion process. Furthermore, the mass fraction associated with each unique reaction was obtained. The ability to accurately determine multiple reactions and changes in the kinetic parameters during the reaction distinguishes the algorithm as a unique and robust method for determining kinetic parameters for the pyrolysis of complex fuels. The novelty in this research was the adaptation of the RPM and other reaction models to the DAEM algorithm, and hence to other conversion processes. The algorithm was tested on simulated conversion data and experimental data from thermogravimetric analysis of the dissociation of a South African coal char and a 50:50 (wt%) coal-biomass blend char under CO₂ atmosphere. The specific mass fraction of the reactive material dissociating under a particular set of kinetic parameters was determined, and all sets of data were successfully modelled to high accuracy.

Keywords

distributed activation energy model, random pore reaction model, kinetics, gasification.

Introduction

Fossil fuels are currently the world's primary energy source. Coal is the most abundant low-cost fossil fuel, but the high carbon to hydrogen ratio results in production of large quantities of CO₂ which, due to concern over global warming, is an unfavourable consequence of the use of this fuel (Irfan, Usman, and Kusakabe, 2011). Coal gasification is one of the most versatile and cleanest ways to convert coal to fuel and energy (Research and Markets, 2006). The ability of the gasification process to eliminate and/or contain air pollutants and greenhouse gases (GHGs) makes this process highly favourable. Hence, it is vital that this process be thoroughly understood to optimize its advantages over conventional coal conversion processes.

One particular aspect of the gasification process which is considered in this research is the determination of the kinetic parameters of the reactions occurring when biomass and coal

chars are gasified. A comprehensive review of the many factors affecting the kinetics of gasification in CO₂ is given by Irfan, Usman, and Kusakabe (2011). Various methods of determining kinetic parameters have been proposed and explored over the years, with varying degrees of success. Of particular interest is collection of methods which are commonly known as model-free/integral iso-conversion methods (Starink, 2003). While the model-dependent methods (Rotaru and Goêa, 2009) are based mainly on the Langmuir-Hinshelwood model, the iso-conversion methods are based on the premise that reaction rate is a product of two functions: one depending solely on temperature, and the other depending solely on the fraction transformed. This is demonstrated by Equation [1].

$$\frac{dx}{dt} = f(x)k(T) \quad [1]$$

The temperature-dependent function generally assumes Arrhenius dependency (Starink, 2003):

$$k = A e^{-E/RT} \quad [2]$$

In Equation [2], E is the activation energy (kJ/mol), A is the grouped pre-exponential factor (m^{1.5}s⁻¹), R is the universal gas constant (8.314 J/(mol K)), and T is the reaction temperature (K). By substituting and integrating Equations [1] and [2], for non-isothermal conversion at a constant heating rate (β), Equation [3] is obtained.

$$\int_0^x \frac{dx}{f(x)} = \frac{A}{\beta} \int_{T_0}^T \frac{-E}{e^{RT}} dT \quad [3]$$

* School of Chemical Engineering, University of Witwatersrand, Johannesburg, South Africa..

© The Southern African Institute of Mining and Metallurgy, 2016. ISSN 2225-6253. Paper received Apr. 2015; revised paper received Jun. 2015.

An algorithm for determining kinetic parameters

The right-hand side expression of Equation [3] is known as the 'temperature integral'. Integral iso-conversion methods make an approximation to the temperature integral¹ and then find E . Since the iso-conversion methods evaluate E for the reaction independent of the reaction model, various methods must further be applied to determine the rest of the kinetic triplet. The kinetic triplet consists of the reaction model function, $f(x)$, where x is conversion; E , the activation energy of the conversion reaction; and A , the grouped pre-exponential factor. Iso-conversion methods are usually followed by discrimination procedures for identifying the true conversion function of each linear non-isothermal process (Rotaru and Goêa, 2009; Vyazovkin, 2008). Note that some of these methods are applicable to single step conversions where the E evaluated does not show systematic variation with x (Vyazovkin, 2008). For heterogeneous fuels like coal, where multiple step processes occur, a different approach must be taken. Such scenarios are considered in the distributed activation energy model (DAEM)-based algorithm presented in the current paper.

The presented method evaluates the E model independently, as an iso-conversion method. Upon the evaluation of E , a reaction model is assumed, and is used to evaluate the corresponding A . The algorithm provides a way of inverting the DAEM, resulting in the determination of discrete mass-fraction values and accurate identification of E and A for each parallel step participating in the thermal decomposition of the fuel. The current study focuses on extending this method to conversions best described by the random pore reaction model (RPM).

The algorithm developed by Scott *et al.* (2006a) is based on the DAEM. Coal was first treated as a mixture of a large number of species decomposing by parallel first-order reactions by Pitt (1962). The DAEM makes use of this description, and further assumes that the complexity of the fuel is such that a continuous distribution of E values exists for a discretized number of arbitrary reactions. This allows a function of E , and time, to define the mass of volatile material with E values between the initial activation energy (E_0) and the activation energy at some point in time (E_t) (Scott *et al.*, 2006a). The assumption leads to the formation of a double exponential term, which acts over a narrow range of E values and changes as time progresses (Please, McGuinness, and McElwain, 2003). According to Please, McGuinness, and McElwain, this term is the main source of numerical difficulty in application of the DAEM. Scott *et al.* (2006a) describe this term as given by Equations [4] and [5].

$$\frac{M_v(t)}{M_{v0}} = \int_0^\infty g(E) \times \exp \left[-A(E) \int_0^\tau \exp(-E/RT) dt \right] dE \quad [4]$$

where

$$\Psi(E, t) = \exp \left[-A(E) \int_0^\tau \exp(-E/RT) dt \right] \quad [5]$$

Here, $M_v(t)$ is the total mass of volatile matter, M_{v0} is the initial value of $M_v(t)$, $g(E)$ is the underlying initial distribution of E which characterizes the material, and $g(E)$ may be evaluated from:

$$g(E) = \frac{m_o(E)}{\int_0^\infty m_o(E) dE} \quad [6]$$

Please, McGuinness, and McElwain (2003) outline a number of numerical approximations to the evaluation of Equation [4]. Different approaches to the evaluation of the initial distribution of E have been adopted; for example, a Gaussian distribution has been assumed to characterize the distribution of E by some authors (*e.g.* Kirtania and Bhattacharya, 2012). Numerous approximations have also been suggested to give a closed form of the double integral term. An approximate closed form of the model can be obtained by assuming that, as conversion proceeds, the functional groups with the lowest E values (*i.e.* weakest bonds) dissociate first, as demonstrated by Rostami, Hajalgol, and Wrenn (2004). Other approaches were taken by various authors, as illustrated by Scott *et al.* (2006a). From these, it is noted that Miura and Maki (1998) showed that it is possible to evaluate the A and E of a particular reaction assumed to dominate at a given conversion by comparing the same volatile yield in two or more experiments performed at different heating rates (Scott *et al.*, 2006a). Braun and Burnham (1987) also demonstrated the first discretization of the distribution of E . This was carried out by assuming a finite set of discrete first-order reactions in the place of the continuous distribution of E outlined in Equation [6]. Using these approaches to solving the DAEM, Scott *et al.* (2006a) proposed an algorithm based on this discretization. This algorithm will be referred to as Scott's algorithm. Scott's algorithm was developed to determine the pyrolysis kinetics of complex solid fuels using the first-order reaction model. Coals and biomasses are complex fuels due to their heterogeneous nature. In the current study, the algorithm was adapted to the RPM; due to the complicated form of the RPM, it was selected for demonstration of the algorithm's capability to be adapted to other reaction models. A general format for adaptation of the model is also outlined in this study. Many authors have proven the DAEM to be a successful method of determining the kinetic parameters of the pyrolysis of complex fuels (*e.g.* Kirtania and Bhattacharya, 2012; Scott *et al.*, 2006a, 2006b; Miura and Maki, 1998; Maki, Takatsuno, and Miura, 1997). The application of the DAEM to other conversion processes is set to benefit the study of the gasification and combustion processes of complex heterogeneous fuels.

Algorithm development

The original DAEM-based algorithm was derived and shown to be effective in determining the kinetic parameters for pyrolysis (Scott *et al.*, 2006a, 2006b). The algorithm is applied in three main steps, where E , A , and the mass fraction, f , for a candidate reaction, i , are calculated. The original algorithm is presented in Equation [7]:

$$\frac{M(t)}{M_0} = w + \sum_{\text{All reactions, } i} f_{i,0} \exp \left[-A_i \int_0^\tau \exp(-E_i/RT(t)) dt \right] \quad [7]$$

where $M(t)$ is the sample mass of initial value M_0 containing a fraction w of inert material, and $f_{(i,0)}$ is the initial mass

¹Integral iso-conversion methods that do not make an approximation to the temperature integral are known as 'algorithmic methods', but are generally considered highly calculation-intensive.

An algorithm for determining kinetic parameters

fraction of M_0 which decomposes with activation energy E_i and pre-exponential factor A_i . The double-exponential term can be expressed as Ψ_i . Note that f_i represents the discrete fractional density function, or remaining mass fraction as a function of conversion. The full derivation of the algorithm can be found in Scott *et al.* (2006a). The double-exponential term in Equation (7) is identified as:

$$\Psi_i = \exp \left[-A_i \int_0^{\tau} \exp \left(-\frac{E_i}{RT} \right) dt \right] \quad [8]$$

which, if it is multiplied by a constant heating rate, can be expressed as:

$$\Psi_i(t) = \Psi_i(T) = \exp \left[-\frac{A_i}{\beta} \int_{T_0}^T \exp \left(-\frac{E_i}{RT} \right) dT \right] \quad [9]$$

Like the DAEM, the algorithm proposes that the reactions in a complex solid fuel occur in parallel and assumes that at each fractional conversion, a single reaction is dominant. The algorithm uses this assumption and the expression in Equation [9] to calculate E without the use of a proposed reaction model. At this point, the method is akin to an iso-conversion method; significant differences between this method and iso-conversion versions appear later.

The first step of the algorithm considers the conversion at two different heating rates, say β_1 and β_2 . If it is then assumed that the i^{th} reaction is the only reaction taking place at this conversion, then $f_i(\beta_1, T_1) = f_i(\beta_2, T_2)$. It then follows, since Ψ is also a function of heating rate, that:

$$\Psi_i(\beta_1, T_1) = \Psi_i(\beta_2, T_2) \quad [10]$$

Then, substituting the heating rate and taking natural logarithms on both sides yields:

$$\begin{aligned} & \frac{1}{\beta_1} \left[T_0 \exp \left(\frac{-E_i}{RT_0} \right) \right. \\ & \left. - \frac{E_i}{R} \int_{E_i/RT_0}^{\infty} \frac{\exp(-u)}{u} du - T_1 \exp \left(\frac{-E_i}{RT_1} \right) + \frac{E_i}{R} \int_{E_i/RT_1}^{\infty} \frac{\exp(-u)}{u} du \right] \\ & = \frac{1}{\beta_2} \left[T_0 \exp \left(\frac{-E_i}{RT_0} \right) \right. \\ & \left. - \frac{E_i}{R} \int_{E_i/RT_0}^{\infty} \frac{\exp(-u)}{u} du - T_2 \exp \left(\frac{-E_i}{RT_2} \right) + \frac{E_i}{R} \int_{E_i/RT_2}^{\infty} \frac{\exp(-u)}{u} du \right] \end{aligned} \quad [11]$$

From this, E_i can be determined using temperature-conversion data and the heating rates used. This result is presented as a conversion range with corresponding E_i values. Since this step is model-independent, no modification is required.

Once E_i has been found using Equation [11], A_i can be evaluated (Scott *et al.*, 2006a). It is assumed that the reaction of component i is at its maximum rate of decomposition at the particular conversion. This assumption follows from how the approach is posed, *i.e.* that at each fractional conversion, only one reaction is dominating. The assumption is best explained by Miura (1995). Miura demonstrates how the $\Psi_i(T)$ function changes steeply with E at a given temperature. This then allows the $\Psi_i(T)$ function to be assumed by a step function (U) at a particular activation energy E_s such that:

$$\Psi_i(E, T) = U(E - E_s) \quad [12]$$

This approximation then corresponds to the assumption that only one reaction (with activation energy E_s) is occurring

at a particular temperature, T (Miura and Maki, 1998; Miura, 1995). The assumption was found to hold at an approximate E_s value evaluated at $\Psi_i(E, T) = 0.58$ for many combinations of the distribution curve and the pre-exponential factor.

Based on this assumption, the value of conversion x that results in this maximum decomposition rate must be evaluated. For a single first-order reaction, the maximum decomposition rate is described by Equation [13]:

$$\begin{aligned} \frac{d}{dt} \left(\frac{df_i}{dt} \right) &= \frac{d}{dt} \left\{ f_{i,0} A_i \exp(-E_i/RT) \times \exp \right. \\ & \left. \left[-A_i \int_0^t \exp(-E_i/RT) dt \right] \right\} = 0 \end{aligned} \quad [13]$$

Equation [13] can be expressed as Equation [14] at a constant heating rate:

$$\frac{d}{dT} \left(\frac{dx}{dT} \right) = \frac{d}{dT} \left\{ \left(\frac{A_i}{\beta} \exp \left(\frac{-E}{RT} \right) \right) (1-x) \right\} = 0 \quad [14]$$

since $\frac{dx}{dT} = x$, for a single reaction taking place during a conversion. The determined conversion value (called x_{max}) is then used to calculate the corresponding Ψ_{imax} . At this point, A_i can be evaluated using Equation [15]:

$$\begin{aligned} \ln \Psi_i &= \frac{A_i}{\beta} \left[T_0 \exp \left(\frac{-E_i}{RT_0} \right) - \frac{E_i}{R} \int_{E_i/RT_0}^{\infty} \frac{\exp(-u)}{u} du \right. \\ & \left. - T \exp \left(\frac{-E_i}{RT} \right) + \frac{E_i}{R} \int_{E_i/RT}^{\infty} \frac{\exp(-u)}{u} du \right] \end{aligned} \quad [15]$$

To demonstrate, for a first-order reaction, a value of $x=1-e^{-1}$ ratifies Equation [14]. Then, if the first-order reaction model is expressed in terms of Ψ :

$$\Psi_i = 1 - x \quad [16]$$

Hence

$$\ln(\Psi_i(T)) = -1 \quad [17]$$

To adapt this algorithm to any other reaction model, this value of conversion (x) and corresponding value of $\ln[(\Psi_i(T))]$ must be modified. Hence, following the same approach, the x_{max} value for a single reaction dissociating according to a particular reaction model taking place must be evaluated. This is described by Equation [18]:

$$\frac{d}{dT} \left(\frac{dx}{dT} \right) = \frac{d}{dT} \left[\left(\frac{A_i}{\beta} \exp \left(\frac{-E}{RT} \right) \right) f(x) \right] = 0 \quad [18]$$

The x_{max} values for each reaction model can be evaluated graphically or analytically for both reaction models. Equation [19] demonstrates the dependence of the Ψ expression on the reaction model.

$$g(x) = \ln \Psi = \int_0^x \frac{dx}{f(x)} \quad [19]$$

Table I presents the results obtained upon the evaluation of Equations [18] and [19].

It is noted that the RPM reaction model has an extra parameter; this is referred to as the structural parameter φ . For the RPM, analytical evaluation of Equation [18] results in Equation [20]:

An algorithm for determining kinetic parameters

Table 1

First-order reaction model and RPM expressions for algorithm modification

Model	$f(x)$	$\int_0^x \frac{dx}{f(x)} = g(x) = \ln \Psi(x)$	x_{max}	$\ln \Psi_{max}$
First order	$1-x$	$\ln(1-x)$	0.6321	-1
RPM	$(1-x)\sqrt{(1-\varphi)\ln(1-x)}$	$\frac{2}{\varphi} (\sqrt{(1-\varphi)\ln(1-x)} - 1)$	0.6502	-0.8801

$$\frac{\varphi A^2 \exp\left(\frac{-2E}{RT}\right)(1-x)}{2\beta^2} - \frac{A^2 \exp\left(\frac{-2E}{RT}\right)(1-x)(1-\varphi \ln(1-x))}{\beta^2} - \frac{AE \exp\left(\frac{-E}{RT}\right)(1-x)\sqrt{1-\varphi \ln(1-x)}}{\beta RT^2} = 0 \quad [20]$$

where φ is a dimensionless structural parameter in the RPM, A ($s^{-1}.m^{-1}$) is the grouped pre-exponential factor, and β is the constant heating rate (K/s). The structural parameter φ is calculated for all simulations using values applicable to common porous solids (Bhatia and Perlmutter, 1980). The values provided result in a structural parameter value of $\varphi = 0.88$. This value is used in the simulations presented in the current study.

However, when applying the algorithm to experimental data, the structural parameter is initially unknown. It is evaluated by regression for the particular data in the algorithm. It is also noted that the x_{max} value varies with the structural parameter as described by Equation [20]. A parametric study was carried out to evaluate the sensitivity of x_{max} as the structural parameter is varied at different sets of A and E . During this study, negligible changes in the x_{max} value were observed. It was then assumed that the value of x_{max} at 0.6502 was applicable as a fixed point of maximum rate of dissociation for the RPM.

Equation [20] cannot be expressed explicitly in terms of x . An error minimization method can be applied, with a series of proposed values of E , A , and φ to determine x at which the i th reaction (not the overall material reaction) reaches a maximum rate of decomposition. This value is substituted into the manipulated RPM expression in order to determine $\ln[\Psi_i(T)]$. The modification of the original algorithm (Scott *et al.*, 2006a) is needed in the evaluation of Ψ .

Following each fractional conversion, a set of E_i and A_i values can be determined. At this stage the algorithm has departed from iso-conversion methods in that it has determined the pre-exponential factor values without the need for an entirely separate method.

Lastly, the mass fractions must be determined. This step is vital since it further distinguishes the algorithm from other common methods. The mass fraction values allocated to each fractional conversion help identify which reactions are actually happening, and which reactions are spurious (Scott *et al.*, 2006a). This result will produce discreet kinetic parameter values rather than a range of values which would otherwise have to be averaged, thus compromising accuracy. Now Equation [7] can be written in matrix form as $M = \Psi f$ such that:

$$\frac{1}{M_0} \begin{bmatrix} M(t_0) \\ M(t_1) \\ M(t_2) \\ \vdots \\ \vdots \end{bmatrix} = \begin{bmatrix} \Psi_1(t_0) & \Psi_2(t_0) & \dots & \Psi_n(t_0) & 1 \\ \Psi_1(t_1) & \Psi_2(t_1) & \dots & \Psi_n(t_1) & 1 \\ \Psi_1(t_2) & \Psi_2(t_2) & \dots & \Psi_n(t_2) & 1 \\ \vdots & \vdots & \vdots & \vdots & \vdots \\ \vdots & \vdots & \vdots & \vdots & \vdots \end{bmatrix} \times \begin{bmatrix} f_{1,0} \\ f_{2,0} \\ f_{3,0} \\ \vdots \\ w \end{bmatrix} \quad [21]$$

This form is used in the final step. The f_{i0} values for each component i are calculated using linear least squares. Equation [21] is used by specifying an E and A value and generating the candidate reactions to populate the matrix Ψ . The M vector is the predetermined mass loss profile of the simulated or experimental reaction. Note that resulting matrix Ψ is not a square matrix. Therefore, when the f vector is calculated using matrix inversion such that $M \cdot \Psi^{-1} = f$, there is no exact solution. The least squares (non-negative constraint) function in Matlab (*lsqnonneg*) is therefore used to numerically determine the f_{i0} elements in the f vector that satisfy $M \cdot \Psi^{-1} = f$.

As derived in Table I, Equation [22] is used for the evaluation of the matrix Ψ for the RPM.

$$\Psi = \exp \left[\frac{2}{\varphi} (\sqrt{1-\varphi \ln(1-x)} - 1) \right] \quad [22]$$

The evaluated matrix is then used in the *lsqnonneg* algorithm in Matlab® to do the matrix inversion and generate the vector f . The E_i and A_i values corresponding to non-zero f_i value(s) are the kinetic parameters considered to represent the reaction(s) occurring in the fuel mass.

Results and discussion

The modified algorithm was tested on two different sets of data. Following the methodology of Scott *et al.* (2006a), the algorithm was tested on (1) simulated conversion data, and (2) experimental thermogravimetric measurements obtained from the decomposition of a South African coal char and a 50:50 (wt%) coal-biomass blend char under CO_2 atmosphere. Using Matlab software and Equation [22], typical thermogravimetric data of a reaction progressing according to a particular reaction model at a specified heating rate and kinetic parameters was generated. The algorithm was then applied to the simulated data; the kinetic parameters determined by the algorithm were compared to the kinetic parameters specified for the simulation of the data as a measure of accuracy.

Application to simulated conversion data

Test 1: Single RPM reaction

A single RPM reaction was simulated at three different heating rates: 10, 30, and 100 K/min. The first two heating rates were used for determining the kinetic parameters, whereas the third heating rate was merely used to show how

An algorithm for determining kinetic parameters

the kinetic parameters derived by the algorithm extrapolate to different heating rates (Scott *et al.*, 2006a). Figures 1 and 2 display the results obtained. The error values reported are the correlation coefficient (R^2) and the root mean square (RMS) error value. The correlation coefficient is defined by Equation [23] (Draper and Smith, 1981).

$$R^2 = 1 - \frac{\sum(y_i - \hat{y}_i)^2}{\sum(y_i - \bar{y})^2} \quad [23]$$

Here, \hat{y}_i is the model-predicted dependant variable, y_i is the experimentally determined dependant variable, and \bar{y} is the mean of the experimental values. The RMS error value is defined as:

$$RMS = \sqrt{\frac{1}{i} \sum (y_i - \hat{y}_i)^2} \quad [24]$$

As observed in Figure 1, the model predicts the simulated data to accuracies with a R^2 error of 1, and a corresponding RMS error of 0.00071. For this reaction, an E of 200 kJ/mol and an A of $108 \text{ m}^{-1}\text{s}^{-1}$ is prescribed for the simulation.

Figure 2 presents the actual kinetic parameters evaluated by the model for 50 candidate reactions; *i.e.* 50 unique conversion points. As noted by Scott *et al.* (2006a), the mass fractions allocated are zero for all the other reactions except for the two points straddling the value of $x = 0.6502$. This is the value at which the reaction is assumed to be dominating.

Test 2: Seven RPM reactions

Seven RPM reactions were in turn simulated at the three heating rates. The kinetic parameters used in the simulation are displayed in Table II. The simulated data was applied on to the algorithm and Figures 3 and 4 display the results obtained.

Once more, overlapping parallel reactions of E values of 225, 235, and 250 kJ/mol, were selected.

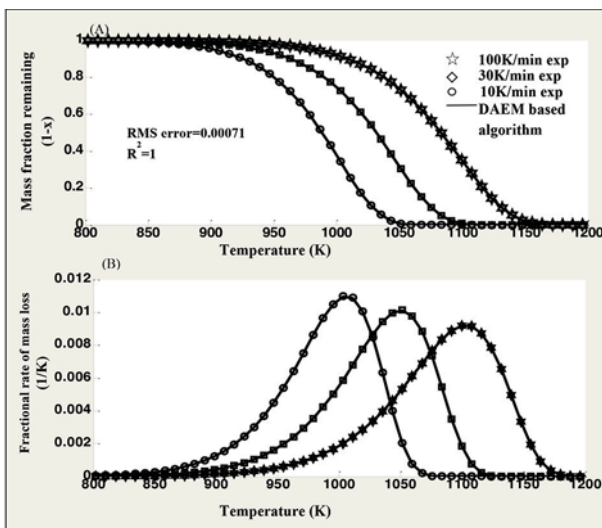


Figure 1—Modelling of a simulated single RPM reaction at an $E = 200 \text{ kJ/mol}$ and an A of $10^8 \text{ m}^{-1}\text{s}^{-1}$. (A) displays the conversion vs. time plots at the three different heating rates for both the simulated data and the algorithm predictions. (B) displays the time derivative of the mass fraction against temperature plots

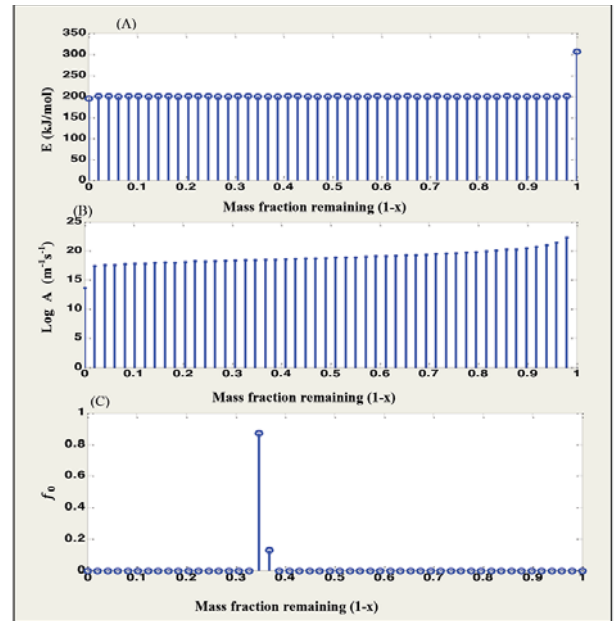


Figure 2—Modelling of an imaginary fuel dissociating according to a single RPM reaction. The actual values of E , A , and f_0 for 50 candidate reactions are displayed in (A), (B), and (C) respectively

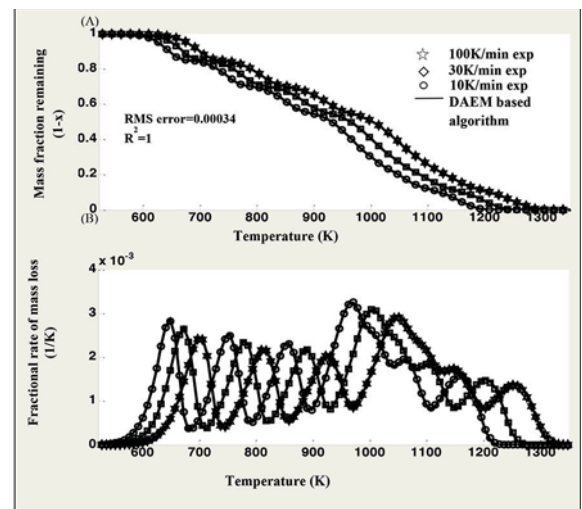


Figure 3—Modelling of an imaginary fuel dissociating according to seven RPM reactions. (A) displays the conversion vs. time plots at the three different heating rates for both the simulated conversion data and the algorithm predictions. (B) displays the time derivative of the mass fraction against temperature plots

Table II
Specified kinetic parameters for the seven simulated RPM reactions

Reaction	1	2	3	4	5	6	7
E (kJ/mol)	150	175	200	225	235	250	275
f_0	1/7	1/7	1/7	1/7	1/7	1/7	1/7
A ($\text{m}^{-1}\text{s}^{-1}$)	10^{10}						

An algorithm for determining kinetic parameters

As observed in Figure 3, the kinetic parameters determined by the algorithm predict the simulated data, even at the 100 K/min heating rate, which was not used for kinetics determination. A RMS error value of 0.00034 and R^2 value of 1 are reported.

Figure 4 displays the actual kinetic parameters evaluated by the algorithm for 50 candidate reactions. Once more, the mass fractions are allocated to the actual reactions taking place at the point of dominance. At this point it can be concluded that the algorithm presented by Scott *et al.* (2006a), for determining the kinetic parameters of a complex fuel dissociating under the first-order reaction model has been successfully adapted to RPM behaviour.

Figure 5 presents the general steps for the adaptation of the algorithm to other reaction models.

Application of the DAEM-based algorithm to thermogravimetric analysis

Thermogravimetric analysis was carried out on the decomposition of a South African coal char and a 50:50 (wt%) coal and biomass (pinewood chips) blend under CO_2 atmosphere. The samples were characterized by the use of proximate analysis as given in Table III.

A significant increase in moisture and volatile matter is observed in the coal-biomass blend when compared to the plain coal proximate analysis, as illustrated by Table III. A decrease in the fixed carbon and ash content is also observed.

A TA Instruments SDT-Q600 high-temperature thermogravimetric analyser (TGA) was used for the experiments. Samples with nominal diameters up to 150 μm were used to produce the chars via thermogravimetry. The samples were heated at 20 K/min to 1623 K and then held at 1023 K for 15 minutes to ensure all volatiles were driven off. The coal char samples were heated at three heating rates, 12, 15, and 20 K/min, from ambient temperature to 1573 K. A

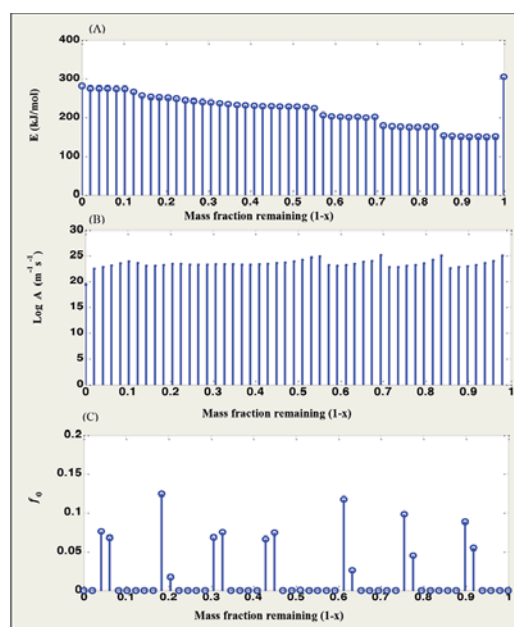


Figure 4—Modelling of an imaginary fuel dissociating according to seven RPM reactions. The actual values of E , A , and f_0 for 50 candidate reactions are displayed in (A), (B), and (C) respectively

constant air flow rate of 65 ml/min CO_2 and 5 ml/min N_2 was maintained throughout the analysis. The measurements were applied to the algorithm, and the outcome is presented in Figures 6 and 7. When dealing with experimental data, the structural parameter (ϕ) is not known. While it can be measured experimentally (Su and Perlmutter, 1985), other studies (Everson *et al.*, 2006; Bhatia and Vartak, 1996) suggest that it is best to find the structural parameter via regression analysis to avoid the need for lengthy experimental procedures, as well to ensure improved accuracy and reliability of the kinetic parameters. This was carried out using an error minimizing regression method presented by Sangtong-Ngam and Narasingha (2008). This approach is characterized by Equation [25]:

$$\sigma = \sqrt{\frac{err_1^2 + \dots + err_n^2}{n}} \quad [25]$$

where err_1 is the error between the calculated and experimental data at point 1, err_n is the error between the calculated and experimental data at point n , and n is the number of points in the data-set. The *fminbnd* algorithm in Matlab (Matlab R14, The Mathworks Inc.) is used to vary the value of ϕ within a predetermined range until σ is minimized. This is a further modification applied to the original algorithm which is necessary for processing RPM data.

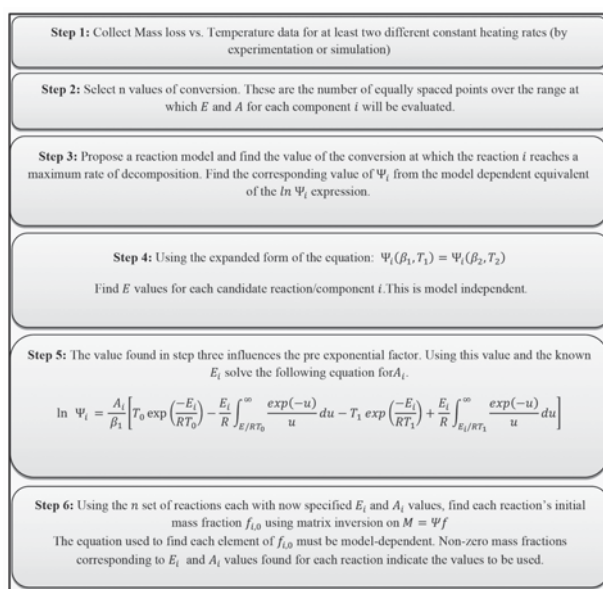


Figure 5—General steps for adapting the DAEM-based algorithm to other reaction models

Table III
Proximate analysis results

Sample component	Coal, wt%	Coal-biomass blend, wt%
Moisture	2.44	6.23
Volatile matter	18.93	50.68
Fixed carbon	44.80	25.93
Ash content	33.83	17.16

An algorithm for determining kinetic parameters

As presented in Figure 6, the algorithm results demonstrate excellent agreement with the experimental results obtained. RMS error values of 0.0043 and 0.0050 were determined for the plain coal char and coal-biomass blend char respectively. Corresponding R^2 values of 0.9999 and 0.9998 are reported for the two chars as illustrated by Figure 6. The actual kinetics obtained are as outlined in Table IV. The RPM was suitable for the modelling of the conversion of both chars.

Table IV illustrates changes in the kinetic parameters of the Boudouard reaction for both chars. The different sets of kinetic parameters determined during the reaction may be aligned to the limited predicting capabilities of the RPM, such as 'catalytic effects, initially closed porosity, inhomogeneities of the active surface area, incomplete pore utilization and changes in concentrations of active sites with conversion' (Smith *et al.*, 1994) among others. However, the variation in kinetic parameters has also been explained in the literature as due to the shifting of the reaction from the chemical reaction-controlled regime towards the pore diffusion-controlled regime (Babinski *et al.*, 2013). This was indicated by the decrease in E from the beginning of the reaction towards its completion (Lahijani, Zainal, and Mohamed,

2012; Mani, Mahinpey, and Murugan, 2011; Hurt and Calo, 2001). The ratio of the initial E to the final E is only 0.87 and 0.93 for the plain coal char and the coal-biomass blend char respectively, instead of 0.5 for a complete shift into the diffusion-controlled regime (Babinski *et al.*, 2013). This indicates that the reaction is predominantly taking place under the chemical reaction-controlled regime. Table IV also presents three sets of kinetic parameters for the plain coal char conversion and two sets of kinetic parameters determined during the conversion of the coal and biomass char blend. The different number of reactions/kinetic parameter sets identified may indicate the presence of synergy between the two materials during gasification. Unlike most iso-conversion methods, *e.g.* Vyazovkin and Friedman methods (Babinski *et al.*, 2003), which evaluate the reaction kinetics at a particular conversion, the algorithm was able to provide the specific mass fraction of the reactive material dissociating under a particular set of kinetic parameters. This provides more detailed kinetic information which could potentially improve the application of kinetic parameters in the design and optimization of conversion systems.

The actual E values determined by the algorithm for both the pure coal char and the coal and biomass char blend were found comparable to values reported by Zhu, Sing, and Lin (2008) and Liu *et al.* (2000) for the gasification of coal chars. Table IV also displays the determined φ values of 12.2 and 11.7 for the two chars, which compare to the range of values of 2.2 to 50 reported in the literature (Liu and Niksa, 2004; Zolin, 2001; Charpenay, Serio, and Solomon, 1992). A single φ for both chars was sufficient to describe the reaction progression despite the changes observed in the rest of the kinetic parameters.

It is essential to define the kinetic parameters in context prior to comparison. E has been described as the minimum amount of energy required to start a chemical reaction (Vittee, 2012; Brown, LeMay, and Bursten, 2009). Lower E reactions have therefore been interpreted to imply that the reaction takes place more spontaneously, or that the conditions and reactants are more reactive compared to reactions of higher E . The pre-exponential factor, also termed the frequency factor, indicates the number of collisions of particles occurring with the correct orientation and sufficient energy to enable a reaction to take place (Brown, LeMay, and Bursten, 2009). A lower E and higher pre-exponential factor

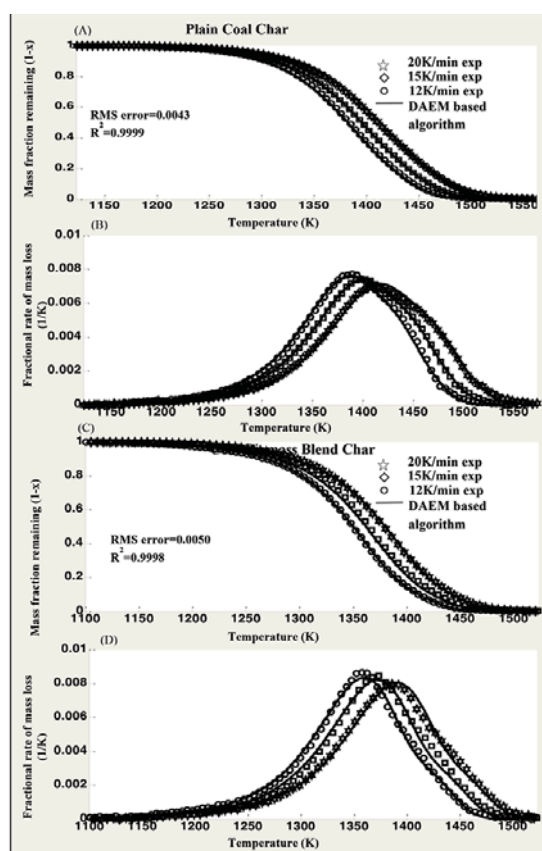


Figure 6—Modelling of thermogravimetric analysis data obtained from the dissociation of a South African coal char and a coal-biomass blend char under CO_2 atmosphere. (A) and (C) display the conversion vs. time plots at the three different heating rates for both the experimental data and the algorithm predictions for the plain coal char and coal-biomass blend char respectively. (B) and (D) display the time derivative of the mass fraction against temperature plots for the plain coal char and biomass-coal char blend respectively

Coal char			
(f_0)	E (kJ/mol)	A ($\text{s}^{-1} \cdot \text{m}^{-1}$)	(φ)
0.313	261.7	1.60E+07	12.2
0.315	246.4	2.08E+06	
0.366	227.6	2.75E+05	
Coal-biomass blend char			
0.315	259.1	6.59E+06	11.7
0.671	239.8	2.85E+06	

An algorithm for determining kinetic parameters

relates to a higher degree of reactivity, whereas a higher E and lower pre-exponential factor indicates a lower degree of reactivity.

When comparing the kinetics of the plain coal char and that of the coal-biomass blend, the differences are not quite palpable. When simply considering the average E and A , the blend would be interpreted to have less reactive kinetics. However, the unique feature of the DAEM allows for a more detailed analysis and comparison of the obtained kinetics by determining the mass fractions associated with each reaction taking place.

The blend presents an E range between 239.8 kJ/mol and 259.1 kJ/mol and corresponding grouped pre-exponential factors in the range of $2.85E+6$ to $6.59E+6$. The lower E describes the dissociation of the majority of the reactive material (67%). The plain coal char is described by an E range of 227.6 kJ/mol to 261.6 kJ/mol, and a corresponding A range of $2.75E+5$ to $1.6E+7$ attributed to three virtually equal mass fractions. The relatively high frequency factor ($1.6E+7$), requires a high activation energy (261.6 kJ/mol) for the first fraction; this reaction is comparable to the higher E (259.1 kJ/mol) reaction in the blend. The second mass fraction is described by an E of 246.4 kJ/mol and A of $2.08E+6$, both parameters implying a slightly less reactive profile than those of the major components of the blend. The last mass fraction component of the pure coal char presents a lower E of 227.6 kJ/mol and significantly lower A of $2.75E+5$, making the reaction profile somewhat comparable to that of the major mass fraction component in the blend ($E = 239.8$ kJ/mol and $A = 2.85E+6$). Hence, a complete analysis of the kinetics, considering the mass fraction components, shows an improvement in reactivity in the coal-biomass blend char compared to the plain coal char. It is also clear that the φ value has been reduced slightly from the pure coal char to the coal and biomass char blend. As described by Bhatia and Perlmutter (1980), two opposing forces contribute to surface area growth; pore expansion and pore collapse due to coalescence. A φ greater than 2 has been determined to indicate the prevalence of pore growth, whereas that lower than 2 is believed to demonstrate higher pore coalescence (Bhatia and Perlmutter, 1980). Since the two φ values already indicate significant pore growth, the lower φ value is assumed to indicate a slightly higher prevalence of pore coalescence; this is considered to be a possible contributing factor to the improved reactivity of the blended chars.

Conclusion

The DAEM-based model developed by Scott *et al.* (2006a) has been successfully modified for the dissociation of complex fuels according to the RPM. Despite the derivation of the DAEM-based algorithm being based upon first-order reaction kinetics, a general method to adapt the algorithm to other reaction models has been outlined. The DAEM-based algorithm has also been shown to be model-independent in the determination of E .

The modified algorithm has been tested on simulated conversion data for a typical fuel dissociating according to

- Single RPM reactions
- Seven RPM reactions, each with a specified E and A .

The modified DAEM-based algorithm was also applied to experimental data obtained from the conversion of a South

African coal char and a coal-biomass blend char via thermogravimetry in a CO_2 atmosphere. The algorithm evaluated E , A , and f values for the number of reactions taking place during the tests. The kinetic parameters determined by the algorithm predicted the simulated and experimental data to high accuracies with R^2 values of 1 to 0.9998, and RMS error values of 0.00034 to 0.0050.

The algorithm also demonstrates the ability to determine any changes in the kinetic parameters occurring during the reaction; this provides more insight to the reaction mechanisms taking place during the conversion.

By determining the reactive mass fraction component that is reacting according to a particular set of kinetic parameters, the DAEM-based algorithm provides unique and accurate kinetic details for the modelling of conversion processes. The value of the mass transfer component was demonstrated in comparing kinetic parameters of different char blends. The mass fraction components provide a higher degree of detail, which is valuable as it enhances the understanding, analysis, and comparison of the reaction profiles of complex fuels. The addition of biomass to the coal char was shown to improve the overall reactivity of the coal. A reduction in the number of reactions taking place during the conversion of the pure coal char and biomass/coal blend was observed, indicating the possibility of synergetic behaviour between the blended char components. A reduction in the structural parameter was also observed. The determined kinetic parameters are comparable to values reported in the literature.

Notation

A_0	Pre-exponential factor (s^{-1})
A	Grouped pre-exponential factor ($s^{-1}m^{-1}$)
b	Dimensionless constant
C_g	Concentration of gaseous reactant ($mol.m^{-3}$)
E	Activation energy ($J.mol^{-1}$)
f_i	Mass fraction of material
$M_v(t)$	Total mass of volatile matter at time t , (kg)
$M(t)$	Total mass remaining at time t , (kg)
M_0	Initial sample mass (kg)
R	Ideal gas constant ($kJ.mol^{-1}K^{-1}$)
R^2	Coefficient of linear correlation
T	Temperature (K)
T_0	Initial temperature (K)
μ	Dummy variable
x_0	Initial char mass fraction
x	Mass fraction of char at a given time during conversion
y_i	Experimentally determined dependent variable
\hat{y}_i	Model-predicted dependent variable
\bar{y}_i	Mean of experimentally determined dependent variables

Subscripts

i	indicates reaction number, or component number
v	indicates property of volatile matter
0	indicates initial state

An algorithm for determining kinetic parameters

Greek letters

α	Fractional conversion
β	Heating rate (K.s ⁻¹)
φ	Structural parameter
Ψ	$\exp \left[A(E) \int_0^t \exp(-E/RT) dt \right]$ (reaction function)

References

- BABINSKI, P., ŁABOJKO, G., KOTYCZKA-MORAN' SKA, M., and PLIS, A. 2013. Kinetics of coal and char oxycombustion studied by TG-FTIR. *Journal of Thermal Analysis and Calorimetry*, vol. 113, no. 1. pp. 371–378. DOI 10.1007/s10973-013-3002-x
- BHATIA, S.K. and VARTAK, B.J. 1996. Reaction of microporous solids: The discrete random pore model. *Carbon*, vol. 34, no. 11. pp. 1383–1391.
- BHATIA, S.K. and PERLMUTTER, D.D. 1980. A random pore model for fluid-solid reactions: I. Isothermal, kinetic control. *AIChE Journal*, vol. 26. pp. 379–386.
- BRAUN, R.L. and BURNHAM, A.K. 1987. Analysis of chemical reaction kinetics using a distribution of activation energies and simpler models. *Energy and Fuels*, vol. 1, no. 2. pp. 153–161.
- BROWN, T., LEMAY, H., and BURSTEN, B. 2009. Chemistry: The Central Science. International edition. Pearson Prentice Hall.
- CHARPENAY, S., SERIO, M.A., and SOLOMON, P.R. 1992. The prediction of coal char reactivity under combustion conditions. *Twenty-Fourth Symposium (International) on Combustion/The Combustion Institute*. pp. 1189–1197.
- DRAPER, N.R.W. and SMITH, H. 1981. Applied Regression Analysis. 2nd edn. Wiley, New York.
- EVERSON, R.C., NEOMAGUS, H.W.J.P., KASAINI, H., and NJAPHA, D. 2006. Reaction kinetics of pulverized coal-chars derived from inertinite-rich coal discards: Gasification with carbon dioxide and steam. *Fuel*, vol. 85, no. 7–8. pp. 1076–1082.
- HURT, R.H. and CALO, J.M. 2001. Semi-global intrinsic kinetics for char combustion modeling. *Combustion and Flame*, vol. 125, no. 3. pp. 1138–1149.
- IRFAN, M.F., USMAN, M.R., and KUSAKABE, K. 2011. Coal gasification in CO₂ atmosphere and its kinetics since 1948: a brief review. *Energy*, vol. 36, no. 1. pp. 12–40.
- KIRTANIA, K. and BHATTACHARYA, S. 2012. Application of the distributed activation energy model to the kinetic study of pyrolysis of the fresh water algae *Chlorococcum humicola*. *Bioresource Technology*, vol. 107. pp. 476–487.
- LAHIJANI, P., ZAINAL, Z.A., and MOHAMED, A.R. 2012. Catalytic effect of iron species on CO₂ gasification reactivity of oil palm shell char. *Thermochimica Acta*, vol. 546. pp. 24–31.
- LIU, G. and NIKSA, S. 2004. Coal conversion submodels for design applications at elevated pressures. Part II. Char gasification. *Progress in Energy and Combustion Science*, vol. 30, no. 6. pp. 679–717.
- LIU, G., TATE, A.G., BRYANT, G.W., and WALL, T.F. 2000. Mathematical modeling of coal char reactivity with CO₂ at high pressures and temperatures. *Fuel*, vol. 79. pp. 1145–1154.
- MAKI, T., TAKATSUNO, A., and MIURA, K. 1997. Analysis of pyrolysis reactions of various coals including argonne premium coals using a new distributed activation energy model. *Energy and Fuels*, vol. 11. pp. 972–977.
- MANI, T., MAHINPEY, N., and MURUGAN, P. 2011. Reaction kinetics and mass transfer studies of biomass char gasification with CO₂. *Chemical Engineering Science*, vol. 66, no. 1. pp. 36–41.
- MIURA, K. 1995. A new and simple method to estimate $f(E)$ and $k_0(E)$ in the distributed activation energy model from three sets of experimental data. *Energy and Fuels*, vol. 9. pp. 302–307.
- MIURA, K. and MAKI, T. 1998. A simple method for estimating $f(E)$ and $k_0(E)$ in the distributed activation energy model. *Energy and Fuels*, vol. 12. pp. 864–869.
- PITT, G.J. 1962. The kinetics of the evolution of volatile products from coal. *Fuel*, vol. 41. pp. 264–274.
- PLEASE, C.P., MCGUINNESS, M.J., and McELWAIN, D.L.S. 2003. Approximations to the distributed activation energy model for the pyrolysis of various coals. *Combustion and Flame*, vol. 133. pp. 107–117.
- RESEARCH AND MARKETS. 2006. Market Analysis – Gasification of Coal and its Importance in the Power Sector.
- ROSTAMI, A.A., HAJALGOL, M.R., and WRENN, S.E. 2004. A biomass pyrolysis sub-model for CFD applications. *Fuel*, vol. 83. pp. 1519–1525.
- ROTARU, A. and GOEA, M., 2009. Computational thermal and kinetic analysis: Complete standard procedure to evaluate the kinetic triplet from non-isothermal data. *Journal of Thermal Analysis and Calorimetry*, vol. 97, no. 2. pp. 421–426.
- SANGTONG-NGAM, K. and NARASINGHA, M.H. 2008. Kinetic study of Thai-lignite char gasification using the random pore model. *Thammasat International Journal of Science and Technology*, vol. 13. pp. 16–26.
- Scott, S.A., Dennis, J.S., Davidson, J.F., and Hayhurst, A.N. 2006a. An algorithm for determining the kinetics of devolatilisation of complex solid fuels from thermo-gravimetric experiments. *Chemical Engineering Science*, vol. 61, no. 8. pp. 2339–2348.
- SCOTT, S.A., DENNIS, J.S., DAVIDSON, J.F., and HAYHURST, A.N. 2006b. Thermogravimetric measurements of the kinetics of pyrolysis of dried sewage sludge. *Fuel*, vol. 85, no. 9. pp. 1248–1253.
- SMITH, K.L., SMOOT, L.D., FLETCHER, T.H., and PUGMIRE, R.J. 1994. The Structure and Reaction Processes of Coal. *Plenus Chemical Engineering Series*. 387 pp.
- STARINK, M.J. 2003. The determination of activation energy from linear heating rate experiments : a comparison of the accuracy of iso-conversion methods. *Thermochimica Acta*, vol. 404, no. 1–2. pp.163–176.
- SU, J.L. and PERLMUTTER, D. 1985. Effect of pore structure on char oxidation kinetics. *AIChE Journal*, vol. 31. pp. 973–981.
- VITTEE, T. 2012. Determination of Kinetics of Char Reactivity with Carbon Dioxide using Thermogravimetry and the Distributed Activation Energy Model. MSc dissertation, University of the Witwatersrand, Johannesburg, South Africa.
- VYAZOVKIN, S. 2008. Isoconversional kinetics. *Handbook of Thermal Analysis and Calorimetry*. Brown, M.E. and Gallagher, P.K. (eds.). Elsevier. Chapter 13, pp. 503–537.
- ZHU, W., SONG, W., and LIN, W. 2008. Catalytic gasification of char from co-pyrolysis of coal and biomass. *Fuel Processing Technology*, vol. 89, no. 9. pp. 890–896.
- ZOLIN, A. 2001. Reactivity of Solid Fuels. PhD dissertation, Department of Chemical Engineering, Technical University of Denmark, Denmark. ◆



THE SAMREC/SAMVAL COMPANION VOLUME CONFERENCE

An Industry Standard for Mining Professionals in South Africa
17–18 May 2016, Johannesburg

BACKGROUND

The SAMREC and SAMVAL Codes have been updated and will be released in 2016. In the process of updating these Codes numerous aspects were discussed that required more explanation and guidelines than could be included in the codes. In addition it was noted that the SAMCODES have no recognised guidelines or recognised standards, besides the coal commodity specific SANS 10320 National Standard

OBJECTIVES

The conference provides Competent Persons and Competent Valuers the opportunity to prepare and present details of recognised standards and industry benchmarks in all aspects of the SAMREC and SAMVAL Codes. These contributions will be collated into a Companion Volume to provide a guideline and industry standard for the public reporting of Exploration Results, Mineral Resources and Mineral Reserves and the Valuation of Mineral Projects.

The conference will provide a wide range of information pertaining to industry best practice including aspects of a various geological deposit types, commodities, permitting and legal obligations, resource estimation, mining engineering methodologies, metallurgical and process arrangements, engineering/infrastructure design, social and environmental factors etc for SAMREC Code reporting. Other papers will cover the application of the various methods of valuation and where and when they should be applied in accordance with the SAMVAL Code.

This is a valuable opportunity to be involved in the compilation of industry standards and benchmarks to support in all fields related to the SAMREC and SAMVAL Codes.

SAMREC CODE

Exploration Targets

Reporting of Exploration Results
Exploration Targets
Target generation

Mineral Resources

Geological data collection
Drilling techniques and drilling density
Bulk density
Sampling theory
QA/QC
Sampling and analysis protocols
Geological interpretation and geological modelling
Mineral Resource estimation
Conditional simulation
Mineral Resource estimation
Classification and reporting
Audits and reviews
Deleterious elements/minerals

Mineral Reserves

The modifying factors
Selecting a mining method
Metallurgy
Markets
Optimal mine scheduling
Cut-off grades
Feasibility studies
Risk assessment in Resource and Reserve
Classification and reporting
Grade reconciliation

Other Aspects

Legal aspects
Environmental
Sustainability issues
Social and labour planning

Diamond Resource and Reserve Reporting

Coal Resource and Reserve Reporting

WHO SHOULD ATTEND

The conference provides a platform for:

- Resource geologists
- Resource investors
- Project Finance Practitioners
- Exploration geologists
- Geoscientists
- Mining engineers
- Mineral Resource and Reserve managers
- Mineral Resource and Reserve practitioners
- Competent Valuers.

SAMVAL CODE

Cost Approach

Valuation of exploration properties using the cost approach

Market Approach

A review of market-based approaches
Valuation of mineral properties without Mineral Resources
Valuation methods for exploration properties and undeveloped Mineral Resources

Cashflow Approach

A Review of cashflow approaches
Discounted cash flow analysis input parameters and sensitivity
Discounted cash flow analysis methodology and discount rates
The valuation of advanced mining projects and operating mines
Valuing mineral opportunities as options

SPONSORSHIP

Sponsorship opportunities are available. Companies wishing to sponsor should contact the Conference Co-ordinator.

For further information contact:
Head of Conferencing, Raymond van der Berg
SAIMM, P O Box 61127, Marshalltown 2107
Tel: +27 11 834-1273/7 · Fax: +27 11 833-8156 or +27 11 838-5923
E-mail: raymond@saimm.co.za · Website: http://www.saimm.co.za



New gas nitriding technique using the interior of the nitrated pressure vessel as the process chamber

by R.W. Nell*, M. Kleingeld^{†‡}, and L. Liebenberg^{†‡}

Synopsis

The need to nitride the interior of large machine housings, which are also pressure vessels, for use in a high-temperature gas reactor resulted in the development of a suitable new nitriding technique whereby the vessel interior is used as a process chamber while being heated in a conventional top-hat heat treatment furnace. However, this new concept introduced several mechanical design challenges, such as an extended-length fan shaft, a high-temperature bearing, and sealing flanges for operation under extremely high temperatures. A prototype nitriding plant was constructed and operated to verify the design. The different tunnels machined inside the forged vessel were nitrated evenly by measuring and balancing the gas flow through each tunnel.

Test specimens placed at different positions in the housing were also nitrated during the process. The nitrated specimens were subjected to microhardness and layer thickness tests. Measured gas flow rates and other operational data confirmed the inverse proportionality between ammonia supply flow rate and measured crack ratio, as well as a crack ratio temperature dependence, typical of conventional gas nitriding processes.

The design and operation of the nitriding plant were successful and a nitride layer thickness of 400 μm and a hardness of approximately 1100 VHN were achieved. This proves that a large pressure vessel can be successfully nitrated using the vessel's interior as a process chamber.

Keywords

gas nitriding, pressure vessel, process chamber.

Introduction

Nitriding of the inner surface of the housing of an experimental Pebble Bed Modular Reactor (PBMR¹) core unloading device (CUD) was required. The CUD housing is a pressure vessel measuring 3 × 2.2 × 1.5 m and weighs 14 t. It forms the housing and structure for a large machine assembly with a number of moving metal parts and valves which make contact with the housing interior surface.

The most important reason for nitriding the CUD housing was to prevent cold welding between the moving metal parts and its lining surface, especially inside the PBMR helium gas pressure boundary. Friction in a helium environment causes cold welding between components made of similar steels, since there is no oxygen to replenish the oxide layer on the surface of the steel when wear takes place; a similar phenomenon is encountered in space

and high-vacuum applications (Johnson and Keller, 1996; Moeller and Noland, 1968; Lúcia *et al.*, 2006). A nitride layer also provides improved wear, corrosion, and fatigue resistance (Pye, 2003; Nisbett, 2005; Ashrafizadeh, 2003; Kenan, Mehmet, and Mehmet, 2000; Nathalie and Yves, 2006).

However, there are no nitriding facilities in South Africa that are able to nitride such a large pressure vessel. Furthermore, no records or evidence could be found that such a large workpiece had ever been nitrated before. Most commercial off-the-shelf nitriding systems (*e.g.* Nitrex) cannot contain a component as large as the CUD housing. The cost of a custom-built commercial system was prohibitive, and therefore an alternative methodology had to be adopted. The objectives of this work were the purposeful design, building, commissioning, and qualification of a suitable nitriding plant to nitride the housing of the first PBMR CUD prototype.

The CUD housing was designed as an ASME VIII (Division 1) pressure vessel (American Society of Mechanical Engineers, 2003a) and was constructed from ASME pressure vessel code steel. The CUD housing forging material is a Cr-Mo steel alloy that meets the ASME specification of SA 336 Grade F22, with chemical composition shown in

¹South African engineering company PBMR (Pty) Ltd designed the Pebble Bed Modular Reactor.

* Westinghouse Electric SA, Zwartkop, South Africa, Postgraduate candidate, North-West University.

†‡ Centre for Research and Continued Engineering Development, North-West University (Pretoria Campus), Lynnwood Ridge, South Africa, also Consultants to TEMM International (Pty) Ltd. and MCI (Pty) Ltd.

© The Southern African Institute of Mining and Metallurgy, 2016. ISSN 2225-6253. Paper received Feb. 2013; revised paper received Sep. 2015.

New gas nitriding technique using the interior of the nitrified pressure vessel

Table I

Chemical composition of SA 336 F22 Class1/2 ([10] ASME II Subpart A), wt%

C	Mn	P	S	Si	Ni	Cr	Mo	V	Cu	N
0.05–0.15	0.3–0.6	0.025	0.025	0.5max	0	2.0-2.5	0.9-1.1	0	0	0

Table I. The Cr and Mo contents are similar to those of the British Nitralloy steels (En 40 and En 41). No nickel is present because it is a nitriding inhibitor (Pye, 2003).

Gas nitriding

Nitriding was chosen above other surface treatment options as it is economical (Darbelly, 2006), requires no post-machining, and prevents cold welding during operation. Due to the fine tolerances of the CUD machined surfaces, nitriding is preferred as it can be performed after final machining. Also, when a steel surface is nitrided, it is chemically altered (nitrides), which inhibits the formation of an iron oxide layer.

Gas nitriding was found to be more suitable than plasma nitriding for this particular application, because a major disadvantage of plasma nitriding is the undesirable results obtained inside nitrided holes (Nisbett, 2005) due to hollow cathode/hole discharges. The CUD housing features many interconnected tunnels (holes) of varying diameter, thus rendering plasma nitriding unsuitable. Furthermore, modifying an existing plasma nitriding vacuum chamber to carry the weight of the CUD would be costly. Thus, gas nitriding was selected as the most suitable and economical process.

Development of a new nitriding plant

Since commercial off-the-shelf gas nitriding systems (*e.g.* Nitrex) cannot house a vessel as large as the CUD, a new method had to be developed. The new method proposed that the interior of the nitrided workpiece could be used as the process chamber, as this would be more economical and safer than building a large process chamber inside an existing

furnace (*cf.* Figure 1). This method would also be appropriate, as only the interior of the workpiece needed to be nitrided.

However, before the full-scale plant was built, laboratory tests were performed in an electrical furnace on a small-scale vessel of the same material, in order to prove the concept's viability. The successful laboratory test resulted in the compilation of a set of operating instructions for the new nitriding process. These include the main nitriding parameters such as the process temperature, ammonia flow rate, and required process time. The two-stage Floe process (Floe, 1977) was also used to reduce the compound layer², more often called the 'white' layer, thickness. Oxygen gas was used both as a catalyst and to prepare the surface for nitriding (Baranowska and Wysiecki, 2000).

From this experimental and literature data, the main nitriding parameters were thus determined to be:

- A process temperature of 555°C
- An ammonia flow rate of approximately 3000 l/h, as determined by the vessel's internal volume and required ammonia crack ratio
- A nitriding cycle duration of 48 hours.

The basic process requirements for the new nitriding process are similar to those of conventional gas nitriding (Pye, 2003; Nisbett, 2005).

²A dual-phase γ' (Fe_4N) and ϵ (Fe_3N) iron nitride ceramic layer that forms as an undesirable constituent in conventional single-stage nitriding. It is extremely hard and brittle, and can flake during operation if more than just 1 μm thick

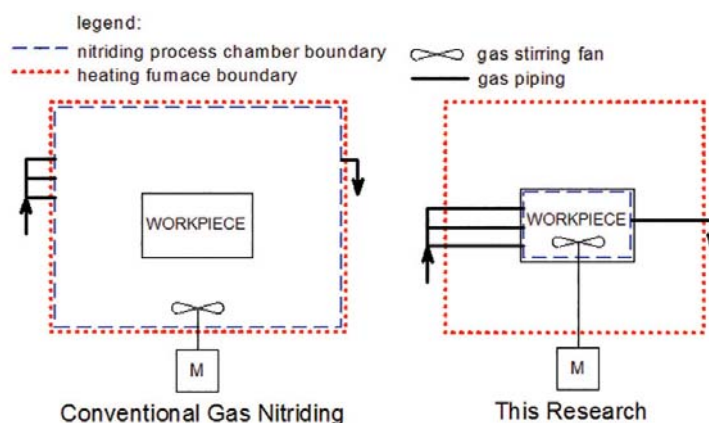


Figure 1—Illustration of the new nitriding method using the nitrified workpiece as the process chamber

New gas nitriding technique using the interior of the nitrided pressure vessel

- ▶ A process chamber is prepared inside the furnace. It contains the gases at a slight overpressure to prevent oxygen ingress. This overpressure can be provided by allowing gas to exit through water at a specific depth to provide back-pressure
- ▶ Nitrogen gas is used for purging before heating the vessel
- ▶ Oxygen can be used for surface preparation, *i.e.* to oxidize the surface, and as a catalyst. Other surface preparation techniques such as sputtering can also be used (Baranowska and Wysiecki, 2000; Baranowska, Szczecinkski, and Wysiecki, 2002)
- ▶ Gas nitriding is mostly performed by cracking anhydrous ammonia. This is because ammonia is metastable at the nitriding temperature and decomposes on contact with iron (Darbelly, 2006)
- ▶ A stirring fan is used to ensure even distribution of the process gas and heat (Matin, 1974)
- ▶ A gas analyser/Bunte burette is used to measure the ammonia dissociation rate.

The basic equipment requirements for a gas nitriding plant that uses the interior of a large workpiece as the process chamber are as follows.

- ▶ *Heating furnace*—An electrical or gas-fired furnace of a suitable size, capable of reaching 800°C, sustaining a heating rate of 50–100°C/h, and maintaining a temperature variance of $\pm 5^\circ\text{C}$ is required
- ▶ *Workpiece vessel preparation*—Flanges for sealing all the ports on the vessel must be manufactured. Only 20–30 kPa overpressure will be required in the vessel to prevent air ingress. Flange seals must also be able to withstand a continuous operating temperature of 555°C
- ▶ *Flange*—rotating shaft penetration and fan. One sealing flange must be adapted to allow for a rotating shaft to penetrate. This shaft must penetrate deep into the vessel and allow the fitment of an impeller to the front end. For the CUD, this required the design of an extended shaft (2.5 m) for critical (whirling) speed and a high-temperature graphite bearing for operation inside the furnace at 600°C. The fan must further create sufficient turbulence in the NH_3 gas to ensure adequate circulation
- ▶ *Gas inlets*—Sealing flanges should also be modified with three gas inlet pipe penetrations for N_2 , O_2 , and NH_3 . All inlet pipes should have flow control valves and flow meters. All piping, valves, and flow meters in direct contact with NH_3 must be made of stainless steel and glass to avoid reaction between the NH_3 and standard brass meters
- ▶ *Gas outlet*—A sealing flange should also be modified with an outlet pipe to allow gas to escape from the highest point in the vessel. The outlet gas includes H_2 , undissociated NH_3 , and N_2 . Therefore the gas should be bubbled through a water trap to dissolve the NH_3 , while the H_2 should be flared off
- ▶ *Temperature measurement*—High-temperature thermocouples are required both inside and outside the

pressure vessel to maintain the correct process temperature. The CUD vessel's inner surface temperature is more important than the furnace temperature because of the large temperature gradient through the thick steel. Therefore, at least four thermocouples should be strategically positioned inside the vessel to record the temperature variation during operation. High-temperature thermocouple penetration fittings can be used to penetrate the sealing flanges for internal measurements. Depending on the size of the furnace, a sufficient number of thermocouples would also be required outside the vessel.

Figure 2(a) shows the constructed plant and CUD vessel process chamber, with the top-hat gas-fired furnace being placed over it. The orientation of the vessel inside the furnace is shown in Figure 2(b). The gas piping is buried underneath the sand of the top-hat furnace. Only the stirring fan shaft requires furnace wall penetration.

Operation of the new nitriding plant

The new nitriding procedure detailed above was tested in a large-scale implementation on the housing of the PBMR CUD prototype mentioned earlier. The process was controlled in such a manner as to fulfil the specific nitrided case requirements of a large depth and high hardness. Furthermore, to reduce the thickness of the white layer the double-stage gas nitriding cycle (Floe process) (Nisbett, 2005; Key to Metals, n.d.) was used.

The first cycle was planned as a normal nitriding cycle at 500°C and 15–30% ammonia dissociation. To achieve this dissociation rate at 500°C, a flow rate of four atmosphere changes per hour was required (Key to Metals, n.d.). This produced the nitrogen-rich compound layer at the surface. This cycle was maintained for 4–10 hours.

For the next cycle, the furnace was to be heated to 560°C and gas dissociation increased to between 75% and 85%. This two-stage process reduces the thickness of the white layer. The thin white layer that resulted (<0.025 mm) could be polished off after nitriding (Nisbett, 2005). According to Darbelly (2006) and Winter (2009), low K_N set-points are required to achieve a zero-thickness compound layer (a low nitriding potential results in a low dissociation rate). The low dissociation rate during the first cycle of the Floe process therefore forms a thin-surface white layer. Further, during the high dissociation rate of the second stage, the deeper interior of the case was nitrided (Key to Metals, n.d.).

The parameters that were controlled for the desired nitrided case are:

- ▶ Increased furnace temperature, which resulted in increased case depth but reduced surface hardness (Pye, 2003). This also increased the dissociation rate (Darbelly, 2006; Winter, 2009)
- ▶ Increased process time, which resulted in increased case depth
- ▶ Increased gas supply rate, which reduced residence or incubation time, to retard nucleation (dissociation) for the formation of a compound white layer (Darbelly, 2006; Key to Metals, n.d.)

New gas nitriding technique using the interior of the nitrided pressure vessel

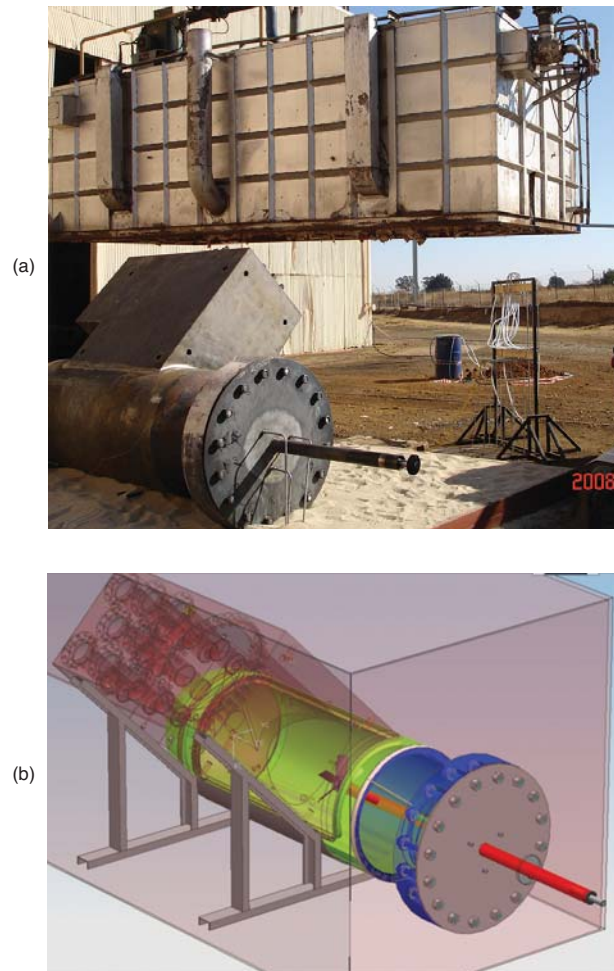


Figure 2—The application of the new nitriding method using the workpiece as the process chamber. (a) The gas-fired furnace being lifted over the workpiece and sealed nitriding process chamber, (b) three-dimensional CAD model of the workpiece placed inside the furnace, showing sealing flanges

- Increased core material hardness and alloying element content, resulting in increased case hardness
- The correct surface pre-treatment (a high level of cleanliness and degreasing) and slight oxidation (which at temperature removes the last traces of organic residue and forms a very thin iron oxide catalyst layer for nitrogen infusion into the iron matrix) ensured a deeper case (Baranowska and Wysocki, 2000).

Results

Plant operation observations

The plant was operated according to the procedure described in the previous section. Several significant observations were made.

The first significant observation was a deviation from ideal behaviour concerning the actual heating rate that was recorded. To prevent excessive thermal distortion caused by an excessive temperature gradient in the metal workpiece, ASME VIII (American Society of Mechanical Engineers, 2003a) recommends a maximum heating rate of 56°C/h. Therefore, during operation, the burners were kept on hold.

This prevented the temperature from exceeding the prescribed limit within the thinner metal, with a lower thermal inertia. However, this led to a much lower heating rate of 20°C/h above 200°C being observed, as shown in Figure 3. The furnace workpiece thermocouples are used to measure the temperature of the thickest and thinnest metal sections, respectively. The temperature gradient limit was set to 20°C.

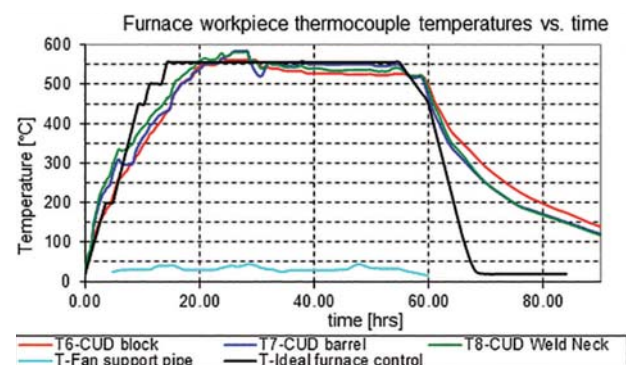


Figure 3—Temperature vs. time graph from the furnace control thermocouple readings

New gas nitriding technique using the interior of the nitrated pressure vessel

The second significant observation was that the ammonia dissociation rate is temperature-dependent. At a temperature of 500°C, during preparation for the nitriding cycle, dissociation rates of 45% were already measured. However, as the temperature was increased to 555°C at the same flow rate, the dissociation rate increased to more than 60%, which was too high.

A third significant observation was a problem encountered with the ammonia supply. The anhydrous ammonia cylinders froze in the cold winter morning conditions of the outdoor test site and could not provide the required continuous flow rate of 3000 l/h. It was therefore decided to reduce the furnace temperature to allow a lower ammonia flow rate to be supplied and to reduce the crack ratio and dissociation rate.

Finally, from the start of the nitriding process, it was noted that the flow rates of the nine gas exit flow meters were equal and did not require equalizing. Figure 4 shows that the exiting flow rate through each of the nine insert holes was equal to one-ninth the supply flow rate. However, an unexpected flow rate drop through the large hole (no. 9) of the CUD block (FI004, see Table II for numbering scheme) was recorded. This might have been due to nitriding fan turbulence.

Between 8 and 15 hours, during the oxygen supply cycle, the exit gas flow through each of the nine insert holes was 350 l/h. After 34 hours into the nitriding cycle, a peak of 333 l/h was observed through each of the holes. At the reduced NH₃ supply flow of 1050 l/h, the exit flow was 100 l/h from each hole.

Measured and predicted crack ratios

Generally, the double-stage nitriding process requires a low dissociation rate for the first 4–10 hours of the nitriding cycle (Key to Metals, n.d.). This produces a shallow white layer from which diffusion into the main case structure occurs. In the second stage, a higher dissociation rate of 75 to 85% is required (Key to Metals, n.d.).

To achieve the low initial dissociation rate of between 15% and 35% at 500°C, ammonia needs to be supplied at a sufficient flow rate so that four atmosphere changes per hour are maintained in the process chamber (Key to Metals, n.d.). According to calculations for the CUD, this equates to an ammonia supply flow rate of 3000 l/h at 550°C.

The CUD interior reached the required nitriding temperature after 23 hours. However, crack ratios of 64% were already measured after 18 hours. This occurred at 2 am and thus the available flow was low because the ammonia cylinders had already cooled considerably due to the high flow and low ambient temperature of 2°C. Unfortunately, due to the low ambient temperature the operators at the time could not adjust the flow rate upward and reduce the crack

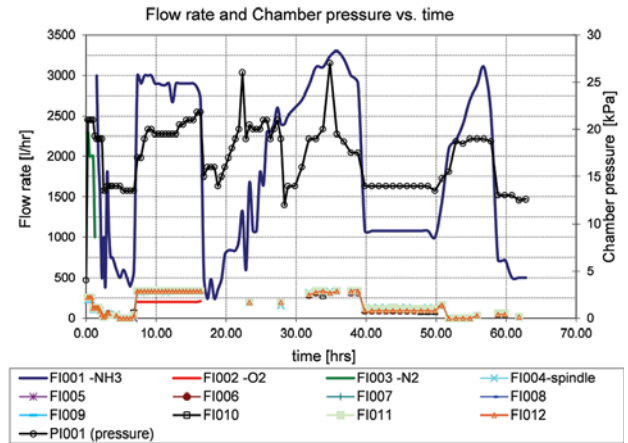


Figure 4—Measured flow rates vs. pressure

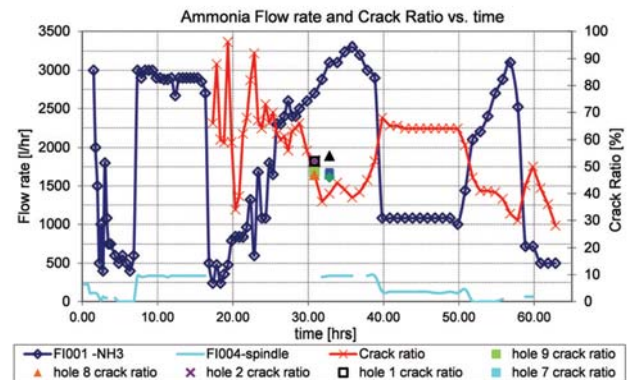


Figure 5—Ammonia flow rate and individual hole crack ratio vs. time

Flow meter no.	CUD block hole no.	CUD block drawing
FI004	9	
FI005	8	
FI006	7	
FI007	6	
FI008	5	
FI009	4	
FI010	3	
FI011	2	
FI012	1	

New gas nitriding technique using the interior of the nitrided pressure vessel

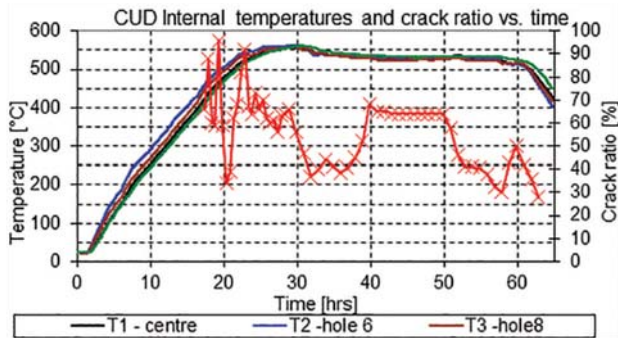


Figure 6—CUD interior temperature and crack ratio vs. time

ratio. This would have resulted in the formation of a thicker white layer than planned. Due to the deviation in supplied flow, the two-stage Floe nitriding process was not followed correctly.

Figure 5 shows the crack ratio and flow rates as a function of time. It is apparent that the crack ratio and ammonia supply flow rates are inversely proportional to each other (Key to Metals, n.d.). The unexpected low measurements at about 20 hours might be due to human error in operating the Bunte burette. Figure 6 shows the overall trend of lower crack ratios obtained at lower surface temperatures.

Figure 5 further shows that with a supply flow rate of 3000 ℓ/h and stable temperature conditions after 31–37 hours, a desired crack ratio of 35% to 37% was measured. This confirms instructions from Nisbett (2005) and Key to Metals (n.d.). Later, between 40 and 50 hours when a supply rate of only 1000 ℓ/h could be reached, a higher crack ratio of 65–70% was measured. An external ammonia dissociator was therefore not necessary.

Figure 5 also shows the crack ratios measured from the flow of the individual insert holes at 31–34 hours. These measurements correlate well with the measurement of all nine combined tube flows. The crack ratios of insert holes no. 3, 4, 5, and 7 were close to 48% at 33 hours, and those of insert holes no. 1, 2, 8, and 9 were close to the combined flow measurement of 47% at 31 hours. This proves that the mixing fan functioned effectively and that all nine insert holes of the CUD would be nitrided equally. The good correlation can also be attributed to the fact that all nine exit tubes were subjected to the same back-pressure.

Nitriding specimens

After the plant was decommissioned and the sealing flanges were removed, several nitriding specimens were collected from the insert holes. Specimens were marked according to the insert holes in which they were placed.

First, micrographs were taken of each prepared nitrided specimen's cross-section. The polished surface was etched with Nital specially prepared for the grade F22 steel. Some micrographs are shown in Figure 7, where the samples in the figure have a cross-section of approximately 10 \times 5 mm. A distinctly darker region (the nitrided layer) was seen on all nitrided specimens. It was deduced from the micrographs that all nine insert holes were nitrided to an equal depth.

A microhardness profile was then generated by making indentations with a 100 g Vickers indenter from the specimen surface, on the edge of the cross section, to beyond the nitrided ridge, as seen in Figure 7. This procedure was followed for three of the specimens (holes no. 2, 8, and 9), with the results shown in Figure 8. Since similar results were found for all three holes, it was deemed not necessary to

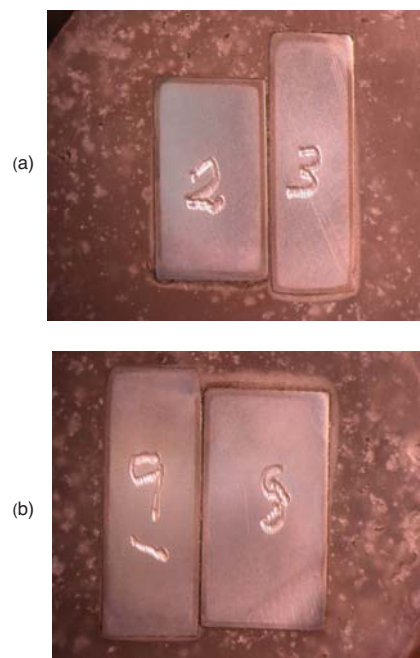


Figure 7—Nitrided specimen micrographs. (a) Etched specimen surfaces of holes 2 and 3, (b) etched specimen surfaces of holes 8 and 9. The thickness (width of the cross-sections) of the specimens was in the range of 6 mm to 9 mm

New gas nitriding technique using the interior of the nitrided pressure vessel

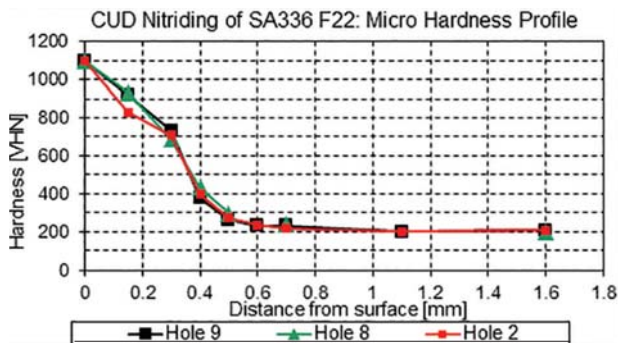


Figure 8—Nitride specimen microhardness vs. depth

obtain microhardness profiles for the rest of the holes. The samples tested from the three holes are representative of the different insert hole geometries, thus implying similar microhardness profiles for the other specimens.

Figure 8 shows that that a surface hardness of 1100 HV was obtained on all three samples. The hardness then gradually decreased to 740 HV at a depth of 300 μm at a rate of 1.2 HV/ μm . At a depth of 300 μm the hardness underwent a sharper decrease to 376 HV at the end of the effective case depth of 400 μm . The hardness curve then decreased more gradually to a depth of 700 μm . From 700 μm to 1 mm depth the hardness reduced at a very low rate to the material core hardness of 200 VHN.

The total nitride layer thickness can also be deduced from the microhardness profile. Ashrafizadeh (2003) defined the nitrided case depth as the depth where the hardness is 10% above the core hardness. From Figure 8 it can thus be deduced that the nitrided case depth is 500 μm .

In comparison to microhardness profiles recorded in other applications (Pye, 2003; Ashrafizadeh, 2003), the high surface hardness recorded here is maintained to a relatively deep depth. However, since the measurement resolution for this test was only every 150 μm , the existence of a constant hardness up to 150 μm could not be established. Comparison of the hardness profile in Figure 9 with those of other steels (Ashrafizadeh, 2003), however, reveals that it is rare to have both a surface hardness above 800 HV and a case depth more than 200 μm . For instance, plasma nitrided En 40B steel, nitridable steel, has a surface hardness of 900 HV and a case depth of only 220 μm (Ashrafizadeh, 2003).

It can thus be concluded that the CUD nitriding process was successful, since both a high hardness and a deep nitride case were achieved. This can be attributed to the high a nitridability of the SA 336 F22 CUD housing steel and the long duration of the nitriding cycle (48 hours).

Discussion

The following factors were found to influence the quality of the nitrided case.

- An increased furnace temperature resulted in an increased case depth. However, the high nitriding temperature of 555°C was maintained for only the first

10 of the 48 hours of the nitriding cycle, as shown in Figure 6. It is therefore uncertain whether furnace temperature could have contributed much to the 400 μm effective case depth that was achieved

- The second important parameter is the process time. The long nitriding cycle time of 48 hours is the only parameter guaranteed to be responsible for the increased nitrided case depth
- Correct surface pre-treatment also resulted in increased case depth. Since the initial oxygen supply lasted seven hours, much longer than the intended two hours, this could have caused the high initial dissociation rate
- The low initial ammonia supply flow rate resulted in an increased crack ratio. The high initial crack ratio could have caused a compound, or 'white', layer (see footnote 2) and also the high surface hardness. If ammonia flow had been better controlled during the first four hours of the nitriding cycle, a shallower white layer of less than 25 μm with the Floe process (Nisbett, 2005) should have been guaranteed. It is therefore possible that a hard, brittle, white layer had formed on the surface. Unfortunately this cannot be confirmed from a microhardness profile, since the actual hardness of the white layer could not be measured because it was too thin (Ashrafizadeh, 2003). The existence of this layer can be confirmed only by scanning electron microscopy (SEM) or X-ray diffraction, whereby a ($\epsilon + \gamma$) phase needs to be identified
- The nitriding tests on the specimens from all nine insert holes were similar. This can be attributed both to the equal flow rates and the equal crack ratios that were measured, as shown in Figure 7
- The maximum attainable hardness was effectively limited by the material composition. The SA 336 F22 material contains 2–2.5% chromium and 0.9–1.1% molybdenum (Table I). Owing to the high Cr concentration, CrN forms, which results in a hardness of more than 800 HV (Nisbett, 2005). The high surface hardness of 1100 HV is therefore attributed to the chromium content of the F22 material.

Conclusions

A new method of constructing a nitriding process chamber has been developed, using the large nitrided workpiece itself as the process chamber. This required the design of an extended-length, 2.5 m mixing fan shaft to penetrate a pressure boundary at a temperature of 600°C. A high-temperature gas sealing bearing was also developed, as well as various high-temperature gas-sealing penetrations. This new method also required the temporary modification of a conventional gas-fired heat treatment furnace for use as a gas nitriding heating facility.

This novel gas nitriding technique (Preisser and Seif, (1993) patented a dissimilar, but related technique) can be applied for nitriding the interior of engine blocks (Pinedo, 2003), large valves, or any enclosed vessel where the interior will be subjected to high friction, a moderately corrosive environment, or cold welding of internal components.

New gas nitriding technique using the interior of the nitrided pressure vessel

The successful operation of this new gas nitriding technique represents a first attempt at producing one of the largest single nitrided forgings to date. Micrographs and microhardness profiles confirmed a nitride layer thickness of 400 µm and a surface hardness of 1100 HV. These results meet and exceed the target values for the nitride layer.

The experimental investigation further confirms previous research showing the inverse proportionality between ammonia flow rate and dissociation as well as the dependence of crack ratio on temperature (Pye, 2003). The observed flow rate and crack ratio data validate the theory that ammonia should be supplied at four atmosphere changes per hour to ensure a crack ratio of 15–30% (Pye, 2003; American Society of Mechanical Engineers, 2003b). By monitoring the gas flow and crack ratio through each of the nine holes in the CUD housing, it was confirmed that equal flow rates and crack ratios resulted in equal nitrided case depths and hardness.

This work also shows the importance of maintaining low crack ratios during the first stages of the nitriding process. Adequate process control is, however, difficult due to the slow temperature transients involved with such a large workpiece. Although the process control was not ideal and various other experimental errors were made, the prototype nitriding plant nevertheless operated successfully. With improved process control and other minor adjustments, it would therefore be possible for this novel, semi-portable nitriding technique to compete with commercial gas nitriding furnaces at a fraction of the cost.

Acknowledgements

The authors would like to thank the following people for their contributions to the project:

Chris Koch (metallurgical engineer at SAMS (Pty) Ltd and contractor for Westinghouse Electric South Africa (Pty) Ltd performed laboratory testing and provided dissociation measurement tools.

Mike Nieuwoudt (CUD design engineer at Westinghouse Electric South Africa (Pty) Ltd) assisted with the design of the high-temperature equipment and defined the need for the project.

George Mathews and Doug Velleman proofread the manuscript and made valuable suggestions.

Professor Waldo Stumpf of the University of Pretoria's Department of Materials Science and Metallurgical Engineering for advising that there is no need for further phase identification tests or SEM micrographs to prove the existence of the nitriding layer (even if a white layer could have formed).

References

- AMERICAN SOCIETY OF MECHANICAL ENGINEERS. 2003a. Boiler and Pressure Vessel Code (ASME), Section VIII Division 1, Edition 2001 with Addenda.
- AMERICAN SOCIETY OF MECHANICAL ENGINEERS. 2003b. Boiler and Pressure Vessel Code (ASME), Section II Materials Edition 2001 with Addenda.
- ASHRAFIZADEH, F. 2003. Influence of plasma and gas nitriding on fatigue resistance of plain carbon (Ck45) steel. *Surface and Coatings Technology*, vol. 173/174. pp. 1196–1200.

- BARANOWSKA, J. and WYSIECKI, M. 2000. Influence of surface pretreatment on case formation during gaseous nitriding. *Surface and Coatings Technology*, vol. 125. pp. 30–34.
- BARANOWSKA, J., SZCZECINKSI, K., and WYSIECKI, M. 2002. Increasing of gas nitriding kinetics via surface pre-treatment. *Surface and Coatings Technology*, vol. 1151-1152. pp. 534–539.
- DARBELLY, J. 2006. Gas nitriding: an industrial perspective. Presentation, Department of Materials Science and Engineering, McMaster University. <http://mse.mcmaster.ca/graduate/seminar/2005/> [Accessed 28 July 2009].
- FLOE, C.F. 1977. A study of the nitriding process effect of ammonia dissociation on case depth and structure. *Source Book on Nitriding*. Unterweiser, M. and Gray, A.G. (eds.), American Society for Metals. pp. 144–171.
- JOHNSON, K.I. and KELLER, D.V. 1966. Adhesion between atomically pure metallic surfaces; Part IV—the effect of contamination on the adhesion of metallic couples in ultrahigh vacuum. NASA-CR-71147, Syracuse University, New York.
- KENAN, G., MEHMET, D., and MEHMET, C. 2000. Effect of ion nitriding on fatigue behavior of AISI 4140 steel. *Materials Science and Engineering A*, vol. 279. pp. 207–216.
- KEY TO METALS. Not dated. Cast steel: gas nitriding. www.steel.keytometals.com/Articles/Art132.htm [Accessed 28 July 2009].
- LÚCIA, V., SANTOS, A.B., VLADIMIR, J., TRAVA-AIROLDI, A., EVALDO, J., CORAT, A., NOGUEIRA, C., and NELIA, F.L. 2006. DLC cold welding prevention films on a Ti6Al4V alloy for space applications. *Surface and Coatings Technology*, vol. 200. pp. 2587–2593.
- MATIN, Y.I. 1974. Means of improving furnaces for gas nitriding, UDC (047): 621.785.532.662.5:621.783. Translated from *Metallovedenie I Termicheskaya Obrabotka Metallov*, vol. 3, pp. 42–46. Consultants Bureau (a division of Plenum Publishing), New York.
- MOELLER, C.E. and NOLAND, M.C. 1968. Cold welding tendencies and frictional studies of clean metals in ultra-high vacuum. *Wear*, vol. 11. p. 386.
- NATHALIE, L. and YVES, V. 2006. Fatigue strength improvement of a 4140 steel by gas nitriding: Influence of notch severity. *Materials Science and Engineering A*, vol. 435–436. pp. 460–467.
- NISBETT, E.G. 2005. Steel forgings: design, production, selection, testing, and application. ASTM International, Materials Park, Ohio, USA.
- PINEDO, C.E. 2003. The use of selective plasma nitriding on piston rings for performance improvement. *Materials and Design*, vol. 24. pp. 131–135.
- PREISSER, F. and SEIF, R. 1993. Method of nitriding workpieces of steel under pressure. US patent 5211768. www.freepatentsonline.com/5211768.html [Accessed 28 July 2009].
- PYE, D. 2003. Practical Nitriding and Ferritic Nitrocarburizing. ASM International, Materials Park, Ohio, USA.
- WINTER, K.M. 2009. Gaseous nitriding: in theory and in real life. Technical Paper of United Process Controls, Process-Electronic GmbH, Heiningen, Germany. ◆



Statistical analysis of coal mining safety in China with reference to the impact of technology

by C. Chu*, R. Jain†, N. Muradian†, and G. Zhang*

Synopsis

This paper presents a statistical analysis of coal mining safety which shows a positive relationship between technological innovation and the state of safety in Chinese coal mines. Fatalities per million tons, labour productivity, and fatalities per 10 000 exposure hours are the indicators used to analyse the situation of Chinese coal mining safety during the years 2001–2010. A correlation analysis is provided using Statistics Package for Social Science (SPSS). The results show that during this period, there was a positive correlation between technological development, financial investment in safety, and coal mine safety in China. The Huainan Mining Group is taken as an example to illustrate the improvement in coal mine safety due to technological development. Finally, some suggestions are proposed to further improve safety in Chinese coal mines from the perspective of risk assessment, an interdisciplinary approach, and safety culture.

Keywords

coal mining safety, correlation analysis, labour productivity, technological development.

Introduction

Coal is an important energy source that accounted for more than 60% of Chinese primary energy consumption during the period 2001–2010 (Xie *et al.*, 2013). In China, nearly 90% of the total coal production is from underground mining. Deep mines and mines in areas with high gas levels and high groundwater pressure are associated with high accident rates (Sui, 2013; Sui *et al.*, 2011). The average mining depth of Chinese coal mines was around 700 m in 2010, and the deepest mine is deeper than 1200 m. In addition, more than half of the coal mines are located in formations with high gas concentrations. From 2001 to 2012, 30 848 accidents were reported in Chinese coal mines, resulting in 51 232 fatalities, as shown in Figure 1 (Chen *et al.*, 2012). These statistics demonstrate that the coal industry is clearly a high-risk industry in China.

Much research has been conducted on Chinese coal mine safety. Feng and Chen (2013) postulated that the relationship between coal production and safety inputs reflected the relationship between economic development and occupational safety. Based

on the data for coal production and safety inputs, the safety level of a country can be divided into a developing stage, stable stage, and transcending stage. At present, China is in the first stage, with a simultaneous growth in coal production and safety inputs. By considering the essential factors causing coal mine accidents, Liang *et al.* (2011) set up a coal mine accident causation model based on hazard theory to analyse typical coal mine accidents. Focusing on small-scale coal mines, Shi (2013) postulated that China's policy on small coal mines had changed from encouragement to restriction, and ownership had converted from privatization to nationalization in some provinces in the past decades, resulting in improved safety. Liu and Luo (2012) in an analysis of the effect of the psychological factors in coal mine accidents, concluded that accidents in Chinese coal mines were often caused by human factors, such as unsafe behaviour tied to psychological conditions.

This paper presents a more comprehensive statistical analysis to investigate the influence of technical innovation and financial investment on mining safety. Firstly, labour productivity and fatalities per 10 000 exposure hours are used to analyse the progress of Chinese coal mine safety from 2001 to 2010 after comparing the fatality rates per million tons produced in Chinese, USA, and Indian coal mines during this period. Secondly, a correlation analysis is conducted through Statistics Package for Social Science (SPSS) to further analyse the impact of technological development and financial investment in

* School of Resources and Geosciences, China University of Mining and Technology, Xuzhou, Jiangsu, China.

† School of Engineering and Computer Science, University of the Pacific, Stockton, USA.

© The Southern African Institute of Mining and Metallurgy, 2016. ISSN 2225-6253. Paper received Apr. 2015; revised paper received Jul. 2015.

Statistical analysis of coal mining safety in China

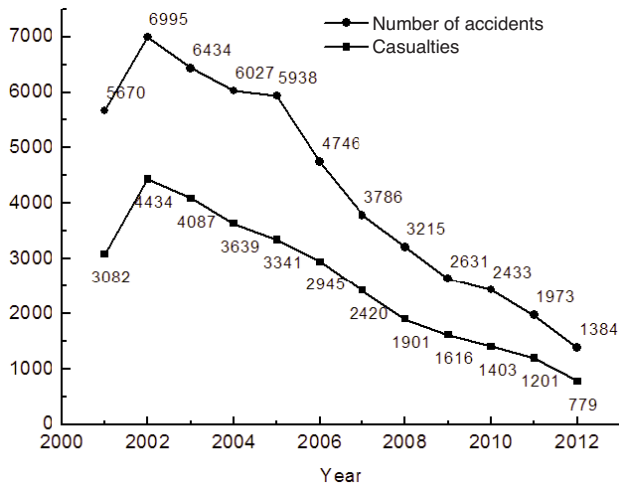


Figure 1—Casualties and number of accidents in Chinese coal mines, 2001–2012

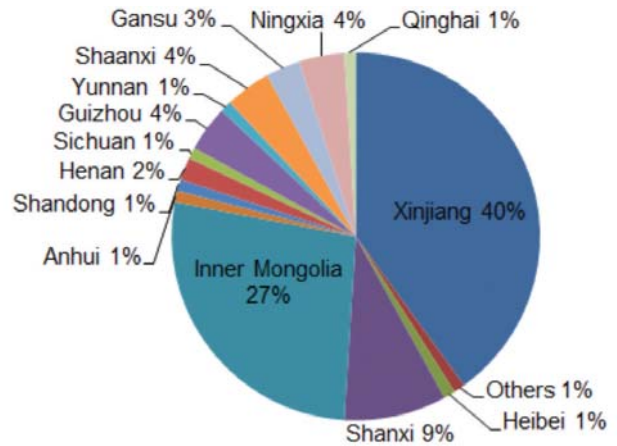


Figure 2—Distribution of coal resources in China

safety on Chinese coal mine safety during the period 2001–2010. A case study is provided to present the development of coal mine safety due to technological innovation. Finally, some suggestions to improve Chinese coal mine safety are proposed from the perspective of risk assessment, an interdisciplinary approach, and safety culture.

Comparative analysis between China and the global mining community

China is the world's top producer and consumer of coal, accounting for nearly 50% of the world's production and consumption. The majority of Chinese coal resources are distributed in the western and northern China, such as Xinjiang and Inner Mongolia, as shown in Figure 2.

China is currently emerging from a period of industrialization and great economic growth, and is in the same position as Britain and the USA many years ago. Chinese coal mine safety is lacking compared with other countries. In 2003, world coal production was 5 billion tons and about 8000 miners died worldwide, with China making up 80.4% of the total fatalities in coal mine accidents. According to a 2011 report, in China, gas explosions were the most severe type of accident due to the number of fatalities per accident, and collapses were the most frequent type of accident (Wang *et al.*, 2011). Groundwater inrush hazards also caused significant economic losses and casualties (Sui *et al.*, 2011; 2015a). Figure 3 shows the fatality rate per million tons in Chinese coal mines from 2001 to 2010. During this period, the average fatality rate per million tons in China was 2.6, 87 times that of the USA (Figure 4) and 10 times that of India (Figure 5). However, the Chinese death rate declined steadily from 2001, to 0.89 per million tons in 2009, a decrease of 82%. During the same period, the fatality rate per million tons declined by 72% in India, and by 51% in the USA.

Labour productivity is commonly used in the coal mining industry as a general indicator of changes in the efficiency of the coal production process. In this paper, labour productivity

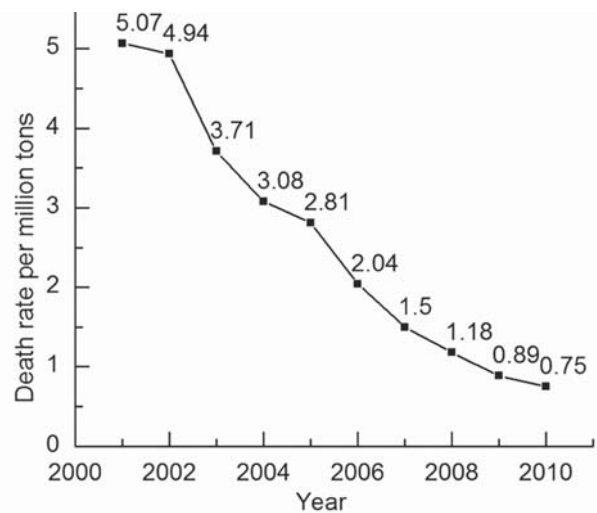


Figure 3—Fatality rate per million tons in Chinese coal mines, 2001–2010

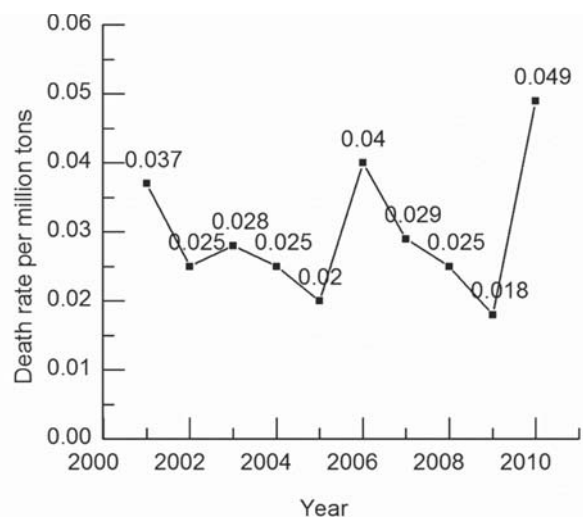


Figure 4—Fatality rate per million tons related to coal mining accidents in the USA

Statistical analysis of coal mining safety in China

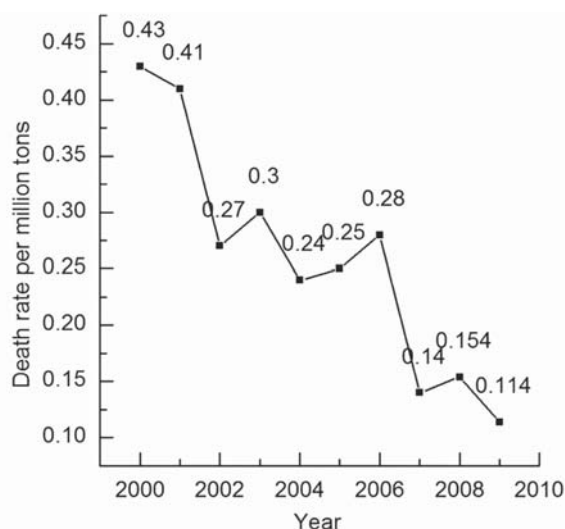


Figure 5—Fatality rate per million tons due to coal mine accidents in India

is measured by total coal production divided by man-hours worked by all employees engaged in production, processing, development, maintenance, repair shop, or yard work at mining operations, including office workers. In each country, working hours are assumed to be 2080 hours per year per worker based on 52 weeks in a year, 5 days a week, and 8 hours a day, excluding vacations and overtime (Sari *et al.*, 2001). New South Wales and Western Australia are used as two examples to present labour productivity in Australia. As shown in Table I, in 2010 the labour productivity in China

was approximately one-third that of the UK, one-eleventh that of Australia, and one-fourteenth that of the USA. In the same year, the fatality rate per million tons in China was fifteen times that of the USA, indicating that low labour productivity is correlated with high deaths rates.

Even with low labour productivity, Chinese coal mine safety has increased during of 2001–2010, as illustrated by a decrease in deaths per 10 000 exposure hours, shown in Table II. In 2010, the fatality rate per 10 000 exposure hours in China was only 1.15 times that in the USA, compared to six times that in the USA in 2002 (Department of Energy and Climate Change, 2013; Mines Safety and Health Administration, 2014; Wikipedia, 2014).

Statistics from 2001 to 2010 (Table III) shows that the Chinese government made an effort to improve coal mine safety through increasing financial investment and improving technology (Chen *et al.*, 2012; Feng and Chen *et al.*, 2013). The physical output of a worker can be assumed to remain constant over the time period considered. Hence, any increase in productivity per person is likely to be due to a change in technology. Thus, the rate of technological progress was represented by labour productivity in tons per person-day.

One of the striking features of this data is that investment in safety increased from a modest 36.2 billion dollars in 2001 to 628.4 billion dollars in 2010. This investment was accompanied by a decrease in the death rate per million tons from 5.07 in 2001 to 0.75 in 2010. Additionally, although not presented in Table III, the death rate per million tons decreased even further to 0.25 in 2014, the lowest ever recorded. Over the same time period, the rate of technological progress rose from approximately 1 in 2001 to 2.37 in 2010.

It seems that the decrease in fatalities per million tons has a close relationship with financial investment in safety.

Table I

Labour productivity (tons per exposure hour)

Year	2001	2002	2003	2004	2005	2006	2007	2008	2009	2010
China	0.20	0.21	0.25	0.28	0.31	0.32	0.34	0.37	0.38	0.42
USA	7.00	7.00	7.26	7.23	6.86	6.74	6.78	6.49	5.89	6.05
UK	1.40	1.44	1.68	1.50	1.60	1.83	1.36	1.44	1.44	1.44
New South Wales	-	6.94	7.05	7.07	6.66	6.13	6.11	5.54	5.16	4.76
Western Australia	4.40	4.64	4.52	4.66	4.30	4.52	3.45	3.61	4.35	-

Table II

Comparison of fatalities per 10 000 exposure hours, China and the USA

Year	China			USA			China / USA Fatalities per 10 000 exposure hours
	Casualties	Exposure hours	Fatalities per 10 000 exposure hours	Casualties	Exposure hours	Fatalities per 10 000 exposure hours	
2001	5670	6 889 740 000	0.0082	42	160 343 040	0.0026	3.15
2002	6995	6 840 656 160	0.0102	27	156 969 280	0.0017	6.00
2003	6434	6 895 276 960	0.0093	30	147 727 840	0.0020	4.65
2004	6027	7 102 819 360	0.0085	28	153 737 960	0.0018	4.72
2005	5938	7 212 154 560	0.0082	23	164 908 640	0.0014	5.86
2006	4746	7 513 760 800	0.0063	47	172 554 720	0.0027	2.33
2007	3786	7 499 554 400	0.0050	33	169 058 240	0.0020	2.50
2008	3215	7 584 595 200	0.0042	29	180 666 720	0.0016	2.63
2009	2631	7 878 037 440	0.0033	18	182 530 400	0.0010	3.30
2010	2433	7 783 726 080	0.0031	48	179 285 600	0.0027	1.15

Statistical analysis of coal mining safety in China

Table III
Statistics of coal industry in China, 2001–2010

Year	Fatality rate per million tons	Coal production (billion tons)	Coal production growth rate (%)	Investments (billion dollars)	Investment growth rate (%)	Labour force	Labour growth rate	Rate of technological progress
2001	5.07	1.38	6.3	36.2	-	3 312 375	0.0195	1.141
2002	4.94	1.46	5.8	47.7	31.7	3 288 777	-0.0071	1.216
2003	3.71	1.72	17.8	69.0	44.6	3 315 037	0.0080	1.421
2004	3.08	1.99	15.7	115.1	66.8	3 414 817	0.0301	1.600
2005	2.81	2.21	11.1	103.9	-9.6	3 467 382	0.0154	1.746
2006	2.04	2.37	7.2	126.6	21.8	3 612 385	0.0418	1.797
2007	1.50	2.53	6.8	139.4	10.1	3 605 555	-0.0019	1.922
2008	1.18	2.80	10.7	169.1	21.3	3 646 440	0.0113	2.100
2009	0.89	2.97	6.1	206.8	22.3	3 787 518	0.0384	2.148
2010	0.75	3.24	9.1	628.4	203.8	3 742 176	-0.0120	2.372

Table IV
Pearson correlation coefficients for the relationship between fatality rate per million tons and contributing parameters

	Technological progress rate		Financial investment		Coal production growth rate		Labour growth rate	
	<i>R</i>	<i>P</i>	<i>R</i>	<i>P</i>	<i>R</i>	<i>P</i>	<i>R</i>	<i>P</i>
Fatalities rate per million tons	-0.982	0.000	-0.658	0.039	0.078	0.830	-0.084	0.818

Bold values denote significant correlations for the fatality rate per million tons (*R* approaches 1, significance < 0.05)

Meanwhile, with the output per person increasing by about the same degree as the fall in death rate, the decline could also be attributed to increasing mechanization. Further analysis to clarify the influence of technological development and financial investment in safety on Chinese coal mine safety during this period should be conducted.

The impact of technological development and financial investment in safety on Chinese coal mine safety

Statistical analysis

Using the data presented in Table III and SPSS, a correlation analysis was developed. The fatality rate per million tons was used as the dependent variable, while technological progress rate, coal production growth rate, financial investment, and labour growth rate were independent variables. With a significance coefficient (*P*) less than 0.05, a correlational value (*R*) approaching -1 or 1 indicates there is a significant negative or positive correlation, respectively, between the death rate per million tons and the independent variable of interest. Table IV shows that the correlation value and significance coefficient between technological development and death rate per million tons are estimated to be -0.982 and 0.000, respectively. The correlation value of financial investment is -0.658, while the significance coefficient is 0.039. The labour growth rate and coal production growth rate have little influence on the fatality rate.

Therefore, there is a positive correlation between technological development, financial investment in safety,

and coal mine safety in China from 2001 to 2010. With the development of technology and increasing financial investment in safety, the death rate per million tons decreased dramatically. During this period, technological development had a stronger influence on coal mine safety than financial investment in safety

Case study

As mentioned above, in the past years, with the rapid development of technology in Chinese coal mines, including improvements in mining technology, drilling technology, and disaster prevention and control technology, coal mine accidents rates decreased dramatically even though coal production increased. The Huainan Mining Group, which is located in a developed economic area of East China, is a good example to present this point. The Huainan Mining Group is an important coal base in China due to its favourable geographical location and high-quality coal resources. Coal production in the Huainan Mining Group increased from 17.74 Mt in 2001 to 71.06 Mt in 2012. However, the coal mines in the Huainan mine area are characterized by complex geological structures, great depths (800–1500 m), high *in situ* water and gas pressure (greater than 6.2 MPa), high gas content (12–26 m³/t), soft coal mass (rigidity coefficient about 0.2–0.8), and low permeability (0.001 mD). Gas extraction in such geological conditions remains a problem worldwide (Wang *et al.*, 2012). Historically, the Huainan mine area was known as a 'disaster zone' in the Chinese coal industry due to the frequent gas extraction accidents. From 1980 to 1997, there were 17 gas extraction accidents in Huainan coal mines, with 392 deaths. Since the year 2002,

Statistical analysis of coal mining safety in China

the Huainan Mining Group has begun to strengthen technological innovation in gas control by increasing the input to technological research and development and employing professionals. From 2002 to 2004, financial investment in technology research and development was approximately 0.67 billion dollars. During 2005–2007, the investment in technological innovation relied on a tax of 5.5 dollars per ton of coal sold. The income from this tax has increased to 8.3 dollars per ton since 2008. During 2002–2010, the total investment in technological development for gas control was up to 2.3 billion dollars. By the end of 2012, the Huainan Mining Group had employed more than 4000 professionals in the field of gas control, and developed some key technological innovations and patents, such as ‘simultaneous mining technology of coal and gas in low-permeability seam group’ in 2009. Due to the efforts devoted to the development of technology, a new method of coal and gas mining by roadway retention and borehole drilling behind the working face has been developed and proved to be successful in the Huainan coal mines (Yuan, 2008). The technological development for gas control resulted in ‘zero gas extraction accidents’ from 2002 to 2012, and the fatality rate in the Huainan coal mines declined from an average of 4.01 per million tons before 2001 to 0.1 in 2011.

Recommendations for improvement of safety in Chinese coal mines

Many scholars have presented suggestions for improving safety in Chinese coal mines, including financial investment, regulations, and risk management. To continue to improve safety, the reader’s attention is directed towards the improvement of risk assessment, an interdisciplinary approach, and safety culture.

Risk assessment in coal mines

Around the globe, legislation regulating the health and safety of mine workers, including requirements for risk assessment, is increasing (Joy, 2004). Risk assessment is the scientific process that characterizes the nature and magnitude of health risks to humans and ecological receptors from chemical contaminants and other stressors that may be present in the environment. Risk assessment can be used to conduct a risk analysis to support decision-making, as well as provide an important basis for finding the right balance between different concerns, such as safety and costs (Mahdevari *et al.*, 2014).

Figure 6 shows the procedure of risk assessment according to the US Environmental Protection Agency (2014). To assess a risk, health problems caused by the pollutant should be identified, and then the health problems at different levels of exposure and the number of exposed

people should be estimated. Finally, the extra risk of health problems in the exposed population should be analysed.

Risk assessment in coal mines is an important step in protecting workers as well as complying with regulations. In China, risk assessment has been introduced at certain coal mines for evaluating the hazards associated with ground instability, groundwater inrush, fire, explosions, and electrical works. Wide application of risk assessment in coal mines is an effective way to improve Chinese coal mine safety in the future.

Development of an interdisciplinary approach

The lack of coal mine safety has multiple facets in technology, the environment, society, economics, and ecology. Therefore, the development of an interdisciplinary approach, such as safety geology and environmental economics, can promote research into coal mine safety and increase the knowledge needed to make comprehensive decisions.

Safety geology is an especially important field that should be taken into consideration. Complex geological conditions associated with incorrect assessment or interpretation are a major contributing factor to frequent accidents in coal mines. Safety geology focuses on finding solutions to these problems from a geological perspective, using geophysical exploration for investigation and predication and risk assessment for gas explosion and groundwater inrush (Sui, 2013).

Environmental economics is an interdisciplinary study of the relationship between the environment and economics. Traditional economics attaches more importance to commercial activities, ignoring social cost (Coase, 1960). However, when profits are made by exploiting natural resources, the environment will be affected. Environmental issues specific to coal mining operations that should be taken into consideration when decisions are made include environmental pollution, ecological damage, and the depletion of natural resources (Sui *et al.*, 2015b).

Safety culture

A culture of safety is a fundamental building block in safety management. Life should be respected and company cultures should promote the concept of being ‘people-oriented’ rather than ‘profit-oriented’. ‘Humans are powerless before nature’ is a negative perspective that does not promote safety. Employees need to have confidence that humans can live in harmony with nature. A strong safety culture will allow managers to make practical regulations that emphasize a harmonious relationship between humans and nature, and strengthen miners’ awareness of coal mine safety.

Training and education of employees and managers plays a vital role in improving coal mine safety and is an important aspect of safety culture. Training and education should be

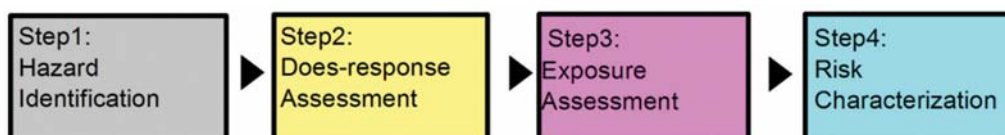


Figure 6—NAS (National Academy of Sciences) risk assessment procedure

Statistical analysis of coal mining safety in China

provided to new miners as well as experienced miners. Regular training and education should be required each year or every few months, while a special course should be provided when miners switch jobs or come into contact with new geological conditions. Employees and managers should attend training classes and be tested by written and practical examination. Then, their performances can be made public in a networking system and can be a key factor in their career development.

Psychological education should be more widely implemented in training. Miners' perceptions of safety regulations affect their responses to the regulations, creating situations that may be dangerous. A perception of 'I want to be safe' results in a safer environment than the perception of 'You want me to be safe' (Guo and Wu, 2011). Psychological education can help miners learn how to understand their perceptions and make safe decisions.

Conclusions

Mining remains a high-risk industry in China, with high accident rates. However, the Chinese fatality rate per million tons of coal produced dropped from 5.07 in 2001 to 0.25 in 2014 through a series of active mitigation measures. In 2010, the fatality rate per 10 000 exposure hours in China was only 1.15 times that of the USA. A correlation analysis through Statistics Package for Social Science (SPSS) has shown that technological progress and financial investment in safety had a positive correlation with Chinese coal mine safety during the period 2001–2010. A case study of Huainan Mining Group illustrates that technological development of gas control decreased the gas extraction accident rate dramatically in Huainan coal mines.

Some suggestions have been proposed to further improve safety in Chinese coal mines, including wider application of risk assessment, continued development of interdisciplinary approaches, and the introduction of a strong safety culture.

In the current study, statistical analysis focuses on the impact of technological improvement and financial investment in safety on Chinese coal mine safety. However, many other aspects should be taken into consideration, such as geological conditions, human factors, and safety management. Correlation analysis considering more factors will be conducted in further studies.

Acknowledgements

This work was supported by the National Natural Science Foundation of China under Grant No. 41172291 and a project funded by the Priority Academic Program Development of Jiangsu Higher Education Institutions (PAPD). The first author was funded by the China Scholarship Council (CSC) during her visit to the USA. Many faculty members and research associates at the School of Engineering and Computer Science, University of the Pacific reviewed the manuscript and provided helpful comments. Their support is gratefully acknowledged. We are also very grateful to the referees for their invaluable and constructive comments.

References

CHEN, H., QI, H., LONG, R.Y., and ZHANG, M.L. 2012. Research on 10-year tendency of China coal mine accidents and the characteristics of human factors. *Safety Science*, vol. 50. pp. 745–750.

- COASE, R.H. 1960. The problem of social cost. *Journal of Law and Economics*, vol. 3. pp. 1–44.
- DEPARTMENT OF ENERGY AND CLIMATE CHANGE. Coal statistics, 2013. <http://www.gov.uk> [Accessed 20 June 2014].
- FENG, Q. and CHEN, H. 2103. The safety-level gap between China and the US in view of the interaction between coal production and safety management. *Safety Science*, vol. 54. pp. 80–86.
- GUO, W.C. and WU, C. 2011. Comparative study on coal mine safety between China and the US from a safety society perspective. *Procedia Engineering*, vol. 26. pp. 2003–2011.
- JOY, J. 2004. Occupational safety risk management in Australian mining. *Occupational Medicine*, vol. 54. pp. 311–315.
- LIANG, K.W., LIU, J.K., and WANG, C.X. 2011. The coal mine accident causation model based on the hazard theory. *Procedia Engineering*, vol. 26. pp. 2199–2205.
- LIU, G.Y. and LUO, C.L. 2012. Analysis of the safety psychological factors in the coal mine safety. *Procedia Engineering*, vol. 45. pp. 253–258.
- MAHDEVARI, S., SHAHRIAR, K., and ESFAHANIPOUR, A. 2014. Human health and safety risks management in underground coal mines using fuzzy TOPSIS. *Science of the Total Environment*, vol. 488–489. pp. 8599.
- MINES SAFETY AND HEALTH ADMINISTRATION, DEPARTMENT OF LABOR, USA. 2014. <http://www.msha.gov> [Accessed 5 July 2014].
- SARI, M., KARPUZ, C., and SELCUK, A.S. 2001. An international comparison of Turkish coal mining industry safety performance. *Proceedings of Mine Planning and Equipment Selection*, New Delhi, India. vol. 1. pp. 917–922.
- SHI, X.P. 2013. China's small coal mine policy in the 2000s: a case study of trusteeship and consolidation. *Resources Policy*, vol. 38. pp. 598–604.
- SUI, W.H. 2013. Safety geology and geological education for mining engineers. *Global View of Engineering Geology and the Environment*. Wu, F. and Qi, S. (eds.). CRC Press, Boca Raton, FL. pp. 563–567.
- SUI, W.H., ZHANG, D.Y., CUI CINDY, Z.D., WU, Z.Y., and ZHAO, Q.J. 2015a. Environmental implications of mitigating overburden failure and subsidences using paste-like backfill mining: a case study. *International Journal of Mining, Reclamation, and Environment*, vol. 29, no. 6. pp. 521–543. DOI: 10.1080/17480930.2014.969049
- SUI, W.H., HANG, Y., MA, L.X., WU, Z.Y., ZHOU, Y.J., LONG, G.Q., and WEI, L.B. 2015b. Interactions of overburden failure zones due to multiple-seam mining using longwall caving. *Bulletin of Engineering Geology and the Environment*, vol. 74, no.3. pp. 1019–1035. DOI: 10.1007/s10064-014-0674-9.
- SUI, W.H., LIU, J.Y., YANG, S.G., CHEN, Z.S., and HU, Y.S. 2011. Hydrogeological analysis and salvage of a deep coalmine after a groundwater inrush. *Environment Earth Sciences*, vol. 62. pp. 735–749.
- US ENVIRONMENTAL PROTECTION AGENCY. 2014. <http://www.epa.gov/ttnatw01/toxsource/paradigm.html> [Accessed 10 July 2014].
- WANG, F.T., REN, T., TU, S.H., HUNGERFORD, F., and AZIZ, N. 2012. Implementation of underground longhole directional drilling technology for greenhouse gas mitigation in Chinese coal mines. *International Journal of Greenhouse Gas Control*, vol. 11. pp. 209–303.
- WANG, M.X., ZHANG, T., XIE, M.R., ZHANG, B., and JIA, M.Q. 2011. Analysis of national coal-mining accident data in China, 2001–2008. *Public Health Reports*, vol. 126. pp. 270–275.
- WIKIPEDIA. 2014. Mining in Western Australia. http://en.wikipedia.org/wiki/Mining_in_Western_Australia#Coal [Accessed 5 July 2014].
- XIE, H.P., LIU, H., and WU, G. 2013. China's coal industry must follow the path of sustainable production capacity. *Official Journal of the World Coal Industry*. pp. 11–15.
- Yuan, L. 2008. The technique of coal mining and gas extraction by roadway retaining and borehole drilling. *Journal of China Coal Society*, vol. 33. no. 8. pp. 898–902. ◆



Coal seam fracturing by a high-pressure waterjet technique to increase efficiency of coal mine gas drainage

by T. Lu*, Y. Guo*, and X. Yang*

Synopsis

In an effort to eliminate the hazard posed by coal seam gas and increase the efficiency of coal seam gas drainage in an underground coal mine, a high-pressure waterjet fracturing technique has been developed, optimized experimentally and numerically, and trialled underground. Numerical and laboratory results indicate that the slotting capacity of the high-pressure waterjet fracturing system can be improved by optimizing the geometrical structure and parameters of the nozzle. The results from field investigation showed that the gas production rate can be more than doubled by using the high-pressure waterjet-assisted method before and during longwall extraction.

Keywords

coal seam fracturing, water jet, parametric optimization, gas drainage.

Introduction

Gas drainage is a major issue in underground coal mining in China. The difficulties associated with underground gas drainage are the chief cause of coal gas accidents, which in turn limit coal production and threaten safety in underground operations. In an effort to improve gas drainage and eliminate the coal gas hazard, a high-pressure waterjet technique has been developed, optimized experimentally and numerically, and trialled underground.

The aim of the high-pressure waterjet technique is to create artificial fractures along the length of the in-seam gas drainage boreholes with rotary slotting, and form fracture networks in a longwall panel, thus improving the efficiency of in-seam gas drainage before and during the longwall extraction. The particular aims of the current investigation include:

- ▶ Optimizing key geometrical parameters of the nozzle by laboratory tests and numerical modelling
- ▶ Evaluating improvement of methane drainage of individual boreholes by the high-pressure waterjet equipment before and during longwall extraction.

High-pressure waterjet technique

Waterjet cutting can be traced back to hydraulic coal mining in the former Soviet

Union and New Zealand, where water was diverted from streams for the purpose of washing over a blasted rock face and carrying away the loose coal and rock. This method of mining was redeveloped in South African gold mines to remove blasted rock from work areas into a collection drift or tunnel. In the California goldfields between 1853–1886, pressurized water was first used to excavate gold-bearing rock from mining surfaces (Shanmugam and Chen, 2002). Pressurized water allowed the miner to stand further back from the face being washed. This was safer because there was less danger from a collapsing wall of blasted rock. Actual rock cutting using pressurized water was first attempted in Russia in the 1930s, where water cannons were used to generate a high water pressure (Shanmugam and Morsi, 2003).

Theoretically, the energy required for cutting material is obtained by pressurizing water to ultra-high levels and forming an intense cutting stream by focusing this high-speed water through a small, precisely machined diamond orifice (Liu, 2004). There are two main steps involved in the waterjet cutting process. First, the ultra-high pressure pump or intensifier pressurizes normal mine service water to pressure levels up to 100 MPa (in the current case) to produce the energy required for coal cutting. In the second step, water is focused through a small precise diamond orifice to form an intense cutting stream. The stream moves at a velocity of Mach 3, three times the speed of sound, depending on how the water pressure is exerted (Snyder, 2007).

The equipment developed consists of a number of major components, including a water pump to pressurize water to the desired

* School of Energy Science and Engineering, Henan Polytechnic University, Jiaozuo, Henan, China.

© The Southern African Institute of Mining and Metallurgy, 2016. ISSN 2225-6253. Paper received Jun. 2014; revised paper received Sep. 2015.

Coal seam fracturing by a high-pressure waterjet technique to increase efficiency

level; a dedicated filter, which is used to remove harmful minerals from the water; a high-pressure water tube, which transfers high-pressure water from the pump to the drilling rig; a water swivel, which connects the high-pressure water tube and the rotating part of the drilling rig; a sealed drilling pipe, which transfer high-pressure water from the drilling rig to the cutting device, which is installed on the first section of drilling pipe; and the control valve, which is used to control and adjust the water pressure and ensure a safe water pressure is always available during operation.

The cutting capacity of the equipment is affected by several parameters such as hydraulics, nozzle geometry, and mechanical properties of the coal. Some of these parameters, such as water pressure and jet traverse rate, are precisely controllable. Other parameters, such as the size of the orifice and focusing nozzle, change continuously due to wear and thus are uncontrollable (Grygla, 2007). Parameters that significantly affect the cutting capacity (depth of cutting) are shown in Figure 1 (Srinivasu and Babu, 2008).

During the experimental work, it was noted that nozzle geometric parameters may have a dominant effect on the cutting capacity of the equipment. Laboratory and numerical studies were therefore carried out in order to obtain the optimized geometries of the nozzle.

Determination of nozzle structure and geometric parameters

Effect of nozzle diameter on cutting quality

During the design of the waterjet system, it was found that the most important parameter is the nozzle diameter, which significantly affects the cutting quality (thickness and length of fractures), when other parameters remain constant. Therefore, the laboratory experiments were conducted to determine the effect of nozzle diameter on cutting quality.

Initially, seven different nozzle diameters, being 3, 4, 5, 6, 7, 8, and 9 mm, were selected to test the effect of nozzle diameter on cutting capacity at a fixed water pressure of 50 MPa. The results (Table 1) indicated that the cutting capacity is reduced with increases in both nozzle diameter and spray angle (Figure 2). This implies that a smaller nozzle

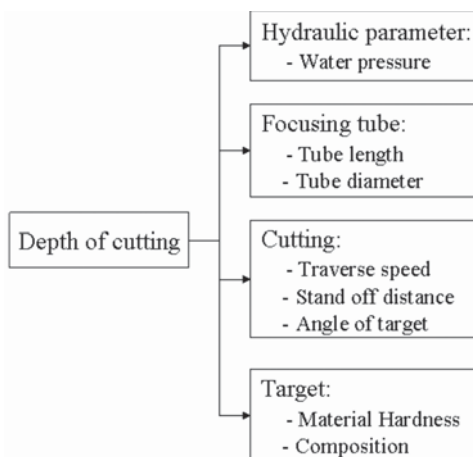


Figure 1—Parameters that may affect cutting capacity

diameter may achieve much more satisfactory cutting results under the condition of fixed water pressure. Therefore, a 1.6 mm diameter nozzle was selected for the subsequent tests.

Effect of water pressure on cutting quality

After determining the optimum nozzle diameter, the effect of water pressure on cutting quality was tested. During the test, a 1.6 mm nozzle diameter was selected in conjunction with various levels of water pressure, *i.e.* 10, 20, 30, 40, and 50 MPa. Figure 3 shows that the spray angle increases

Table 1

Effect of nozzle diameter on spray angle

Parameter	Value					
Nozzle diameter (mm)	3	4	5	6	7	8
Spray angle (°)	3	9	12	19	24	29

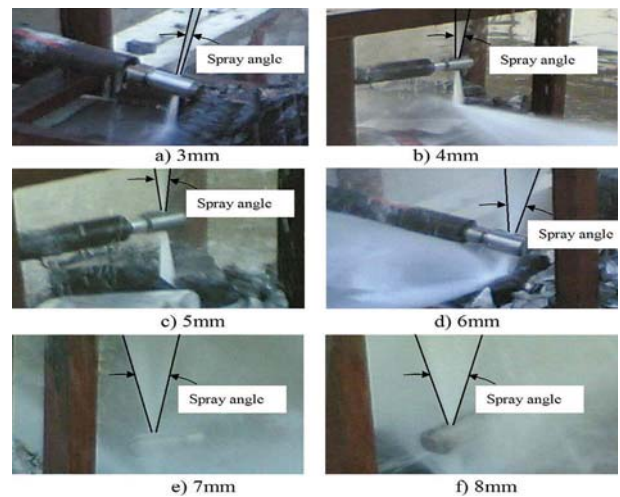


Figure 2—Spray angles at different nozzle diameters

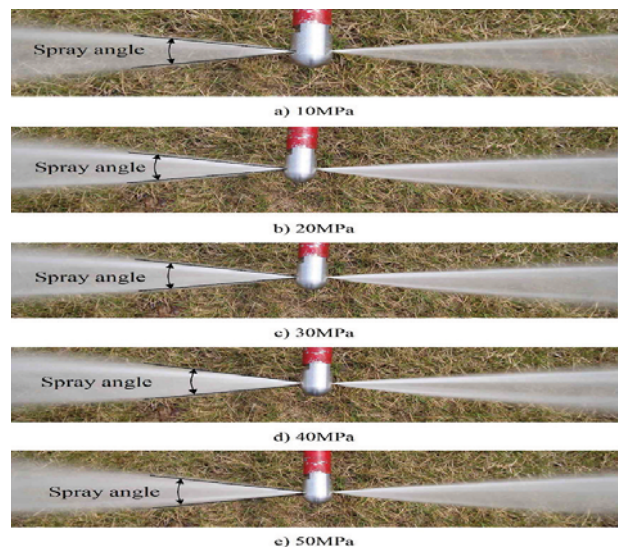


Figure 3 – Effect of pump pressure on spray angle

Coal seam fracturing by a high-pressure waterjet technique to increase efficiency

slightly with increasing water pressure, since a gradually increasing water speed causes a much stronger interaction between water and air, resulting in wider spray angles.

Table II presents the size of the spray angles obtained with different water pressures. It is to be noted that the variation of spray angle at different levels of water pressure is limited, which suggests that when an appropriate nozzle diameter is selected, we should be aware that the cutting capacity increases with increasing water pressure.

Geometric structure of nozzle

There are many types of nozzle, with different structural and geometric parameters, that can be used for material cutting (Figure 4). In order to understand the effect of nozzle structure on cutting capacity, numerical modelling was carried out on the basis of the experimental results presented above. The numerical modelling was conducted using the commercial Fluent software. This is a powerful finite-volume-based program for modelling general fluid flows in complex geometries (Pallares, Parra, and Garcia, 2009). The main components of the Fluent package are the flow solver FLUENT, the geometry and mesh generator GAMBIT, and the meshing tool TGRID (Younggil, Atul, and Kiso, 2009).

To obtain the optimized cutting capacity, the basic geometric parameters (Table III) were evaluated under 100 MPa water pressure to optimize the structure and geometric parameters of nozzles using the boundary conditions provided in Table IV

Based on the numerical modelling, the parameters, including water velocity and dynamic pressure, which significantly affect the cutting capacity associated with different nozzle structures and other parameters, were evaluated. It was noted that the cutting capacity increases with changing nozzle geometry from type A to C (Figure 5). Figure 6 demonstrates that the cutting capacity increases with increasing water pressure using the best nozzle structure (type C). It was also found that there is almost no linear relationship between water velocity and the angle θ , nozzle diameter (ϕ), or tube length (L). However, there is a closer linear relationship between water velocity and water

Table II

Effect of pump pressure on spray angle

Parameter	Value				
Pump pressure (MPa)	10	20	30	40	50
Spray angle (°)	20	22	21	24	24

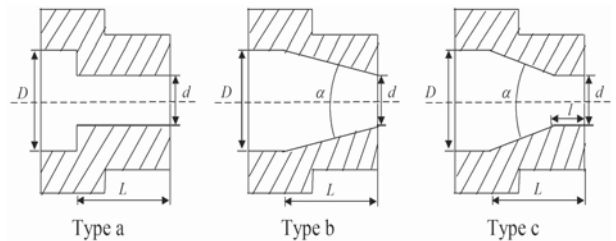


Figure 4—Nozzles with different structures

Table III

Basic geometric parameters for modelling

Parameter	Type a	Type b	Type c
Diameter d (mm)	2	2	2
Convergence angle (°)	—	13	13
Cone straight length L (mm)	—	14	14
Line straight length l (mm)	14	—	6

Table IV

Boundary conditions and modelling set-up

Boundary conditions		Discretization scheme	
Name	Type	Variable	Scheme
Wall	Wall	Pressure-velocity coupling	SIMPLE
Outlet	Pressure-outlet	Momentum	First-order upwind
Inlet	Pressure-inlet	Turbulence kinetic energy	First-order upwind

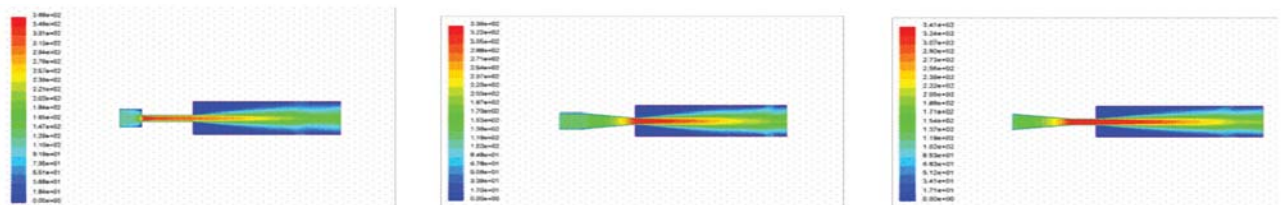


Figure 5—Effect of nozzle geometry on water velocity

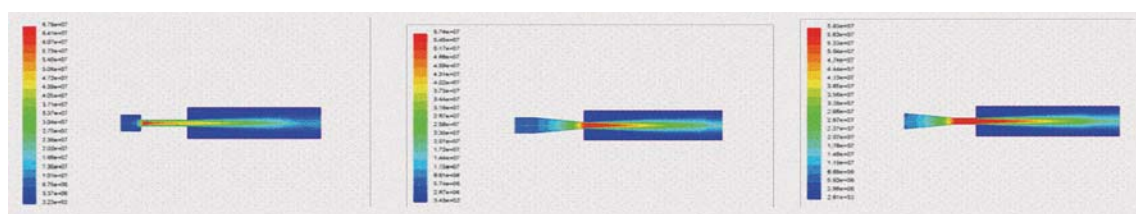


Figure 6—Effect of nozzle geometry on dynamic pressure

Coal seam fracturing by a high-pressure waterjet technique to increase efficiency

pressure (Figure 7), which indicates that the higher the water pressure, the better the cutting capacity. The optimized nozzle geometrical parameters were determined and are presented in Table V for a 65 MPa water pressure.

Field investigation

After completion of the numerical and laboratory experiments, field trials were conducted in Rujigou Colliery, which is located 98 km from Yinchuan City, northwestern China. There are 10 coal seams, with minimum and maximum thickness of 0.62 m and 11.2 m, and separated by mudstone, fine sandstone, and sandstone. The total coal seam thickness is about 234 m. The possibility of outbursts is identified for each of the coal seams. The colliery has one longwall face which is mined using a block caving method, and one face using a blasting method, which together produce annually 120 Mt of the highest quality coal in China. According to the geological report of the colliery, the major mining seams are high gas content coalbeds.

Geological and geomechanical characteristics of coal seams

The roofs of the coal seams consist normally of relatively stable sandstone strata with a minimum compressive strength of 40 MPa. Laboratory tests were undertaken to determine the properties of the coal samples, including natural density, the P-wave velocity, and traditional strength parameters such as UCS, triaxial compressive strength, modulus of elasticity, and Poisson's ratio. The results are given in Table VI.

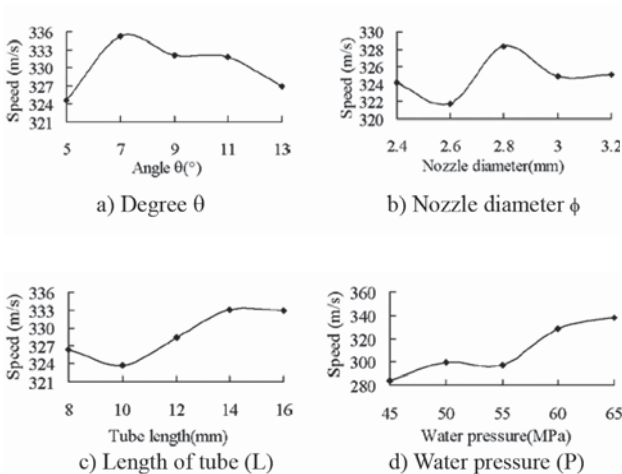


Figure 7—Effect of geometrical and hydraulic parameters on the water velocity

Parameter	Value
Diameter d (mm)	2
Convergence angle α (°)	13
Cone straight length L (mm)	9
Line straight length l (mm)	6

Underground trial set-up and monitoring arrangement

An underground trial was established in panel 3211, where the coal seam is 12 m thick. Three gas drainage stations were selected for the trial. The boreholes, with lengths of 87 m, were drilled on the rib side of the heading about 1.5 m above the floor.

After completion of drilling, first cutting started at the end of the borehole. Each cut took about 3 minutes, with 1.5 m intervals between cuts. After completion of all the cuttings, artificial fractures along the borehole were created as shown in Figure 8.

As soon as the cutting was completed, monitoring began on each individual borehole. The rate of total gas production was measured by using a gas flow meter installed at each borehole collar, and the data was collected once every day. Gas concentration was monitored regularly by collecting gas samples and measured using gas detection equipment. The average gas concentration reached 47%.

In order to compare the differences in the rate of total gas production before and after cutting, two boreholes without cutting were monitored. Figure 9a and b shows the variation in the rate of total gas production before and during panel extraction, using a traditional gas drainage method (without cutting).

For other boreholes, after formation of the artificial fractures along the length of the borehole, gas drainage was monitored up to 65 days to determine the variation in the rate of gas production before and after cutting associated with different mining activities (Figure 10a and b). Table VII gives the rate of gas production before and after the cutting operation. The monitoring results indicate that there was a

Items	Coal	
	Min ~ Max	Average
Wave velocity (m/s)	1974–2245	2105
Density (kN/m ³)	13.40 ~ 14.13	13.63
UCS (MPa)	12.74 ~ 16.00	14.64
Modular of elasticity (GPa)	3.64 ~ 3.91	3.79
Modular of deformability (GPa)	2.61 ~ 2.92	2.81
Poisson's ratio	0.37 ~ 0.42	0.39
f-value	1.3 ~ 1.6	1.5
Cohesion (MPa)	10.13	
Internal friction angle (°)	30.7	

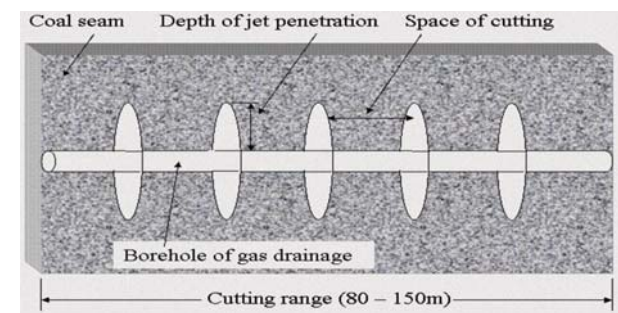


Figure 8—Cutting arrangement

Coal seam fracturing by a high-pressure waterjet technique to increase efficiency

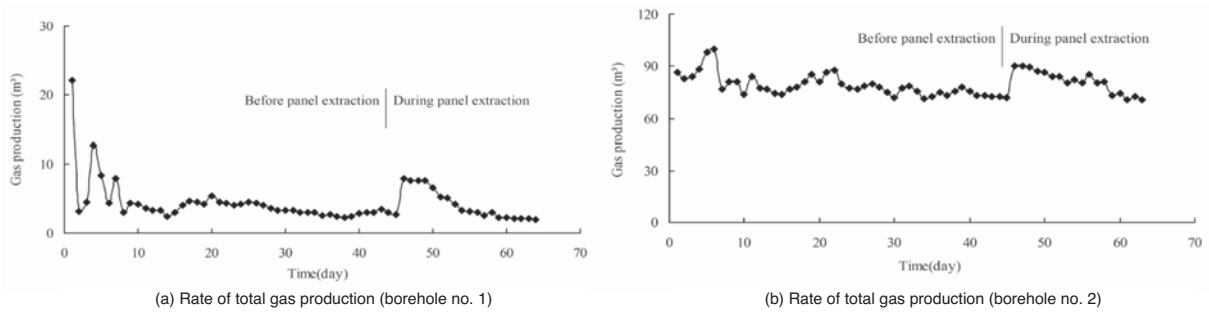


Figure 9—Traditional gas drainage methods (without cutting)

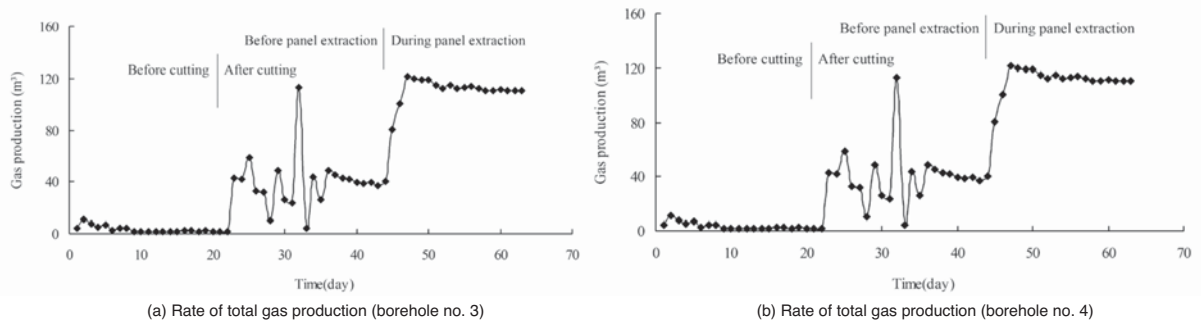


Figure 10—Rate of gas production with and without cutting at different stages of mining activities

Borehole no.	Average rate of gas production before cutting (m ³ /min)	Average rate of gas production after cutting (m ³ /min)	Incremental percentage before and after cutting (%)
1	0.0021	0.0182	7.67
2	0.0197	0.1004	4.10
3	0.0232	0.1144	3.93
4	0.0145	0.0279	0.92
5	0.0214	0.0383	0.79
6	0.0181	0.0189	0.04
7	0.0022	0.0023	0.05
8	0.0234	0.1131	3.83
9	0.0021	0.0028	0.33
10	0.0246	0.1533	5.23
11	0.0169	0.0361	1.14
12	0.0026	0.0043	0.65
13	0.053		
14	0.0103	0.0416	3.04
15	0.0026	0.006	1.31
16	0.0025		
17	0.0218	0.052	1.39
18	0.003	0.007	1.13
Average			3.31

significant increase in the rate of gas production after cutting, to more than twice that of traditional borehole drainage.

Comparing the results obtained from the traditional and the high-pressure waterjet-assisted gas drainage methods, it is seen that the process of gas drainage can be divided into two stages, *i.e.* (1) formation of a gas drainage borehole and (2) panel extraction.

For the traditional method, gas drainage starts with the drilling of the drainage borehole; the results clearly indicate that the rate of gas production decreases within a very short time after the initiation of gas drainage, due to the low permeability.

For the waterjet-assisted method, the amount of gas captured in the first stage is significantly larger than that captured by the traditional method, since additional artificial fractures are created along the length of the borehole.

The second gas production stage commences at the beginning of longwall extraction. During this stage, the front abutment stress, induced by the panel extraction of the coal seam, creates new fractures, which may connect with the fractures created previously by the waterjet cutting system, forming a gas drainage network within the coal seam and resulted in an increased rate of gas drainage.

Coal seam fracturing by a high-pressure waterjet technique to increase efficiency

Conclusions

The results obtained from the laboratory tests and numerical modelling indicated that the cutting capacity of the high-pressure waterjet system developed can be improved by optimizing the nozzle geometrical parameters such as tube length, diameter of nozzle, and convergence angle.

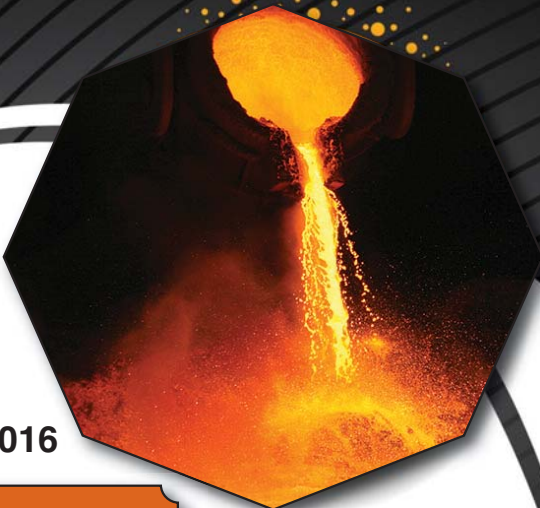
Field investigation showed that use of the high-pressure waterjet system resulted in significant improvement in the efficiency of gas drainage. For an individual borehole, the minimum gas flow rate increased 0.0181 m³/min to 0.0189 m³/min, and the maximum flow from 0.1533 m³/min to 0.26 m³/min. The average rate of gas production for each individual borehole more than doubled after the waterjet operation.

References

- GRYGLA, M.S. 2007. An investigation of methods to homogeneously entrain and suspend abrasive particles in a low pressure dental water jet. PhD dissertation, Brigham Young University, UT, USA.
- LIU, H.A. 2004. Study of the cutting performance in abrasive waterjet contouring of alumina ceramics and associated jet dynamic characteristics.

PhD dissertation, School of Mechanical, Manufacturing and Medical Engineering, Queensland University of Technology, Brisbane, Australia.

- LUNARZEWSKI, L.W. 1998. Gas emission prediction and recovery in underground coal mines. *International Journal of Coal Geology*, vol. 35, no. 1-4. pp. 117-145.
- PALLARES, J.S., PARRA, S.M.T., and GARCIA, S.J. 2009. Numerical analysis of high-pressure fluid jets: Application to RTD prediction in supercritical reactors. *Journal of Supercritical Fluids*, vol. 49, no. 2. pp. 249-255.
- SHANMUGAM, D.K. and CHEN, F.L. 2002. Comparative study of jetting machining technologies over laser machining technology for cutting composite materials. *Journal of Composite Structures*, vol. 57, no. 1-4. pp. 289-296.
- SHANMUGAM, D.K. and MORSI, Y. 2003. Study of ice production using experimental and computational fluid dynamic methods. *WJTA American Waterjet Conference*, Houston, TX. pp. 574-579.
- SNYDER, R.M. 2007. Mixing control in supersonic rectangular jets using plasma actuators. PhD dissertation, Ohio State University, USA.
- SRINIVASU, D.S., and BABU, R.A. 2008. Neuro-genetic approach for selection of process parameters in abrasive waterjet cutting considering variation in diameter of focusing nozzle. *Applied Soft Computing*, vol. 8, no. 1. pp. 809-819.
- YOUNGIL, K., ATUL, K., and KISOO, J. 2009. Evaluation of an optical particle sensor to determine the effect of nozzle shape on counting efficiency. *Journal of Aerosol Science*, vol. 40, no. 5. pp. 469-476. ◆



**The 2nd School on
Manganese Ferroalloy
Production**

27-28 June 2016

MAIN PRESENTER—MERETE TANGSTAD
Professor at NTNU (Norwegian University of Science and Technology).



Merete took her Master degree and PhD degree at NTNU. In the following years, she worked for Elkem and Eramet, mostly within ferromanganese and silico-manganese production, and mainly with research within these processes. Since 2004, she has been a professor at the Norwegian University of Science and Technology within Material Science and Engineering, with the main emphasis on manganese ferro-alloy production, and upgrading metallurgical silicon to solar-grade silicon. Merete is co-author of the definitive textbook on manganese ferroalloy production: *Production of Manganese Ferroalloys*, published by Tapir Press in Norway.

For further information contact:
For further information on the conference, please contact: Raymond van der Berg,
Head of Conferencing, SAIMM,
Tel: +27 11 834-1273/7
E-mail: raymond@saimm.co.za



Virgin rock temperature study of Venetia diamond mine

by M.Q.W. Jones*

Synopsis

Temperature surveys in 13 boreholes at Venetia diamond mine, Limpopo Province, South Africa, in 1994 (shortly after the mine opened) and in 2006 (during the feasibility phase of the Venetia underground project) have resulted in a comprehensive database of rock temperatures and geothermal gradients. The database permits clear identification of some factors that perturb rock temperatures, the most important being underground flow of water and recent climate change, and identification of depth intervals showing linear temperature trends that are useful for establishing geothermal gradients. The Venetia data demonstrates the value of such detailed virgin rock temperature studies for mine refrigeration purposes. The average ground surface temperature, estimated by upward extrapolation of the borehole data, is $25.9 \pm 0.5^\circ\text{C}$, and the geothermal gradient, estimated by averaging the gradients in linear sections of the boreholes, is $19.5 \pm 1.0 \text{ K/km}$. A plot of unperturbed borehole temperature *versus* depth below mine datum (696 m above mean sea level) yields a linear array with an intercept of 25.3°C and a slope of 20.1 K/km , which are compatible with the above averages. The average thermal conductivity of Limpopo Belt rocks of similar composition and metamorphic grade to the country rocks at Venetia is $3.01 \pm 0.55 \text{ W m}^{-1} \text{ K}^{-1}$. The geothermal heat flux calculated from this value and the measured geothermal gradients is $58 \pm 3 \text{ mW m}^{-2}$.

Keywords

Venetia diamond mine, mine refrigeration, rock temperature, geothermal heat flux.

Introduction

Investigation of mine refrigeration and ventilation requirements depends on a knowledge of virgin rock temperature (VRT) and thermal properties of rocks involved in excavations. Studies of these parameters have been conducted on regional scales in the Witwatersrand gold mining areas and the Bushveld platinum mining areas (Jones, 2003a, 2003b, 2015), but few detailed studies have been conducted for individual mines. Venetia diamond mine is one example where virgin rock temperature has been studied in a thorough and systematic manner.

Venetia mine, situated in Limpopo Province in northern South Africa (Figure 1), is the country's largest producer of diamonds. There are 14 known kimberlite pipes in the area and two of them, K1 and K2, are currently being mined in the same open pit operation (Figure 2). Although the existence of alluvial

diamonds near the Limpopo River was known as early as 1903, kimberlite pipes were discovered in only 1980. Mining commenced in 1992 and it is estimated that open pit mining can continue until approximately 2020. Beyond this date the life of the mine can most effectively be extended by underground mining. Extensive feasibility studies, including mine refrigeration investigations, during the last decade indicate that underground operations below the existing open pit will permit mining until approximately 2045. The underground project was launched in 2013.

The first detailed rock temperature measurements were made shortly after the mine opened, primarily for academic purposes, by the University of the Witwatersrand (Wits). More extensive surveys were conducted in 2006 during the feasibility stage of the underground project by a commercial company, GAP Geophysics (Pty) Ltd (GAP Geophysics) and subsequently by Wits in conjunction with De Beers Consolidated Mines Ltd (De Beers). The net result is a very detailed database of virgin rock temperatures and geothermal gradients, in 13 boreholes, to a depth of nearly 1000 m below surface. This database permits accurate estimation of rock temperatures as well as extrapolation to greater depths and plays an essential role in the estimation of mine refrigeration and ventilation requirements.

The primary purpose of this paper is to describe and discuss the borehole temperature database. The relevance of thermal conductivity measurements on similar rocks from the Limpopo Belt and kimberlite for mine refrigeration are also discussed. Finally, the data are used to make a new estimate for the geothermal heat flux in the area.

* School of Geosciences, University of the Witwatersrand, Johannesburg.

© The Southern African Institute of Mining and Metallurgy, 2016. ISSN 2225-6253. Paper received May 2015; revised paper received Jul. 2015.



Virgin rock temperature study of Venetia diamond mine

Geological background

Venetia mine is situated in the Limpopo Belt (Figure 1) which is situated between the Zimbabwe Craton to the north and the Kaapvaal Craton in the south (Kramers *et al.*, 2007). The cratons consist essentially of relatively undeformed and weakly metamorphosed granite-greenstone terrains that have undergone little tectonic activity since they stabilized at approximately 2500 Ma. In contrast, the Limpopo Belt is a broad zone of highly deformed and high-grade metamorphic rocks. It is separated from the cratons by prominent shear zones (Figure 1). Although radiometric ages exceeding 3200 Ma are preserved in some rocks, the belt underwent widespread tectonism approximately at 2650 Ma ago and again at approximately 2000 Ma. The Limpopo Belt is subdivided into a Southern Marginal Zone, a Northern Marginal Zone, and a Central Zone, in which Venetia is located (Figure 1). Like the boundaries of the Limpopo Belt with the cratons, these subdivisions are separated by major shear or fault zones.

Rocks constituting the Southern Marginal Zone are dominated by granitic gneisses, intermingled with metasediments and mafic-ultramafic rocks. The Northern Marginal Zone consists predominantly of granitic gneisses with minor mafic-ultramafic rocks (amphibolites) and some metasediments. Rocks constituting the Central Zone form a complex ensemble of gneisses of various composition, schists, and high-grade metasediments and amphibolites. Late tectonic and post-tectonic granitoid and/or syenite intrusions occur in all three zones, and much of the Limpopo Belt is buried beneath younger sedimentary and volcanic cover.

Rocks through which the Venetia kimberlite cluster was extruded are predominantly biotite gneiss, biotite schist, amphibolite, some quartzofeldspathic gneiss, and a younger Proterozoic diabase sill (Barton *et al.*, 2003; Kurszluakis and Barnett, 2003, a detailed geological log of one of the boreholes investigated here, DDH132). These rocks are enveloped by medium- to high-grade metasedimentary rocks. For the most part the country rocks discussed in this paper can be collectively referred to as 'granite gneiss'. The kimberlite pipes and their hypabyssal equivalents (intrusive

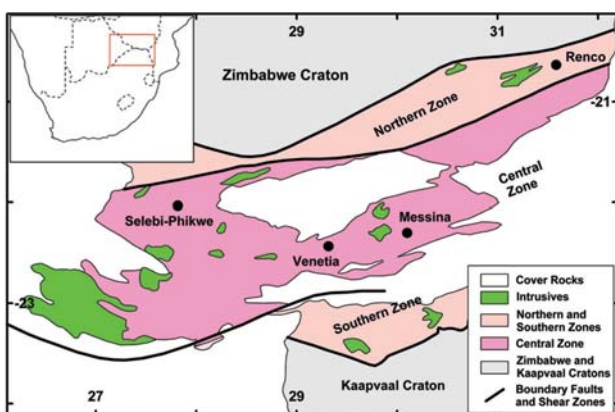


Figure 1—Locality of Venetia diamond mine (inset and main map) and simplified geological map of the Limpopo Belt (after Kramers *et al.*, 2007). Black circles are localities where other geothermal measurements have been made in the Limpopo Belt

dykes) were emplaced at approximately 520 Ma. The kimberlite is an ultramafic rock but occurs in a variety of forms, from massive volcanoclastic material to volcanic breccias that may include variable amounts of country rock fragments (Brown *et al.*, 2009; Kurszluakis and Barnett, 2003).

Borehole temperature database

Temperature measurements were made during three separate surveys in 13 boreholes (one of which, GDH062, was surveyed twice) in and around kimberlites K1, K2, and K3 (Figure 2). The first survey was conducted in two boreholes in 1994, shortly after the mine opened, by Wits as part of a national scientific programme aimed at determining the heat flux through the Earth's crust in South Africa. More extensive surveys were conducted in 2006 during the feasibility stage of the Venetia underground project, firstly by GAP Geophysics on behalf of De Beers and subsequently by Wits in conjunction with De Beers. Table 1 lists important borehole parameters, including locality (in local mine coordinates), elevation in metres above mean sea level, and average dip as well as relevant details regarding drilling and survey dates and surveyors. Four of the holes are collared within the kimberlites and the rest in country rock surrounding the kimberlites.

Borehole temperature surveys

Temperature surveys conducted by Wits were made using a custom-made logging unit. The sensor, a temperature transducer, is housed in a watertight probe attached to an 800 m length of cable, surrounded by a stainless steel sleeve which serves to protect the conductor and minimize cable stretch during surveys. The probe is capable of withstanding hydrostatic pressures to depths exceeding 2000 m. The probe can detect temperature differences of as little as 0.005°C, and calibration experiments ensured that its accuracy is better

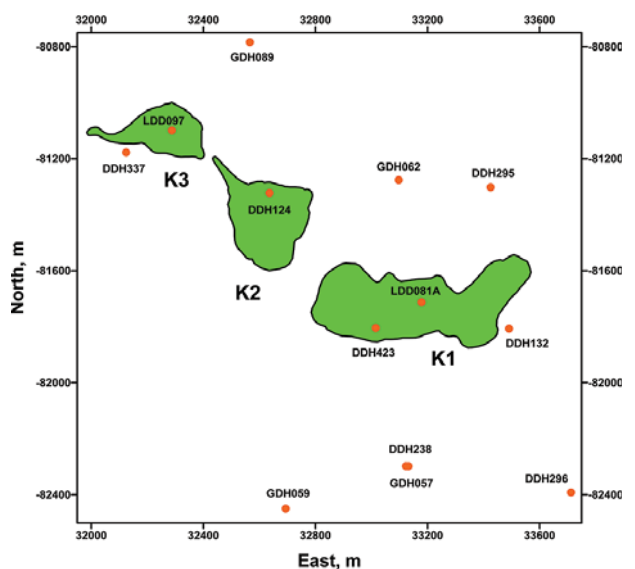


Figure 2—Collar localities of surface boreholes (red circles), in which rock temperatures have been measured, in relation to kimberlites K1, K2, and K3 (courtesy De Beers). X and Y localities in local mine coordinates

Virgin rock temperature study of Venetia diamond mine

Table 1

List of boreholes surveyed*

Borehole	East, m	North, m	Elevation, m	Average inclination	Drilling completed	Date surveyed	Surveyor
DDH124	32635.9	-81322.6	686.8	60°	Pre-1994	03/10/1994	Wits
DDH132	33490.8	-81807.0	674.6	77°	Pre-1994	03/10/1994	Wits
DDH295	33425.2	-81302.4	684.4	74°	09/11/2005	28/10/2006	De Beers/Wits
DDH337	32124.4	-81177.7	692.8	70°	21/04/2006	29/10/2006	De Beers/Wits
DDH423	33015.1	-81804.5	504.7	75°	26/10/2006	29/10/2006	De Beers/Wits
GDH059	32693.7	-82450.1	702.7	51°	27/07/2005	27/10/2006	De Beers/Wits
GDH062*	33097.0	-81276.5	676.0	54°	26/08/2005	28/10/2006	De Beers/Wits
GDH089	32566.0	-80784.0	681.6	54°	15/10/2006	29/10/2006	De Beers/Wits
DDH238	33123.0	-82298.0	682.0	55°	13/05/2005	2006	De Beers/Gap Geophysics
DDH296	33712.0	-82391.8	699.4	65°	21/10/2005	2006	De Beers/Gap Geophysics
GDH057	33131.8	-82298.2	685.3	49°	16/06/2005	2006	De Beers/Gap Geophysics
GDH062*	33097.0	-81276.5	676.0	54°	26/08/2005	2006	De Beers/Gap Geophysics
LDD081A	33178.5	-81712.6	528.5	90°	28/06/2005	2006	De Beers/Gap Geophysics
LDD097	32287.6	-81099.0	686.2	90°	12/12/2005	2006	De Beers/Gap Geophysics

*Note: temperatures were measured in borehole GDH062 during two different surveys (see text)

than 0.05°C. Temperatures were measured at discrete depth intervals of 10 or 20 m along the holes after allowing the probe to equilibrate for two minutes at each depth. Depths were recorded using a calibrated depth counter attached to a pulley over which the cable runs and are estimated to be accurate to within 10 cm. Vertical depths below borehole collar were calculated from De Beers borehole survey data. Further details regarding the measurement procedures are given by Jones (1981, 1987).

Surveys conducted by GAP Geophysics were made using a commercial logging device. In these surveys, temperatures were recorded continuously, while the probe was being lowered down the boreholes, to the nearest 0.1°C. These measurements are therefore intrinsically less precise than, but as accurate as, the above measurements. Temperatures were determined at 20 m intervals along the holes from the digital output of the logger and depths were corrected for borehole inclination as above. Continuous temperature logging may lead to errors if the rate of probe descent is too rapid compared with the probe equilibration time constant. This does not appear to be a problem in these surveys. One of the boreholes logged by GAP Geophysics (GDH062, Table 1) was subsequently logged by Wits and the results are within experimental uncertainty, the average difference in temperature at specific depths being less than 0.1°C.

Perturbations of underground temperatures

A number of factors can contribute to errors in determining equilibrium temperatures and thermal gradients. These can be categorized as those associated with the measurements themselves and those associated with environmental problems (Jones and Booyen, 2007).

Potential surveying-related issues include continuous logging, drilling transients, convection in boreholes and uncertainties in determining depth near the bottom of boreholes. The risks entailed in continuous logging are noted above. These can be minimized by ensuring that recordings are made while probes are descending and by careful survey design. Temperature measurements in boreholes shortly after cessation of drilling are subject to thermal transients. In theory it can take months for rock surrounding a borehole to

re-equilibrate after drilling (Bullard, 1947), but in practice this appears to be achieved much sooner. All the boreholes surveyed at Venetia were filled with water or drilling fluid. This is actually important because probes take a long time to equilibrate in air, and measurements in dry holes often lead to erroneous results. Although this raises the question of convection in boreholes, this phenomenon appears to be significant only if thermal gradients are very high and borehole diameters are large (Diment and Robertson, 1963; Diment, 1967). It is often difficult to determine whether a probe has reached the bottom of a hole, particularly if the hole is deep and the probe is heavy, and whether true depths are being measured if the borehole inclination is small; measurements close to the base of boreholes can therefore be misleading.

Environmental factors include topography, surface temperature change, heat diversion due to lateral thermal conductivity contrasts, and heat transport by underground water flow. In regions of high relief, the flow of heat away from hills and towards valleys can perturb subsurface temperatures (Bullard, 1938), but this is unlikely to be significant at Venetia except perhaps in the upper 100 or so metres of two boreholes that are collared in the open pit. Temperature profiles in the upper 100–300 m in many boreholes in South Africa, and elsewhere, demonstrate a marked curvature that reflects a surface temperature increase of up to 2°C during the last 100–300 years. This is predominantly due to recent climate change (Jones *et al.*, 1999) but may be exacerbated at Venetia because mining activities effectively increase ground surface temperature. Measurements in shallow holes should therefore be treated with caution. Non-vertical heat transfer in regions of complex geological structure involving rocks of different thermal conductivity may lead to significant perturbations in borehole temperature profiles. Corrections can be made for this effect but the work is tedious and time-consuming. Underground water flows through fissures or permeable lithologies intersected by boreholes constitute the most common cause of borehole temperature perturbations and sometimes render the data useless. Water flows may show up as fluctuating temperatures at particular depths during measurement, but

Virgin rock temperature study of Venetia diamond mine

otherwise can be difficult to identify. Water flows often reflect as spikes or discontinuities in temperature profiles and as irregular thermal gradients. Temperatures in affected zones should be discarded, and the data must be examined carefully in order to establish the extent to which temperatures and thermal gradients above the disturbances are affected.

Observations in individual boreholes

Temperature observations and calculated thermal gradients in each borehole are presented in Figures 3a–3n. The figures are arranged according to the temperature survey and borehole number as listed in Table I. In all these diagrams, temperature and thermal gradient are plotted against vertical depth below the borehole collar. The vertical and horizontal scales are identical so that the results can be compared directly. Red dots represent temperature measurements and refer to the left-hand vertical axes (also shown in red). Black lines are least squares fits to temperature-depth data in linear sections of the borehole profiles. Least squares parameters (intercept and slope) are listed in Table II. The blue curves represent calculated thermal gradients between successive temperature observations and are referred to the right-hand vertical axes (also shown in blue). Salient notes relating to each borehole are presented below and should be read with reference to Table I and Figure 3.

- DDH124 (Figure 3a) is collared in kimberlite but passes into country rock. Temperatures were recorded at 10 m intervals along the hole. The temperature profile shows a clear curvature, reflecting an increase in thermal gradient, at depth shallower than 120 m
- DDH132 (Figure 3b) is collared in country rock but penetrates kimberlite. Temperatures were recorded at 10 m intervals along the hole. The temperature profile shows a clear curvature above 120 m. The spike in geothermal gradient at approximately 140 m is almost certainly due to an aquifer
- DDH295 (Figure 3c) is collared in country rock but penetrates kimberlite. Temperatures were recorded at 20 m intervals along the hole. There is a clear curvature in temperature profile above 180 m. The sudden changes in thermal gradient at approximately 450–500 m are most probably due to water flow associated with diabase intersected at approximately this depth
- DDH337 (Figure 3d) is collared in country rock but penetrates kimberlite. Temperatures were recorded at 20 m intervals along the hole. The curvature in the temperature profile extends to approximately 220 m. The increased thermal gradient near the base of hole is associated with the occurrence of diabase and kimberlite
- DDH423 (Figure 3e) is collared in kimberlite in the open pit but penetrates country rock. Temperatures were recorded at 20 m intervals along the hole. The borehole may not have fully reached thermal equilibrium after drilling. Spikes in the thermal gradient at approximately 250–300 m and 490–520 m probably reflect water flows
- GDH059 (Figure 3f) is in country rock. Temperatures were recorded at 20 m intervals along the hole. This

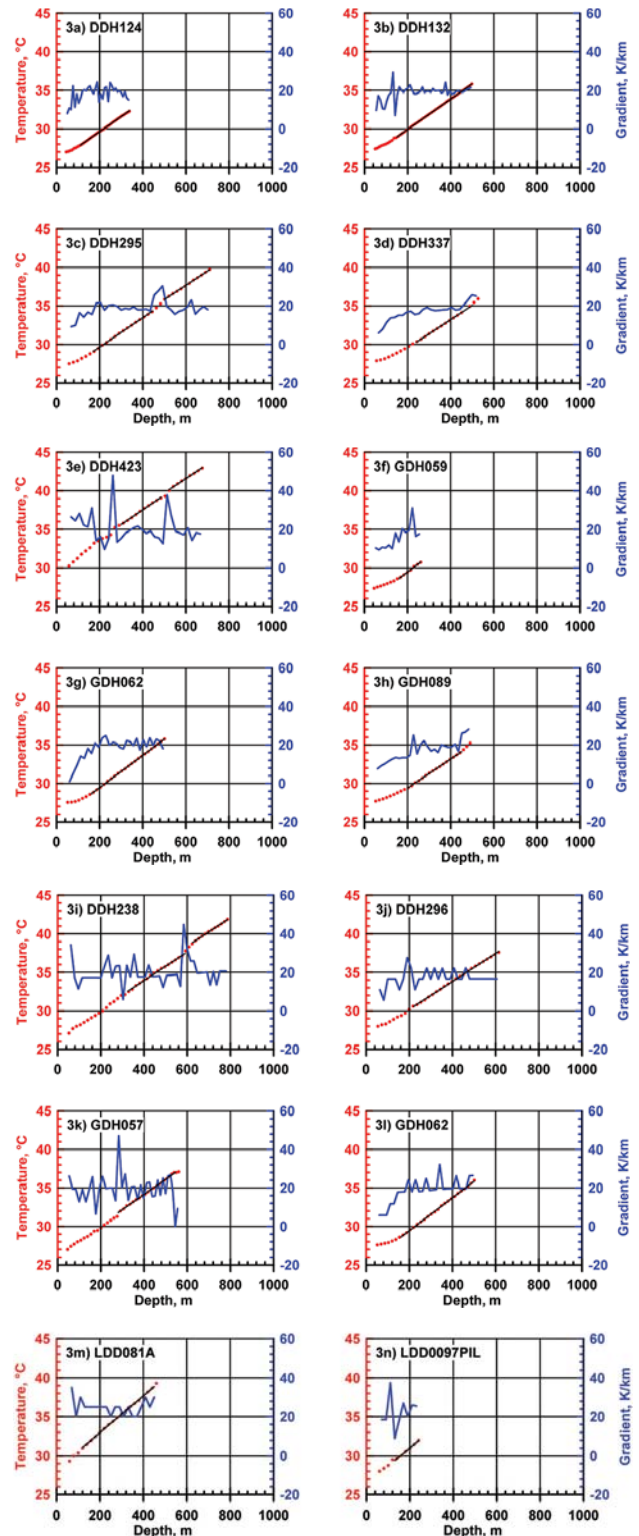


Figure 3—Observed temperatures and calculated thermal gradients plotted against depth below collar for boreholes listed in Table I. All diagrams (Figures 3a–3n) are plotted using the same scales so that they can be compared directly. In each diagram, red dots represent temperature and are plotted relative to the left-hand vertical axis (also shown in red); black lines represent least squares fits to temperature vs depth data for selected depth intervals, and are also plotted relative to the left-hand axis; blue curves represent thermal gradients, calculated from successive temperature measurements, and are plotted relative to the right-hand vertical axis (also shown in blue). Note that measurements in borehole GDH062 (Figures 3g and 3l) were made twice in separate surveys in 2006

Virgin rock temperature study of Venetia diamond mine

Table II

Estimated surface temperature, geothermal gradient, and geothermal heat flux. Values in parentheses were excluded when calculating means as they are regarded as less reliable or are not compatible with the bulk of the data (see text)

Borehole	Depth range, m	Surface temperature, °C	Thermal gradient, K/km	Heat flux, mW m ⁻²
DDH124	115-338	25.7	19.8	60
DDH132	156-498	26.0	19.8	60
DDH295	174-443	25.8	19.3	-
	501-714	(26.6)	18.6	56
DDH337	243-488	25.9	18.6	56
DDH423	310-465	(29.7)	19.7	-
	523-676	(30.3)	18.9	57
GDH059	168-261	25.2	21.3	-
GDH062	171-501	25.3	21.0	63
GDH089	202-444	25.6	19.0	57
DDH238	328-576	26.6	18.6	-
	638-787	(27.4)	18.5	56
DDH296	235-614	26.6	18.3	55
GDH057	290-539	26.3	19.7	59
GDH062	171-501	25.2	21.4	-
LDD081A	120-450	(28.3)	(23.5)	-
LDD097	130-240	26.3	(23.5)	-

borehole is relatively shallow and the results are less reliable. There is a clear curvature in temperature profile above 160 m

- GDH062 (Figure 3g) is collared in country rock but penetrates kimberlite. Temperatures were recorded at 20 m intervals along the hole. This temperature survey was conducted by Wits; the hole was previously surveyed by GAP Geophysics (see below). There is a clear curvature in temperature profile above 170 m
- GDH089 (Figure 3h) is in country rock. The borehole may not have fully reached thermal equilibrium after drilling. Temperatures were recorded at 20 m intervals along the hole. There is a clear curvature in the temperature profile above 200 m. The reason for the increased thermal gradient at base of the hole is not known; it is possibly due to uncertainty in depth since the hole inclination at the base is only 50°
- DDH238 (Figure 3i) is predominantly in country rock. Temperatures were recorded continuously. There is a probable water flow associated with diabase at approximately 580–620 m
- DDH296 (Figure 3j) is predominantly in country rock. Temperatures were recorded continuously. There is a clear curvature in temperature profile above 180 m
- GDH057 (Figure 3k) is predominantly in country rock. Temperatures were recorded continuously. There is a probable water flow associated with a shear zone at approximately 290 m. The reason for the decreased thermal gradient at base of hole is unknown; it is probably due to uncertainty in depth since the hole inclination at the base is only 33°
- GDH062 (Figure 3l). See above. This first survey was conducted by GAP Geophysics. Temperatures were recorded continuously. The borehole may not have reached thermal equilibrium after drilling
- LDD081A (Figure 3m) is collared in the open pit. It is in kimberlite. Temperatures were recorded

continuously. The thermal gradient is higher than in most previous boreholes.

- LDD097PIL (Figure 3n) is in kimberlite. Temperatures were recorded continuously. It is a relatively shallow borehole and the results are less reliable. The thermal gradient is higher than in most previous boreholes.

Discussion of virgin rock temperatures

The individual plots in Figure 3 are useful for assessing the data quality, identifying depth intervals with uniform geothermal gradient, and determining least squares parameters relating temperature to depth. Table II lists depth ranges characterized by linear trends in each borehole along with the least squares intercept (or extrapolated surface temperature) and slope (or average thermal gradient).

With the exception of boreholes DDH423 and LDD081A, which are collared in the open pit, the surface temperatures fall in a relatively narrow range (Table II). If the data from these two holes and estimates from the deeper sections of DDH295 and DDH238 (which yield less reliable surface temperature estimates purely because of the depth of the data) are excluded, the mean surface temperature is $25.9 \pm 0.5^\circ\text{C}$ (12 values). This is the 'ground surface temperature' for the average collar elevation of the boreholes (except for holes DDH423 and LDD081A), 686 ± 9 m (12 values) (Table I). This temperature is approximately 4°C higher than the mean annual air temperature for the region (the nearest weather station, Alldays, yields a value of 22.1°C for the period January 1999 to December 2002) because excess heat is carried into the ground in summer rainfall regions.

The least squares thermal gradients (column 4, Table II) are relatively uniform except for LDD081A and LDD097PIL, which are significantly higher. This may partly reflect the fact that these holes are in kimberlite. The remaining data average at 19.5 ± 1.0 K/km (15 values).

Virgin rock temperature study of Venetia diamond mine

In order to illustrate the regional trend more clearly, individual temperature observations and calculated thermal gradients are plotted in combined diagrams in Figures 4 and 5. This is not possible using depth below collar, because boreholes DDH423 and LDD081A are collared in the open pit approximately 160–180 m below the remaining boreholes. The recorded temperatures at given depths below collar in these two boreholes are therefore offset to higher temperature by approximately 4°C compared with the other holes (see Figures 3e and 3m). The easiest way to correct for this is to plot the data relative to the local datum elevation (696 m above sea level). This procedure has the added advantage in that it directly yields the mean temperature of a particular mining level measured in metres below datum.

The combined temperature plot using all the data is presented in Figure 4a and the corresponding thermal gradient plot is shown in Figure 5a. These diagrams show the regional trends reasonably well but reveal considerable noise. This is partly due to the climatically and/or mining induced curvature in the upper 200 m of most boreholes and partly to disturbances associated with underground water flow (Figures 3a–3n). As noted above, data from boreholes LDD081A and LDD097PIL also do not match the trends defined by the rest of the data-set (Table II).

Figure 4b was constructed using only those data that define linear trends (Figure 3, Table II) and excluding data from LDD081A and LDD097PIL. The scatter is considerably reduced compared with Figure 4a. There is also far less noise in the corresponding geothermal gradient plot (Figure 5b), which shows that the gradients are close to 20 K/km. The least squares regression line to the data in Figure 4b is $T(x) = 25.3 + 20.1x$, where T is in degrees Celsius and x is in kilometers below datum. This line provides a direct way of calculating temperature at different levels in underground workings at Venetia. It can also be used with confidence for extrapolating to greater depth provided there are no significant vertical changes in rock type.

Thermal conductivity

A knowledge of the thermal conductivity (K , units $W m^{-1} K^{-1}$), density (ρ , $kg m^{-3}$), heat capacity (C , $J kg^{-1} K^{-1}$), and the derived parameter thermal diffusivity ($\kappa = K/\rho C$, $mm^2 m^{-1}$) is important for transient calculations involving heat flux into underground workings. Unfortunately there are no data from Venetia mine, but estimates can be made based on measurements from other localities or published values.

Typical density ranges for the rocks discussed here are: amphibolite, 2900–3100 $kg m^{-3}$; diabase, 2800–3100 $kg m^{-3}$; kimberlite, 2400–3000 $kg m^{-3}$; granite gneiss, 2600–2900 $kg m^{-3}$; schist, 2400–2900 $kg m^{-3}$. The ranges are quite large, but accurate values are easy to obtain because measurement of density is relatively quick and simple. Heat capacity is relatively uniform for most silicate rocks. For example, average values for various rock types in the Witwatersrand gold mining area fall in the range 810–880 $J kg^{-1} K^{-1}$ (Jones, 2003b) and the range of averages for volumetrically important rocks associated with platinum mining in the Bushveld Complex is 820–870 $J kg^{-1} K^{-1}$ (Jones, 2015); a value between 800 and 1000 $J kg^{-1} K^{-1}$ will suffice for most calculations.

Thermal conductivity is the most variable parameter and has the greatest influence on thermal diffusivity. Numerous measurements have been made, on rocks of similar composition and metamorphic grade to the granite gneisses and associated rocks at Venetia, at three localities in the Limpopo Belt (Figure 1), namely Selebe-Phikwe (Ballard, 1987; Ballard *et al.*, 1987; M.Q.W. Jones, unpublished data, 2015), Messina (Carte, 1954; M.Q.W. Jones, unpublished data, 2015) and Renco (Nyblade, 1992; Nyblade *et al.*, 1990). Figure 6 shows a histogram of 150 analyses conducted on amphibolite, quartzofeldspathic gneiss, biotite gneiss, and hornblende gneiss. The distribution is nearly Gaussian and the mean thermal conductivity is $3.01 \pm 0.55 W m^{-1} K^{-1}$. Data for kimberlite are sparse; Ballard (1987) gives a value of $1.9 \pm 0.2 W m^{-1} K^{-1}$ on the basis of five measurements, and 21 unpublished measurements by the author yield an average of $1.88 \pm 0.21 W m^{-1} K^{-1}$ (M.Q.W. Jones, unpublished data, 2016).

Geothermal heat flux

The borehole temperature data provides the opportunity to estimate the heat flux through the Earth's crust at Venetia. At

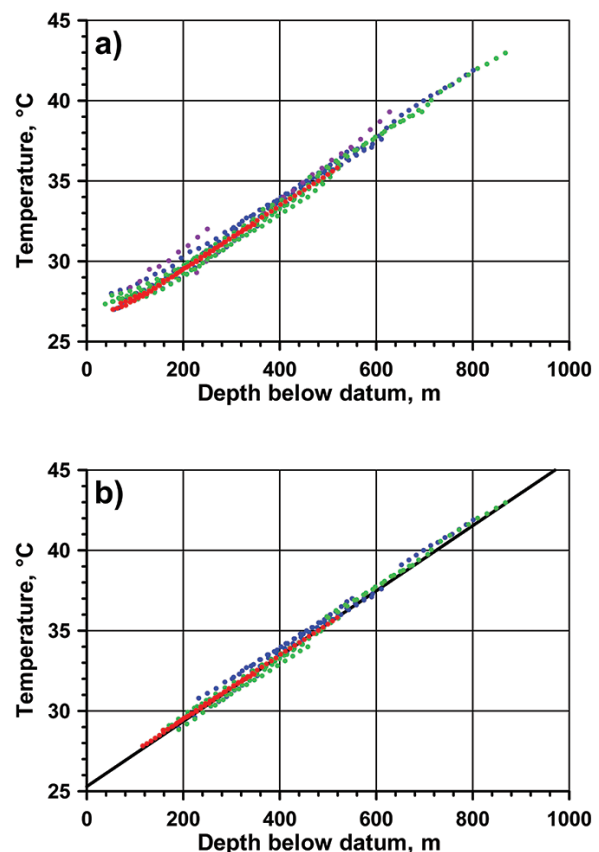


Figure 4—(a) Combined plot of all borehole temperature data versus depth below datum. Red dots, 1994 Wits survey; green dots, 2006 Wits/De Beers survey; blue and purple dots, 2006 GAP Geophysics/De Beers survey (purple, data from boreholes LDD081A and LDD097PIL). (b) Combined plot of selected borehole temperature data versus depth below datum. Colours as in Figure 4a. Selected data include only those temperature-depth pairs falling on linear trends delineated in Figure 3 and defined in Table II. Black line, least squares linear fit to data in the figure

Virgin rock temperature study of Venetia diamond mine

the surface this parameter is given by Fourier's Law of heat conduction: $q_0 = K(dT/dx)_0$ where $(dT/dx)_0$ is the near-surface equilibrium thermal gradient and K is the average thermal conductivity of near-surface rocks.

Heat flux values, found by multiplying the average thermal conductivity for country rock ($3.01 \text{ W m}^{-1} \text{ K}^{-1}$) by the least squares thermal gradients in Table II, are listed in column 5 of the table. Two boreholes, LDD081A and LDD097PIL, are entirely within kimberlite and have not been

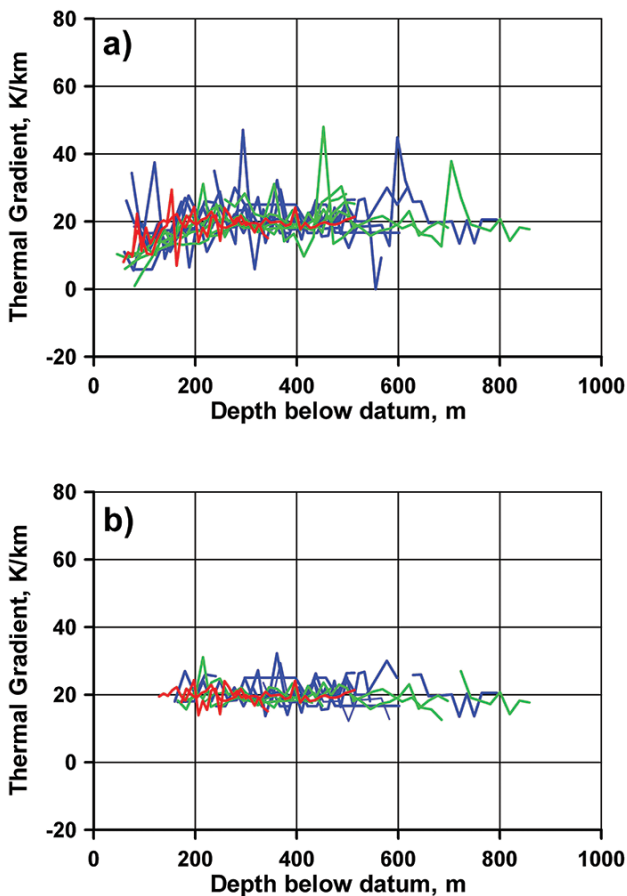


Figure 5 – (a) Combined plot of all calculated thermal gradients presented in Figure 3 versus depth below datum. Red curves, 1994 Wits survey; green curves, 2006 Wits/De Beers survey; blue curves, 2006 GAP Geophysics/De Beers survey. (b) Combined plot of selected thermal gradients versus depth below datum. Colours as in Figure 5a. Selected data include only those data falling within linear trends delineated in Figure 3 and defined in Table II

used. GDH059 is quite shallow and its value is regarded as less reliable; it has been excluded from further analysis. Deeper borehole data generally lead to more reliable heat flow estimates, and only the deeper sections of DDH295, DDH423, and DDH238 are used here. The second heat flow estimate for borehole GDH062 is really a repeat measurement (Table II) and only the first estimate is used. The average heat flux for Venetia is thus determined as $58 \pm 3 \text{ mW m}^{-2}$ (10 values). Because of the absence of conductivity data from Venetia, the estimated percentage error is increased to 10%. The heat flow from Venetia is compared with previous heat flow measurements in the Limpopo Belt in Table III. The results are compatible and the overall heat flow from the Belt is $54 \pm 4 \text{ mW m}^{-2}$. This is substantially higher than that in the adjacent cratonic regions (Figure 1) and has important geodynamic implications which will be discussed elsewhere.

Conclusions

Comprehensive borehole temperature surveys at Venetia mine shortly after opening of the mine and during the feasibility phase of the underground project permit detailed analysis of local rock temperature variations. Temperature disturbances associated with environmental factors such as climate change and underground water flow are clearly evident in the database. After removal of such noisy data and outliers, the database yields consistent values for the ground surface

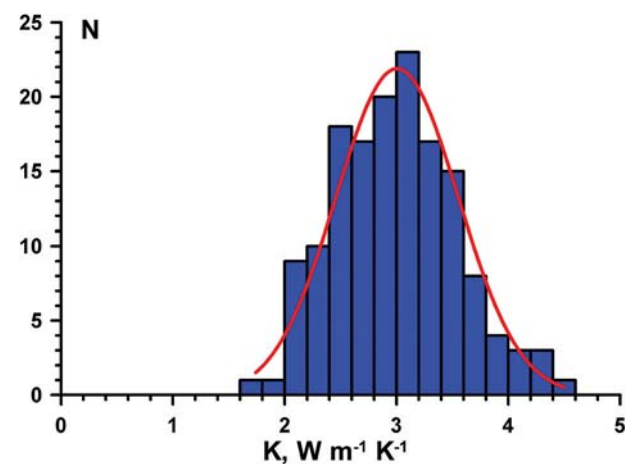


Figure 6—Histogram of thermal conductivity data for amphibolites, quartzofeldspathic gneisses, biotite gneisses, and hornblende gneisses from the Limpopo Belt (blue). Normal Gaussian distribution shown in red

Table III

Heat flow in the Limpopo Belt

Locality	Latitude	Longitude	Heat flow, mW m^{-2}	Uncertainty, %	Reference
Venetia	22° 26'	29° 19'	58	10	This paper
Renco	20° 38'	31° 35'	49	10	Nyblade <i>et al.</i> (1990)
Messina	22° 18'	30° 06'	57	7	Carte (1954)
Selebi-Phikwe	22° 02'	27° 49'	53	5	Ballard <i>et al.</i> (1987)

Virgin rock temperature study of Venetia diamond mine

temperature, underground thermal gradients, and a linear relationship between virgin rock temperature and depth below local datum. These data are important for refrigeration studies of currently planned underground workings and potentially useful for future extrapolation to greater depth. Thermal conductivity data from country rock of similar composition and metamorphic grade to those encountered at Venetia and on kimberlites permit estimates for rock properties in calculating heat loads on underground workings. The thermal gradients, together with thermal conductivity data, yield a new estimate for the heat flux through the Earth's crust.

Acknowledgements

I am grateful to De Beers Consolidated Mines Ltd for logistical and financial support for surveys conducted by Wits, for providing essential data, and for permission to publish this paper, which would not have been possible without De Beers' thorough feasibility study. Jannie Booysen organized the Wits/De Beers surveys in 2006 and played a big part in making the field measurements. Jay Barton likewise assisted in the 1994 surveys. Geoff Campbell provided useful information regarding the 2006 GAP Geophysics surveys. The author is grateful to Terence McCarthy and two anonymous reviewers for useful comments.

References

- BALLARD, S. 1987. Terrestrial heat flow and thermal structure of the lithosphere in southern Africa. PhD thesis, University of Michigan, Ann Arbor, USA. 140 pp.
- BALLARD, S., POLLACK, H.N., and SKINNER, N. 1987. Terrestrial heat flow in Botswana and Namibia. *Journal of Geophysical Research*, vol. 92. pp. 6291–6300.
- BARTON, J.M., BARNETT, W.P., BARTON, E.S., BARNETT, M., DOORGAPERSHAD, A., TWIGGS, C., KLEMD, R., MARTIN, J., MELLONIG, L., and ZENGLIN, R. 2005. The geology of the area surrounding Venetia kimberlite pipes, Limpopo Belt, South Africa: a complex interplay of nappe tectonics and granitoid magmatism. *South African Journal of Geology*, vol. 106. pp. 109–128.
- BROWN, R.J., TAIT, M., and SPARKS, R.S.J. 2009. Geology of a complex kimberlite pipe (K2 pipe, Venetia Mine, South Africa): insights into conduit processes during explosive ultrabasic eruptions. *Bulletin of Volcanology*, vol. 71. pp. 95–112.
- BULLARD, E.C. 1938. The disturbance of temperature gradient in the Earth's crust by inequalities of height. *Monthly Notices of the Royal Astronomical Society, Geophysics Supplement*, vol. 4. pp. 360–362.
- BULLARD, E.C. 1947. The time necessary for a borehole to attain temperature equilibrium. *Monthly Notices of the Royal Astronomical Society, Geophysics Supplement*, vol. 5. pp. 127–130.
- CARTE, A.E. 1954. Heat flow in the Transvaal and Orange Free State. *Proceedings of the Physical Society of London, Series B*, vol. 67. pp. 664–672.
- DIMENT, W.H. 1967. Thermal regime of a large diameter borehole: instability of the water column and comparison of air- and water-filled conditions. *Geophysics*, vol. 32. pp. 720–726.
- DIMENT, W.H. and ROBERTSON, E.C. 1963. Temperature, thermal conductivity and heat flow in a drilled hole near Oak Ridge, Tennessee. *Journal of Geophysical Research*, vol. 68. pp. 5035–5047.
- JONES, M.Q.W. 1981. Heat flow and heat production studies in the Namaqua Mobile Belt and Kaapvaal Craton. PhD. Thesis, University of the Witwatersrand, Johannesburg. 319 pp.
- JONES, M.Q.W. 1987. Heat flow and heat production in the Namaqua Mobile Belt, South Africa. *Journal of Geophysical Research*, vol. 92. pp. 6273–6289.
- JONES, M.Q.W. 2003a. An update in virgin rock temperature analysis of the Witwatersrand Basin. *Journal of the Mine Ventilation Society of South Africa*, vol. 56. pp. 107–112.
- JONES, M.Q.W. 2003b. Thermal properties of stratified rocks from Witwatersrand gold mining areas. *Journal of the Southern African Institute of Mining and Metallurgy*, vol. 101. pp. 173–185.
- JONES, M.Q.W. 2015. Thermophysical properties of rocks from the Bushveld Complex. *Journal of the Southern African Institute of Mining and Metallurgy*, vol. 115. pp. 153–160.
- JONES, M.Q.W. and BOOYSEN, J. 2007. Rock temperature and thermal gradient. *MHSC Handbook on Mine Occupational Hygiene Measurements*. Stanton, D.W., Kielblock, J.J., and Johnston, J.R. (eds.). Mine Health and Safety Council, Johannesburg. pp. 237–245.
- JONES, M.Q.W., TYSON, P.D., and COOPER, G.R.J. 1999. Modelling climatic change in South Africa from perturbed borehole temperature profiles. *Quaternary International*, vol. 57/58. pp. 185–192.
- KRAMERS, J.D., MCCOURT, S., and VAN REENEN, D.D. 2007. The Limpopo Belt. *The Geology of South Africa*. Johnson, M.R., Anhaeusser, C.R., and Thomas, R.J. (eds.). Geological Society of South Africa/Council for Geoscience, Johannesburg/Pretoria. pp. 209–236.
- KURSZAUKIS, S. and BARNETT, W. 2003. Volcanological and structural aspects of the Venetia kimberlite cluster – a case of South African kimberlite maar-diatreme volcanoes. *South African Journal of Geology*, vol. 106. pp. 145–172.
- NYBLADE, A.A. 1992. Terrestrial heat flow in east and southern Africa and the thermal structure of Precambrian lithosphere. PhD thesis, University of Michigan, Ann Arbor, USA. 165 pp.
- NYBLADE, A.A., POLLACK, H.N., JONES, D.L., PODMORE, F., and MUSHAYANDEBVU, M. 1990. Terrestrial heat flow in east and southern Africa. *Journal of Geophysical Research*, vol. 95. pp. 17,371–17,384. ◆



Solvent extraction and separation of hafnium from zirconium using Ionquest 801

by L. de Beer*, D.J. van der Westhuizen*, and H.M. Krieg*

Synopsis

The solvent extraction (SX) characteristics of Ionquest 801 were investigated to determine if the selective extraction of hafnium (Hf) over zirconium (Zr) is possible. Firstly, Ionquest 801 was screened for its suitability as a function of acid concentration. The solvent consisted of 5wt % extractant, corresponding to a extractant to metal ratio ($E:M_{Zr}$) of 14:1, in cyclohexane with 5% v/v 1-octanol added as modifier. Aqueous solutions of $ZrCl_4$ with 3 wt% $HfCl_4$ were prepared by dissolution of the salts in HNO_3 to obtain 1.0 g/l $Zr(Hf)Cl_4(aq)$ feed solutions (aged 24 hours). Subsequently, the extractant concentration was varied at optimal acid molarities. The most favourable extraction percentages were attained at 0.7 M HNO_3 and an $E:M_{Zr}$ ratio of 5:1. Artifices in the form of aqueous additives were used to maximize the Hf selectivity at these optimal conditions. These included the addition of 1.5 M NaCl, $NaNO_3$, Na_2SO_4 , and $NaClO_4 \cdot H_2O$, as well as tartaric, oxalic, mandelic, and citric acid with and without the addition of 6 wt% hydrogen peroxide (H_2O_2). Exploratory studies on the influence and usability of the most promising factors such as $[SO_4^{2-}]$, $[H_2O_2]$, and combinations thereof in a SX system were undertaken.

Keywords

solvent extraction, Ionquest 801, PC88A, organophosphorus, hafnium, zirconium.

Introduction

While zirconium (Zr) is used in a variety of industries, its nuclear properties in the pure metallic form make it highly desirable for nuclear applications. Zr is highly corrosion resistant and has a high melting point (2128 K) with a low thermal neutron absorption cross-section of $Zr_{\sigma T} = 0.18 b$, which is significantly smaller than that of hafnium $Hf_{\sigma T} = 115 b$ (Speer, 1982), an element that coexists with Zr in nature. This makes Zr ideal for nuclear cladding material and for an inert fuel matrix (Chadwick *et al.*, 2011). Since unrefined Zr metal is more prone to corrosion in a high-temperature aqueous and steam environment (due to metallic and nonmetallic impurities), stringent quality standards have to be met to ensure optimal performance of the zirconium alloy in a nuclear environment. This requires zirconium alloys with a low neutron capture coefficient, high corrosion resistance with regard to nuclear coolants, high manufacturability, and cracking resistance of components during

operation, as well as in the manufacturing process itself. While Zr for use in the nuclear industry needs to contain less than 100 ppm Hf, various aspects of metal procurement, purification, and production have to be taken into account to make zirconium alloy of the highest grade. The <100 ppm Hf requirement is likely to be replaced soon by an American equivalent, Zircaloy-4; or Russian equivalent, Zr-1%Nb. These zirconium alloys, which are already in use in nuclear reactors, contain Hf concentrations as low as 42 ppm and 80 ppm respectively (Nikulina and Malgin, 2008).

The main impurities found in nuclear-grade Zr are titanium (Ti), boron (B), cadmium (Cd), cobalt (Co), manganese (Mn), molybdenum (Mo), sodium (Na), magnesium (Mg), silicon (Si), carbon (C), hydrogen (H), chlorine (Cl), potassium (K), calcium (Ca), fluorine (F), phosphorous (P), oxygen (O), nitrogen (N), iron (Fe), nickel (Ni), chromium (Cr), copper (Cu), aluminum (Al), and hafnium (Hf). The most is known about the effects of O, N, H, C, Si, Al, Fe, Ni, and Hf. The presence of N, C, Al, and Ti results in decreased corrosion resistance (in high-temperature aqueous environments), while the presence of C, H, Si, Cl, P, and F results in decreased fracture toughness and, as a result, poor manufacturability and cracking resistance of parts. Oxygen improves the strength of zirconium alloys, while Fe improves corrosion resistance. Ni intensifies hydrogen absorption, which in turn decreases fracture toughness. The detrimental effects of impurities on the properties of zirconium alloys are synergistic.

* Chemical Resource Beneficiation, North-West University, Potchefstroom, South Africa.

© The Southern African Institute of Mining and Metallurgy, 2016. ISSN 2225-6253. This paper was first presented at the Nuclear Materials Development Network Conference 2015, Nelson Mandela Metropolitan University, North Campus Conference Centre, Port Elizabeth, South Africa.

Solvent extraction and separation of hafnium from zirconium using Ionquest 801

Consequently, concentrations of impurities relative to Zr as well as to other impurities are important. The performance of zirconium alloys therefore depends not only on the thermodynamic properties, but also on the: microstructure, porosity, fracture toughness, and plasticity, as well as residual plasticity (Nikulina and Malgin, 2008).

The South Africa Nuclear Energy Corporation (NECSA) processes South African zircon ore *via* a plasma dissociated zircon (PDZ) process and reports that the following impurities are present after the plasma fluorination process: Hf, Si, Fe, Ti, Al, Cr, Mg, Ca, P, U, Th, Fe, Ti, Al, Cr, Mg, Ca, U, and Th. The impurities are present at this stage as oxide and fluoride complexes.

Once the abovementioned impurities have been removed, the production of pure Zr remains difficult, due to the presence of 0.5–3 wt% Hf impurity in the original ore (Belousova *et al.*, 2002). The difficulty originates from the chemical similarities of Zr and Hf in both metallic and compound form. The most well-known methods of separation include extractive distillation (CEZUS Process, with a separation factor (SF) of approximately 2 (Banda and Lee, 2015) and solvent extraction (SX) using MIBK (SF approx. 7) or TBP (SF approx. 10) (Banda and Lee, 2015). Many alternative methods have been investigated and are summarized in the following paragraphs.

Fritz and Frazee (1965), applied reversed-phase chromatographic separation to solutions containing 250 and 50 μ mole Zr and Hf, respectively, and successfully purified Zr to 0.001–0.002% Hf content. The quantitative separation was obtained using Teflon-6 as solid support and methyl isobutyl ketone, pre-equilibrated with 3 M thiocyanic acid, as the stationary phase. Zr was eluted with an ammonium thiocyanate-ammonium sulphate solution and Hf stripped from the column with an ammonium sulphate or sulphuric acid solution. Successful column separations were also achieved on solutions containing Zr to Hf ratios of 5, 25, and 100 to 1, with resulting impurity levels of 0.01% Hf (in Zr) and 0.01% Zr (in Hf).

Akl *et al.* (2001) demonstrated that with separation-flotation $0\text{--}20 \times 10^{-5}$ mol/L of both Zr and Hf could be completely separated using an aqueous solution of HCl at pH 2 containing Eriochrome Cyanine R (ECR) and an organic solution of the oleic acid surfactant HOL in kerosene. The suggested application of this technique was the separation and microdetermination of Zr and Hf in water samples.

Poriel *et al.* (2006), reported a selectivity (α) of ≥ 2.5 on a 27 mmol Zr and 11 mmol Hf mixed solution, with ligand-enhanced separation *via* ultra/nano-filtration membranes. The best results were obtained with the organic thin-film composite nanofiltration membrane Desal G10 (Osmonics). As EDTA-Hf complexes have a higher thermodynamic stability constant than Zr-EDTA complexes, ethylenediaminetetraacetic acid (EDTA) was used as depolymerization agent. The mechanism of separation is the transport of the EDTA-Hf complexes, which form preferentially, across the membrane.

Smolik *et al.* (2009) utilized 6.5 g Diphonix[®] resin (containing diphosphonic, sulphonic, and carboxylic acid groups) for the separation of Zr from Hf in aqueous sulphuric acid medium (0.5 M) containing 6.38 g/l Zr and 0.154 g/l Hf. They found that a reduction in temperature (22°C to 5°C)

decreased the degree of separation while lower column flow rates increased the extent of separation. Under these conditions, a 10-fold decrease (from 2.4% to 0.24%) of Hf in Zr was achieved with 45% recovery of Zr. The results indicated that Diphonix[®] resin is suitable for the separation of Zr from Hf by a continuous ion exchange process.

Li *et al.* (2011) studied the combination of combustion synthesis and molten-salt electrorefining. Zr metal was produced containing ≤ 70 ppm Hf through separation by exploitation of the differences in the thermodynamic stabilities of Zr and Hf fluorides. Firstly, ZrSi powder was produced by magnesiothermic reduction of ZrSiO₄ in an argon atmosphere at a pressure of 2.5 MPa. The ZrSi was then arc melted and cast into granules for use as raw material in the electrorefining process. The electrorefining cell consisted of a high-purity LiCl-KCl eutectic (chloride electrolyte; 58.5–41.5 mol%, $T_m = 352^\circ\text{C}$) and 5 wt% ZrF₄ (electrorefining initiator, Hf <0.1 wt%). It had a calculated efficiency of 57%.

As can be seen from the above examples, most techniques are limited to analytical use and, however successful, some are not as well suited and easily implemented as others. The purpose of this study was to investigate the separation of Zr and Hf by means of SX, specifically focusing on the interaction of the organophosphorus extractant Ionquest 801 with feed concentrations (≥ 1 g/l ZrCl₄ containing 3 wt% HfCl₄) that exhibits extraction behaviour approximately representative of more concentrated (industrial) feed streams (≥ 10 g/l ZrCl₄ containing 3 wt% HfCl₄). The influence of various additives as a means to reverse the obtained selectivities was also studied.

Materials and methods

Materials and general procedure

Deionized water (pH 7.5) was used throughout (Millipore Milli-Q Plus[®] Q-pack CPMQ004R1) and all reagents were of analytical grade (see Table I). An aqueous feed was prepared by dissolving 1 g/l ZrCl₄ plus 3 wt% HfCl₄ in HNO₃ or H₂SO₄ and ageing for 24 hours prior to extraction. The solvent consisted of cyclohexane (diluent), 5% v/v 1-octanol (modifier) and Ionquest 801 at a concentration of 5 wt% relative to the diluent. The two phases were contacted for 60 minutes in polypropylene containers at temperatures of $26 \pm 4^\circ\text{C}$ at an organic to aqueous (O/A) volume ratio of unity using a batch extraction set-up with a mechanical agitator oscillating at 330 r/min. All extractions were done in triplicate and the average values noted with a 10% relative error. The Zr and Hf concentrations of the feed were determined before and after extraction using ICP-OES (Thermo Scientific iCAP 6000 Series spectrometer and CETAC ASX 520 Autosampler).

Methods

Influence of HNO₃ concentration

Using the general procedure described above, the influence of the HNO₃ concentration on the extraction performance of Ionquest 801 was determined at $[\text{HNO}_3] = 0.01\text{--}5.0$ M.

Solvent extraction and separation of hafnium from zirconium using Ionquest 801

Table 1

Reagents and suppliers

Reagent	Supplier
HfCl ₄ (98%)	Sigma Aldrich (Cas: 13499-05-3)
ZrCl ₄ (99.5%, < 50 ppm Hf)	Sigma Aldrich (Cas: 10026-11-6)
HNO ₃ (55%)	Merck
H ₂ SO ₄ (95–99%)	Merck
1-octanol	Sigma Aldrich (Cas: 111-87-5)
Cyclohexane	Monitoring & Control Laboratories (Pty) Ltd
Ionquest 801 (2-ethylhexyl phosphonic acid mono-2-ethylhexyl ester)	Chemquest
D2EHPA (di-(2-ethylhexyl)phosphoric acid)	Sigma Aldrich (Cas: 298-07-7)
NaCl (99.5%)	Associated Chemical Enterprises (Cas: 7647-14-5)
NaNO ₃ (99.0%)	Minema
Na ₂ SO ₄ anhydrous AR (99%)	Minema
NaClO ₄ ·H ₂ O (98–100%)	Riedel-de Haën (Cas: 7791-07-3)
Mandelic acid (99%)	Sigma Aldrich (Cas: 90-64-2)
L-(+)-tartaric acid (≥99.5%)	Sigma Aldrich (Cas: 87-69-4)
Citric acid (99%)	Sigma Aldrich (Cas: 77-92-9)
Oxalic acid (98%)	Sigma Aldrich (Cas: 144-62-7)
H ₂ O ₂ (30%)	Rochelle Chemicals

Influence of Ionquest 801 concentration

Subsequently, the extraction performance of Ionquest 801 was determined at E:M_{Zr} ratios from 0.1:1 to 20:1 in both 0.7 and 3 M HNO₃.

Influence of carboxylic acids

The extraction performance of Ionquest 801 was determined with additions of 0.1 M tartaric, oxalic, mandelic, and citric acid in 0.7 M HNO₃ and at an E:M_{Zr} ratio of 5:1.

Influence of carboxylic acids in the presence of H₂O₂

The extraction performance of Ionquest 801 was determined with the addition of 6 wt% H₂O₂ and 0.1 M tartaric, oxalic, mandelic, and citric acid, in 0.7 M HNO₃ and at an E:M_{Zr} ratio of 5:1.

Influence of salting-out agents

After optimization of the acid and extractant concentration, the extraction performance of Ionquest 801 was determined with additions of 1.5 M NaCl, NaNO₃, Na₂SO₄, and NaClO₄·H₂O in 0.7 M HNO₃ and at an E:M_{Zr} ratio of 5:1.

Influence of SO₄²⁻ concentration in 0.35 M H₂SO₄

The extraction performance of Ionquest 801 was determined with the addition of 0–1.05 M Na₂SO₄ in 0.35 M H₂SO₄ at an E:M_{Zr} ratio of 5:1.

Influence of H₂O₂ in 0.35 M H₂SO₄

The extraction performance of Ionquest 801 was determined with additions of 0.6, 1.2, 1.8, 2.4, and 3 wt% H₂O₂ in 0.35 M H₂SO₄ and at an E:M_{Zr} ratio of 5:1.

Influence of E:M_{Zr} in 0.35 M H₂SO₄

The extraction performance of Ionquest 801 was determined at E:M_{Zr} ratios of 1:1 to 10:1 in 0.35 M H₂SO₄.

Results and discussion

Influence of HNO₃ concentration

From Figure 1, it is clear that the extraction of both metal complexes remained above 97% over the entire acid concentration range (0–5 M). Although the unselective and high extraction attained could be ascribed to the excess of Ionquest 801 (5 wt%) used, the results clearly show that Ionquest 801 can extract the metal complexes of both Zr and Hf and is thus suitable for further study. It is important to note, however, why this system was chosen to start with. The choice of acid, extractant, and ageing are explained in the paragraphs that follow.

The following are important aspects to consider when optimizing an SX system: type of extractant, ageing, type of acid, and the metal concentration in the feed. Lee *et al.* (2015) studied two SX systems, consisting of Cyanex 272 and D2EHPA (each 0.01–0.07 M) in 2, 4 and 6 M H₂SO₄ solutions for different Zr/Hf ratios. They found that both systems selectively extracted Hf over Zr, irrespective of the

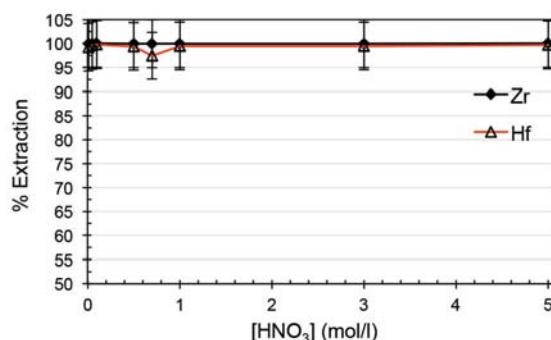


Figure 1—Extraction of Zr and Hf as a function of HNO₃ concentration

Solvent extraction and separation of hafnium from zirconium using Ionquest 801

Zr:Hf ratio (1:1–100:1) with all feed solutions containing 0.2 g/l Hf and the corresponding amount of Zr. Studies have shown that Ionquest 801 not only has a similar structure to D2EHPA, but also similar extraction behaviour. Peppard *et al.* (1969) found that Ionquest 801 showed significantly higher extraction of U(VI) compared to D2EHPA. In addition, high extraction has been observed in less acidic environments, with less emulsion formation and improved stripping. Furthermore, Ionquest 801 was used successfully for the separation of higher valence elements or heavy rare earth elements (REE) as well as for group separations of mixtures containing large amounts of heavy REE (Otu and Westland, 1990). It is for these reasons that the separation of Zr and Hf was investigated using Ionquest 801.

The reason for ageing the acidic aqueous feed solution was as follows. Zr/Hf and Ta/Nb systems are similar in that they are neighbouring groups in the same period of the periodic table of elements. While the speciation of these complexes in solution is unknown, research on the SX of the ammonium hexafluorides ($\text{NH}_4\text{Ta}(\text{Nb})\text{F}_6$) of tantalum (Ta) and niobium (Nb) with D2EHPA and PA in H_2SO_4 medium has clearly shown the influence of time on extraction (De Beer *et al.*, 2014). Although D2EHPA in H_2SO_4 medium exhibited preferential extraction of Ta over Nb, as in Hf extraction over Zr with similar conditions as described above, the amount extracted ($\%_{\text{Ta}}$) was stable for only 3.5 hours after acidification of the feed before decreasing from 96 $\%_{\text{Ta}}$ to 30 $\%_{\text{Ta}}$ after 24 hours. In view of the similarity between the Ta/Nb and the Zr/Hf systems, all feed solutions in this study were hence aged for 24 hours before contact with the solvent. This ensures that the feed (solvated complexes) speciation is representative of leach liquors at chemical equilibrium.

The literature indicates that the use of the more corrosive H_2SO_4 is favourable. However, HNO_3 was chosen to determine whether the manipulation of the SX system with salting-out agents could lead to acceptable extraction values. This would increase safety and applicability to other technologies, *e.g.* membrane-based solvent extraction (MBSX). The study was conducted on a macroscopic scale with respect to metal concentrations, conditions that would conceivably be encountered on an industrial scale. Hence feed concentrations ≥ 1 g/l (ZrCl_4) containing 3–5 wt% HfCl_4 (relative to ZrCl_4) were used and assumed to exhibit extraction characteristics representative of more concentrated (industrial) feed streams.

Influence of Ionquest 801 concentration

As no substantial selectivity was obtained towards either complex, irrespective of the concentration of the HNO_3 (see Figure 1), the influence of Ionquest 801 concentration on the extraction was investigated at both low (0.7 M HNO_3) and high (3.0 M HNO_3) acidities. The results are presented in Figures 2 and 3 respectively.

At 0.7 M HNO_3 , it is clear that there was an initial near-linear increase in extraction with increasing E: M_{Zr} ratio. It is also apparent that Ionquest 801, at low E: M_{Zr} ratios, preferentially extracted Zr, attaining a maximum Zr extraction (near 100%) at an E: M_{Zr} ratio of 5:1. Only when the E: M_{Zr} ratio reached 15:1 was complete extraction of Hf observed. This extraction remained practically unchanged for Zr at both acidities, with Hf extraction at an E: M_{Zr} ratio of 5:1

increasing from 55% at 3 M to 77% at 0.7 M. Wang and Lee (2014) reported similar findings using PC-88A (the same compound as Ionquest 801, obtained from Cytec Canada) in HNO_3 . Varying the PC-88A concentration at 2 M HNO_3 produced a graph exhibiting the same characteristics as those in Figures 2 and 3. Zr extracts preferentially, as shown by the steeper slope, with Hf extraction following roughly the same trend but with lower extraction, until a suitable extractant concentration is reached and both metals extract completely. Direct comparison is, however, not possible as the feed concentrations differed from this study (0.2 g/l Zr + 0.2 g/l Hf vs. 1 g/l ZrCl_4 + 3 wt% HfCl_4). As a higher selectivity is preferred, the conditions of 0.7 M HNO_3 with an E: M_{Zr} ratio of 5:1 were chosen for further optimization.

Influence of carboxylic acids

Table II shows the effect of four different acidic additives to Ionquest 801 on the extraction of Zr and Hf. The addition of mandelic acid to the 0.7 M HNO_3 feed resulted in the complete precipitation of both metal complexes (99.9% $_{\text{Metal}}$ precipitation in feed). Tartaric and citric acid both suppress Zr extraction more than Hf, by a factor of 1.46 and 1.54 respectively. The addition of oxalic acid to the feed rendered both complexes unextractable. These results are surprising, as carboxylic acids and mixtures thereof are often used as extractants themselves (Lee *et al.*, 2004), which would suggest that addition of these acids would increase extraction. The mechanism reported by Lee *et al.* (2004) was the solvation of the metal complex by two molecules of Versatic acid 10. This would most likely be dependent on the variety of extraction mechanisms present and competition

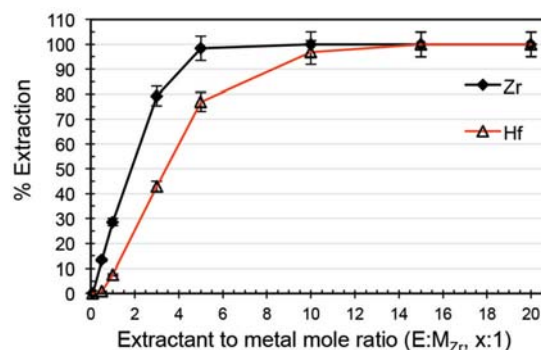


Figure 2—Extraction as a function of Ionquest 801 concentration at 0.7 M HNO_3

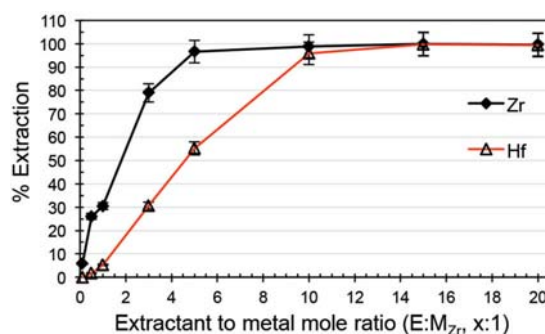


Figure 3—Extraction as a function of Ionquest 801 concentration at 3 M HNO_3

Solvent extraction and separation of hafnium from zirconium using Ionquest 801

between them. The use of carboxylic acids does, however, seem to be beneficial considering the outcome of the study conducted by Das *et al.* (1981). They used radio tracers ($^{175,181}\text{Hf}$, ^{95}Zr) to optimize a SX system consisting of 0.08 M H_2SO_4 , 0.1 M carboxylic acid, 6 wt% H_2O_2 , and 0.01 M D2EHPA in carbon tetrachloride (CCl_4). After extraction with mineral acids, the extraction performance of D2EHPA with organic acids was tested. They found that all the carboxylic acids tested resulted in increased extraction relative to the mineral acids previously tested, including HCl and HF. In their study, the extractions on the carboxylic acids were carried out in the absence of other acids. Cumulatively, each additive resulted in an Hf-selective SX system, which could be of significance if the principles are applicable to high feed concentrations.

Influence of carboxylic acids in the presence of H_2O_2

The experiments presented above were repeated with the addition of 6% H_2O_2 (Table III) to the aqueous phase. With H_2O_2 added, tartaric, mandelic, and citric acid formed organic emulsions after contact with the solvent (organic phase). Only oxalic acid produced results that were similar to those obtained without the addition of H_2O_2 (see Table II).

Das *et al.* (1981) found that the addition of H_2O_2 decreases the extraction of Zr, while the Hf extraction remains unchanged. This effect was most prominent for HClO_4 ($\%_{\text{Zr}}/\%_{\text{Hf}} = 15/63$) and H_2SO_4 ($\%_{\text{Zr}}/\%_{\text{Hf}} = 7/72$). They ascribed the inability of D2EHPA to extract Zr in the presence of H_2O_2 to the fact that at low acidities, the tendency of Zr to polymerize is greater than that of Hf. The proposed metal species formed under these conditions is a highly aggregated complex consisting of Zr metal atoms connected *via* stable oxygen bonds as bridges between the metal centres. These bridges lead to the formation of Zr aggregates that are unextractable by the extractant. Considering the strong similarities between Zr and Hf, it is likely that smaller Hf aggregates do form, but to a lesser extent. It is likely that these Hf aggregates lead to the formation of emulsions and third phases in the solvent, as the higher feed concentrations enable the formation of larger quantities thereof. The precipitation in the feed, however, is assumed to be due to hydrolysis after the aggregation process is saturated (see section below on the influence of H_2O_2 where the extent of the feed precipitation was determined). Thus it seems that the aqueous phase can accommodate both aggregates, with the much smaller Hf aggregates capable of migration to the solvent through extraction with Ionquest 801. The experimental confirmation of this falls, however, beyond the scope of this paper.

Influence of salting-out agents

It is known that reaction additives can have a significant effect on the speciation (and hence extraction characteristics) of a metal complex. This principle dates as far back as Le Chatelier, who stated that a system will rearrange itself (partially) to counteract the change in pressure, volume, temperature, or concentration imposed upon it (Kotz and Treichel, 2003). Thus as soon as ions are introduced, the chemical equilibria change, which can be used to influence the SX system. This was demonstrated by Das *et al.* (1981), who studied the extraction of radio tracers ($^{175,181}\text{Hf}$, ^{95}Zr)

with D2EHPA in the presence of various mineral acids. The presence of SO_4^{2-} ions in the feed enables Zr to form strongly bonded complexes compared to other ions (NO_3^- , Cl^- , ClO_4^-), resulting in a decrease in extraction. The best Hf selectivity was reported using the mineral acids H_2SO_4 , HClO_4 , and HNO_3 . As dissociated acids release protons and anions, the addition of salting agents might produce the same effect if it is assumed that the acids dissociate completely. To study this, the influence of NaCl , NaNO_3 , Na_2SO_4 , and NaClO_4 was evaluated.

It is clear from Table IV that the best results in terms of an inverse Hf selectivity were achieved with the addition of 1.5 M Na_2SO_4 . It is interesting to note that an increase in NO_3^- concentration from 0.7 M HNO_3 to 2.2 M (0.7 M HNO_3 + 1.5 M NaNO_3) resulted in a suppression of Hf extraction ($\Delta\%_{\text{Hf}} = -16.2$) by a factor of 2.84, compared to Zr extraction ($\Delta\%_{\text{Zr}} = -5.7$). Conversely, the addition of 1.5 M Na_2SO_4 to the feed suppressed Zr extraction over Hf extraction by a factor of 1.56, even in the presence of 0.7 M NO_3^- . As nitrate anions suppress Hf extraction preferentially, the use of nitrate was excluded from this study.

Table II
Extraction with carboxylic additives in 0.7 M HNO_3 at an E: M_{Zr} ratio of 5:1

	Zr, %	ΔZr	Hf, %	ΔHf
No additives	98.4	-	77	-
0.1 M mandelic acid	-	-	-	-a
0.1 M tartaric acid	18.9	-79.5	22.5	-54.5
0.1 M citric acid	22.4	-76.0	27.6	-49.4
0.1 M oxalic acid	0	-98.4	0	-77.0

Table III
Extraction with carboxylic acid and H_2O_2 in 0.7 M HNO_3 at an E: M_{Zr} ratio of 5:1

	Zr, %	ΔZr	Hf, %	ΔHf
No additives	98.4	-	77	-
0.1 M oxalic acid + 6% H_2O_2	0	-98.4	0.6	-76.4
0.1 M tartaric acid + 6% H_2O_2	-	-	-	-
0.1 M citric acid + 6% H_2O_2	-	-	-	-
0.1 M mandelic acid + 6% H_2O_2	-	-	-	-

Table IV
Extraction with the addition of salting-out agents in 0.7 M HNO_3 and an E: M_{Zr} ratio of 5:1

	Zr, %	ΔZr	Hf, %	ΔHf
No additives	98.4	-	77	-
1.5 M NaCl	99.7	1.3	80.7	3.7
1.5 M NaNO_3	92.7	-5.7	60.8	-16.2
1.5 M Na_2SO_4	15.3	-83.1	23.7	-53.3
1.5 M $\text{NaClO}_4 \cdot \text{H}_2\text{O}$	84.4	-14.0	54.7	-22.3

Solvent extraction and separation of hafnium from zirconium using Ionquest 801

Influence of SO_4^{2-} concentration in 0.35 M H_2SO_4

In view of the above results it was decided to investigate the characteristics of an H_2SO_4 -based system instead of the hitherto-used HNO_3 system. To maintain the same H^+ concentration (0.7 M) the H_2SO_4 was used at 0.35 M. Considering the dominating strength (in terms of anion displacement and complex stability) of sulphate anion complexes and the polymerization characteristics of Zr and Hf at low acidities, ascribing the extraction or lack thereof to any single cause is difficult and beyond the scope of this study. The nature and extent of the polymerization of these metals at low acidities are unknown, and thus the extraction percentage will be considered as the outcome of the cumulative effects of the phenomena present. As can be seen from Figure 4, the presence of H_2SO_4 resulted in an inverse selectivity in favour of Hf. Extraction of the metal complexes at these conditions led to an extraction difference of roughly 13% in favour of Hf, with a Hf extraction of 39% and Zr 26%. It is clear that increasing the sulphate concentration above 0.35 M, as dissociated Na_2SO_4 , decreased the separation and recovery. The resultant drop in extraction for Hf (from 0.35 M SO_4^{2-} to 0.7 M) is almost double that of Zr, as the equilibrium driving forces alter the speciation.

This is in good agreement with the results of Banda *et al.* (2013). Although the experimental conditions varied somewhat in that the feed contained 0.2 g/l Zr and Hf, and D2EHPA was used as extractant, as previously mentioned, D2EHPA and Ionquest 801 have similar extraction behaviours. It is clear from the results of Banda *et al.* that increased extraction and separation is attained at low acidities (<2 M H_2SO_4) rather than high acidities. Note that at low acidities (0.5 M H_2SO_4) the extraction of Hf is roughly double that of Zr, even for the feed (1 g/l $\text{ZrCl}_4 + 3 \text{ wt}\% \text{HfCl}_4$) used with Ionquest 801 at 0.35 M H_2SO_4 .

From a structural analysis point of view, Hu *et al.* (2013) combined high-energy X-ray scattering (HEXS), Raman spectroscopy, and mathematical manipulations such as Fourier transformations and Gaussian curves to obtain partial pair distribution functions (PDFs). These PDFs show only those correlations involving Zr (specifically including those with complexed species, solvent molecules, and other solute ions) and represent electron counts in Zr ion correlations, enabling possible species to be characterized and elucidated according to relative intensities. Hu *et al.* (2013, Figure 4) plotted changes in the integrated intensities of selected PDF

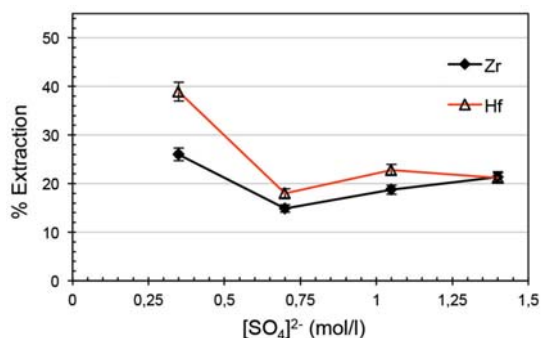


Figure 4—Extraction as a function of sulphate concentration in 0.35 M H_2SO_4 at an $\text{E}:\text{M}_{\text{Zr}}$ ratio of 5:1

peaks (3.56, 4.97, and 6.7 Å) as a function of the total sulphate concentration in solution. All three peaks increase in intensity up to $[\text{SO}_4^{2-}] = 0.5 \text{ M}$ with the peaks at 4.97 and 6.7 Å having roughly the same intensity and that of 3.56 Å being 2–2.5 times more intense. Hu *et al.* (2013) interpret this as follows: 'This behavior is suggestive of changing average cluster size across the series, increasing with increasing sulfate concentration up to 0.5 m in sulfate, and slowly decreasing with higher sulfate concentration.' This then lends merit to the notion that these larger complex clusters may be harder to extract and is likely the reason why extraction is more successful at low acidities and low sulphate concentrations.

Influence of H_2O_2 in 0.35 M H_2SO_4

Addition of $\geq 2.4\%$ v/v H_2O_2 (as the only additive) to the 0.35 M H_2SO_4 feed led to the formation of aqueous precipitates (after 24 hours ageing). Addition of $\leq 1.8\%$ v/v H_2O_2 led to the formation of emulsions after solvent contact. The extent of precipitation was determined in the range of 2.4–4.8% v/v H_2O_2 . The percentage Hf precipitated (11.8–40.3%) is roughly double that of Zr (5.2–25%). It is clear that Hf is hydrolysed more readily than Zr, which is considered to be highly aggregated in this environment. This lends credibility to the notion that at these low acidities the speciation of Zr and Hf differs. Thus the capability of H_2O_2 to influence the system and metal complex speciation is a dominant process that should be studied further. The formation of stable aggregates, monomers, and dimers (whether from H_2O_2 aggregate formation or sulphate-induced polymerization) provide an opportunity for increasing the selectivity of a process, as these might be harder to extract *via* certain mechanisms. For example, ion exchange requires the exchange of ions between the extractant and the complex, which would not occur if the complex were too stable for this process. The processes of polymerization and aggregation, as well as the extent thereof, are not well documented for Zr and Hf systems. However, the data presented gives some support to these principles.

We refer again to the system referenced throughout this article. Das *et al.* (1981) used tartaric acid in their system (0.08 N H_2SO_4 , 0.1 M tartaric acid, 6 wt% H_2O_2 , and 0.01 M D2EHPA in CCl_4) and observed the preferential extraction of $^{175,181}\text{Hf}$ over ^{95}Zr (radio tracers) with extraction percentages of 100% and 1–2% respectively. This shows that the suppressive effects of H_2O_2 and sulphate anions can restrict the extraction of Zr, while the tartaric acid seems to facilitate Hf extraction. These principles seem to be plausible and warrant further investigation.

Influence of $\text{E}:\text{M}_{\text{Zr}}$ in 0.35 M H_2SO_4

To improve the recovery and re-evaluate the selectivity at the new parameters obtained from the experiment on the influence of SO_4^{2-} concentration, the extraction performance of Ionquest 801 was determined over a wider range of $\text{E}:\text{M}_{\text{Zr}}$ values.

A comparison of the extraction values in Figure 4 and Figure 5 shows that the selectivity of the process decreased slightly from $\Delta\%_{\text{E}} = 13\%$ ($\text{E}:\text{M}_{\text{Zr}} = 5:1$ in 0.35 M H_2SO_4 with no addition of Na_2SO_4) to $\Delta\%_{\text{E}} = 10\%$ ($\text{E}:\text{M}_{\text{Zr}} \geq 3:1$ in 0.35 M H_2SO_4). The difference in maximum extraction values at

Solvent extraction and separation of hafnium from zirconium using Ionquest 801

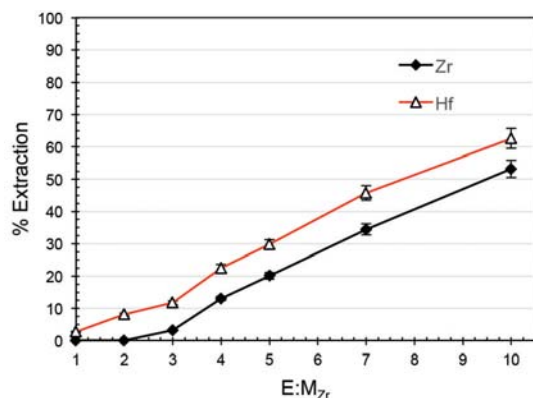


Figure 5—Extraction as a function of E:M_{Zr} ratio in 0.35 M H₂SO₄

corresponding points (E:M_{Zr} = 5:1) of these two figures are most likely due to the values of Figure 5 having been obtained at lower extraction temperatures. From this data it is evident that an E:M_{Zr} ratio 10:1 is already sufficient, with more than 60% Hf extraction.

Conclusions

When using HNO₃, higher extraction of Hf was attained at an E:M_{Zr} ratio of 5:1 in 0.7 M HNO₃ than in 3 M HNO₃, with an extraction of 77%_{Hf} and 55.2%_{Hf} respectively. Zr extraction remained constant ($\geq 97\%$ _{Zr}) at both acidities. Conditions favouring Hf extraction (E:M_{Zr} ratio of 5:1 in 0.7 M HNO₃) were therefore set as the basis of the SX system and further investigated. Addition of 1.5 M Na₂SO₄ to the system suppressed Zr extraction preferentially ($\Delta\%_{Zr} = -83.1$) to a value of 15.3%_{Zr}, while Hf extraction decreased to 23.7%_{Hf} ($\Delta\%_{Hf} = -53.3$). Addition of 1.5 M NaNO₃ to the system suppressed Hf extraction preferentially ($\Delta\%_{Hf} = -16.2$) to a value of 60.8%_{Hf}, while Zr extraction merely decreased to 92.7%_{Zr} ($\Delta\%_{Zr} = -5.7$). This indicated that NO₃⁻ ions are detrimental to Hf extraction and should be excluded from the SX system, while SO₄²⁻ ions are detrimental to Zr extraction and could be used to suppress Zr extraction preferentially. Nitrate ions were excluded, while maintaining the acidity and sulphate ions, by addition of protons and sulphate ions as H₂SO₄ and Na₂SO₄. The best salting-out agent tested was Na₂SO₄, which was used for further optimization. Carboxylic acids have a suppressive effect (in 0.7 M HNO₃) on extraction, favouring Hf extraction. However, this may change significantly with the use of H₂SO₄ and addition of H₂O₂. It was shown that low acidity (0.7 M H⁺ with the use of 0.35 M H₂SO₄) resulted in the highest selectivity and recovery of Hf. However, the use of H₂O₂ led to feed precipitation or emulsions forming in this batch SX process. The use of a hollow-fibre membrane (MBSX) would avoid emulsions, enabling the use of H₂O₂. In addition, the influence of higher E:M_{Zr} ($\geq 5:1$) ratios was investigated on the optimized system containing only 0.35 M H₂SO₄. An E:M_{Zr} ratio of 10:1 was sufficient to obtain $\geq 50\%$ extraction of the solute of interest with a trivial change in selectivity. Acidities below 1.5 M H⁺ (via addition of HCl) and anion concentrations below 0.35 M [SO₄²⁻] could be further investigated to maximize Hf recovery and possibly increase selectivity.

References

- AKL, M.A., KABIL, M.A., ABDALLAH, A.M., and ISMAIL, D.S. 2001. Use of eriochrome cyanine R for separation-flotation and microdetermination of hafnium and zirconium in real samples. *Separation Science and Technology*, vol. 36, no. 12. pp. 2747–2760.
- BANDA, R. and LEE, M.S. 2015. Solvent extraction for the separation of Zr and Hf from aqueous solutions. *Separation and Purification Reviews*, vol. 44, no. 3. pp. 199–215.
- BANDA, R., MIN, S.H., and LEE, M.S. 2013. Selective extraction of Hf(IV) over Zr(IV) from aqueous H₂SO₄ solutions by solvent extraction with acidic organophosphorous based extractants. *Journal of Chemical Technology and Biotechnology*, vol. 89, no. 11. pp. 1712–1719.
- BELOUSOVA, E., GRIFFIN, W.L., O'REILLY, S.Y., and FISHER, N. 2002. Igneous zircon: trace element composition as an indicator of source rock type. *Contributions to Mineralogy and Petrology*, vol. 143, no. 5. pp. 602–622.
- CHADWICK, M.B., HERMAN, M., OBLOŽINSKÝ, P., DUNN, M.E., DANON, Y., and KAHLER, A.C. et al. 2011. ENDF/B-VII.1 Nuclear Data for Science and Technology: Cross Sections, Covariances, Fission Product Yields and Decay Data. *Nuclear Data Sheets*, vol. 112, no. 12. pp. 2887–2996.
- DAS, N.R., NANDI, B., and BHATTACHARYYA, S.N. 1981. Sequential separation of hafnium, zirconium and niobium from sulphuric acid medium using di(2-ethylhexyl) phosphoric acid as an extractant. *International Journal of Applied Radiation and Isotopes*, vol. 32, no. 4. pp. 205–209.
- DE BEER, L., UNGERER, M.J., VAN DER WESTHUIZEN, D.J., and KRIEG, H.M. 2014. The time dependent solvent extraction of Ta and Nb. *Advanced Materials Research*. <http://www.scientific.net/AMR.1019.433>
- FRITZ, J.S. and FRAZEE, R.T. 1965. Reversed-phase chromatographic separation of zirconium and hafnium. *Analytical Chemistry*, vol. 37, no. 11. pp. 1358–1361.
- HU, Y.-J., KNOPE, K.E., SKANTHAKUMAR, S., KANATZIDIS, M.G., MITCHELL, J.F., and SODERHOLM, L. 2013. Understanding the role of aqueous solution speciation and its application to the directed syntheses of complex oxidic Zr chlorides and sulfates. *Journal of the American Chemical Society*, vol. 135, no. 38. pp. 14240–14248.
- KOTZ, J.C. and TREICHEL, J.P.M. 2003. *Chemistry and Chemical Reactivity*. 5th edn. Thomson Learning. 997 pp.
- LEE, H.Y., KIM, S.G., and OH, J.K. 2004. Stoichiometric relation for extraction of zirconium and hafnium from acidic chloride solutions with Versatic acid 10. *Hydrometallurgy*, vol. 73, no. 1–2. pp. 91–97.
- LEE, M.S., BANDA, R., and MIN, S.H. 2015. Separation of Hf(IV)–Zr(IV) in H₂SO₄ solutions using solvent extraction with D2EHPA or Cyanex 272 at different reagent and metal ion concentrations. *Hydrometallurgy*, vol. 152, no. 0. pp. 84–90.
- LI, H., NERSISYAN, H.H., PARK, K.-T., PARK, S.-B., KIM, J.-G., LEE, J.-M., and LEE, J.-H. 2011. Nuclear-grade zirconium prepared by combining combustion synthesis with molten-salt electrorefining technique. *Journal of Nuclear Materials*, vol. 413, no. 2. pp. 107–113.
- NIKULINA, A.V. and MALGIN, A.G. 2008. Impurities and their effect on the structure and properties of zirconium parts in nuclear reactors. *Atomic Energy*, vol. 105, no. 5. pp. 328–339.
- OTU, E.O. and WESTLAND, A.D. 1990. Solvent extraction with organophosphonic mono-acidic esters. *Solvent Extraction and Ion Exchange*, vol. 8, no. 6. pp. 759–781.
- PEPPARD, D., MASON, G., and LEWEY, S. 1969. A tetrad effect in the liquid-liquid extraction ordering of lanthanides (III). *Journal of Inorganic and Nuclear Chemistry*, vol. 31, no. 7. pp. 2271–2272.
- PORIEL, L., CHITRY, F., PELLET-ROSTAING, S., LEMAIRE, M., and FAVRE-RÉGUILLON, A. 2006. Zirconium and hafnium separation, Part 3. Ligand-enhanced separation of zirconium and hafnium from aqueous solution using nanofiltration. *Separation Science and Technology*, vol. 41, no. 13. pp. 2883–2893.
- SMOLIK, M., JAKÓBIK-KOLON, A., and PORÁNSKI, M. 2009. Separation of zirconium and hafnium using Diphonix® chelating ion-exchange resin. *Hydrometallurgy*, vol. 95, no. 3–4. pp. 350–353.
- SPEER, J.A.C. and COOPER, B. J. 1982. Crystal structure of synthetic hafnon, HfSiO₄, comparison with zircon and the actinide orthosilicates. *American Mineralogist*, vol. 67. pp. 804–808.
- WANG, L.Y. and LEE, M.S. 2014. Separation of zirconium and hafnium from nitric acid solutions with LIX 63, PC 88A and their mixture by solvent extraction. *Hydrometallurgy*, vol. 150, no. 0. pp. 153–160. ◆

New technology and innovation in the Minerals Industry Colloquium

Driving mining productivity improvement through technology and innovation

9–10 June 2016 • Mintek, Randburg



BACKGROUND

The South African mining industry finds itself at a crossroads where current levels of productivity and safety, which are driven by current mining methods, will no longer be either socially or economically acceptable.

The future competitiveness of the Southern African mining industry depends on the application of appropriate and workable technologies, as well as innovative mining methods, that improve safety and productivity. These will be based on process based organisations that are enabled and empowered by increasing levels of real time data and information integrated across the value chain.

This event is aimed at presenting examples of how technology can improve the costs and competitiveness of the SA Mining industry, within the next 10 years and technology that is in use now. Not only will it draw on case studies and examples of technology development, but it will also explore innovative ways of applying state of the art technologies from other sectors, to the mining environment.

OBJECTIVES

To showcase, explain and demonstrate the potential for operational improvement through innovative but practical technological solutions aimed at improvements in quality, output and productivity.

It is also aimed at achieving a common vision of 'the art of the possible' as well as exploring new paradigms for mining in the future.

WHO SHOULD ATTEND

- Mine managers
- Operational managers
- Mine engineers
- Mine planners
- Geologists
- Mining technical staff
- Technical information specialists
- Consultants
- Contractors
- Students
- Academics
- Researchers

EXHIBITION/SPONSORSHIP

Sponsorship opportunities are available. Companies wishing to sponsor or exhibit should contact the Conference Co-ordinator.

SPONSORS:

CIDRA
Minerals Processing

MINTEK
A global leader in mineral and metallurgical innovation



New Concept Mining

For further information contact:
Conference Co-ordinator, Camielah Jardine
SAIMM, P O Box 61127, Marshalltown 2107
Tel: (011) 834-1273/7
Fax: (011) 833-8156 or (011) 838-5923
E-mail: camialah@saimm.co.za
Website: <http://www.saimm.co.za>



SAIMM
THE SOUTHERN AFRICAN INSTITUTE
OF MINING AND METALLURGY



Conference Announcement & Call for Papers/Presentations



Insights into the potential for reduced refractory wear in silicomanganese smelters

by J.D. Steenkamp*, P.C. Pistorius†, and J. Muller‡

Synopsis

Excavation of an industrial-scale submerged arc furnace, utilized in the production of silicomanganese, identified two high-wear areas in the refractory lining: the tap-hole, built with cold rammed carbon paste and SiC bricks, and the hearth, built with cold rammed carbon paste. To obtain insight into the potential causes of wear, thermodynamic calculations were conducted on eight sets of data, obtained for seven furnaces on three plants based in South Africa. FACTSage software and associated databases – FACTPS, FToxid, and FSstel – as well as the Mn-Fe-Si-C database of Tang and Olsen (2006), were applied. Theoretical indications are that chemical reaction between carbon refractory and slag, as well as dissolution of carbon and SiC refractory in metal, contributed to tap-hole refractory wear; and dissolution of carbon in metal contributed to hearth refractory wear.

Keywords

tap-hole, silicomanganese, submerged arc furnace, refractory, refractory wear, FactStage.

Introduction

During the excavation of a 48 MVA submerged arc furnace (SAF) used for silicomanganese (SiMn) production, it was found that the tap-hole and hearth were high refractory wear areas (Steenkamp, 2014). In both these high-wear areas, carbon-based cold ramming paste formed the hot face refractory lining (crucible). The wear profile of this SAF is presented in Figure 1.

The hot face refractory lining was formed by cold ramming of high-grade carbon ramming material. This material consisted of 50–70% anthracite, 15–25% graphite, 6–12% resin, 2–7% tar, 1–5% clay, and 1–5% alumina. The tap-hole was built using SiC bricks, consisting of 75% SiC, 23.4% Si₃N₄, 0.3% Fe₂O₃, 0.3% Al₂O₃, and 0.2% CaO.

In the tap-hole area, the wear of the SiC refractory material was estimated at 0.4 t, and that of the high-grade carbon ramming material, at 1.9 t (Steenkamp, Pistorius, and Tangstad, 2015). The amounts of slag and metal tapped during six years of operation of the tap-hole (September 2007 to April 2013) were estimated at 33 088 t (Steenkamp *et al.*, 2015) and 41 360 t, respectively.

The original thickness of the high-grade carbon ramming paste installed in the hearth was 850 mm, of which a minimum of 600 mm was seen to remain after ten years of operation (April 2003 to April 2013). Over the lifetime of the hearth refractory, 384 000 t of SiMn metal was tapped from the furnace (Gous, 2015).

The difference in metal exposure of hearth and tap-hole is due to the fact that the furnace had two single-level tap-holes, and that the tap-holes were rebuilt during the lifetime of the hearth refractory. Further details of the refractory design, and history of operations have been discussed elsewhere (Steenkamp *et al.*, 2014, 2015; Steenkamp, 2014).

Analysis of the potential for chemical wear in the tap-hole area of the SAF excavated in 2013 (Figure 1) was included in a larger study on tap-hole wear in SAFs producing SiMn (Steenkamp, 2014). In that study the potential for chemical reaction between slag (and metal) and refractory materials being responsible for wear in a single-level tap-hole where slag and metal are tapped typically at 1600°C was tested.

It was previously established that reaction between silicomanganese slag and carbon-based tap-hole refractory is possible (Steenkamp, 2014). Predictions by thermodynamic calculations were supported by laboratory-scale experiments with nominally pure materials as well as industrial materials (Steenkamp, 2014), as reaction products SiC and SiMn droplets formed. For the reaction of C-based refractory with slag, if the SiC

* Mintek, Randburg South Africa.

† Carnegie Mellon University, Pittsburgh PA USA.

‡ EXXARO Resources, Pretoria West, South Africa.

© The Southern African Institute of Mining and Metallurgy, 2016. ISSN 2225-6253. Parts of this paper was first presented at, INFACON XIV, Kyiv, Ukraine.

Insights into the potential for reduced refractory wear in silicomanganese smelters

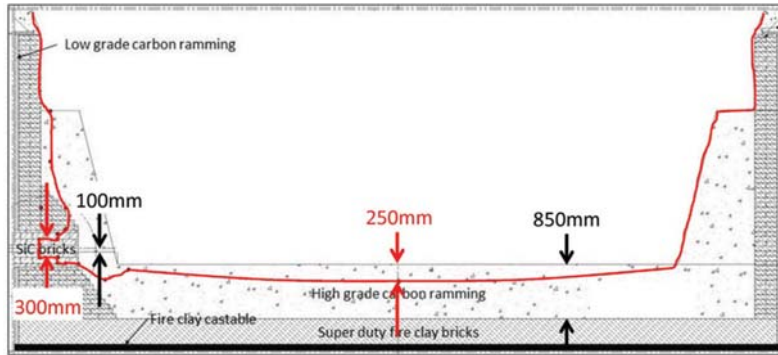


Figure 1 – Refractory wear profile of a 48 MVA SAF, used for SiMn production, excavated in 2013 in South Africa. The red line indicates the refractory hot face, as determined during excavation

reaction product were to form an *in situ* refractory layer at the slag/refractory interface, the potential for refractory wear by chemical reaction would be reduced (Lee and Moore, 1998). However, in all laboratory-scale experiments conducted, the SiC that formed detached from the surface of the carbon-based refractory (Steenkamp, 2014), as was found by others (Mølnås, 2011). Thermodynamic calculations on the industrial materials applied, and produced, in the SAF excavated in 2013 (Figure 1) supported the observation that reaction between silicomanganese slag, and carbon-based tap-hole refractory is possible. Mass transfer calculations (SiO₂ only) indicated that chemical reaction would not be the only wear mechanism applicable.

The previous study (Steenkamp, 2014) focused primarily on refractory/slag interaction. The thermodynamic calculations in that study were based on published slag and metal compositions, as well as plant data for the SAF excavated in 2013, where the average metal and slag compositions were calculated for daily compositions over a 4-month period prior to excavation – Table I and Table II.

Based on these calculations, the slag can react with graphite at 1600°C to form solid SiC, liquid metal, and gas. MnO is reduced to form Mn in liquid metal and in gas; SiO₂ is reduced to form solid SiC, Si dissolved in liquid metal, and SiO in the gas. Carbon would dissolve in the Mn-Si-C metal.

The potential for reaction of metal with carbon was assessed by using the FSstel database in FactSage 6.4 (Bale *et al.*, 2002). It was found that the carbon solubility predicted with FactSage is very similar to that predicted by Tang and Olsen (2006), if slightly lower (see Figure 2). Most importantly for this discussion, the silicon content at double saturation of the metal (saturation with both graphite and silicon carbide) is essentially the same; see Table III. Metal

containing more silicon than required for double saturation would tend to dissolve carbon and precipitate silicon carbide if it were to come into contact with carbon. At 1600°C, the silicon concentration at double saturation is approximately 16.3% (by mass); as Table I indicates, typical industrially produced silicomanganese contains more silicon than this, and hence would be expected to dissolve carbon-based refractory.

To test these observations (possibility of SiC formation through reduction of SiO₂ in tapped slag; dissolution of C into tapped metal), the plant data, for which the averaged compositions are reported in Table I and Table II, was analysed in more detail. The results were presented at INFACON XIV (Steenkamp and Pistorius, 2015). An extract was included in the first part of the paper.

To test whether metal dissolving the carbon in the refractory would contribute to the wear observed in the hearth, the study was expanded to include tap data from seven furnaces (designated Furnace A to Furnace G), based

Table I

Compositions of tapped SiMn metal (mass percentages): typical metal (Olsen, Tangstad, and Lindstad, 2007) and industrial metal (Steenkamp, 2014) (averages, with standard deviation in parenthesis, where applicable)

	%Mn	%Si	%C	%Fe
Typical (Olsen, Tangstad, and Lindstad, 2007)	68	20	2	10
Industrial (Steenkamp, 2014)	66.3 (0.5)	17.1 (0.8)	1.8 (0.2)	14.8 (0.6)

Table II

Compositions of tapped SiMn slags (mass percentages): typical slag (Olsen, Tangstad, and Lindstad, 2007) and industrial slag (Steenkamp, 2014) (averages, with standard deviation in parenthesis where applicable)

	%MnO	%SiO ₂	%Al ₂ O ₃	%CaO	%MgO	%FeO
Typical (Olsen, Tangstad, and Lindstad, 2007)	9	45	16	21	9	0
Industrial (Steenkamp, 2014)	11.9 (1.8)	48.3 (0.8)	6.3 (0.7)	27.1 (1.0)	6.4 (0.4)	0

Insights into the potential for reduced refractory wear in silicomanganese smelters

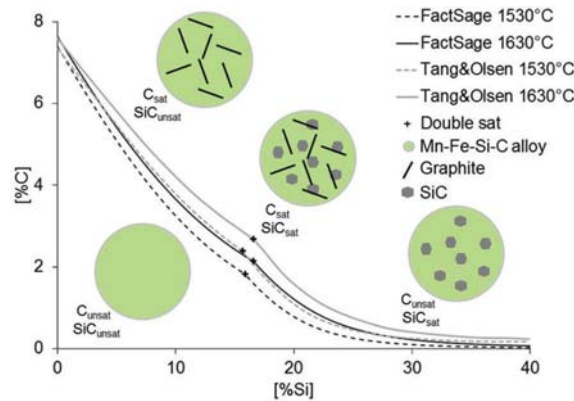


Figure 2—Carbon solubility in Mn-Fe-Si-C metals with mass ratio Mn:Fe = 5, at 1530°C and 1630°C, calculated with FactSage 6.4 (FSstel database; black lines) and by Tang and Olsen (2006) (grey lines). For silicon contents below the inflection in the curve, the stable solid phase at saturation is graphite; SiC is the stable phase at saturation for higher silicon contents. Representations of potential equilibrium phases at different compositions are shown

Table III
Comparison of the silicon concentration (mass percentage) in Mn₅Fe-Si-C melts at double saturation, as reported by Tang and Olsen (2006), and calculated with FactSage

Temperature (°C)	[%Si]-double saturation	
	Tang and Olsen	FactSage
1530	15.7	15.9
1630	16.6	16.6

Table IV
Summary of daily average tap information for Furnace A at Plant A prior to digout (Steenkamp Pistorius, and Tangstad, 2015)

Furnace	Plant	Tap dates	Number of days
A	A	2012/11/01–2013/02/24	116

at three different plants (designated Plant A to Plant C) in South Africa. The results are discussed in the second part of this paper.

Methodology

The first set of calculations was based on bulk chemical compositions of daily average slag and metal analyses, calculated from samples taken per tap. The tap dates are indicated in Table IV.

The second set of calculations was based on bulk chemical compositions of metal sampled per tap. Table V summarizes the tap dates and number of taps for each of the seven furnaces, based at the three different plants in South Africa.

The average slag and metal compositions, and standard deviations between analyses, as-received, were calculated per furnace, and are reported in Table VI.

In preparation of the thermodynamic calculations, the received metal and slag analyses were normalized.

To correct the slag compositions for entrained metal, it was assumed that all Fe reported in the slag analyses was present as entrained metal droplets, and that these droplets had the same composition as the daily tapped bulk metal (containing mainly Fe, Si, Mn, and C). The assumption was previously validated by SEM-EDS analysis on an industrial slag sample obtained from the same plant (Steenkamp,

Table V
Summary of tap information for the seven SAFs

Furnace	Plant	Tap dates	Number of taps
A	A	2014/08/01–2014/11/01	777
B	A	2014/08/01–2014/11/01	679
C	A	2014/08/01–2014/11/01	655
D	B	2014/09/01–2014/11/30	680
E	C	2011/09/01–2012/01/12	777
F	A	2014/08/01–2014/11/01	609
G	A	2014/08/01–2014/11/01	673

Table VI
As-received compositions of tapped SiMn metal (mass percentages with standard deviation in parenthesis)

	%Mn	%Si	%C	%Fe
Furnace A	67.1 (1.1)	16.5 (0.7)	1.8 (0.2)	13.8 (0.5)
Furnace B	67.3 (1.0)	16.4 (0.6)	1.9 (0.2)	13.7 (0.5)
Furnace C	67.4 (1.0)	16.5 (0.7)	2.0 (0.2)	13.7 (0.5)
Furnace D	65.6 (0.2)	17.3 (0.4)	1.7 (0.2)	14.7 (0.3)
Furnace E	66.1 (0.8)	16.4 (1.1)	1.8 (0.2)	15.1 (0.9)
Furnace F	67.2 (1.1)	16.6 (0.8)	1.8 (0.2)	13.7 (0.5)
Furnace G	67.1 (1.2)	16.7 (0.8)	1.8 (0.3)	13.7 (0.5)

Insights into the potential for reduced refractory wear in silicomanganese smelters

Pistorius, and Tangstad, 2015). Mass balance calculations were conducted to correct the reported slag composition for FeO (recalculated to be zero), SiO₂, and MnO (recalculated, based on entrained metal mass, to be lower). As part of this calculation, the mass of metal entrained per 100 g slag, was estimated.

The average slag and metal compositions, and standard deviations between analyses normalized, were calculated per furnace, and are reported in Table I, Table II, and Table VII.

Thermodynamic calculations were conducted in FactSage 6.4, using the FToxid, FSstel, and FactPS databases, and the liquid Mn-Fe-Si-C database of Tang and Olsen (2006). Process temperatures between 1530°C and 1600°C are required to produce Mn₇FeSiC_{sat} containing 17% Si in equilibrium with slag where the SiO₂ activity ranges between 0.2 and saturation, at 1 atmosphere pressure (Olsen, Tangstad, and Lindstad, 2007). Tapping temperatures are typically 50°C lower than process temperatures (Olsen, Tangstad, and Lindstad, 2007; Steenkamp, 2014). Therefore, calculations performed to study tap-hole refractory interaction with slag/metal were for 1550°C and 1600°C; and 1550°C, 1600°C, and 1650°C to study hearth refractory/metal interaction. In all instances a pressure of 1 atmosphere was specified. Selected reference states were graphite for carbon, solid SiC for SiC, and cristobalite for SiO₂.

Results and discussion

Potential for metal dissolving refractory in tap-hole

To test whether the metal would tend to dissolve carbon or SiC, contributing to tap-hole refractory wear, the activities of carbon (graphite reference state) and silicon carbide (solid SiC as reference state) in the metal, were calculated for 1600°C and 1550°C. The calculations were mainly performed in two ways: first, the metal was taken to be fully liquid (allowing no precipitation of solids); in this case, activities of SiC and graphite could exceed unity. Second, precipitation of solids allowed (graphite or SiC, in this case) and changes in composition and saturation conditions were noted. In these calculations, the analysed concentrations of Si, Mn, Fe, and C were used.

To give a more general indication, a graphite/silicon carbide saturation diagram for 1600°C was also calculated for a Mn:Fe mass ratio of 4.47 (the average mass ratio of the daily average tapped metal compositions), using the FSstel database (see Figure 3). The double saturation point at 1600°C was found to be 2.04% C and 16.26% Si for the Si-Mn-Fe-C metal with a Mn:Fe mass ratio of 4.47. Superimposed onto the metal saturation diagram in Figure 3 are the daily average tapped metal compositions for the 4-month period.

Figure 3 indicates that, as was the case for the average metal composition (Steenkamp, 2014), many of the metal compositions were supersaturated in SiC, and not saturated in C. To illustrate this differently, the calculated activities of C (with respect to graphite) and SiC for the case where precipitation of solids was suppressed are reported in Figure 4 (FSstel database). Figure 5 reports the calculated activities of C (with respect to graphite) and SiC for the case where precipitation of solids was allowed for both the FSstel and Tang and Olsen (2006) databases.

Table VII

Compositions of tapped SiMn metal (mass percentages): typical metal (Olsen, Tangstad, and Lindstad, 2007); industrial metal (Steenkamp, 2014) (average of normalized daily averages) and industrial metals (average of normalized tap analyses). Standard deviation in parentheses where applicable

	%Mn	%Si	%C	%Fe
Typical (Olsen, Tangstad, and Lindstad., 2007)	68	20	2	10
Industrial (Steenkamp, 2014)	66.3 (0.5)	17.1 (0.8)	1.8 (0.2)	14.8 (0.6)
Furnace A	67.6 (0.7)	16.7 (0.7)	1.8 (0.2)	13.9 (0.5)
Furnace B	67.8 (0.6)	16.5 (0.7)	1.9 (0.2)	13.8 (0.4)
Furnace C	67.7 (0.6)	16.6 (0.7)	2.0 (0.2)	13.8 (0.4)
Furnace D	66.1 (0.3)	17.5 (0.4)	1.7 (0.2)	14.8 (0.3)
Furnace E	66.6 (0.8)	16.5 (1.1)	1.8 (0.2)	15.2 (0.8)
Furnace F	67.6 (0.6)	16.8 (0.9)	1.8 (0.2)	13.8 (0.5)
Furnace G	67.6 (0.7)	16.8 (0.9)	1.8 (0.2)	13.8 (0.5)

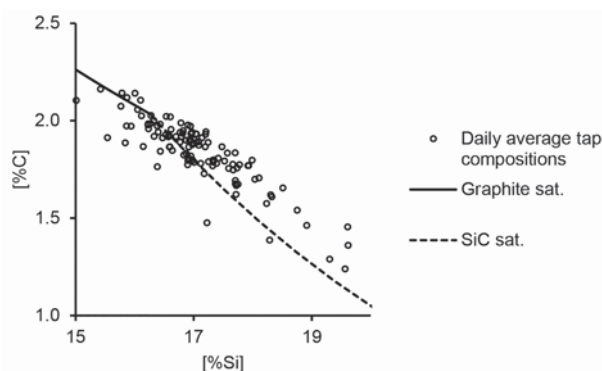


Figure 3—Carbon solubility in Mn-Fe-Si-C metals with Mn:Fe mass ratio of 4.47 at 1600°C, calculated with FactSage 6.4 (FSstel database); compositions given as mass percentages. The symbols show reported daily average silicomanganese compositions over a four-month period

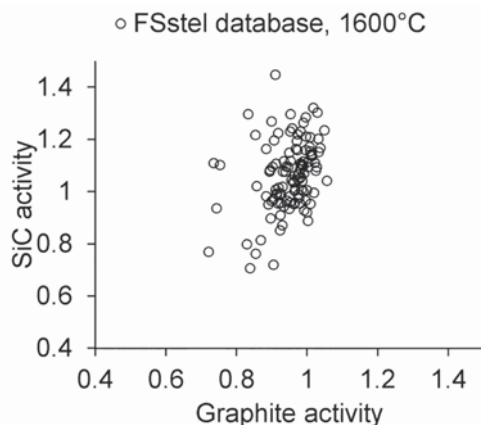


Figure 4—Activity of SiC (solid SiC as reference state) and activity of C (solid graphite as reference state) in Mn-Fe-Si-C metals at 1600°C, calculated with FactSage 6.4 (FSstel database) for the daily average tapped metal compositions. (Precipitation of solids suppressed)

Insights into the potential for reduced refractory wear in silicomanganese smelters

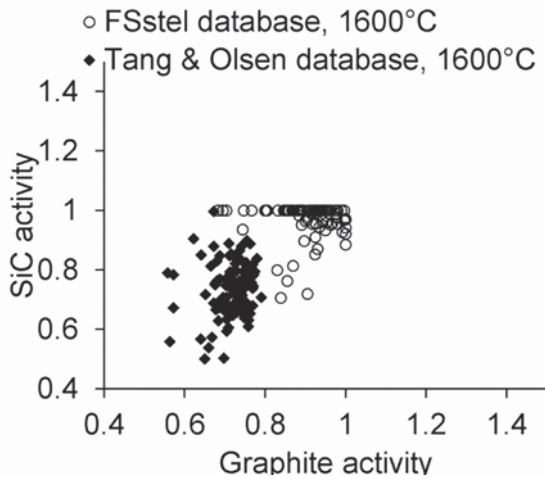


Figure 5—Activity of SiC and C in Mn-Fe-Si-C metals at 1600°C, calculated with FactSage 6.4 (FSstel and Tang and Olsen databases) for the daily average tapped metal compositions. (Precipitation of solids allowed)

Based on the calculated activities of SiC and C (FSstel), for the case where precipitation of solids was suppressed (Figure 4), 67% of the metal taps had SiC activities greater than unity, whereas only 20% of the taps were supersaturated in graphite. In the cases where solid precipitation was allowed to proceed to equilibrium (Figure 5), the proportion of graphite-saturated melts was even smaller (Table VIII); this is because SiC precipitation (which would occur in SiC-saturated melts) would remove carbon from solution, moving the metal composition even further from graphite saturation. Where the calculations were based on the Tang and Olsen (2006) database, the calculated activities of SiC and C, were lower than for FSstel (Table VIII).

It is worth noting that the predicted proportion of graphite-saturated melts remained low, even at a lower temperature of 1550°C (Table VIII). This is mainly because the silicon content at double saturation does not change much upon cooling to the lower temperature (as also indicated by Figure 2). This means that lowering the metal temperature (or slight cooling of the tap-block) would not necessarily help to avoid chemical wear of carbon tap-blocks by silicomanganese. This contrasts with the potential for reaction of SiO₂ in the slag with carbon (next section), which would be eliminated by cooling to 1550°C.

Potential for slag reduction refractory wear by slag in the tap-hole

The driving force for SiC formation, according to Equation [1], depends on the activity of SiO₂ in the slag, assuming unit activity for all other components.



Should the activity of SiO₂ in the slag be higher than the equilibrium activity (calculated to be 0.17 at 1600°C; reference state cristobalite), chemical attack of carbon refractory by SiO₂ in the slag would be possible. Calculated SiO₂ activities (for 1600°C) are reported in Figure 6. For all

slag compositions, the activity of SiO₂ was higher than the equilibrium activity of SiO₂ for SiC formation with C at 1600°C, *i.e.* all slag compositions had the potential to react chemically with C-based refractory materials. However, a decrease in temperature to 1550°C would render SiO₂ non-reactive towards carbon (Figure 6). (SiO₂ activities in the slag do change with temperature; these activities were also recalculated for 1550°C, but were found to be only slightly lower from the 1600°C values, shown in Figure 6.)

Also illustrated in Figure 6 is the effect of variation in slag composition on the activity of SiO₂ in the slag for a constant SiO₂ content (mass percentage), and the expected increase in SiO₂ activity with increased SiO₂ content of the slag.

In Figure 7, the SiO₂ contents of the tapped slag, and the Si contents of the tapped metal, are summarized (daily average; mass percentages) to illustrate variations in both. Also indicated in Figure 7 is the Si content of the metal for double saturation at 1600°C (Mn:Fe ratio of 4.47; broken line), emphasizing that most metal compositions have silicon concentrations greater than dual saturation.

The velocity and diffusion boundary layers that are taken into account in mass transfer calculations (Steenkamp, 2014) would develop near the wall inside a tap-hole, due to the effects of viscosity. Muller (2014) demonstrated that metal

Table VIII

Calculated proportions of metal taps that remained supersaturated with SiC or graphite after solids were allowed to precipitate in the metal, for temperatures of 1550°C and 1600°C. Numbers in parentheses for calculations were based on the Tang and Olsen (Tang and Olsen, 2006) database

Temperature (°C)	a _{SiC} = 1	a _c = 1
1550	92% (20%)	10% (0%)
1600	66% (0%)	4% (0%)

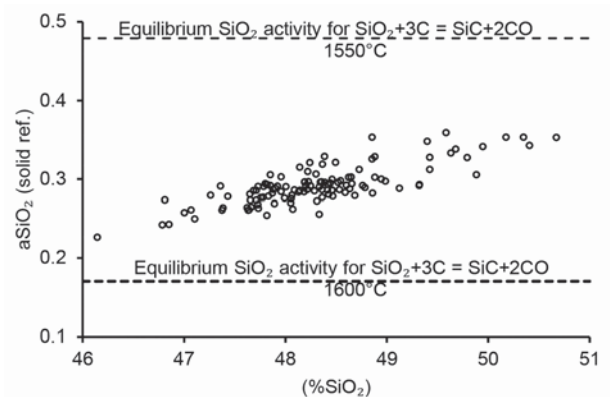


Figure 6—Activity of SiO₂ (solid SiO₂ [cristobalite] reference state) at 1600°C, calculated with FactSage 6.4 (FToxid database) as a function of SiO₂ content for the daily average tapped slag compositions. The broken lines give the equilibrium SiO₂ activities for possible reaction with carbon at 1550°C and 1600°C

Insights into the potential for reduced refractory wear in silicomanganese smelters

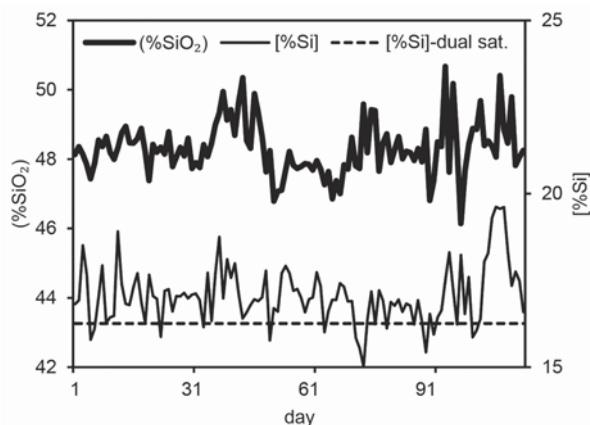


Figure 7—SiO₂ contents of the tapped slag (heavier line) and Si contents of the tapped metal (thinner line) (daily average mass percentages); also shown is the Si content of the metal for dual saturation at 1600°C (Mn:Fe ratio of 4.47) calculated with FactSage 6.4 (FSstel database) (broken line)

entrained in the slag phase has an influence on the effective viscosity, and therefore also on the volumetric flow rate through a tap-hole. Both factors would influence the rate at which SiO₂ is transferred to the slag/refractory interface, where chemical reaction between slag and refractory would occur.

In Figure 8 the entrained metal concentration (grams per 100 g slag) in slag samples, calculated for the daily average tapped slag compositions, is presented. A distinct shift in entrainment is observed after 45 days of production (for unknown reasons).

Potential for metal dissolving refractory in hearth

To test whether the metal would tend to dissolve carbon and therefore contribute to hearth refractory wear, the activities of carbon (graphite reference state) and silicon carbide (solid SiC as reference state) in the metal were calculated for 1550°C, 1600°C, and 1650°C. SiC was included in the calculations, as it could potentially be utilized as an alternative hot face lining material in the hearth. In the calculations, precipitation of solids (graphite or SiC) was allowed, and changes in composition and saturation conditions were noted. In these calculations, the normalized concentrations of Si, Mn, Fe, and C were used.

Based on the calculated activities of SiC, and C (FSstel, Table IX), the number of metal taps that had SiC activities greater than or equal to unity decreased with increasing temperature. This was not the case for supersaturation in graphite: from 1550°C to 1600°C the number of taps decreased, but from 1600°C to 1650°C the number of taps increased. Where the calculations were based on the Tang and Olsen (2006) database (Table X), the number of supersaturated metal taps decreased with increase in temperature, both from a graphite and a SiC saturation perspective. Again where the calculations were based on the Tang and Olsen (2006) database (Table X), the calculated activities of SiC and C, were lower than for FSstel (Table IX). This was the case for all furnaces from all plants.

The results are presented differently in Figure 9 (data from FSstel) and Figure 10 (data from Tang and Olsen): the cumulative fraction of metal taps, as a function of SiC or

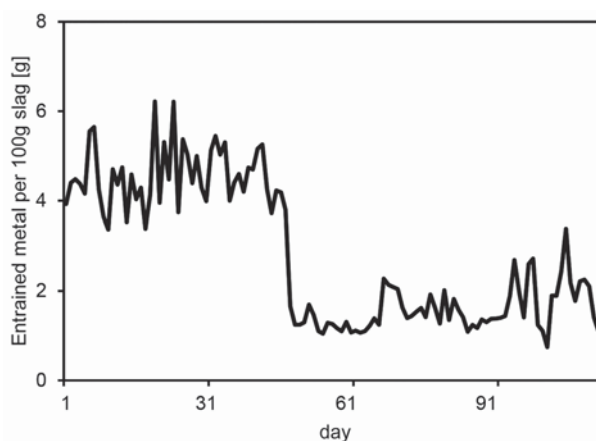


Figure 8—Calculated entrained metal (grams per 100 g slag) in tapped slag, calculated from %Fe reported in daily average tapped slag compositions

Table IX

Calculated percentages of metal taps that remained supersaturated with SiC or graphite after solids were allowed to precipitate in the metal, for temperatures of 1550°C, 1600°C, and 1650°C. Calculations based on the FSstel database

Furnace	Plant	a _{SiC} = 1			a _C = 1		
		1550°C	1600°C	1650°C	1550°C	1600°C	1650°C
A	A	65.4	19	3	14.3	1.7	9
B	A	73.9	15.8	1	22.7	9.6	16
C	A	79.8	32.7	4	34	24.3	46
D	B	99.1	53.7	1.2	0.3	0.4	0
E	C	65.4	15.7	1.2	14.3	1.7	4
F	A	76.4	15.3	1	11.8	3.4	5
G	A	81.1	22.6	2.2	13.8	5.8	10

Table X

Calculated percentages of metal taps that remained supersaturated with SiC or graphite after solids were allowed to precipitate in the metal, for temperatures of 1550°C, 1600°C, and 1650°C. Calculations based on the Tang and Olsen (2006) database

Furnace	Plant	a _{SiC} = 1			a _C = 1		
		1550°C	1600°C	1650°C	1550°C	1600°C	1650°C
A	A	6.4	0.4	0	0.3	0	0
B	A	4.4	0.1	0.1	0.7	0	0
C	A	15.3	0.6	0	2	0.6	0.3
D	B	11.8	0.3	0	0	0	0
E	C	5.4	0.1	0	0.1	0	0
F	A	4.3	0.2	0.2	0.3	0	0
G	A	6.4	1	0	0.4	0.1	0

Insights into the potential for reduced refractory wear in silicomanganese smelters

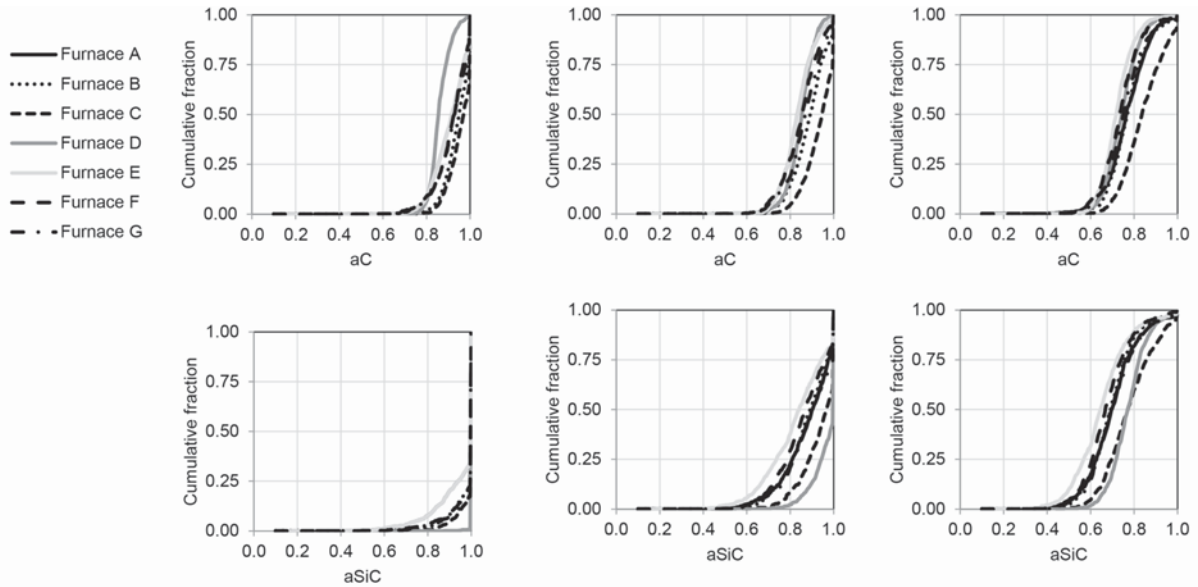


Figure 9—Cumulative fraction of metal taps as a function of SiC or graphite activity after solids were allowed to precipitate in the metal, for temperatures of 1550°C, 1600°C, and 1650°C. Calculations based on the FSstel database

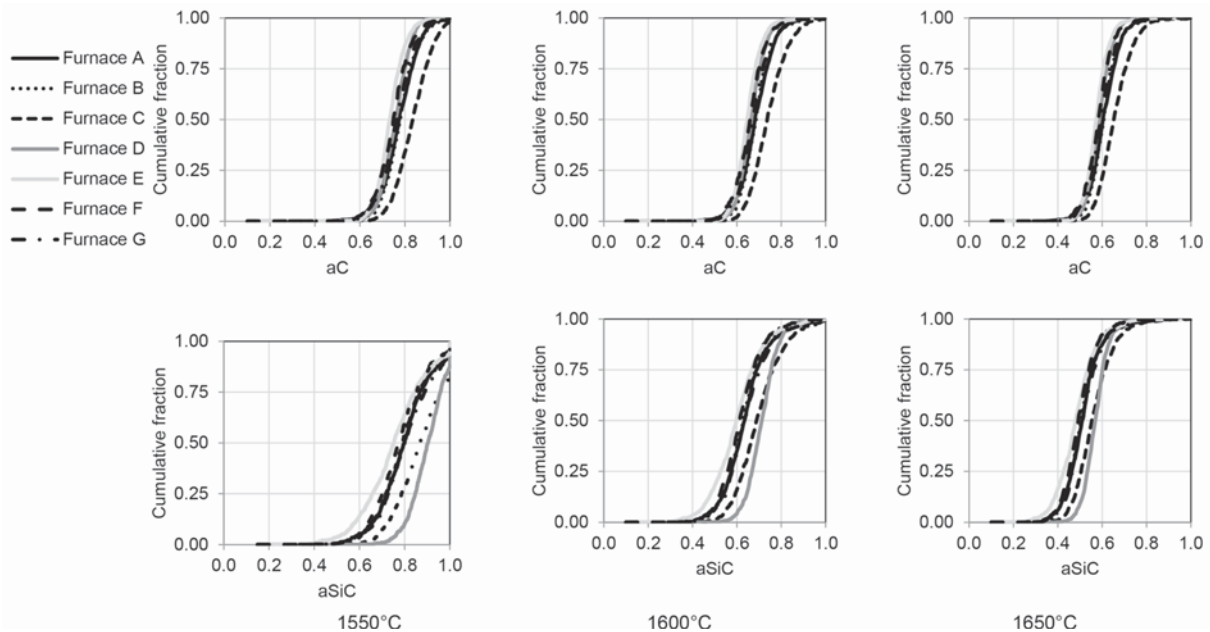


Figure 10—Cumulative fraction of metal taps as a function of SiC or graphite activity after solids were allowed to precipitate in the metal, for temperatures of 1550°C, 1600°C, and 1650°C. Calculations based on the Tang and Olsen (2006) database

graphite activity (after solids were allowed to precipitate in the metal), for temperatures of 1550°C, 1600°C, and 1650°C, per furnace. The differences in results obtained from the two different databases – discussed before – were again observed.

If the deviation of a_C or a_{SiC} from unity is taken as an indication of the driving force for refractory wear through dissolution into the metal, the driving force for SiC dissolution at 1550°C is lower than for carbon. At 1650°C the opposite seems to occur, with the driving force for SiC dissolution being slightly higher than for carbon. The effect on refractory wear is illustrated in Figure 11, where SiC

solubility has a greater sensitivity to increases in temperature than carbon.

As was done for the thermodynamic calculations studying slag/refractory interaction (Steenkamp, 2014), the next step would be to test these observations on laboratory scale.

Conclusions

During excavation of a 48 MVA submerged arc furnace used for SiMn production, two high-wear areas were found: the tap-hole area and the furnace hearth. Carbon-based

Insights into the potential for reduced refractory wear in silicomanganese smelters

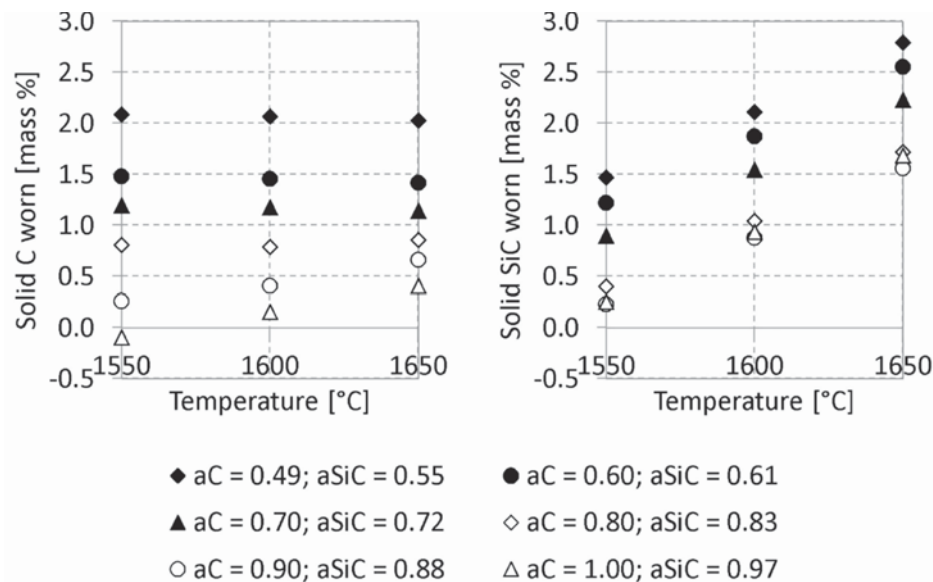


Figure 11—Refractory wear (expressed as mass % metal), calculated for 100% C or 100% SiC, and normalized tapped metal compositions for temperatures of 1550°C, 1600°C, and 1650°C. The metal compositions were selected from the data-set for Furnace A, Plant A, to represent increased activities of carbon and SiC. Calculations based on the Tang and Olsen (2006) database

refractory material formed the hot face refractory. Analysis of daily average tapped slag and metal compositions produced in the four months prior to excavation confirmed the potential for refractory wear in the tap-hole through C dissolution in the metal and SiC formation by chemical reaction with SiO₂ in the slag. Similar analysis of tapped metal data from seven SiMn smelters situated at three plants in South Africa indicated the potential for refractory wear in the hearth through C dissolution in the metal. From a metal dissolution perspective, theoretical indications are that SiC would be more suitable as tap-hole refractory, and C as hearth refractory. Experimental confirmation of the observations from thermodynamic calculations would be useful.

Acknowledgements

This paper is published with the permission of Mintek, after being reviewed internally by Isabel Geldenhuys, Glen Denton, and Herman Lagendijk. The authors would like to thank Oleg Ostrovski, and Merete Tangstad, for discussions around activity of C and SiC in metal, and SiO₂ in slag produced in SiMn smelters, Kai Tang for the supply of the database, and management at the three different plants for supply of plant data.

References

- BALE, C., CHARTRAND, P., DEGTEROV, S., and ERIKSSON, G. 2002. FactSage thermochemical software and databases. *Calphad*, vol. 26. pp. 189–228. <http://www.sciencedirect.com/science/article/pii/S0364591602000354>
- GOUS, J. 2015. Personal communication.
- LEE, W.E. and MOORE, R.E. 1998. Evolution of in situ refractories in the 20th century. *Journal of the American Ceramic Society*, vol. 81, no. 6. pp. 1385–1410.

- MØLNÅS, H. 2011. Compatibility Study of Carbon-Based Refractory Materials utilized in Silicomanganese Production Furnaces. Norwegian University of Science and Technology.
- MULLER, J. 2014. Evaluation of HCFeMn and SiMn Slag Tapping Flow Behaviour Using Physicochemical Property Modelling and Analytical Flow Modelling. MSc thesis, University of Pretoria.
- OLSEN, S.E., TANGSTAD, M., and LINDSTAD, T. 2007. Production of Manganese Ferrometals. Tapir Academic Press, Trondheim, Norway.
- STEENKAMP, J.D. 2014. Chemical Wear of Carbon-based Refractory Materials in a Silicomanganese Furnace Tap-hole. PhD thesis, University of Pretoria.
- STEENKAMP, J.D., GOUS, J.P., PISTORIUS, P.C., TANGSTAD, M., and ZIETSMAN, J.H. 2014. Wear analysis of a taphole from a SiMn production furnace. *Furnace Tapping Conference 2014*, Muldersdrift, South Africa, 27–28 May 2014. Southern African Institute of Mining and Metallurgy, Johannesburg. pp. 51–64.
- STEENKAMP, J.D. and PISTORIUS, P.C. 2015. Chemical wear of carbon-based refractory materials in a silicomanganese furnace tap-hole. *INFACON XIV*, Kiev, Ukraine. pp. 505–510.
- STEENKAMP, J.D., PISTORIUS, P.C., and TANGSTAD, M. 2015. Chemical wear analysis of a tap-hole on a SiMn production furnace. *Journal of the Southern African Institute of Mining and Metallurgy*, vol. 115, no. 3. pp. 199–208.
- TANG, K. and OLSEN, S.E. 2006. Computer simulation of equilibrium relations in manganese ferrometal production. *Metallurgical and Materials Transactions B*, vol. 37. pp. 599–606. ◆



UNIVERSITEIT VAN PRETORIA
UNIVERSITY OF PRETORIA
YUNIBESITHI YA PRETORIA
Denkiesers • Leading Minds • Dikgopolo tsa Dihlatse



SAIMM
THE SOUTHERN AFRICAN INSTITUTE
OF MINING AND METALLURGY

The Southern African Institute of Mining and Metallurgy and the
Mining Resilience Research Institute at the University of Pretoria
presents the

Resilience in the Mining Industry Conference 2016



ABOUT THE CONFERENCE

Many international standards have been designed to monitor the behaviour of multinationals to ensure that their footprint is not associated with human rights abuses, environmental degradation, corruption and tax evasion and avoidance. The large mining houses make great effort to tick the compliance boxes regarding these international requirements. But South Africa needs more than that. South Africa needs a modernised mining industry with informed and committed role-players.

At this conference papers will be presented addressing the current status of and guide future research. These should inform the day-to-day challenges that industry and communities are grappling with.

The issues faced by the mining industry in Africa are by nature complex and require a multidisciplinary and integrated approach to resolution. Thus research needs to be focused on multi-disciplinary cooperation, drawing on a broad pool of people, resulting in innovative solutions. Innovation does not occur in isolation.

We aim contribute towards the collective effort to modernise the industry, by creating platforms for discussion and engagement. With the founding principles including accessibility, independence and transparency, the institute is ideally positioned to facilitate dialogue to find new ways for the industry. For the mining industry to fulfil its role as a significant source of economic growth and social transformation in Africa, serious complex challenges need to be overcome.



13–14 July 2016: Conference
15 July 2016: VR Mining Site Visit
University of Pretoria

OBJECTIVES

- South Africa's future is still intricately linked to what happens in its mining industry, however the industry needs re-positioning as a valued source of national economic growth and social transformation;
- To conduct and share current and future research which will assist with this re-positioning of our Industry and actively contribute towards solutions for the complex challenges faced by the industry;
- Aim to host a conference in an attempt to widen the solution-seeking net to include all potential stakeholders such as the University of Pretoria, Industry Leaders, Policy makers and associated Research and Academic Institutions. Issues around legacy, responsibility, impact and innovation will be discussed and current and future research requirements will be presented.

WHO SHOULD ATTEND

- Mining Industry leaders
- Academia
- Policy makers
- State organisations
- Labour

*Conference Announcement
and Call for Papers*

For further information contact:

Conference Co-ordinator, Camielah Jardine
SAIMM, P O Box 61127, Marshalltown 2107
Tel: (011) 834-1273/7 • Fax: (011) 833-8156 or (011) 838-5923
E-mail: camialah@saimm.co.za • Website: <http://www.saimm.co.za>

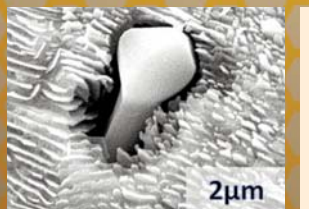
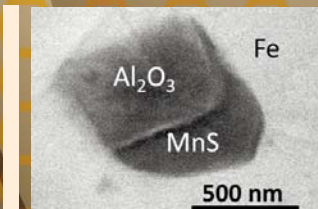
SCHOOL PRODUCTION of CLEAN STEEL

25–26 July 2016

Mintek, Johannesburg



Photographs courtesy of Jason Pieterse and Chris Pistorius



INTRODUCTION

South Africa has a proud history in the production of both mild steel and stainless steel with production facilities in Gauteng, Kwazulu-Natal, Mpumalanga, the Eastern and Western Cape provinces. At these facilities steel is produced from scrap or from ore via ironmaking facilities.

The Center for Iron and Steelmaking Research at Carnegie Mellon University in Pittsburgh, Pennsylvania, USA has a proud history on iron and steelmaking. Collaboration between CMU and the South African iron and steel industry includes a school on steelmaking presented by Prof. Richard Fruehan in Vanderbijlpark in 1996.

At Clean Steel 2015 Prof. Chris Pistorius will continue the collaboration by addressing the following topics:

CONTROLLING DISSOLVED ELEMENTS

1. What is clean steel?
2. Relevant process conditions in blast furnace, steelmaking converter, electric arc furnace, ladle furnace and caster (temperatures, oxygen activity, slag basicity, stirring).
3. Control of dissolved elements (C, H, N, O, P, S, Cu, Sn):
 - a. Sources (raw materials; environment)
 - b. Thermodynamic and kinetic principles of control
 - c. Practical control methods:
 - i. hot metal desulfurization and dephosphorization
 - ii. metal-slag reactions in blast furnace, steelmaking and ladle
 - iii. clean tapping
 - iv. metal-gas reactions, including nitrogen pick-up
 - v. deoxidation
 - vi. role of slag
 - vii. mitigating the surface quality effects of Cu & Sn.

CONTROLLING MICRO-INCLUSIONS

1. Principles of control:
 - a. inclusion composition evolution over time
 - b. removing inclusions to slag or fluxes: gas stirring and flotation kinetics
 - c. inclusion-metal-slag reactions: equilibria and kinetics (spinel formation)
 - d. calcium modification.
2. Sources of micro-inclusions:
 - a. deoxidation and reoxidation products
 - b. ladle glaze
 - c. inclusions in ferro-alloys and ferro-alloy reaction products
 - d. mold flux entrainment
 - e. reoxidation.
3. Assessing micro-inclusions:
 - a. overall steel composition
 - b. caster behavior
 - c. microanalysis (polished sections; extracted inclusions)
 - d. other analytical approaches.
4. Summary: general guidelines for clean-steel practice; opportunities to learn more and share information.

LECTURER

Prof. C Pistorius



Chris Pistorius is the POSCO Professor of Iron and Steelmaking in the Department of Materials Science and Engineering at Carnegie Mellon University (Pittsburgh, PA, USA), where he has been since 2008. Previously he was Professor and Head of Department of Materials Science and Metallurgical Engineering at the University of Pretoria. He holds Bachelor's and Master's degrees in Metallurgical Engineering from the University of Pretoria, and a PhD from the University of Cambridge, United Kingdom. His current research interests include the fundamentals of ironmaking and steelmaking reactions, and electrochemistry of corrosion and metals production.

WHO SHOULD ATTEND

The school is aimed at delegates from steel producing companies in South Africa or those who support them, and includes:

- Senior management
- First line management
- Process/development engineers
- Researchers
- Middle management
- Plant/production engineers
- Design engineers

EXHIBITION/SPONSORSHIP

Sponsorship opportunities are available. Companies wishing to sponsor or exhibit should contact the Conference Co-ordinator.



SAIMM
THE SOUTHERN AFRICAN INSTITUTE
OF MINING AND METALLURGY

For further information contact:

Head of Conferencing, Raymond van der Berg, SAIMM
P O Box 61127, Marshalltown 2107
Tel: (011) 834-1273/7 · Fax: (011) 833-8156 or (011) 838-5923
E-mail: raymond@saimm.co.za · Website: <http://www.saimm.co.za>

F
i
r
s
t

A
n
n
o
u
n
c
e
m
e
n
t

INTERNATIONAL ACTIVITIES

2016

15–16 February 2016 — Global Mining Standards and Guidelines Group ‘GMSG—SAIMM Forum 2016: Building towards the future of mining’

Emperor's Palace, Johannesburg, Gauteng
Contact: Raymond van der Berg
Tel: +27 11 834-1273/7, Fax: +27 11 838-5923/833-8156
E-mail: raymond@saimm.co.za, Website: <http://www.saimm.co.za>

14–17 March 2016 — Diamonds still Sparkle 2016 Conference

Gaborone International Convention Centre
Contact: Yolanda Ramokgadi
Tel: +27 11 834-1273/7, Fax: +27 11 838-5923/833-8156
E-mail: yolanda@saimm.co.za, Website: <http://www.saimm.co.za>

17–18 May 2016 — The SAMREC/SAMVAL Companion Volume Conference

Johannesburg
Contact: Raymond van der Berg
Tel: +27 11 834-1273/7, Fax: +27 11 838-5923/833-8156
E-mail: raymond@saimm.co.za, Website: <http://www.saimm.co.za>

18–19 May 2016 — Aachen International Mining Symposia (AIMS 2016) First International Conference Mining in Europe

Aachen, Germany
Contact: Conference Organisation of AIMS
Tel: +49-(0)241-80 95673, Fax: +49-(0)241-80 92272
E-mail: aims@mre.rwth-aachen.de
Website: <http://www.aims.rwth-aachen.de>

21–28 May 2016 — ALTA 2016

Perth, Western Australia
Contact: Allison Taylor
Tel: +61 (0) 411 692 442, E-mail: allison.taylor@altamet.com.au
Website: <http://www.altamet.com.au>

9–10 June 2016 — New technology and innovation in the Minerals Industry Colloquium

Mintek, Randburg
Contact: Camielah Jardine
Tel: +27 11 834-1273/7, Fax: +27 11 838-5923/833-8156
E-mail: camielah@saimm.co.za, Website: <http://www.saimm.co.za>

27–28 June 2016 — The 2nd School on Manganese Ferroalloy Production

Johannesburg
Contact: Yolanda Ramokgadi
Tel: +27 11 834-1273/7, Fax: +27 11 838-5923/833-8156
E-mail: yolanda@saimm.co.za, Website: <http://www.saimm.co.za>

13–15 July 2016 — Resilience in the Mining Industry Conference 2016

University of Pretoria
Contact: Camielah Jardine
Tel: +27 11 834-1273/7, Fax: +27 11 838-5923/833-8156
E-mail: camielah@saimm.co.za, Website: <http://www.saimm.co.za>

25–26 July 2016 — Production of Clean Steel

Mintek, Randburg
Contact: Raymond van der Berg
Tel: +27 11 834-1273/7, Fax: +27 11 838-5923/833-8156
E-mail: raymond@saimm.co.za, Website: <http://www.saimm.co.za>

1–3 August 2016 — Hydrometallurgy Conference 2016

‘Sustainability and the Environment’
in collaboration with MinProc and the Western Cape Branch
Belmont Mount Nelson Hotel, Cape Town
Contact: Yolanda Ramokgadi
Tel: +27 11 834-1273/7, Fax: +27 11 838-5923/833-8156
E-mail: yolanda@saimm.co.za, Website: <http://www.saimm.co.za>

16–18 August 2016 — The Tenth International Heavy Minerals Conference ‘Expanding the horizon’

Sun City, South Africa
Contact: Camielah Jardine
Tel: +27 11 834-1273/7, Fax: +27 11 838-5923/833-8156
E-mail: camielah@saimm.co.za, Website: <http://www.saimm.co.za>

12–14 September 2016 — 8th International Symposium on Ground Support in Mining and Underground Construction

Kulturens Hus – Conference & Congress, Luleå, Sweden
Contact: Erling Nordlund
Tel: +46-920493535, Fax: +46-920491935
E-mail: erling.nordlund@ltu.se, Website: <http://groundsupport2016.com>

9–11 November 2016 — AMI Ferrous and Base Metals Development Network Conference 2016

KwaZulu-Natal
Contact: Raymond van der Berg
Tel: +27 11 834-1273/7, Fax: +27 11 838-5923/833-8156
E-mail: raymond@saimm.co.za, Website: <http://www.saimm.co.za>

2017

25–28 June 2017 — Emc 2017: European Metallurgical Conference

Leipzig, Germany
Contact: Paul-Ernst-Straße
Tel: +49 5323 9379-0, Fax: +49 5323 9379-37
E-mail: EMC@gdmg.de, Website: <http://emc.gdmg.de>

2–7 October 2017 — AfriRock 2017: ISRM International Symposium ‘Rock Mechanics for Africa’

Cape Town Convention Centre, Cape Town
Contact: Raymond van der Berg
Tel: +27 11 834-1273/7, Fax: +27 11 838-5923/833-8156
E-mail: raymond@saimm.co.za, Website: <http://www.saimm.co.za>

Company Affiliates

The following organizations have been admitted to the Institute as Company Affiliates

3 M South Africa	Elbroc Mining Products (Pty) Ltd	Nalco Africa (Pty) Ltd
AECOM SA (Pty) Ltd	Engineering and Project Company Ltd	Namakwa Sands (Pty) Ltd
AEL Mining Services Limited	eThekweni Municipality	New Concept Mining (Pty) Limited
Air Liquide (PTY) Ltd	Exxaro Coal (Pty) Ltd	Northam Platinum Ltd - Zondereinde
AMEC Mining and Metals	Exxaro Resources Limited	Outotec (RSA) (Proprietary) Limited
AMIRA International Africa (Pty) Ltd	Fasken Martineau	PANalytical (Pty) Ltd
ANDRITZ Delkor(Pty) Ltd	FLSmidth Minerals (Pty) Ltd	Paterson and Cooke Consulting Engineers (Pty) Ltd
Anglo Operations Ltd	Fluor Daniel SA (Pty) Ltd	Polysius A Division Of Thyssenkrupp Industrial Solutions (Pty) Ltd
Anglo Platinum Management Services (Pty) Ltd	Franki Africa (Pty) Ltd Johannesburg	Precious Metals Refiners
Anglogold Ashanti Ltd	Fraser Alexander Group	Rand Refinery Limited
Atlas Copco Holdings South Africa (Pty) Limited	Geobrugg Southern Africa	Redpath Mining (South Africa) (Pty) Ltd
Aurecon South Africa (Pty) Ltd	Glencore	Rosond (Pty) Ltd
Aveng Moolmans (Pty) Ltd	Goba (Pty) Ltd	Royal Bafokeng Platinum
Axis House (Pty) Ltd	Hall Core Drilling (Pty) Ltd	Roymec Tecvhnologies (Pty) Ltd
Bafokeng Rasimone Platinum Mine	Hatch (Pty) Ltd	Runge Pincock Minarco Limited
Barloworld Equipment -Mining	Herrenknecht AG	Rustenburg Platinum Mines Limited
BASF Holdings SA (Pty) Ltd	HPE Hydro Power Equipment (Pty) Ltd	SAIEG
Bateman Minerals and Metals (Pty) Ltd	Impala Platinum Limited	Salene Mining (Pty) Ltd
BCL Limited	IMS Engineering (Pty) Ltd	Sandvik Mining and Construction Delmas (Pty) Ltd
Becker Mining (Pty) Ltd	Ivanhoe Mines SA	Sandvik Mining and Construction RSA(Pty) Ltd
BedRock Mining Support (Pty) Ltd	JENNMAR South Africa	SANIRE
Bell Equipment Company (Pty) Ltd	Joy Global Inc. (Africa)	Sasol Mining(Pty) Ltd
Blue Cube Systems (Pty) Ltd	Kadumane Manganese Resources	Sebilo Resources (Pty) Ltd
Bluhm Burton Engineering (Pty) Ltd	Leco Africa (Pty) Limited	SENET
Blyvooruitzicht Gold Mining Company Ltd	Longyear South Africa (Pty) Ltd	Senmin International (Pty) Ltd
BSC Resources	Lonmin Plc	Shaft Sinkers (Pty) Limited
CAE Mining (Pty) Limited	Lull Storm Trading (PTY)Ltd	Sibanye Gold (Pty) Ltd
Caledonia Mining Corporation	T/A Wekaba Engineering	Smec SA
CDM Group	Magnetech (Pty) Ltd	SMS Siemag South Africa (Pty) Ltd
CGG Services SA	Magotteaux(PTY) LTD	Sound Mining Solutions (Pty) Ltd
Chamber of Mines	MBE Minerals SA Pty Ltd	South 32
Concor Mining	MCC Contracts (Pty) Ltd	SRK Consulting SA (Pty) Ltd
Concor Technicrete	MDM Technical Africa (Pty) Ltd	Technology Innovation Agency
Council for Geoscience Library	Metalock Industrial Services Africa (Pty)Ltd	Time Mining and Processing (Pty) Ltd
CSIR-Natural Resources and the Environment	Metorex Limited	Tomra Sorting Solutions Mining (Pty) Ltd
Department of Water Affairs and Forestry	Metso Minerals (South Africa) (Pty) Ltd	Ukwazi Mining Solutions (Pty) Ltd
Digby Wells and Associates	Minerals Operations Executive (Pty) Ltd	Umgeni Water
Downer EDI Mining	MineRP Holding (Pty) Ltd	VBKOM Consulting Engineers
DRA Mineral Projects (Pty) Ltd	Mintek	Webber Wentzel
DTP Mining	MIP Process Technologies	Weir Minerals Africa
Duraset	Modular Mining Systems Africa (Pty) Ltd	WorleyParsons (Pty) Ltd
	MSA Group (Pty) Ltd	
	Multotec (Pty) Ltd	
	Murray and Roberts Cementation	

Forthcoming SAIMM events...

EXHIBITS/SPONSORSHIP

Companies wishing to sponsor
and/or exhibit at any of these
events should contact the
conference co-ordinator
as soon as possible

For the past 120 years, the Southern African Institute of Mining and Metallurgy, has promoted technical excellence in the minerals industry. We strive to continuously stay at the cutting edge of new developments in the mining and metallurgy industry. The SAIMM acts as the corporate voice for the mining and metallurgy industry in the South African economy. We actively encourage contact and networking between members and the strengthening of ties. The SAIMM offers a variety of conferences that are designed to bring you technical knowledge and information of interest for the good of the industry. Here is a glimpse of the events we have lined up for 2016. Visit our website for more information.



For further information contact:

Conferecing, SAIMM
P O Box 61127, Marshalltown 2107
Tel: (011) 834-1273/7
Fax: (011) 833-8156 or (011) 838-5923
E-mail: raymond@saimm.co.za

SAIMM DIARY

2016

- ◆ **FORUM**
Global Mining Standards and Guidelines Group 'GMSG—
SAIMM Forum 2016: Building towards the future of mining'
15–16 February 2016
Emperor's Palace, Johannesburg, Gauteng
- ◆ **CONFERENCE**
Diamonds still Sparkle 2016 Conference
14–17 March 2016
Gaborone International Convention Centre
- ◆ **CONFERENCE**
The SAMREC/SAMVAL Companion Volume Conference
17–18 May 2016
Johannesburg
- ◆ **COLLOQUIUM**
New technology and innovation in the Minerals Industry
Colloquium
9–10 June 2016
Mintek, Randburg
- ◆ **SCHOOL**
The 2nd School on Manganese Ferroalloy Production
Johannesburg
27–28 June 2016
- ◆ **CONFERENCE**
Resilience in the Mining Industry Conference 2016
University of Pretoria
13–15 July 2016
- ◆ **SCHOOL**
Production of Clean Steel
Mintek, Randburg
25–26 July 2016
- ◆ **CONFERENCE**
Hydrometallurgy Conference 2016
'Sustainability and the Environment'
in collaboration with MinProc and the Western Cape Branch
Belmont Mount Nelson Hotel, Cape Town
1–3 August 2016
- ◆ **CONFERENCE**
The Tenth International
Heavy Minerals Conference 'Expanding the horizon'
Sun City, South Africa
16–18 August 2016
- ◆ **CONFERENCE**
AMI Ferrous and Base Metals Development Network
Conference 2016
KwaZulu-Natal
9–11 November 2016



ELBROC
MINING PRODUCTS (PTY) LTD

PRE-STRESSED YIELDING ARCH SUPPORT



TUNNEL SUPPORT

Benefits

- Simple and fast installation
- Very high load carrying capacity
- Long operational life
- Active support by the arch set using hydraulic prop technology
- Cost effective
- Dimensional and design flexibility
- Suitable for various excavation heights
- Reduced cribbing required

Applications

- Tunnel junctions
- Over and under ore passes
- Haulage
- Incline shaft portals
- Active support through bad ground conditions, dykes, faults, friable ground



**FOR OUR FULL PRODUCT RANGE
PLEASE VISIT OUR WEBPAGE**

a member of the

rbh
royal bafokeng holdings



Tel: 011 974 8013 • Fax: 011 974 2019 • sales@elbroc.co.za

www.elbroc.co.za

mogs